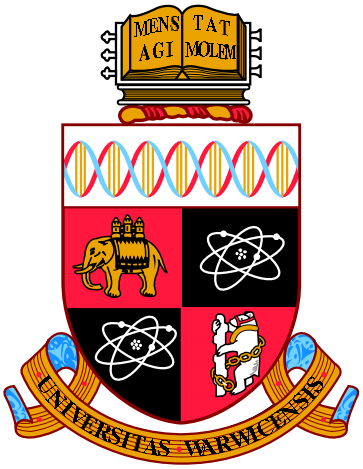

Vertical variation in diffusion coefficient within sediments

by

I. D. Chandler

Thesis

Submitted to the University of Warwick

for the degree of

Doctor of Philosophy

School of Engineering

May 2012

THE UNIVERSITY OF WARWICK

Contents

List of Figures

List of Tables

Acknowledgments

Firstly, I would like to express my gratitude to my supervisors Dr Jonathan Pearson and Prof Ian Guymer for giving me the opportunity to study for the PhD, and for providing advice and guidance along the way.

I gratefully acknowledge the Engineering and Physical Sciences Research Council (EPSRC, CASE/CNA/07/75) and Unilever Safety and Environmental Assurance Centre (SEAC) for their financial support. I thank Dr Roger Van-Egmond, Dr Oliver Price and Dr Chris Finnegan from SEAC for the support and input throughout the PhD.

I would like to thank the academic staff at the School of Engineering, most importantly Dr Petr Denissenko for the loan of his water bath and Mr Neil Reynolds for use of the high speed camera. The technical staff at the School of Engineering are thanked for all their support, particularly Mr Ian Baylis and Mr Colin Banks.

My colleagues, especially Dr Jop VlasKamp, Dr David Hunter, Dr Andrew Skeen, Dr Paul Dunkley, Dr Visoth Tiev, Dr Amy Jones, Mr James Hart and Mr Andrew King who have been a infinite source of friendship and support throughout my time at the University of Warwick, for which I am very grateful.

Finally, most of all, I would like to thank my family and my fiancée for all their emotional and moral support. Without them, this thesis would not have been completed. Thank you very much.

Declarations

I declare that the work in this thesis has been composed by myself and that no portion of this material has been submitted in support of another degree or qualification at a degree granting institution. The work as been my own except where indicated and all quotations have been distinguished by quotation marks and the sources of information have been acknowledged.

Abstract

River ecosystems can be strongly influenced by contaminants in the water column, in the pore water and attached to sediment particles. Current models [TGD, 2003] predict exposure to sediments based on equilibrium partitioning between dissolved and suspended-particle-sorbed phase in the water column despite numerous studies showing significant direct mass transfer across the sediment water interface. When exchange across the interface (hyporheic exchange) is included in modelling the diffusion coefficient is assumed to be constant with depth.

The overall aims of this research were to quantify the vertical variation in diffusion coefficient below the sediment water interface and asses the use of a modified EROSIMESS-System (erosimeter) in the study of hyporheic exchange.

The modified erosimeter and novel fibre optic fluorometers measuring in-bed concentrations Rhodamine WT were employed in an experimental investigation. Five different diameter glass sphere beds (0.15 to 5.0mm) and five bed shear velocities (0.01 to 0.04m/s) allowed the vertical variation in diffusion coefficient to be quantified to a depth of 0.134m below the sediment water interface.

The vertical variation in diffusion coefficient can be described using an exponential function that was found to be consistent for all the parameter combinations tested. This function, combined with the scaling relationship proposed by O'Connor and Harvey [2008] allows a prediction of the diffusion coefficient below the sediment water interface based on bed shear velocity, roughness height and permeability. 1D numerical diffusion model simulations using the exponential function compare favourably with the experimental data.

Chapter 1

Introduction

In recent years there has been greater awareness of the impact chemical pollutants have on the environment, particularly aquatic ecosystems and the concentrations within sediment beds. River ecosystems include macro-invertebrate benthic communities which may be strongly influenced by contaminant concentrations, both in the pore water and attached to fine sediment particles [Bottacin-Busolin *et al.*, 2009]. Various different modelling approaches have been proposed including transient storage (e.g. Runkel [1998]) and risk assessment models based on the 'impact zone' concept [McAvoy *et al.*, 2003]. As part of these models, the movement of solute chemical pollutants from the water column across the sediment water interface, and then into the sediment bed, or vice versa, may be required. This process of mass transfer across the sediment water interface is referred to as hyporheic exchange. The models currently employed [TGD, 2003] to predict chemical exposure in sediments are based on an assumption of equilibrium partitioning between dissolved and suspended-particle-sorbed phase in the water column. The bed sediment is assumed to consist of deposited suspended solids (with associated sorbed chemicals). Direct solute interactions with the bed (via diffusive or advective transfer from the water column to sediment pore water) are not taken into account. When an exchange coefficient has been included in modelling it has been assumed to be constant with depth below the sediment water interface [Fries, 2007].

Numerous studies [Marion *et al.*, 2002; Packman *et al.*, 2004; Tonina and Buffington, 2007; Rehg *et al.*, 2005; Ren and Packman, 2004] have shown significant mass transfer across the sediment water interface into the hyporheic zone. However these studies investigated the interface or bulk exchange and not any variation with depth. Nagaoka and Ohgaki [1990] and Shimizu *et al.* [1990] both showed a reduction in diffusion coefficient with depth, but the studies were limited to depths of a few

particle diameters below the interface and used large diameter glass spheres ($d_g \geq$ 17mm) for the sediment bed. Neither study quantified the variation in diffusion coefficient with depth. Quantifying the variation in diffusion coefficient with depth would allow an active layer of solute mixing to be defined accurately, instead of the arbitrary values used currently. The majority of previous work has been conducted using non-reactive (conservative) solute tracers, which is the case in this study.

Previous studies have used re-circulating laboratory flumes to study hyporheic exchange. These generally require large volumes of sediment and an extensive setup period, which restricts the range of conditions that can be tested in one series. Smaller volumes of both sediment and water would significantly reduce the time required, however this is difficult to achieve in a laboratory flume whilst maintaining a realistic physical scale. The solution would be to use apparatus smaller than a flume, but generating realistic scale turbulence driven exchange becomes a problem. The EROSIMESS-System [Liem *et al.*, 1997] (shortened to erosimeter) is an instrument designed to generate realistic scale turbulence to investigate critical bed shear stress of sediment beds. The erosimeter has been modified perviously to study the effect of sediment re-suspension on dissolved oxygen (DO) content of river water [Jubb *et al.*, 2001] and could be modified further to allow the study of hyporheic exchange.

1.1 Aims

The aim of this study is to improve the fundamental understanding of hyporheic exchange and specifically to determine the vertical variation in diffusion coefficient below the sediment water interface. The specific objectives of the research were:

1. Evaluation of the vertical variation in diffusion coefficient
2. To evaluate the use of the erosimeter in the study of hyporheic exchange

1.2 Thesis outline

Chapter 2: Background theory and Previous Work

This chapter covers the mechanisms which drive hyporheic exchange along with methods for predicting and modelling it. A summary of previous field and laboratory studies investigating hyporheic exchange is given, along with an evaluation of the data analysis techniques used in the laboratory studies. Several parameters

associated with sediment material are discussed and the EROSIMESS-system is introduced. Finally a summary of the chapter and the test hypothesis drawn from it are presented.

Chapter 3: Experimental Setup

Chapter 3 describes the development of the experimental setup along with the final erosimeter setup used to investigate the variation in diffusion coefficient with depth below the sediment water interface. The chapter also presents a particle image velocimetry (PIV) study undertaken to quantify the flow field within the erosimeter. Finally details of the experimental procedure are given.

Chapter 4: Experimental Results and Analysis

Experimental results and analysis are presented in Chapter 4. Example raw data are given and both the water column and in-bed concentration profiles are analysed and compared to previous published work. The relationships between bed shear velocity, permeability and other experimental parameters and diffusion coefficient are discussed and the vertical variation in diffusion coefficient is examined.

Chapter 5: Discussion

In this chapter the vertical variation in diffusion coefficient is quantified and aspects of the experimental data discussed. The relationship is incorporated in a 1D numerical diffusion model and a comparison between the model simulations and experimental data given. Applications for the findings of this study are also discussed.

Chapter 6: Conclusion

Chapter 6 presents the conclusions and recommendations for further work drawn from the work presented in this thesis. Recommendations include further use of the erosimeter to study various parameters that could affect hyporheic exchange and the vertical variation in diffusion coefficient quantified in this study.

Chapter 2

Background theory and Previous Work

2.1 Synopsis

This chapter covers the background theory and previous work associated with this body of research. It covers mechanisms for hyporheic exchange along with methods for predicting and modelling it. A summary is made of previous laboratory and field experiments investigating hyporheic exchange, several parameters associated with sediment material are discussed and the EROSIMESS-system is introduced. Finally a summary of the chapter and the test hypothesis drawn from it are presented.

2.2 Hyporheic Exchange

Hyporheic exchange refers to the transfer of soluble chemicals between the overlying water column and the interstitial fluid between sediment particles. This can be achieved via a number of different physical processes, including diffusive, either molecular or turbulence, and advective pressure driven movement. There have been attempts to quantify hyporheic exchange through fundamental physical processes and scaling relationships using specific flow or sediment characteristics. The following sections explore the processes that drive hyporheic exchange.

2.2.1 Molecular Diffusion

Molecular diffusion was often assumed to be the driving transport mechanism when examining biogeochemical gradients within sediments [Reimers *et al.*, 2001]. If a neutrally buoyant tracer is added to stationary fluid it will spread in all three di-

mensions. This spread is caused by random molecular motion (Brownian motion) within the fluid and is termed molecular diffusion [Rutherford, 1994]. Molecular diffusion is described by Fick's first law, which states that the rate of solute movement is proportional to the spatial concentration gradient, given, in one dimension, by

$$J_x = -D_m \frac{\partial C}{\partial x} \tag{2.1}$$

where: J_x is the molecular diffusive flux in the x-direction, D_m is the molecular diffusion coefficient and $\partial C/\partial x$ is the tracer concentration gradient in the x-direction (Note that the sign is negative, denoting the movement from a region of high concentration to one of low concentration).

Molecular diffusion coefficients vary depending on the properties of the solvent, solute, temperature and concentrations. For solutes in water the values of molecular diffusion typically range between 0.5 to 2.0×10^{-9} m^2/s and are determined empirically [Rutherford, 1994]. Molecular diffusion values can be determined using NMR or single molecule fluorescence correlation spectroscopy, which gives a value of $2.9 \pm 0.7 \times 10^{-10}$ m^2/s for Rhodamine 6G [Gell *et al.*, 2001]. This value will be taken as the molecular diffusion coefficient of Rhodamine WT for this study.

However the molecular diffusion coefficient through sediment is different from that through free fluid. The solute must flow around the sediment particles, creating a longer flow path and thereby effectively reducing the coefficient. This coefficient, the molecular diffusion coefficient through sediment (D'_m), has been explored theoretically [Berner, 1980], as well as empirically by relating it to sediment tortuosity, which is related, by several studies, to sediment porosity (θ) (e.g. Boudreau [1996]). This leads to the general expression for molecular diffusion in sediments

$$D'_m = \beta D_m \tag{2.2}$$

where: β represents an empirical expression for tortuosity as a function of sediment porosity and is described by Iversen and Jrgenson [1993] as

$$\beta = \frac{1}{1 + n(1 + \theta)} \tag{2.3}$$

where: n is the sediment type constant ($n = 3$ for clay-silts and $n = 2$ for sands). However O'Connor and Harvey [2008] use $n = 3$ throughout their analysis, regardless of sediment type.

2.2.2 Turbulent Diffusion

In the natural and built environment the majority of fluid flows are turbulent in nature [Roberts and Webster, 2002; Tennekes and Lumley, 1972]. Turbulence is difficult to define precisely, however there are several important characteristics that all turbulent flows posses [Roberts and Webster, 2002]. These are rapid diffusivity, unpredictability, high levels of fluctuating vorticity and dissipation of kinetic energy [Roberts and Webster, 2002; Tennekes and Lumley, 1972]. The rapid diffusivity of turbulence causes rapid mixing and increased rates of heat, momentum and mass transfer within the fluid [Tennekes and Lumley, 1972].

Turbulent diffusion is generally much greater than molecular diffusion [Rutherford, 1994], however molecular diffusion is part of turbulent diffusion. Within turbulent flows there are a wide range of length scales [Roberts and Webster, 2002; Tennekes and Lumley, 1972; Rutherford, 1994] and if a patch of material, such as solute tracer, is considered within turbulent flow then the eddies that are smaller than the patch size will distort it, creating concentration gradients, which are smoothed by molecular diffusion [Roberts and Webster, 2002]. Eddies that are larger than the patch size translate the entire patch without contributing to the mixing, only advection [Roberts and Webster, 2002].

In the same manner as molecular diffusion, turbulent diffusion can occur across the sediment water interface. Here the mixing/exchange is driven by bursts and sweeps in the viscous sub-layer as well as pressure fluctuations around surficial grains [Fries, 2007]. Numerous studies have used tracer experiments to quantify the turbulence driven exchange rate between sediments and overlaying flow [Richardson and Parr, 1988; Nagaoka and Ohgaki, 1990; Packman *et al.*, 2004]. Other studies have attempted to measure the velocities and/or pressure fluctuations around the sediment water interface [Shimizu *et al.*, 1990; Manes *et al.*, 2006; Pokrajac and Manes, 2009; Ruff and Gelhar, 1972].

Several different mathematical approaches have been taken in the study of turbulence including Reynolds, Taylor and Prandtl [Rutherford, 1994]. Osborne Reynolds [Reynolds, 1895] made the assumption that the observed velocities could be split into a time averaged and an instantaneous fluctuation component. This is shown mathematically below and graphically in Figure 2.1.

$$u = u' + \bar{u} \tag{2.4}$$

$$v = v' + \bar{v} \tag{2.5}$$

$$w = w' + \bar{w} \tag{2.6}$$

Where: u, v and w are the instantaneous velocities in the x, y and z directions respectively. The instantaneous deviations from the average velocity are denoted by $'$ and the time averaged part with a over bar, e.g. $\bar{u}$.

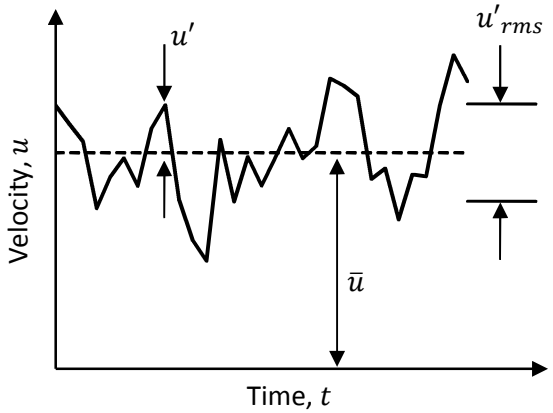

Figure 2.1: Example variation of velocity at a point with time in turbulent flow

By definition the time average of the instantaneous fluctuations $\bar{u'}$ is zero. However, the magnitudes and rapidity with which they fluctuate can give an indication of the structure of the eddy pattern within the turbulent flow [Chadwick *et al.*, 2004]. The magnitude of the fluctuations may be evaluated by using the root-mean-square of the instantaneous fluctuations (u'_{rms}, v'_{rms} and w'_{rms}) which is given for velocities in the x-direction by

$$u'_{rms}{}^2 = \frac{1}{t}\int_0^t (u - \bar{u})^2 \, \mathrm{d}t \tag{2.7}$$

where: t is the time over which the velocity is being evaluated.

Reynolds 'Stress' model

Reynolds proposed a 'stress' model for turbulence [Reynolds, 1895]. Considering only two dimensions (x and y) then only the fluctuations u' and v' are present. Therefore during a time interval Δt, the mass of fluid passing in the y-direction through a small horizontal element of area ∂A is

$$\rho_w v' \partial A \Delta t \tag{2.8}$$

where: ρ_w is the density of the fluid and has instantaneous horizontal velocity $u + u'$. Equation (2.8) is shown graphically in Figure 2.2.

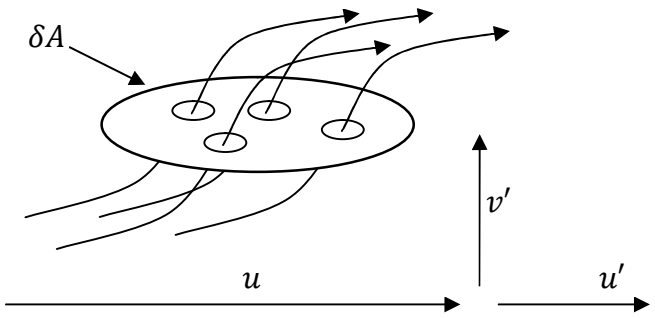

Figure 2.2: Reynolds' eddy model [Chadwick *et al.*, 2004]

The momentum, ∂m, of this mass is

$$\partial m = \rho_w v' \partial A \partial t (u + u'). \tag{2.9}$$

Therefore, the rate of interchange of momentum during a particular instant in time is

$$\frac{\partial m}{\partial t} = \rho_w v' \partial A (u + u') = \rho_w v' \partial A u + \rho_w v' u' \partial A. \tag{2.10}$$

The average rate of interchange of momentum will be a function of the time averaged velocities. The time average value of u is constant, as discussed earlier, and the time average fluctuations u' and v' must be zero. However the time averaged product of the two fluctuations $\overline{u'v'}$ is not necessarily zero, therefore the time averaged version of (2.10) is

$$\overline{\frac{\partial m}{\partial t}} = \rho_w \overline{u'v'} \partial A \tag{2.11}$$

The 'rate of interchange' of momentum implies the existence of a corresponding force (F) within the fluid, so (2.11) becomes

$$\partial F = \rho_w \overline{u'v'} \partial A \tag{2.12}$$

and since stress (τ) is equal to force/area, (2.12) can be written as

$$\tau = \frac{\partial F}{\partial A} = \rho_w \overline{u'v'} \tag{2.13}$$

which is the termed the Reynolds' Stress.

Bed shear velocity

The bed shear or friction velocity, u_*, is a velocity scale for turbulent flow [Tennekes and Lumley, 1972], and is often used to describe the effect of turbulence in diffusion/mixing problems. An example is the approximation for the depth averaged vertical diffusion coefficient, D_y [Rutherford, 1994; Fischer *et al.*, 1979].

$$D_y = 0.067 H u_* \tag{2.14}$$

Where: H is the flow depth.

The bed shear velocity can be calculated or approximated in a number of different ways. In open channel flow u_* is given by

$$u_* = \sqrt{g R_H S} \approx \sqrt{g H S} \tag{2.15}$$

where: R_H is the hydraulic radius ($R_H = A/W_p$ where A is the cross-sectional area of the channel and W_p is the wetted perimeter) and S is the slope of the bed [Rutherford, 1994; Fischer *et al.*, 1979]. In natural rivers u_* is sometimes assumed to be equal to $U/10$ or $U/20$, where U is the longitudinal mean stream velocity.

The bed shear velocity is also defined [Fischer *et al.*, 1979; Tennekes and Lumley, 1972] as

$$u_* = \sqrt{\frac{\tau}{\rho_w}} \tag{2.16}$$

which combined with (2.12) and rearranged produces a relationship between u_* and the turbulent fluctuations within the flow.

$$u_* = \sqrt{\overline{u'v'}} \tag{2.17}$$

Tennekes and Lumley [1972] state that if viscous effects are negligible, that the velocity fluctuations are correlated and that the average vertical flow at the sediment water interface is zero, then (2.17) is valid at any vertical position within the flow.

2.2.3 Other Driving Forces

There are two other main driving forces for exchange between the overlaying flow and the sediment pore water. These are large pressure gradients caused by bed-forms [Marion *et al.*, 2002; Elliott and Brooks, 1997a; Tonina and Buffington, 2007], known as pumping and the exchange caused by aquatic fauna or biodiffusivity [Solan *et al.*, 2004; Berg *et al.*, 1998]. The aquatic fauna promote vertical and lateral redistribution of sediment particles through burrowing, feeding, ventilation and locomotion

[Solan *et al.*, 2004]. This is collectively known as bioturbation and is often species specific [Forster and Graf, 1995]. Whilst this is an important feature of natural systems, biodiffusivity is not investigated further within this study, and is not included in the model approaches detailed below in Section 2.3.

Obstructions in the flow, such as bed-forms, boulders or logs cause high pressure regions upstream of the obstruction causing downwelling, movement from the overlying flow into the sediment, to occur. There is a corresponding area of low pressure downstream of the obstacle which generates an upwelling. Together they cause a hyporheic circulation under the obstruction [Tonina and Buffington, 2007; Elliott and Brooks, 1997a]. Pumping is demonstrated graphically in Figure 2.3.

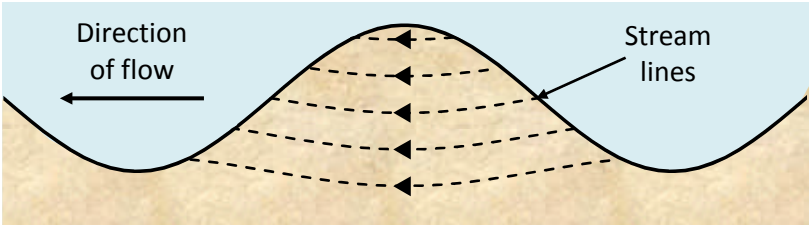

(a) Schematic of pumping through bed-form, including stream lines

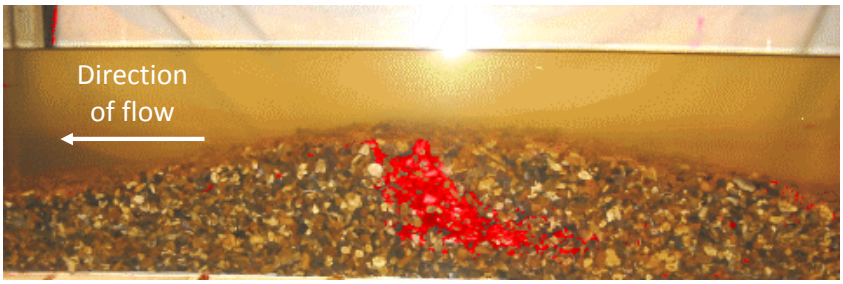

(b) Enhanced photograph of laboratory tracer experiment [Dutton, 2004] showing tracer moving though bed-form, driven by pumping flow

Figure 2.3: Graphical representation of pumping flow through a sinusoidal bed-form

2.2.4 Effective Diffusion

Natural systems are complex and a combination of processes cause net hyporheic exchange. These processes include molecular diffusion, advective pumping, shear-driven flow, turbulent surface penetration and hyporheic water mixing [O'Connor and Harvey, 2008]. No fundamental theory currently exists to predict the resulting hyporheic exchange in terms of measured stream or bed parameters. Instead the bulk solute exchange across the sediment water interface can be modelled with an effective diffusion coefficient (D) [Packman and Salehin, 2003]. The effective diffusion coefficient includes all the factors that influence hyporheic exchange, such

as molecular and turbulent diffusion, pumping and biodiffusivity, and can be shown formulaically by

$$D = \beta(D_m + D_b) + D_d \tag{2.18}$$

where: D_b is the biodiffusivity and D_d is the dispersion coefficient (encompassing turbulent diffusion and pumping), both of which must be obtained empirically or through modelling [Berg *et al.*, 1998].

2.3 Predicting and Modelling Hyporheic Exchange

Several different methods for modelling and/or predicting hyporheic exchange have been published previously.

2.3.1 Pumping Model

The pumping model, presented by Elliott and Brooks [1997a], can be used to quantify hyporheic exchange by examining the sediment domain. As described above, pumping flows are caused by dunes or irregularities in the bed topography which causes a pressure distribution on the bed. This pressure distribution induces flows through porous sediments [Rutherford, 1994].

Elliott and Brooks [1997a] proposed the use of a residence time function approach to calculating the mass transfer into bed sediment and can be considered in three parts.

1. A pulse of solute enters the bed, where the amount of solute entering is related to the concentration in the overlying water and the rate at which fluid enters the bed (volumetric flux).

2. The pulse of solute moves through the bed, and some may leave the bed. The fraction of the pulse that remains in the bed at time ξ after the pulse enters the bed is termed the residence time function, $R(\xi)$.

3. A continuous stream of solute entering the bed can be thought of as a series of pulses. The total mass remaining in the bed is calculated by integrating the mass remaining from the individual pulses.

The simplest case, and one that is generally taken to be 'the' pumping model, is a sinusoidal pressure distribution imposed onto a flat, level, homogeneous, isotropic bed. The assumption that the bed is flat, rather than sinusoidal, has little effect on the model's predictions as proved through the comparison with triangular

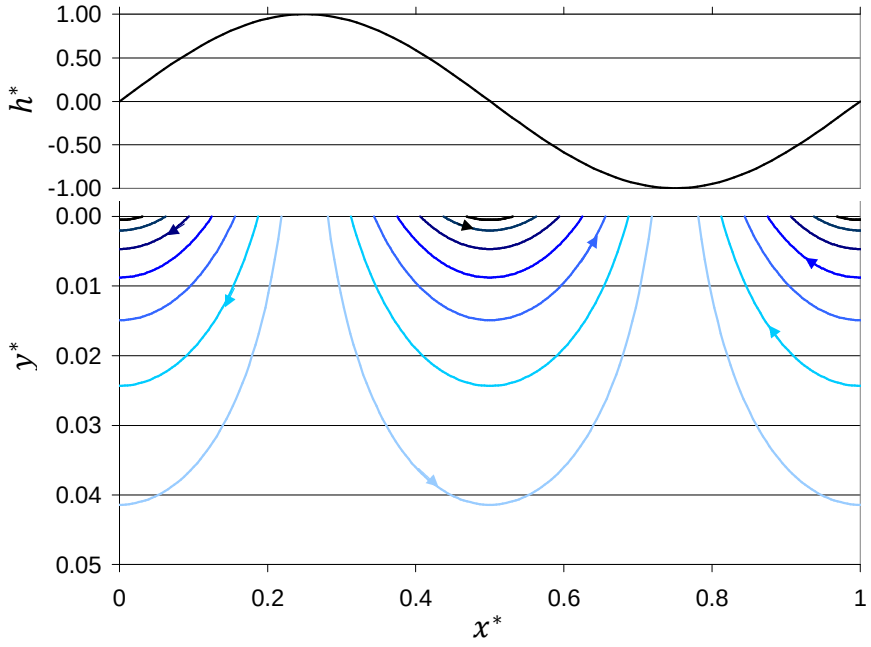

Figure 2.4: Normalised head distribution and particle flow paths (stream lines) predicted using Elliott and Brooks [1997a] model, [Dutton, 2004]

dunes [Elliott and Brooks, 1997a]. Figure 2.4 demonstrates the sinusoidal pressure distribution and the particle flow paths that result from Elliott and Brooks [1997a] numerical model. Equations (2.19), (2.20) and (2.21) describe the axis for Figure 2.4.

$$h^* = \frac{h}{h_m} \tag{2.19}$$

Where: h^* is the normalised head, h is the dynamic head ($h = p/(\rho_w g)$, where p is pressure, ρ_w is fluid density) and h_m is the amplitude of the dynamic head function at the bed surface (total head variation $= 2h_m$).

$$x^* = \frac{x}{\lambda} \tag{2.20}$$

Where: x^* is the normalised horizontal co-ordinate, x is the horizontal co-ordinate and λ is the bed-form wave length.

$$y^* = \frac{y}{2\pi\lambda} \tag{2.21}$$

Where: y^* is the normalised vertical co-ordinate, y is the vertical co-ordinate.

The dynamic head (h) is given by the continuity equation for steady flow in the sediment, assuming constant hydraulic conductivity (K_c), following the solution to Laplace's equation

$$\nabla^2 h = 0. \tag{2.22}$$

The pressure field within the sediment resulting from the sinusoidal head distribution at the sediment water interface is given by

$$h(y=0) = h_m \sin\left(\frac{2\pi}{\lambda}x\right). \tag{2.23}$$

The half amplitude of the dynamic head variation at the bed surface (h_m) is empirically derived by Elliott and Brooks [1997a] as

$$h_m = 0.28\frac{U^2}{2g}\begin{cases} \dfrac{\Delta/H^{3/8}}{0.34} & \text{if } \Delta/H \leq 0.34 \\ \dfrac{\Delta/H^{3/2}}{0.34} & \text{if } \Delta/H > 0.34 \end{cases} \tag{2.24}$$

where: U is the average velocity of the overlying water, Δ is the bed-form height and H is the overlying water depth. The resulting solution for the h distribution is given by (2.25).

$$h = h_m \sin\left(\frac{2\pi}{\lambda}x\right) e^{-\frac{2\pi}{\lambda}y} \tag{2.25}$$

Darcy's law is used to calculate the seepage velocity field in the sediment and produces streamlines (shown in Figure 2.4) entering and exiting the sediment according to

$$\mathbf{v} = -\frac{Kg}{\nu}\nabla h \tag{2.26}$$

where: $\mathbf{v}$ is a volume average interstitial velocity vector, K is the sediment permeability and ν is the kinematic viscosity.

The flux of solute into the bed at a point on the sediment surface is denoted by qC_{wc}, where C_{wc} is the concentration of solute in the water column and q is the volume flux into the bed, which is equivalent to velocity [Elliott and Brooks, 1997a]. If a two dimensional bed profile is assumed (no lateral variation in bed surface elevation) the flux into the surface takes place by two principle mechanisms.

1. The flow of pore water into the bed surface (pumping)

2. The trapping of interstitial water in the advancing face of bed-forms on mobile beds (turnover)

Elliott and Brooks [1997a] show that turnover only has an impact on the net mass transfer when the downstream dune propagation speed is greater than or equal to twice that of the pore water Darcy velocity due to the hydraulic gradient, which is usually not the case. However it has been included here for completeness. Equation (2.27) gives the volume flux into the surface due to pumping and turnover.

$$q(x) = \begin{cases} \mathbf{v}\cdot\mathbf{n} + \theta\dfrac{\partial\eta}{\partial t}\dfrac{\partial x}{\partial s} & \mathbf{v}\cdot\mathbf{n} + \theta\dfrac{\partial\eta}{\partial t}\dfrac{\partial x}{\partial s} \geq 0 \\ \\ 0 & \mathbf{v}\cdot\mathbf{n} + \theta\dfrac{\partial\eta}{\partial t}\dfrac{\partial x}{\partial s} < 0 \end{cases} \tag{2.27}$$

Where: $\mathbf{v}$ is a volume average interstitial velocity vector, $\mathbf{n}$ is the unit vector normal, and into, the bed surface, θ is the sediment porosity, η is the elevation of the bed surface above the mean bed surface and s is the distance along the bed surface (having both x and y components). In the case where a bed-form propagates downstream with a speed, U_b, without changing shape equation (2.27) is modified by

$$\frac{\partial\eta}{\partial t} = -U_b\frac{\partial\eta}{\partial x}. \tag{2.28}$$

The total rate of mass flow into the bed over a plan area (a) of stream is given by (2.29), where $\bar{q}$, the average flux into the surface per unit area is given by (2.30).

$$aC_{wc}\bar{q} \tag{2.29}$$

$$\bar{q} = \frac{1}{a}\int_{A_s} q \,\mathrm{d}s \tag{2.30}$$

Where: A_s is the area of bed surface corresponding to the plan area a.

The residence time within the bed is estimated first for solute entering at a particular point on the bed surface and then averaged over the larger bed area (or a representative portion such as a bed-form wavelength) [Elliott and Brooks, 1997a]. The fraction of solute which enters the bed at x_0 and remains in the bed after an elapse time ξ is denoted by $R(x_0, \xi)$. It is assumed that R is independent of the time at which the particle of solute enters the bed surface.

The average residence time function, $\bar{R}(\xi)$, denotes the fraction of solute that enters the bed in a short time near $t = 0$ and remains in the bed at time ξ. Since the flux into the surface varies with position, $R(x_0, \xi)$ must be weighted by q to determine the spatially averaged residence time function, given by Elliott and

Brooks [1997a] as

$$\bar{R}(\xi) = \frac{\int_{A_s} qR(x_0, \xi)\,\mathrm{d}s}{\int_{A_s} q\,\mathrm{d}s} = \frac{\int_{A_s} qR(x_0, \xi)\,\mathrm{d}s}{a\bar{q}}. \tag{2.31}$$

Most of the solute will remain in the bed shortly after the pulse enters (small ξ), so $\bar{R}$ tends to 1. As time progresses, more of the solute pulse leaves the bed, therefore the remaining fraction ($\bar{R}$) decreases with ξ.

The mass transfer of solute is dependent on the previous history of concentration in the overlying water and is calculated by Elliott and Brooks [1997a] as follows. The mass of solute tracer which enters the bed over a small time $\mathrm{d}\xi$ at a previous time $(t - \xi)$ is given, per unit plan area of streambed, by

$$\bar{q}C_{wc}(t - \xi)\,\mathrm{d}\xi. \tag{2.32}$$

A fraction, $\bar{R}(\xi)$, of the solute remains in the bed at a time t. Thus the incremental contribution to the mass within the bed at time t from flux into the bed at time $t - \xi$ is given by

$$\bar{q}\bar{R}(\xi)C_{wc}(t - \xi)\,\mathrm{d}\xi. \tag{2.33}$$

Therefore the accumulated mass in the bed, considering all elapsed times ξ is given by

$$M_s(t) = \bar{q}\int_{\xi=0}^{\infty} \bar{R}(\xi)C_{wc}(t - \xi)\,\mathrm{d}\xi \tag{2.34}$$

where: M_s is the mass accumulation of solute within the bed sediment.

O'Connor and Harvey [2008] state that the pumping model can be formulated to represent mass transfer by effective diffusion, using the flux across the sediment water interface and the net solute flux derived from the mass balance on the recirculating water in the flume. This leads to (2.35), which describes the solute mass accumulation in the bed sediment.

$$\frac{M'}{\theta} = 2\sqrt{\frac{Dt}{\pi}} \tag{2.35}$$

Where: $M' = M_s/C_0$ (C_0 is the initial solute concentration in the water column) and M'/θ is known as the effective solute penetration depth.

During the initial time period of a tracer experiment Elliott and Brooks [1997a] show that the convolution integral (2.34) can be approximated by (2.36),

which is valid until the bed starts to become saturated with solute.

$$\frac{M'}{\theta} = \frac{3.5}{2\pi}\sqrt{\frac{K_c h_m t}{\theta}} \tag{2.36}$$

Combining (2.35) and (2.36) results in an estimation of D using the pumping model with a sinusoidal pressure gradient at the sediment water interface based only on sediment and fluid-flow variables [O'Connor and Harvey, 2008].

$$D = \frac{1}{\pi\theta}\left(\frac{3.4}{4}\right)^2 K_c h_m \tag{2.37}$$

Tonina and Buffington [2007] developed the pumping model further to include three dimensional bed-forms. They removed the assumption of a planar bed and sinusoidal downstream pressure distribution and replaced it with a measured near bed pressure. This was obtained through approximately 130 micropiezometers, composed of superthane (ether) tubes of 1.59mm internal diameter, and 3.18mm external diameter set at a longitudinal spacing of 0.72m and lateral spacing of approximately 0.1m within a 0.8 by 14m flume.

Tonina and Buffington [2007] changed Elliott and Brooks [1997a] equations by including lateral variations into the residence time function, turning (2.31) into

$$\bar{R}(t) = \frac{1}{W_b \bar{q}} \int_0^L \int_0^{W_p(x)} q(x,z) R(t,x,z)\, \mathrm{d}x\, \mathrm{d}z \tag{2.38}$$

where: W_b is the wetted bathymetry (three-dimensional surface area of wetted topography), $W_p(x)$ is the wetted perimeter as a function of longitudinal position, L is the total length of the experimental reach and z is the lateral co-ordinate.

2.3.2 Slip Flow Model

The slip flow model depicts the transition in physical processes from the overlying fluid-flow to the porous media flow in the sediment [O'Connor and Harvey, 2008], which means equating the Navier-Stokes equation for the overlying flow with Darcy's law in the sediment at the water sediment interface. The slip velocity (u_s) can be defined in experimental terms as the extrapolated horizontal velocity at the sediment water interface, which is significantly larger than the interstitial velocity deeper within the bed driven by the pressure gradient in the channel [Fries, 2007].

This can be demonstrated graphically by the results from Fries [2007], shown in Figure 2.5 and pictorially in Figure 2.6. The solid line (Figure 2.5) represents the lower portion of a Reichardt [1951] velocity profile described by (2.39). The two

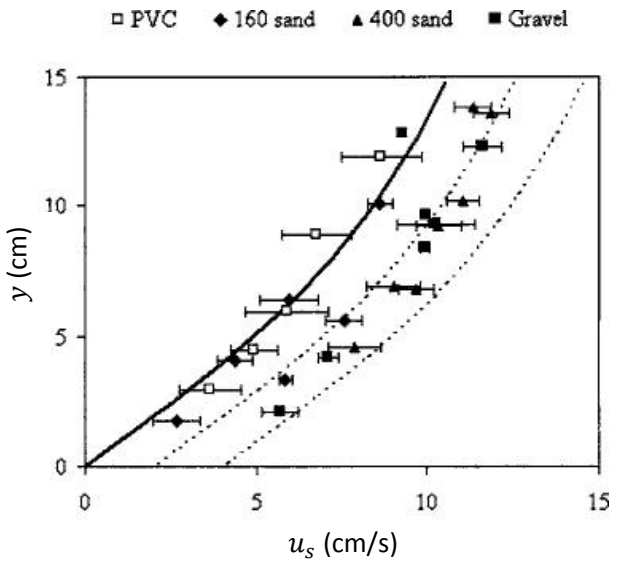

Figure 2.5: Mean velocity profiles in near-bed regions for sediment bed experiments where each point represents an average of measurements from profiles repeated for the same sediment and flow conditions. The Solid curve represents profile (2.39) with zero displacement whilst the dashed curves represent profiles with slip velocities of 2 and 4 Fries [2007]

dashed lines represent the same profile but with a horizontal displacement equal to slip flow velocities $u_s = 2$ and $u_s = 4$ (cm/s). The two dashed profiles fit the rough permeable bed measurements, where as the original (solid) profile fits the smooth impermeable PVC bed measurements.

$$u_+(y_+) = \frac{1}{\kappa}\ln[1 + (y_+ + \psi_+)] + 7.8\left[1 - \exp\left(-\frac{y_+ + \psi_+}{11}\right) - \frac{(Y_+ + \psi_+)}{11}\exp\left(-\frac{y_+ + \psi_+}{3}\right)\right] \quad (2.39)$$

Where: u_+ is the normalised horizontal velocity, y_+ is the normalised elevation above the interface, κ is the Von Kármán constant and ψ_+ is the normalised velocity profile displacement.

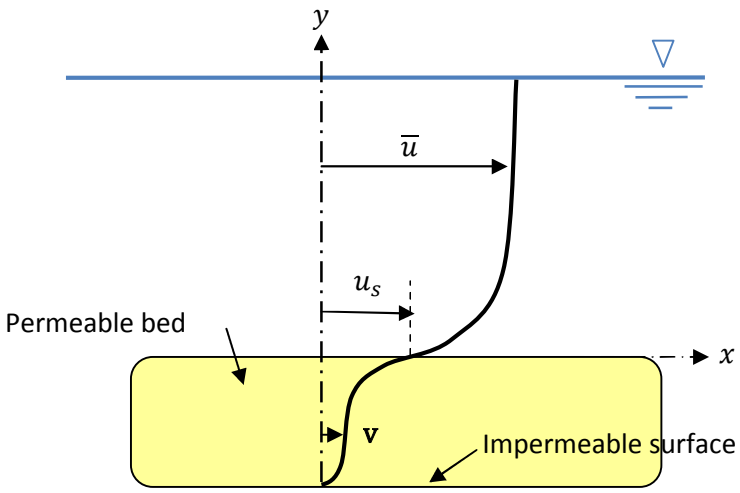

Figure 2.6: Pictorial representation of slip flow

The Navier-Stokes equation is a second order, nonlinear equation and in the overlying flow, in incompressible form, can be expressed as

$$\frac{\partial \mathbf{u}}{\partial t} + \mathbf{u} \cdot \nabla \mathbf{u} = -\frac{\nabla p}{\rho_w} + \nu \nabla^2 \mathbf{u} + \mathbf{F}_b \tag{2.40}$$

where: $\mathbf{u}$ is the velocity vector and $\mathbf{F}_b$ is the net body force or gravity term in free surface problems (which has units of acceleration).

Darcy's law (2.41), which was empirically deduced but can also be derived from the Navier-Stokes equation through averaging over large pore volumes [O'Connor and Harvey, 2008], is a first order, linear equation. Equation (2.41) is the same as (2.26), but written in terms of pressure instead of head.

$$\frac{\nabla p}{\rho_w} = -\frac{\nu}{K}\mathbf{v} \tag{2.41}$$

There are two different approaches taken by researchers when combining (2.40) and (2.41). Some, such as Basu and Khalili [1999] and Zhou and Mendoza [1993] have treated the problem as a single domain (overlying water and sediment bed as one), where as others, such as Beavers and Joseph [1967] and Ruff and Gelhar [1972], use a two domain approach.

The one domain approach starts with the Navier-Stokes equation (2.40) and uses various mathematical techniques including ensemble averaging to derive equations describing the macro-scale transport within the bed [Zhou and Mendoza, 1993] and across the interface [Basu and Khalili, 1999]. Although these techniques do not

require empirically determined interface conditions, such as the two domain problem requires, they have to contend with rapidly changing values of porosity, permeability, etc. across the sediment water interface. Consequently this region requires special treatment and correction steps [Basu and Khalili, 1999].

The two domain approach is simpler, but as stated above, relies on empirically derived interface properties. Generally, only the sediment portion of the problem is considered, but with the inclusion of additional force terms to Darcy's law (2.41) [O'Connor and Harvey, 2008]. Beavers and Joseph [1967] and Ruff and Gelhar [1972] used a conceptual Brinkman boundary layer just blow the sediment water interface. The characteristic length scale for the Brinkman layer is $\sqrt{K}$ [Beavers and Joseph, 1967] over which the additional flow resistance is generated by viscous shear stress and nonlinear form drag which are added to create the extended Darcy equation.

$$\frac{\nabla p}{\rho_w} = -\frac{\nu}{K}\mathbf{v} + \nu_e \nabla^2 \mathbf{v} - \frac{C_D}{\sqrt{K}}\mathbf{v}^2 \tag{2.42}$$

Where: ν_e is the effective viscosity and C_D is a dimensionless drag coefficient.

The third term in (2.42) represents the Brinkman term and the fourth term represents the Forchheimer term and introduces C_D (the dimensionless form drag coefficient), which is a property of the porous sediment bed [Venkataraman and Rama Mohan Rao, 1998]. Ruff and Gelhar [1972] solved for the $\mathbf{v}$ field using (2.42) with an empirically derived value for C_D and evaluating ν_e as a constant varying with depth. This solution for $\mathbf{v}$ also provided an expression of the slip velocity, u_s, tangential to the sediment water interface (the slip velocity is on the water side of the interface and is not a volume average of the interstitial velocity) [O'Connor and Harvey, 2008]. Their resulting expression for slip velocity assuming a constant effective viscosity is given by

$$\left(\frac{u_s}{u_*}\right)^3 + \frac{3}{2C_D Re_K}\left(\frac{u_s}{u_*}\right)^2 = \frac{3Re_K}{2C_D}\frac{\nu}{\nu_e} \tag{2.43}$$

where: u_s is the slip velocity, u_* is the bed shear velocity and $Re_K = u_*\sqrt{K}/\nu$ is the permeability Reynolds number characterising the flow within the Brinkman layer.

Fries [2007] evaluated effective viscosity (ν_e) as an effective diffusion ($\nu_e \approx D$) in (2.43), which can be rearranged into (2.44), allowing D to be estimated using the slip flow model.

$$D = \frac{3\nu Re_K^2}{2C_D Re_K u_{s+}^3 + 3u_{s+}^2} \tag{2.44}$$

Where: $u_{s+} = u_s/u_*$ is the dimensionless slip velocity and was estimated by Fries

[2007] by fitting the Reichardt velocity profile (2.39) to measured velocity profiles.

2.3.3 Effective Diffusion Scaling Relationship

The complex nature of hyporheic exchange has led to the use of an effective diffusion coefficient which combines all the physical, biological and chemical exchange processes. It is therefore unnecessary to assume that the best means of estimating the effective diffusion coefficient is through modelling the physical processes that occur. This has led to a succession of scaling relationships being employed to relate an effective diffusion coefficient to a variety of fluid flow and sediment characteristics [O'Connor and Harvey, 2008].

The idea of a scaling relationship for hyporheic exchange was proposed by Richardson and Parr [1988]. They conducted flume experiments simulating runoff over a uniform bed (1.2m long by 25.4mm deep) of glass beads using a horizontal, 4.9 by 0.15m Plexiglas flume. Three different flow depths and four velocities were passed over five different diameters of bead, which represented fine to very course sands. The bed was saturated with tracer (fluorescein disodium salt) and the flow started. Tracer concentrations were measured at the effluent weir throughout the 30 minute experiments. This research stemmed from environmental pressures on the agricultural industry and is the start of the research into hyporheic exchange. Richardson and Parr [1988] took the Fickian model, and noted that it did not match their observed data. This led them to propose the use of a non-constant, time varying diffusion coefficient which could be used within the standard Fickian diffusion model. The time dependent diffusion coefficient (D_*) is given by

$$D_* = \gamma D \tag{2.45}$$

where: γ is a time dependent variable given by

$$\gamma = \frac{1}{1 - \frac{t}{t_0}\left[1 - \exp\left(\frac{-t}{t_0}\right)\right]}. \tag{2.46}$$

However after the initial non-Fickian phase the diffusion coefficient can be taken as constant. Richardson and Parr [1988] related their measured value for the effective diffusion to the sediment properties, characterised by the permeability Péclet number (Pe_K). Their scaling relationship for a time independent effective diffusion coefficient is given by

$$\frac{D}{D'_m} = 6.59 \times 10^{-5} Pe_K^2 \tag{2.47}$$

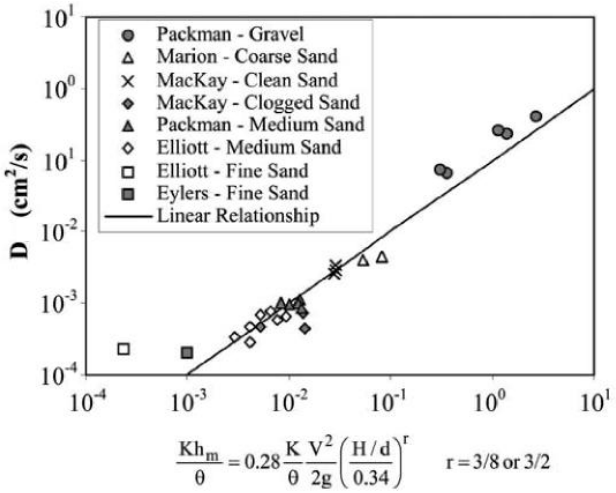

Figure 2.7: Packman and Salehin [2003] pumping model based scaling relationship showing the influence of stream velocity, permeability and porosity of the bed sediments

where: Pe_K is the permeability Péclet number ($u_*\sqrt{K}/D'_m$).

This relationship fits the data set used by Richardson and Parr [1988] well, however the range of sedimentary and flow conditions modelled is relatively small. This gives the relationship limited applicability. Packman and Salehin [2003] used seven different data sets to derive their own scaling relationship. They used data from Elliott and Brooks [1997b], Eylers *et al.* [1995], Packman *et al.* [2000], Packman and MacKay [2003], Marion *et al.* [2002], Packman *et al.* [2004][1] and Nagaoka and Ohgaki [1990], which provided a much wider range of sediment and flow conditions than the single set used by Richardson and Parr [1988].

Packman and Salehin [2003] demonstrate a linear relationship between the effective diffusion coefficient and the parameter grouping Kh_m/θ (where K is the permeability, h_m is the amplitude of the dynamic pressure head given by (2.24) and θ is the sediment porosity), which they demonstrate to hold for more than three orders of magnitude of bed-form driven exchange [Packman and Salehin, 2003]. However the relationship does not hold for fine sands used by Eylers *et al.* [1995], which has a similar effective diffusion coefficient to Elliott and Brooks [1997b] but a much lower Kh_m/θ value (Figure 2.7).

Packman and Salehin [2003] also propose a linear relationship between the effective diffusion coefficient and the parameter grouping $(Re\, d_g)^2$ (where Re is the

[1]This paper was originally submitted in 2002 and referred to by this date in Packman and Salehin [2003], but not accepted until 2004

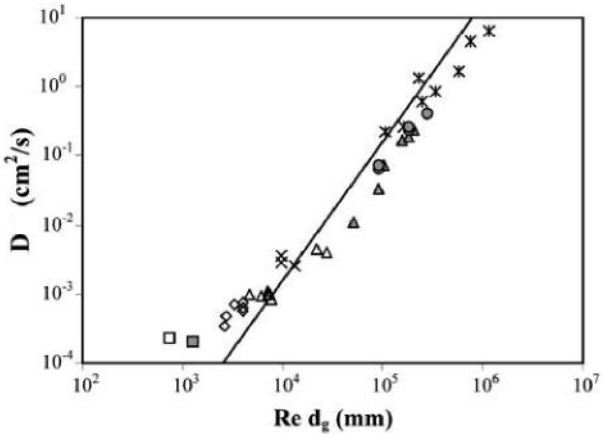

Figure 2.8: Packman and Salehin [2003] second scaling relationship showing exchange is proportional to the sediment size, which suggests that the permeability of the sediment bed controls exchange with both flat beds and bed-forms

stream Reynolds number (UH/ν) and d_g is sediment grain diameter) and report that it holds for almost five orders of magnitude of observed hyporheic exchange behaviour. This represents two orders of magnitude of variation in sediment grain size, almost an order of magnitude variation in stream velocity and distinctly different stream channel topographies [Packman and Salehin, 2003]. In this relationship the sediment grain size is used to represent the sediment properties such as K and θ. However there is still deviation from this relationship within the data sets used, particularly when fine sands are used (Figure 2.8).

O'Connor and Harvey [2008] published a scaling relationship derived from a wide range of data sets that covered different sediment characteristics, flow parameters and topographies. Like Packman and Salehin [2003], O'Connor and Harvey [2008] took data from several studies which are listed below. Table 2.1 gives the experimental parameters as presented by O'Connor and Harvey [2008] and information about each paper is given in Section 2.4.

List of papers used by O'Connor and Harvey [2008] with Table 2.1 references

Richardson and Parr [1988] - a

Nagaoka and Ohgaki [1990] - b

Lai *et al.* [1994] - c

Elliott and Brooks [1997b] - d

Marion *et al.* [2002] - e

Packman *et al.* [2004] - f

Packman *et al.* [2000] - g

Packman and MacKay [2003] - g

Ren and Packman [2004] - g

Rehg *et al.* [2005] - g

Tonina and Buffington [2007] - h

Study	d_g (mm)	K (10^{-6} cm^2)	θ	Δ (cm)	λ (cm)	u_* (cm/s)	U (cm/s)	H (cm)
Richardson[a]	0.1-3.0	0.17-71	0.36-0.40	0	0	0.3-1.3	3.7-22.9	0.6-1.9
Nagaoka[b]	19.0-40.8	500-2300	0.24	0	0	1.1-4.3	8.9-42.8	3.2-7.0
Lai[c]	0.5-3.2	2.3-19	0.36-0.38	0	0	0.2-0.6	7.4-15.4	0.5-2.0
Elliott[d]	0.1-0.5	0.08-1.1	0.30-0.33	1.1-2.5	9-30	1.3-2.4	8.6-13.2	3.1-6.5
Marion[e]	0.85	5.0	0.38	0-3.5	0-120	1.7-1.8	22.0-28.0	10.9-12.3
Packman[f]	4.8	150	0.38	0-3.7	0-32	1.1-3.2	9.0-36.1	11.3-20.5
Various[g]	0.5	0.68-1.8	0.29-0.38	0.8-1.9	15-70	0.5-1.7	12.0-23.7	7.1-12.7
Tonina[h]	9.8-10.8	51	0.34	3.6-12.0	515-560	3.8-5.5	28.2-46.0	3.9-10.4

Table 2.1: Summary of sediment and fluid flow conditions as presented by O'Connor and Harvey [2008]

As stated above, O'Connor and Harvey [2008] compiled data from various flume tracer studies in order to examine a wide range of fluid flow and sediment conditions and their effect on transport in permeable sediments. They evaluated a measured effective diffusion coefficient for all the studies. However the variations in the experimental setups resulted in three different methods of calculation being employed. The deciding factors on which equation to use were where the solute tracer was placed at the start of the experiment and where the sampling of solute tracer occurred. Details of the different analysis techniques are given in Section 2.4.

For all studies O'Connor and Harvey [2008] used plots of either mass or concentration versus the square root of time to compute the slopes needed in the equations detailed in Section 2.4 for calculating experimental D values. Not all fluid flow and sediment parameters were reported within the papers, thus O'Connor and Harvey [2008] used several different equations to estimate the missing parameters. A list is given below (the sediment parameters are discussed in Section 2.6).

- Bed shear velocity (u_*) - (2.15)
- Roughness height (k_s) - (2.131)

- Permeability (K) - (2.129) or (2.130)

Once O'Connor and Harvey [2008] had collated and unified all the data, Buckingham's Π theorem was used to generate dimensionless groups of controlling variables. This process involved three stages, (i) listing the minimum number of variables needed to describe hyporheic exchange, (ii) generating dimensionless groupings of the controlling variables and (iii) using the compiled hyporheic exchange data to determine a power law scaling relationship for effective diffusion [O'Connor and Harvey, 2008].

The control variables chosen represent the controlling fluid flow and sediment conditions according to both the pumping and slip flow models, given by

$$D = f(D'_m, U, u_*, k_s, \sqrt{K}, \nu) \tag{2.48}$$

where: D'_m is defined by (2.2) which includes θ, k_s is roughness height which includes the variables d_{90}, Δ and λ.

The seven variables in (2.48) are composed of two dimensions (L and T), which results in the possibility of five dimensionless groupings. O'Connor and Harvey [2008] simplified the five possible groups into four groupings of dimensionless numbers known to affect hyporheic exchange.

$$\frac{D}{D'_m} \sim \left(\frac{U}{u_*}\right), \left(\frac{u_* k_s}{\nu}\right), \left(\frac{u_*\sqrt{K}}{D'_m}\right) \tag{2.49}$$

Where: $U/u_* = C_z$ is the Chézy resistance coefficient, $u_* k_s/\nu = Re_*$ is the shear Reynolds number and $u_*\sqrt{K}/D'_m = Pe_K$ is the permeability based Péclet number. Equation (2.50) is (2.49) rewritten in the form of a power law scaling relationship.

$$\frac{D}{D'_m} = \alpha C_z^b Re_*^c Pe_K^d \tag{2.50}$$

Where: α is a dimensionless scaling constant and b, c, d are scaling exponents for the dimensionless numbers.

The next stage is to determine scaling exponents and scaling constant. This was achieved by plotting the three dimensionless numbers individually against the dimensionless diffusion coefficient (D/D'_m). This revealed strong relationships between the shear Reynolds number and the permeability Péclet number. However it showed only a weak correlation between D/D'_m and C_z, so the Chézy resistance coefficient was dropped from (2.50) and the slopes of the other plots were taken as the scaling coefficients c and d [O'Connor and Harvey, 2008]. O'Connor and Harvey

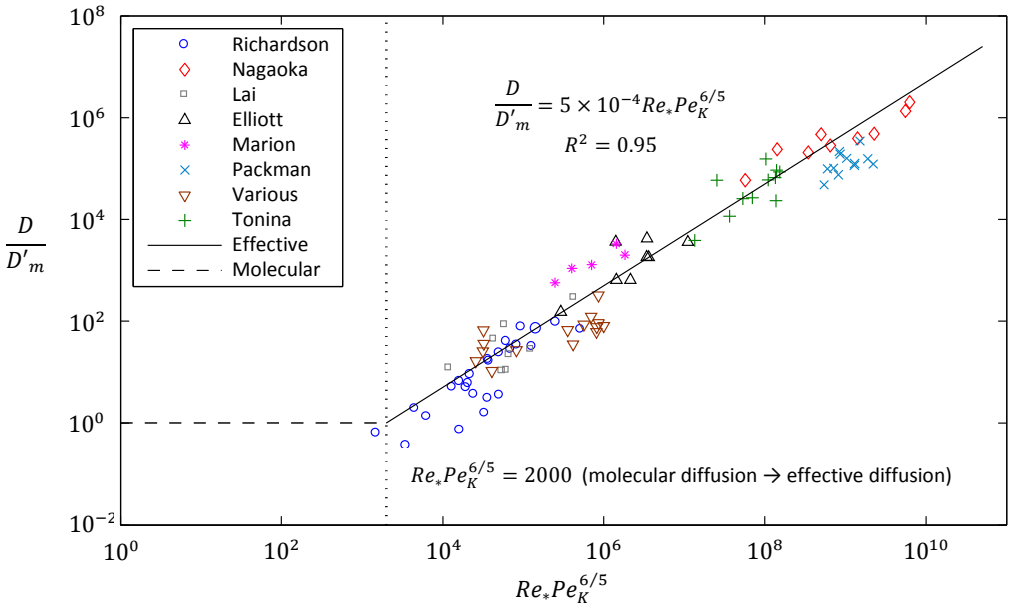

Figure 2.9: Effective diffusion scaling relationship compared against previous experimental data [O'Connor and Harvey, 2008]

[2008] plotted D/D'_m versus $Re_*^{7/4} Pe_K^{9/4}$ and found it had a slope of 0.55, which was combined with the scaling exponents to give the scaling relationship

$$\frac{D}{D'_m} = \begin{cases} 5 \times 10^{-4} Re_* Pe_K^{6/5} & \text{for } Re_* Pe_K^{6/5} \geq 2000 \\ 1 & \text{for } Re_* Pe_K^{6/5} < 2000 \end{cases} \tag{2.51}$$

where the inverse of the scaling constant (5×10^{-4}) provided a threshold value in transport conditions ($Re_* Pe_K^{6/5} = 2000$), below which transport was governed by molecular diffusion, resulting in $D/D'_m = 1$.

Figure 2.9 [O'Connor and Harvey, 2008] demonstrates their scaling relationship and the good fit to the dataset used. All but one of the experimental D (D_e in figure) data points were above the threshold condition for molecular diffusion. The scaling relationship described by (2.51) has a slope of one and explains 95% of the variance with 95% confidence intervals of the slope between 0.93 to 1.02 [O'Connor and Harvey, 2008].

O'Connor and Harvey [2008] conducted a comparison between their scaling relationship and both the pumping and slip flow models (Sections 2.3.1 and 2.3.2 respectively). They found that neither model predicted the effective diffusion coefficient well. O'Connor and Harvey [2008] suggested this was primarily due to the

physics based nature of the models and that it was therefore unrealistic to expect them to accurately predict hyporheic exchange when it is caused by many different types of process. When applying the pumping model to flat beds O'Connor and Harvey [2008] assumed $\Delta = d_g$ in the calculation of h_m (2.24). The scaling relationship proposed by O'Connor and Harvey [2008] (2.51) appears to be a reliable and accurate way of estimating the bulk hyporheic exchange, defined by an effective diffusion coefficient (D).

2.3.4 Transient Storage Models

There have been a number of attempts to use the transient storage models, such as the Advective Dispersion Equation (ADE) model, the Aggregated Dead Zone (ADZ) model, the Hart model [Hart, 1995] and the OTIS model [Runkel, 1998], to characterise hyporheic exchange within natural streams. Initial studies [Hart, 1995; Runkel, 1998; Hart *et al.*, 1999] only used transient storage models and relied on fitting the model to measured profiles to estimate hyporheic exchange parameters. Later studies [Johansson *et al.*, 2001; Wörman *et al.*, 2002; Jonsson *et al.*, 2003; Marion *et al.*, 2003, 2008] used hyporheic exchange models, such as the pumping or 1D diffusion models, to predict the exchange parameters or residence time distributions within the storage zone of a transient storage model.

Other studies [Forsman *et al.*, 2002; Jonsson *et al.*, 2003] have included extra parameters such as sorption, which is described below. The analytical transport model proposed by Forsman *et al.* [2002] takes into account main stream advection, solute exchange with the storage zone, instantaneous equilibrium sorption and first order reactions.

The basis for treating sorption as an instantaneous equilibrium reaction is the large surface area associated with fine grained sediments (such as in the Säva Stream used by Forsman *et al.* [2002]). This large surface area causes sorption to be rapid in comparison to the hydraulic transport in the pore water [Forsman *et al.*, 2002]. The model uses a numerical two-site surface complexation model (SCM) developed by Runkel *et al.* [1999], which includes simultaneous pseudokinetic and equilibrium sorption descriptions. This model was used to "avoid the shortcomings of the empirical 'partitioning coefficient approach' (PCA) to describe reactions in a system with spatially and temporally variable chemical conditions (pH)" [Forsman *et al.*, 2002].

The model used by Forsman *et al.* [2002] is given by (2.52), with the various

parameters described below.

$$C_{wc}(x,y,t) = \begin{cases} \dfrac{e^{((Pe_{em}/\tilde{R}_H)+y)\omega}}{1+ax^b} \displaystyle\int_0^{t^*} \frac{(Pe_{em}/\tilde{R}_H)+y}{2\sqrt{\pi Pe_{es}\varepsilon^3}} \times & t^* > 0 \\ e^{-(Da_{ds}+\omega^2 Pe_{es})\varepsilon\left(((Pe_{em}/\tilde{R}_H)+y)^2\right)/4Pe_{es}\varepsilon}\ \mathrm{d}\varepsilon & \\ 0 & t^* \leq 0 \end{cases} \tag{2.52}$$

Where: Pe_{em} is the exchange Péclet number for the main stream given by (2.53), $\tilde{R}_H$ is the spatially weighted hydraulic radius given by (2.54), ω is porosity depth function given by (2.55), a and b are constants, $t^* = t - x/U$ is the integration upper limit, Pe_{es} is the exchange Péclet number for the storage zone given by (2.56), ε is a dummy variable introduced through the convolution integral and Da_{ds} is the reaction Damköhler number given by (2.57).

$$Pe_{em} = \frac{LD}{UR_0^2(1-K_m)} \tag{2.53}$$

Where: L is the length of the stream reach investigated, D is the diffusion coefficient, U is the main stream average velocity and K_m is the partitioning coefficient within the main channel between the water and suspended sediment particles.

$$\tilde{R}_H = \frac{1}{L}\int_0^L R_H(x)\ \mathrm{d}x \tag{2.54}$$

$$\omega = -\frac{\mathrm{d}\theta}{2\theta \mathrm{d}y} \tag{2.55}$$

$$Pe_{es} = \frac{LD}{UR_0^2(1-K_{ss})} \tag{2.56}$$

Where: K_{ss} is the sorption partitioning coefficient within the sediment.

$$Da_{ds} = \frac{R_s L}{U(1+K_{sr})} \tag{2.57}$$

Where: R_s is the first order reaction rate coefficient and K_{sr} is the reaction partitioning coefficient within the sediment. The total partitioning coefficient within the sediment ($K_{s,tot}$) is given by $K_{ss} + K_{sr}$.

The model provides a good fit to the field data, however there are a number of parameters that can be fitted, which makes this result unsurprising. Despite this the results from the analysis are promising and indicate that transient storage

models may be able to distinguish hyporheic exchange, particularly if simultaneous traces are conducted with conservative and sorptive tracers.

This is generally true for all transient storage model studies. However several studies such as Harvey *et al.* [1996] and Zaramella *et al.* [2003] have concluded that the slower exchange with deeper regions of the sediment are not captured during the analysis if stream tracer injections. This has led several authors (such as Briggs *et al.* [2009]) to suggest multiple storage zone models, which account for in-stream and in-bed storage or different levels within the bed. Briggs *et al.* [2009] used mid-stream and in-stream dead zone measurements to try and isolate the contribution of hyporheic exchange within a multi storage zone model. The problem with such approaches is the heterogeneity of natural streams which increases the effects of sampling location on the analysis. This makes it dificult to conduct predictive modelling based on experimental results.

Sorption

Historically the study of sorption within sediments has been conducted by soil engineers and scientists studying the problems of agricultural leaching [Wierenga and Van Genuchten, 1989]. Sorption is the combination of adsorption (the accumulation of atoms or molecules on the surface of another material) and absorption (where atoms or molecules are taken up into the bulk phase, not just on the surface). These two processes are generally, but not exclusively modelled through an equilibrium partitioning coefficient. The octanol-water partitioning coefficient (K_{ow}) is defined as the ratio of a chemical concentration in n-octanol and water at equilibrium, at a specified temperature [Pontolillo and Eganhouse, 2001]. Pontolillo and Eganhouse [2001] found in their extensive literature review (approximately 700 publications, 1944-2001, reviewed) of K_{ow} values for the organochlorine pesticide DDT, and its persistent metabolite, DDE, that the published values varied greatly and led them to question the validity of parameter values in published literature. Numerous studies have been conducted using leached soil columns to determine the transport and sorption/desorption of chemicals to soils [Wu and Gschwend, 1986]. This research can be applied to river sediments as well as soils because of the wide range of soils that have been analysed, and the different conditions under which this has been done.

These tests have revealed a hysteresis in the sorption/desroption cycle. This was investigated by Kan *et al.* [1998], who showed that a small amount of the sorbate remained irreversible sorbed to the sediment. Each sorption/desorption cycle left more of the sorbate irreversible attached to the sediment, until a maximum irre-

versibly sorbed concentration was reached. After this point sorption was completely reversible. This maximum irreversibly sorption concentration is related to common molecular properties and sediment organic carbon content [Kan *et al.*, 1998]. Kan *et al.* [1998] found that normalising the linear partitioning coefficients for the irreversible component, obtained from their experiments, with the sediments organic carbon content produced an essentially constant number ($K_{OC}^{irr} = 10^{5.53 \pm 0.48}$ ml/g) for all seven compounds and four sediment examined.

Within the literature there are a number of different models for chemical sorption to sediments. They range from the equilibrium partitioning approach [Forsman *et al.*, 2002] to reactive surface diffusion models [Miller and Pedlt, 1992]. Miller and Pedlt [1992] use a dual-resistance surface diffusion model to describe the sorption/desorption hysteresis. The model represents sorption rates as the results of a resistance due to diffusion through a boundary layer and diffusion radially along the solid surface within a spherical particle [Miller and Pedlt, 1992]. They also describe the difference between the surface diffusion model and the pore diffusion model. "Surface-diffusion models usually assume equilibrium between the sorbent and solution at the exterior portion of a particle, whereas pore-diffusion models usually assume equilibrium between the solid and solution phases at all locations within a particle" [Miller and Pedlt, 1992].

Chemical sorption to sediments has also been studied for suspended sediments. Wu and Gschwend [1986] studied the sorption kinetics of hydrophobic organic compounds to natural sediments. The used a modified radial diffusive penetration model and demonstrated that a single effective diffusivity parameter could be used to quantify the sorption kinetics. This coefficient was predictable from the compound solution diffusivity, the octanol-water partitioning coefficient and the sorbent organic content, density and porosity.

All these models deal with the sorption of chemicals within the sediment structure and generally without significant fluid velocities involved. However within a stream bed there may be significant in-bed velocities (such as pumping flows). This has led to the study of chemical sorption within stream reaches in the field, some of which is described below (Section 2.5).

2.3.5 One Dimensional Model

As discussed in Section 2.3.4, one dimensional (1D) diffusion models have been used in conjunction with transient storage models to define the exchange into the sediment storage zone [Jonsson *et al.*, 2003]. Several researchers have concluded that hyporheic exchange can be described as a one dimensional fickian diffusive process

[Elliott and Brooks, 1997a; Wörman *et al.*, 2002; Packman *et al.*, 2004; Habel *et al.*, 2002] with a constant diffusion coefficient throughout the domain often assumed [Fries, 2007].

The purpose of using a 1D model in this study is to simulate the vertical exchange within the experimental system detailed in Chapter 3, and allow comparison of different spatially varying diffusion coefficients to be made. Two different approaches are investigated below, both based on Fick's second law of diffusion (2.58). The first approach uses an analytical solution to (2.58) and the second a finite difference approximation.

$$\frac{\partial C}{\partial t} = D\frac{\partial^2 C}{\partial y^2} \tag{2.58}$$

Where: C is the solute concentration, t is time and y is the vertical co-ordinate.

Equation (2.58) is derived from (2.1) assuming a constant diffusion coefficient and is not the same as (2.59), which would allow the diffusion coefficient to vary with depth.

$$\frac{\partial C}{\partial t} = \frac{\partial}{\partial y}\left(D\frac{\partial C}{\partial y}\right) \tag{2.59}$$

Analytical Model

The analytical model was developed in two stages, model 1 and 2, however both models rely on the same basic equation (2.65). This equation is derived from Fick's second law, (2.58). Differentiation of (2.58), [Crank, 1975], gives

$$C(y,t) = \frac{b}{t^{1/2}}\exp\left(-\frac{y^2}{4Dt}\right) \tag{2.60}$$

where: b is an arbitrary constant.

Equation (2.60) is symmetrical about $y = 0$ and tends to zero as y approaches positive or negative infinity for $t > 0$. For $t = 0$ it vanishes everywhere except $y = 0$, where it becomes infinite. Considering an injection of tracer with mass M into a domain of infinite length and unit cross-section then

$$M = \int_{-\infty}^{\infty} C(y,t)\,\mathrm{d}y \tag{2.61}$$

and if the concentration distribution given by (2.60) is assumed, along with the groupings

$$y^2/4Dt = \varepsilon^2, \qquad \mathrm{d}y = 2\sqrt{Dt}\mathrm{d}\varepsilon \tag{2.62}$$

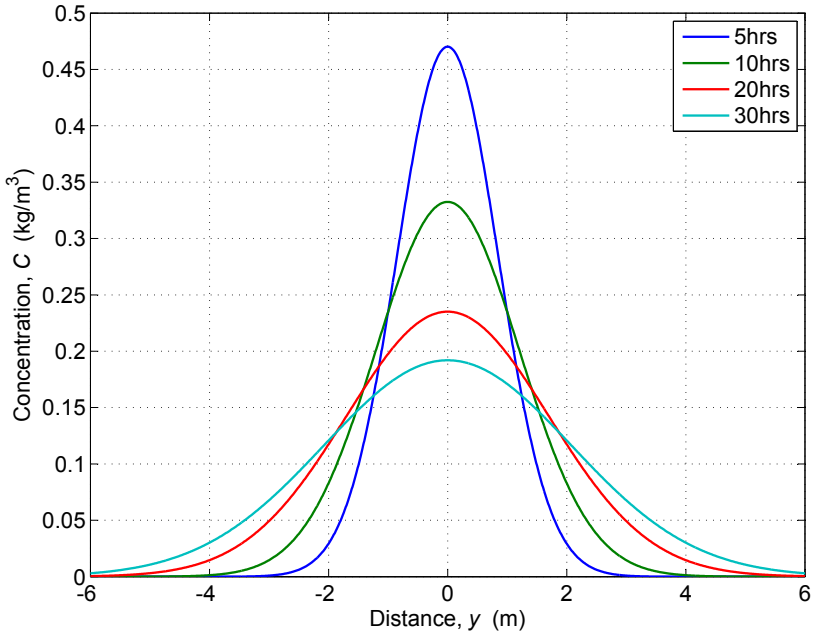

Figure 2.10: Plane injection in an infinite domain with constant diffusion coefficient, $D = 2 \times 10^{-5}\mathrm{m}^2/\mathrm{s}$

then

$$M = 2b\sqrt{D}\int_{-\infty}^{\infty}\exp(-\varepsilon^2)\,\mathrm{d}\varepsilon = 2b\sqrt{\pi D} \tag{2.63}$$

therefore

$$b = \frac{M}{2\sqrt{\pi D}}. \tag{2.64}$$

Substituting (2.64) into (2.60) the analytical solution for one dimensional diffusion in an infinite domain with constant diffusion coefficient is obtained.

$$C(y,t) = \frac{M}{\sqrt{4\pi D t}}\exp\left(-\frac{y^2}{4Dt}\right) \tag{2.65}$$

Model 1 applies (2.65) in an infinite domain with a single point injection. Figure 2.10 shows the diffusion of a point injection at various times after the injection. This was visually compared to plots presented in Crank [1975], which demonstrated that (2.65) had been implemented correctly. The method of moments [Fischer *et al.*, 1979], which relates the temporal increase in spatial variance to the diffusion coefficient, was used to analyse the output from model 1 to ensure that the diffusion coefficient specified was being applied correctly.

The experimental system being modelled is a closed system, like a laboratory

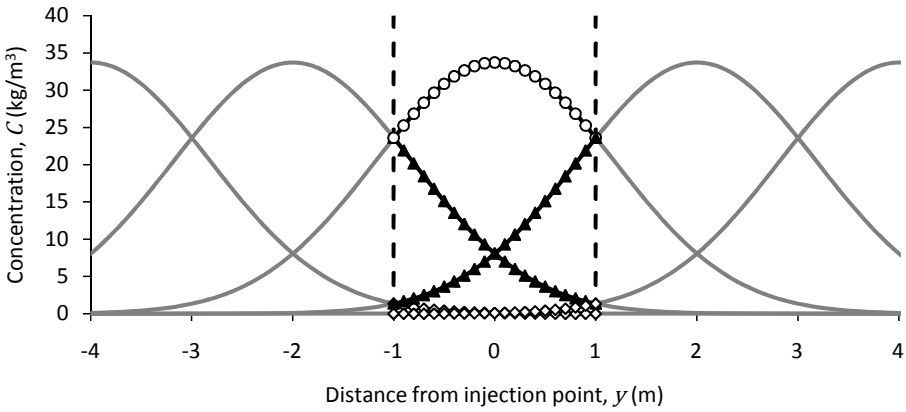

(a) Original and imaginary (grey) profiles with markers indicating portions of each profile used

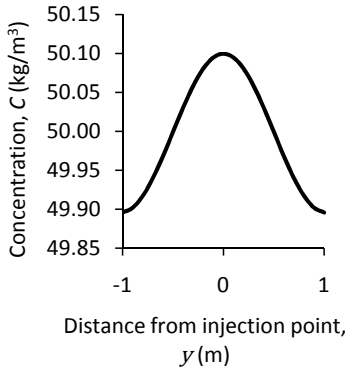

(b) Resultant concentration profile from summing portions marked

Figure 2.11: Pictorial representation of method of images

flume, so the assumption of an infinite domain is not applicable. Model 2 incorporates impermeable boundaries and a block injection instead of a single point. To model an impermeable surface the method of images was implemented, which uses imaginary injections positioned outside the finite domain being modelled [Crank, 1975; Rutherford, 1994]. The spread of tracer from these imaginary injections acts like a reflection of the injection within the domain on the impermeable boundary. Figure 2.11(a) shows the original injection (circles) and the the imaginary injections, outside the finite region, indicated by the vertical dashed lines. The greyed portions of each profile are excluded from the concentration calculations but are included in the Figure 2.11(a) for completeness, only the portions within the finite region are used. At each spatial point within the finite region, the contributions from all the injections are summed, giving the concentration at that point. The resultant profile

from the Figure 2.11(a) is shown in Figure 2.11(b).

Rutherford [1994] states that six imaginary injections are adequate for most applications. However if the model is run for large times the contribution from the imaginary injections increases, accounting for more of the final profile. For very large times, six imaginary injections are not adequate and mass is lost from the model, manifested as a drop in concentration with time. Therefore to model large times the spread of each profile needs to be limited so six reflections is adequate. This can be achieved by using the overall concentration profile from the previous time step to calculate the next, instead of basing the calculation for each time step on the initial, t_0, concentration profile. In a comparison of the two different approaches, either iterative or based on t_0 concentrations, there was a difference in final concentrations of less than 0.3%.

Modelling a block injection is similar to using the method of images described above. A series of point injections are made spatially within the model and the contributions from each, at a particular spatial point are summed together to create the overall concentration profile. This method is called superposition.

The modelling approach described above works well if a constant diffusion coefficient is applied throughout the modelled domain. However this study is investigating the variation in diffusion coefficient. Figure 2.12 shows a point injection at $y = -1$ in an infinite domain. The two dashed lines show two different constant diffusion coefficient simulations. The solid line (Variable D) shows the profile calculated if the coefficient changes at $y = 0$. In the region $y \leq 0$ the coefficient is $0.1\text{m}^2/\text{s}$, but changes to $1\text{m}^2/\text{s}$ for $y > 0$. In each of the regions the dashed line follows the appropriate constant coefficient line, with a jump from one to the other where the coefficient changes. This jump means that the mass in the variable coefficient simulation is 22% greater than the constant coefficient simulations. However, if the injection is moved to $y = 1$ the error in mass balance is not -22%, but -23.4%. The error in mass if the injection is at the interface is 3%. The error in mass balance does not cancel itself out on either side of the interface, leading to a net increase in mass within the system.

The behaviour demonstrated in Figure 2.12 is a direct result of the derivation of (2.65). In deriving (2.65) the assumption was made that the diffusion coefficient was constant, allowing the analytical solution to be obtained. To counteract this problem the time step used within the simulation could be reduced. This will limit the spread of a profile within each time step thereby reducing the error in the mass balance. Unfortunately the smallest time step is limited by (2.65). If a point injection is considered at $y = 0$, then the second part of (2.65) is equal to one, so

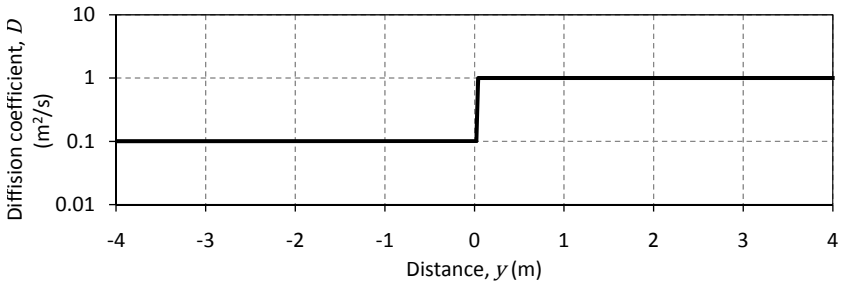

(a) Variation in diffusion coefficient

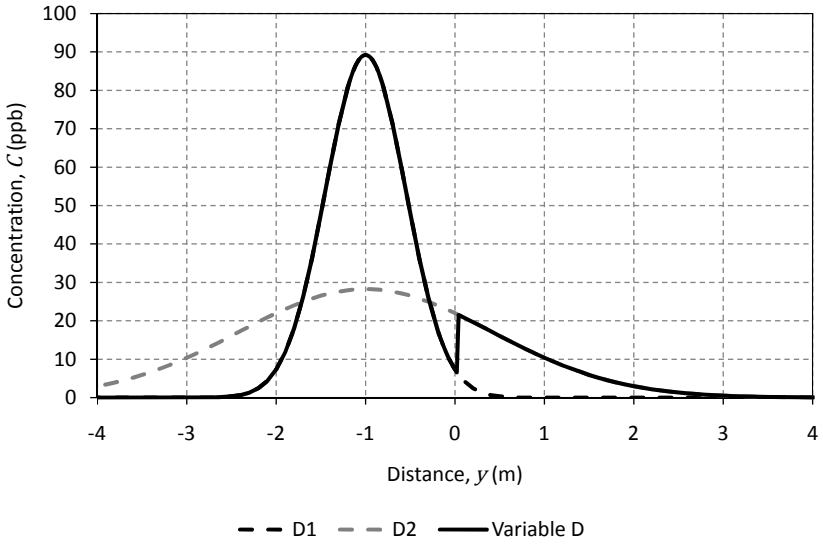

(b) Spatial Concentration profiles

Figure 2.12: Comparison of constant and variable diffusion coefficients ($D1 = 0.1\text{m}^2/\text{s}$ and $D2 = 1\text{m}^2/\text{s}$), showing the effect of varying the diffusion coefficient within a profile

the concentration becomes the mass divided by $\sqrt{4\pi Dt}$. If t (the time step in this simulation) is too small, then $\sqrt{4\pi Dt}$ becomes less than one, and the concentration at $y = 0$ becomes greater than the initial mass injected. This is in accordance with the statement made earlier that as t tends to 0, C tends to infinity [Crank, 1975].

There are several difficulties in applying a model based on the analytical solution to (2.58) in the context of this study. Therefore a different approach is necessary.

Finite Difference Model

The Crank-Nicolson implicit method for solving partial differential equations was proposed by Crank and Nicolson [1947]. It is now widely used in diffusion and other numerical modelling. The method replaces $\partial^2 C/\partial y^2$ with its finite-difference representations on the jth and $(j+1)$th time rows and approximates Fick's second law (2.58) by

$$C_{i,j+1} = C_{i,j} + \frac{D\Delta t}{2(\Delta y)^2}\left\{(C_{i+1,j} - 2C_{i,j} + C_{i-1,j}) + (C_{i+1,j+1} - 2C_{i,j+1} + C_{i-1,j+1})\right\} \tag{2.66}$$

where: i is the spatial co-ordinate and j the temporal. Equation (2.66) can be re-written in the form

$$-rC_{i+1,j+1} + (1+2r)C_{i,j+1} - rC_{i-1,j+1} = rC_{i+1,j} + (1-2r)C_{i,j} + rC_{i-1,j} \tag{2.67}$$

where: $r = D\Delta t/2(\Delta y)^2$.

The left hand side contains three unknowns at the time level $j+1$ and the right contains three known values of C on the jth level. This form can then be solved using any one of several different numerical methods such as Gaussian elimination or the tri-diagonal matrix (Thomas) algorithm. Equation (2.67) is the general solution and would allow modelling within an infinite domain. For a closed finite domain boundary conditions must be imposed.

The boundary condition equations developed below are based on a free surface with evaporation, which is then adapted to imitate an impermeable boundary. A free surface with evaporation can be written as

$$\frac{\partial C}{\partial y} = \alpha(C_s - C_e), \quad y = y_s \tag{2.68}$$

where: C_s is the surface concentration at time t (if the boundary is at $y = 0$ then C_s can be written as $C_{0,j}$) and C_e is the equilibrium surface concentration [Crank, 1975].

Representing this condition in finite difference form gives an extra equation for $C_{0,j}$ at every time step. A more accurate replacement for this extra equation is possible with the introduction of an imaginary or fictitious concentration $C_{-1,j}$ outside the original grid [Crank, 1975]. Condition (2.68) becomes

$$\frac{C_{1,j} - C_{-1,j}}{2\Delta y} \approx \alpha(C_{0,j} - C_e). \tag{2.69}$$

The value of $C_{-1,j}$ is unknown but can be eliminated by using the replacement of the partial differential equation [Crank, 1975], which for the surface point is

$$\frac{\partial C_{0,j}}{\partial t} \approx D\left(\frac{C_{-1,j} - 2C_{0,j} + C_{1,j}}{(\Delta y)^2}\right) \tag{2.70}$$

re-arranging (2.69) and (2.70) and combining to eliminate $C_{-1,j}$ gives

$$\frac{\partial C_{0,j}}{\partial t} \approx \frac{2D}{\Delta y}\left\{\frac{C_{1,j} - C_{0,j}}{\Delta y} - \alpha(C_{0,j} - C_e)\right\}. \tag{2.71}$$

For impermeable surfaces, such as the base of a laboratory flume, $\alpha = 0$ in the above equations [Crank, 1975]. Taking this into account, (2.71) in the Crank-Nicolson implicit form becomes

$$C_{0,j+1} = C_{0,j} + \frac{D\Delta t}{(\Delta y)^2}\left\{(C_{1,j+1} + C_{1,j}) - (C_{0,j+1} + C_{0,j})\right\}. \tag{2.72}$$

The same procedure can be followed for the boundary at the other end of the domain ($i = N$), which produces

$$C_{N,j+1} = C_{N,j} + \frac{D\Delta t}{(\Delta y)^2}\left\{(C_{N-1,j+1} + C_{N-1,j}) - (C_{N,j+1} + C_{N,j})\right\}. \tag{2.73}$$

The purpose of using a finite difference model is to allow the diffusion coefficient to be varied throughout the media. Consider a point source, where the source is at $y = y_s$ and is the interface between two media (regions of differing diffusion coefficients). In the following derivation the suffixes a, b are taken for the left side ($y < y_s$) and right side ($y > y_s$) of the interface respectively. The spatial interval (Δy) is constant through both regions. This is not the case in [Crank, 1975], where the derivation is conducted with different spatial intervals in each media. Letting $J(C_s, t)$ denote the flux across the interface, then the conditions to be satisfied are

$$D_a\frac{\partial C_a}{\Delta y} = D_b\frac{\partial C_b}{\Delta y} = J(C_s, t), \quad y = y_s \tag{2.74}$$

which expresses the fact that tracer enters one region at the same rate it leaves the other, together with some relationship between the concentrations on both sides of the interface.

Rather than simply relating the two concentrations on either side of the interface, it is more accurate to imagine each region extending into the other by one step (Δy) [Crank, 1975]. This fictitious point can be eliminated using (2.74), in the

same way as the fictitious point was eliminated for the boundary conditions.

For the region left of the interface (a), extending one imaginary step right of the interface, the equation for the interface concentration is given by

$$\frac{\partial C_{s,j}}{\partial t} \approx D_a \left(\frac{C_{s-1,j} - 2C_{s,j} + C_{s+1,j}}{(\Delta y)^2} \right) \tag{2.75}$$

which re-arranged in terms of the imaginary extension ($C_{s+1,j}$) is

$$C_{s+1,j} = \frac{\partial C_{s,j}}{\partial t} \frac{(\Delta y)^2}{D_a} - C_{s-1,j} + 2C_{s,j}. \tag{2.76}$$

Equation (2.74) can be written for region (a) as

$$J(C_i nt, t) = D_a \left(\frac{C_{s+1,j} - C_{s-1,j}}{2\Delta y} \right) \tag{2.77}$$

and can be re-arranged like (2.75) to become

$$C_{s+1,j} = \frac{J}{D_a} 2\Delta y + C_{s-1,j} \tag{2.78}$$

Combining (2.76) and (2.78) and re-arranging gives

$$\frac{\partial C_{s,j}}{\partial t} \approx \frac{2D_a}{\Delta y} \left(\frac{C_{s-1,j} - C_{s,j}}{\Delta y} + \frac{J}{D_a} \right). \tag{2.79}$$

The same procedure can be followed for the region to the right of the interface (b), which produces

$$\frac{\partial C_{s,j}}{\partial t} \approx \frac{2D_b}{\Delta y} \left(\frac{C_{s+1,j} - C_{s,j}}{\Delta y} - \frac{J}{D_b} \right) \tag{2.80}$$

Re-arranging (2.79) and (2.80) in terms of J and combining we obtain

$$\frac{\partial C_{s,j}}{\partial t} \approx \frac{D_b}{(\Delta y)^2}(C_{s+1,j} - C_{s,j}) - \frac{D_a}{(\Delta y)^2}(C_{s,j} - C_{s-1,j}) \tag{2.81}$$

which can be re-written in the Crank-Nicolson implicit form to give

$$C_{s,j+1} = C_{s,j} + \frac{D_b \Delta t}{2(\Delta y)^2}\{(C_{s+1,j+1} + C_{s+1,j}) - (C_{s,j+1} + C_{s,j})\} - \frac{D_a \Delta t}{2(\Delta y)^2}\{(C_{s,j+1} + C_{s,j}) - (C_{s-1,j+1} + C_{-1,j})\} \tag{2.82}$$

The equations derived above allow the erosimeter experimental system described in Chapter 3 to be modelled. When implementing a finite difference model

the Courant - Friedrichs - Lewy (CFL) condition [Courant *et al.*, 1967] must be met. This condition is required for the solution at a given time step to converge on the correct solution. For the CFL condition to be met in this model, the largest diffusion coefficient (D_{max}) must satisfy

$$\frac{D_{max}\Delta t}{2(\Delta y)^2} < 1. \tag{2.83}$$

The condition essentially states that some tracer must remain within the region Δy after one time step, it cannot all diffuse out of that region into another. The condition is a balance between D_{max}, Δy and Δt.

The equations described above produce a model (model 3) that allows the movement of tracer within the water column and sediment bed regions of the erosimeter experimental system to be modelled as a 1D diffusion process. Figure 2.13 shows a model 3 simulation of the solute flux out of the sediment region and into the initially solute free water column, with a diffusion coefficient in the water column ($0 < y \leq 0.255$m) of 1×10^{-3}m^2/s and in the bed region ($-0.2 \leq y \leq 0$m) of 4×10^{-7}m^2/s. A spatial resolution (Δy) of 0.001m and temporal resolution (Δt) of 0.001s were used. However the final concentration within the simulation, equal to the fully mixed equilibrium mixing concentration, is not that expected within the experimental system. This is because of the different porosities of the two regions, water column and bed. The bed consists of sediment particles which reduce the volume of the bed region filled with fluid (pore water). The 1D model only accounts for length and gives a 'per unit area' model of what is happening. The different volumes of fluid in each region, in the experimental system, govern the equilibrium mixing concentration. These need to be accounted for in the model if a direct comparison of model simulations and the experimental data are to be made.

To obtain the correct equilibrium concentration within the model, to match that achieved experimentally, the different volumes within the sediment and overlaying flow regions need to be accounted for, not just the physical lengths. The assumption can be made, based on previous work with the erosimeter [Jubb, 2001] and simulations of the water column region, that it mixes instantaneously in comparison to the exchange across the sediment water interface. Therefore, the water column can be modelled by the upper boundary condition to the sediment region and can be factored to take account of the difference in volumes. Therefore the boundary condition at the sediment water interface becomes the governing equation for the equilibrium concentration within the system.

The equations given below have been used to model the erosimeter exper-

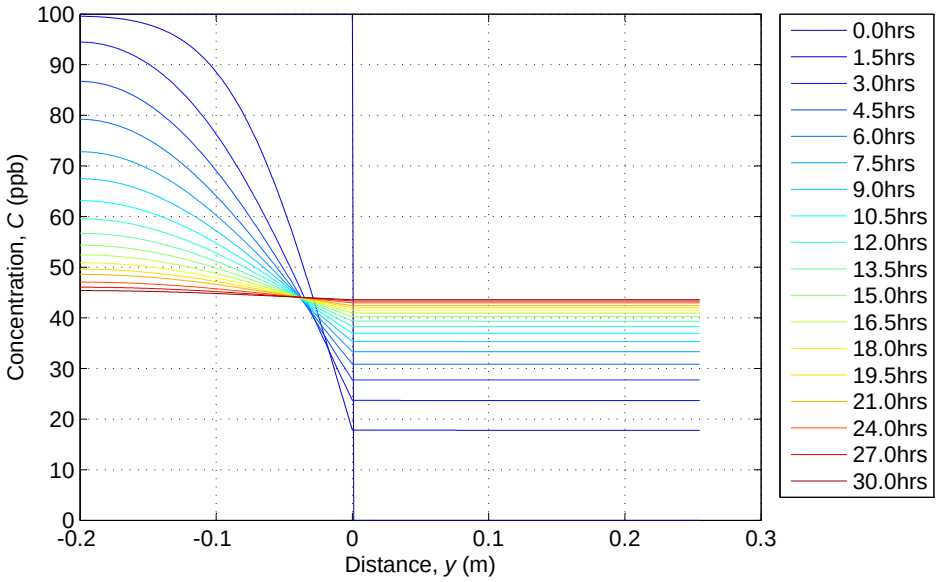

(a) Spatial concentration profile

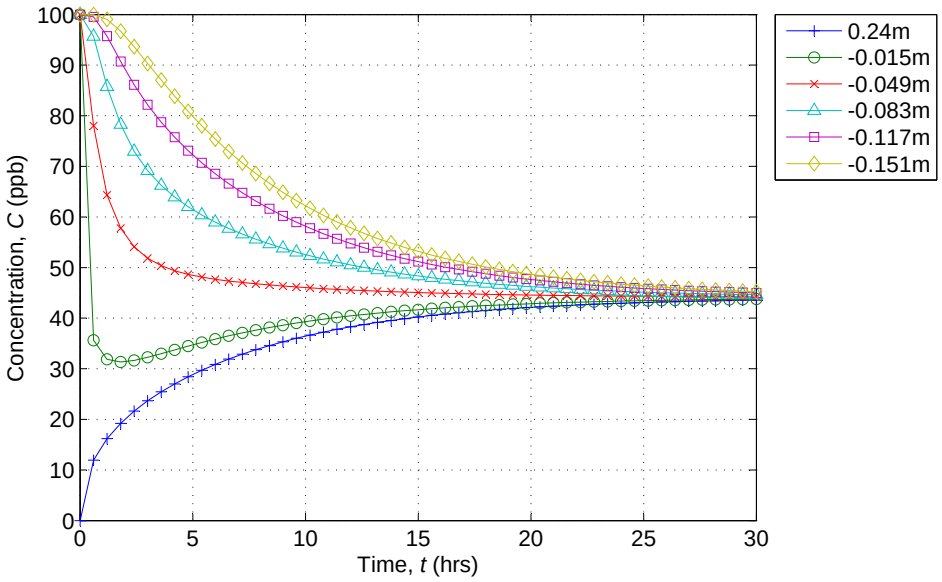

(b) Temporal concentration profile at locations corresponding to the experimental instrument positions

Figure 2.13: Model 3 simulation with diffusion coefficients 1×10^{-3} and $4\times10^{-7}\mathrm{m}^2/\mathrm{s}$ in the regions $0 < y \leq 0.255\mathrm{m}$ and $-0.2 \leq y \leq 0\mathrm{m}$ respectively

imental system throughout the rest of this study. The model will be referred to as model 4. The change from r to f in the equations presented below represents a change in the diffusion coefficient and applies where ever the coefficient changes, although only one change is presented below. The model domain used $-0.2 \leq y \leq \Delta y$ (the dimensions of the erosimeter base section, details in Chapter 3), making $y_N = \Delta y$ in the following equations, where Δy is the spatial resolution.

$$r = \frac{D_a \Delta t}{2(\Delta y)^2}, \quad f = \frac{D_b \Delta t}{2(\Delta y)^2} \tag{2.84}$$

All the equations follow the same form, with the unknown concentrations on the left and the known concentrations on the right. A new constant is introduced in the upper boundary condition, α,

$$\alpha = \frac{2V_r}{\Delta y} \tag{2.85}$$

where: V_r is a length scale representative of the relative water column (V_w) and pore water volumes (V_s).

Boundary Condition ($i = 0$, base of system)

$$-2rC_{1,j+1} + (1+2r)C_{0,j+1} = 2rC_{1,j} + (1-2r)C_{0,j} \tag{2.86}$$

Boundary Condition ($i = N$, sediment water interface)

$$-2fC_{N-1,j+1} + (1+\alpha+2f)C_{N,j+1} = 2fC_{N-1,j} + (1+\alpha-2f)C_{N,j} \tag{2.87}$$

Interface ($i = s$)

$$-fC_{s+1,j+1}+(1+f+r)C_{s,j+1}-rC_{s-1,j+1} = fC_{s+1,j}+(1-f-r)C_{s,j}+rC_{s-1,j} \tag{2.88}$$

Bed, region (a), ($0 \leq i \leq s$)

$$-rC_{i+1,j+1} + (1+2r)C_{i,j+1} - rC_{i-1,j+1} = rC_{i+1,j} + (1-2r)C_{i,j} + rC_{i-1,j} \tag{2.89}$$

Bed, region (b), ($s < i \leq N$)

$$-fC_{i+1,j+1} + (1+2f)C_{i,j+1} - fC_{i-1,j+1} = fC_{i+1,j} + (1-2f)C_{i,j} + fC_{i-1,j} \tag{2.90}$$

The equations described above are solved using the tri-diagonal matrix or Thomas algorithm. Figure 2.14 shows a simulation using model 4 with a constant diffusion coefficient ($1.55 \times 10^{-7}\mathrm{m}^2/\mathrm{s}$) throughout the bed. The simulation shown has reached an equilibrium concentration of 22.8, the expected experimental system

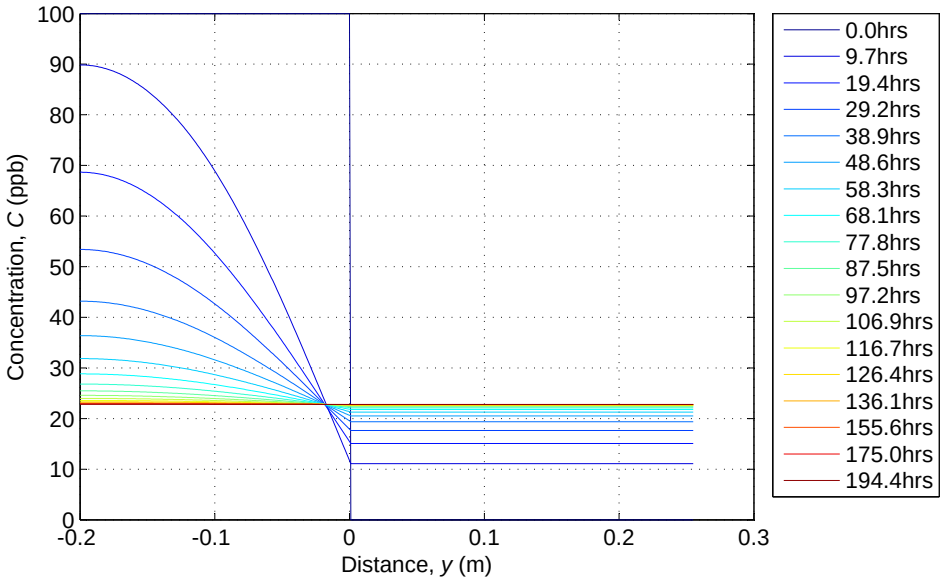

(a) Spatial concentration profile

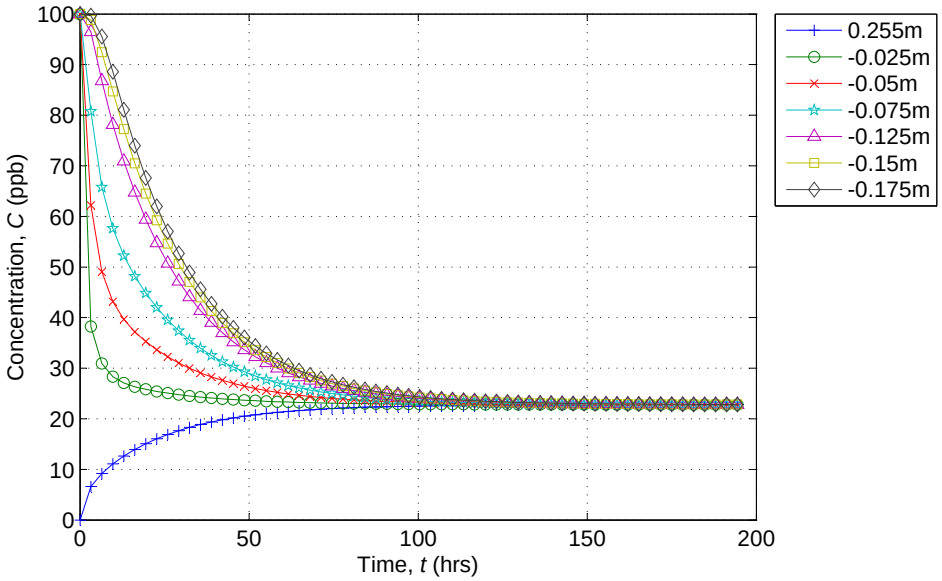

(b) Temporal concentration profile

Figure 2.14: Constant coefficient simulation solute transport between the sediment and water column using model 4 ($D = 1.55 \times 10^{-7}\mathrm{m}^2/\mathrm{s}$)

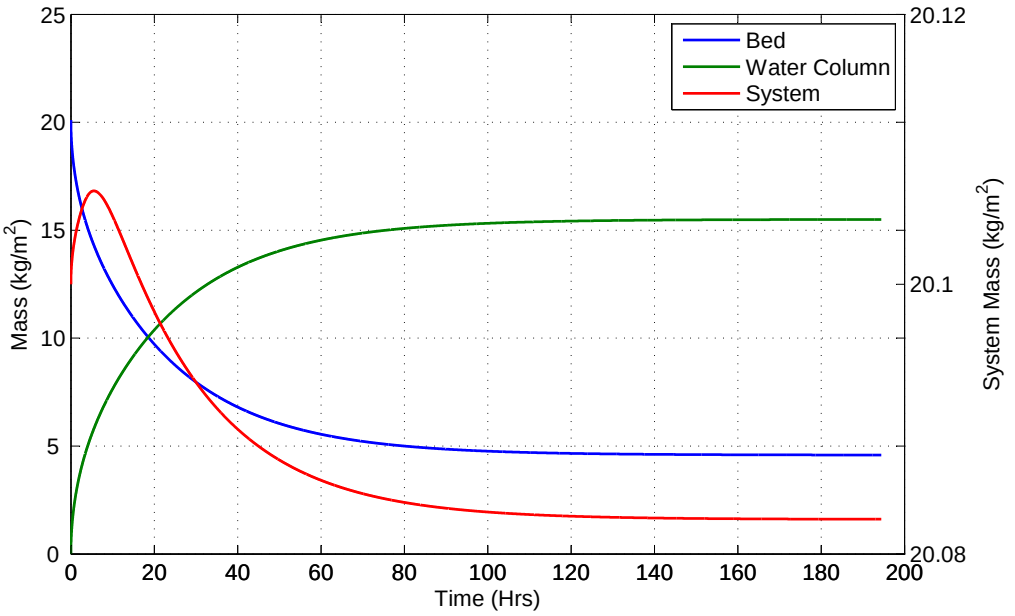

Figure 2.15: System and region mass from Figure 2.14 simulation showing the small overall variation in mass during the simulation

equilibrium concentration. Figure 2.15 shows the mass of tracer in each part of the system and the total system mass. The total system mass varies by 0.1%, however the system mass is likely to be an under estimate because it is based on the slice (Δy) above the sediment water interface. This is taken to be representative of the concentration in the water column. The system mass remains constant as the equilibrium concentration is reached, demonstrating that no mass is being gained or lost, once there is no difference in concentrations. There is a slight loss of mass within the system throughout the simulation (0.08%) which is due to rounding errors within MATLAB®. The problems that were present in the previous models are not demonstrated in this simulation.

To check that the coefficient specified in the model is being applied correctly, a single point injection was simulated in a constant diffusion coefficient region. The spread of this point injection spatially with time should produce a Gaussian profile, similar to Figure 2.10, and through the method of moments [Fischer *et al.*, 1979] the diffusion coefficient can be calculated from these spatial profiles. Model 4 was run with a constant diffusion coefficient of $2.0 \times 10^{-7}\mathrm{m}^2/\mathrm{s}$, and a concentration of 100ppb injected at $y = -0.1\mathrm{m}$, half way down within the bed region. Using the spatial profiles generated at 100 and 300s a diffusion coefficient of $1.9\dot{9} \times 10^{-7}\mathrm{m}^2/\mathrm{s}$ was obtained. This demonstrates that the coefficient specified within the model is

being applied correctly.

Having demonstrated that model 4 is working correctly with a constant diffusion coefficient, a variable coefficient was applied to the bed region. This was applied in seven zones, with a constant diffusion coefficient within each zone. Figure 2.16 shows a simulation using a 7 zone version of model 4. The diffusion coefficients used are given in Table 2.2 with the depths over which they apply.

Start below interface (10^{-3}m)	End below interface (10^{-3}m)	D (m^2/s)
0.000	0.025	2×10^{-6}
0.025	0.050	2×10^{-6}
0.050	0.075	6×10^{-7}
0.075	0.100	2×10^{-7}
0.100	0.125	6×10^{-8}
0.125	0.150	2×10^{-8}
0.150	0.200	2×10^{-8}

Table 2.2: Diffusion coefficients used in Figure 2.16 simulation

The change in diffusion coefficient is clearly visible in the spatial data, Figure 2.16(a), although it is not reflected in the temporal profiles which are taken at the interfaces between the different zones, Figure 2.16(b). This simulation demonstrates that a variable coefficient can be applied within model 4. The final stage in model evaluation is to apply a continuously varying diffusion coefficient that is a function of the depth below the interface. This stage is in preparation for comparing the experimental data with the numerical model which will allow different depth dependent functions to be evaluated. The variation in diffusion coefficient is expected to be a function of the bed shear velocity, permeability and depth below the sediment water interface, but as this relationship will depend on the experimental data, the model is tested here purely on a depth dependent function.

Figure 2.17 gives the results from a simulation using model 4 where the diffusion coefficient varies exponentially with depth below the interface according to (2.91). The steps visible in Figure 2.16(a) are not present in Figure 2.17(a), because of the continuous change in diffusion coefficient with depth. This simulation shows that a continuous depth varying diffusion coefficient can be applied to model 4.

$$D = 9 \times 10^{-7} \exp(80y) \tag{2.91}$$

The section above describes the development of a numerical model to elucidate the processes happening within the erosimeter. The section started with a simple analytical solution to Fick's second law, (2.58), and culminated with a finite

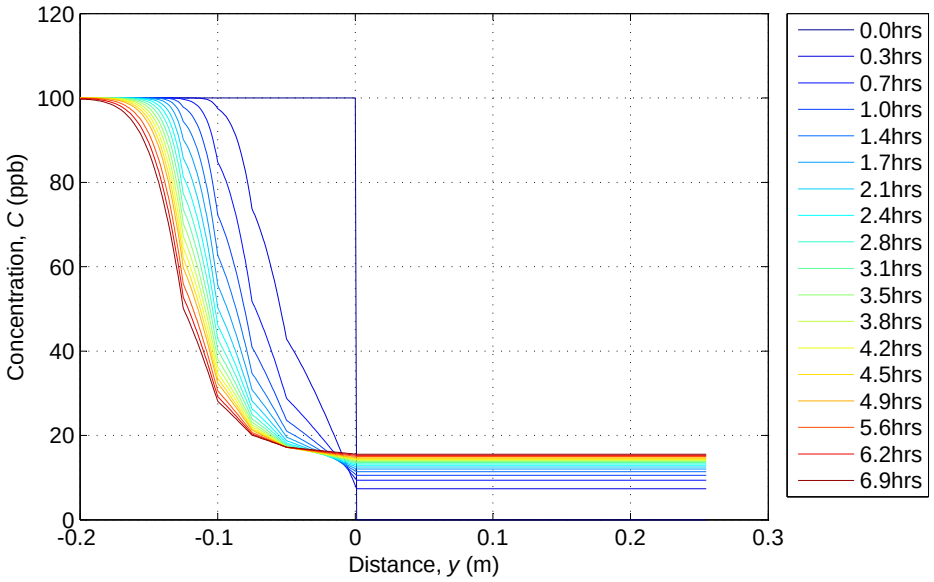

(a) Spatial concentration profile

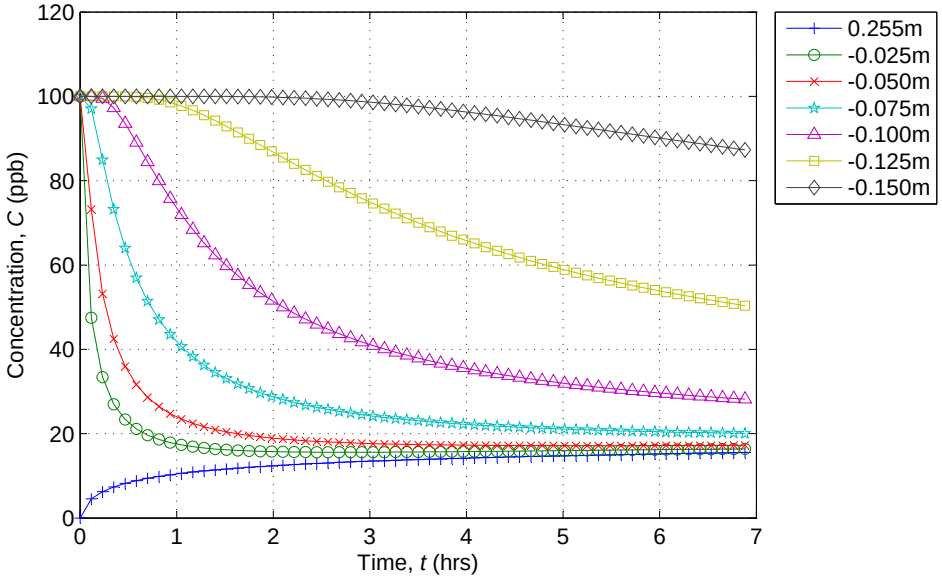

(b) Temporal concentration profile

Figure 2.16: Simulation of solute transport between sediment and water column with discrete variable diffusion coefficients using model 4

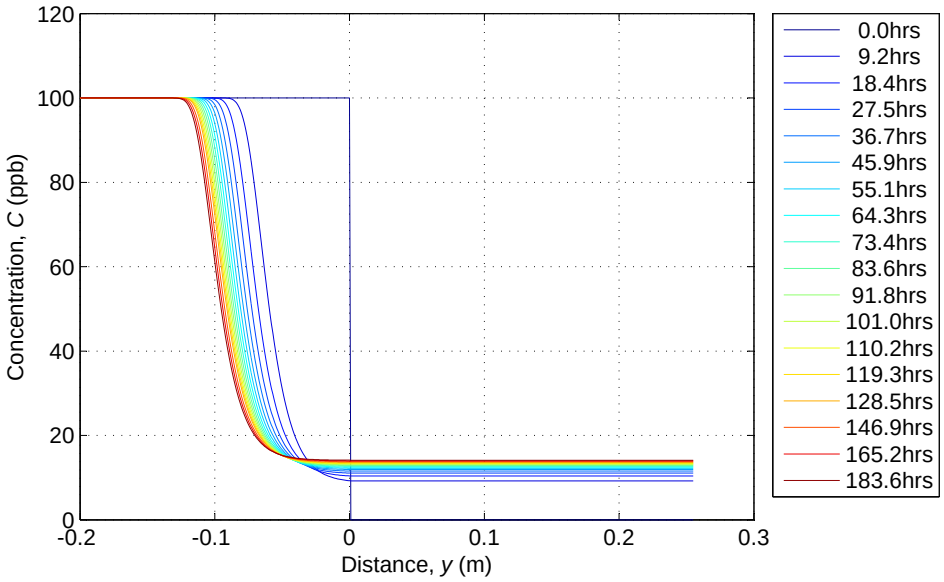

(a) Spatial concentration profile

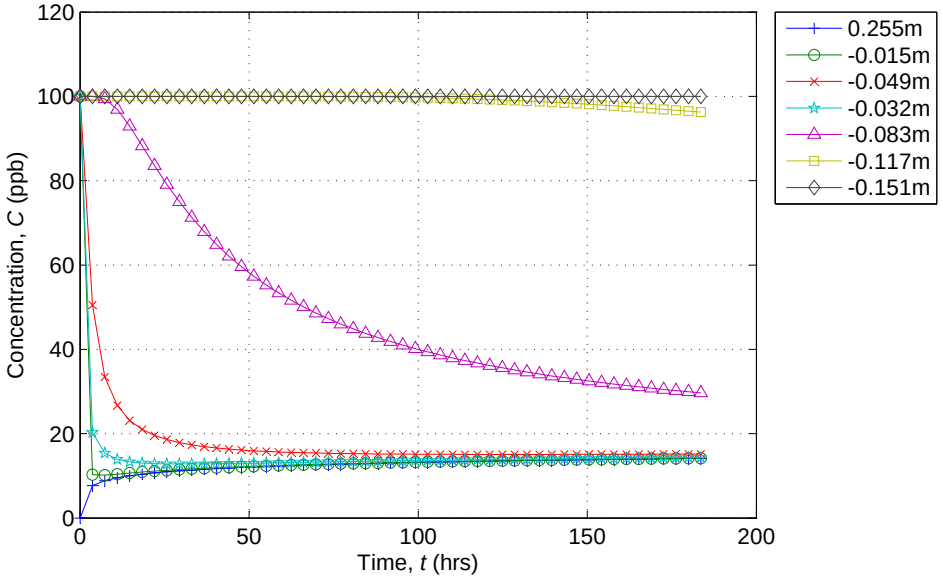

(b) Temporal concentration profile

Figure 2.17: Simulation of solute transport between sediment and water column with continuously variable depth dependent diffusion coefficients using model 4 ($D = 9 \times 10^{-7} \exp(80y)$)

difference model, model 4. The reasons for moving from an analytical to numerical solution to (2.58) were discussed and are primarily due to the requirement that the diffusion coefficient should be variable throughout the bed region. The initial difficulty of equilibrium condition concentration with the finite difference model was solved by not explicitly modelling the water column, and accounting for it with a boundary condition above the sediment water interface. Finally a variable coefficient, first discrete and the continuously varying was applied within the bed region. The final model, model 4, can now be used to determine which analysis techniques should be applied to the erosimeter experimental data, presented in Chapter 4.

2.4 Laboratory Studies

The following sections summarise previous laboratory experimental investigations into hyporheic exchange. The majority of the studies detailed below were used by O'Connor and Harvey [2008] to derive their effective diffusion scaling relationship (2.51). The section is split into those that measured tracer concentrations in the water column and those that took in-bed measurements. For each section the analysis techniques used to obtain diffusion coefficients from the experimental data are presented.

2.4.1 Water Column Measurements

All the studies summarised below measured tracer concentrations in the water column within re-circulating flumes. The initial location of the tracer varied with the particular study, some placing it in the water column and recording the reduction in concentration with time as the tracer mixed with the clean interstitial fluid. Others placed the tracer in the interstitial fluid and recorded the increase in concentration within the water column with time. The analysis techniques used for this type of data are discussed below.

Richardson and Parr [1988]

Richardson and Parr [1988] conducted a series of tests in order to understand and predict the process of chemical flushing from agricultural land by runoff. They used a horizontal, 4.9 by 0.15m Plexiglas flume, with a bed (1.2m long by 25.4mm deep) of glass beads. Three different flow depths and four velocities were passed over five different diameters of bead, which represented fine to very course sands. The bed was saturated with tracer (fluorescein disodium salt) and tracer concentrations were

measured at the effluent weir throughout the 30 minute experiments. The results were used to derive the scaling relationship described in Section 2.3.3.

Lai, Lo, and Lin [1994]

Lai *et al.* [1994] extended the work conducted by Richardson and Parr [1988], using different glass beads, velocities and flow depths. They used potassium chloride as a tracer (placed within the sediment pore water) and sampled the overlying flow at the effluent weir. Lai *et al.* [1994] fitted a proposed two stage release model that is similar to the modified Fickian model proposed by Richardson and Parr [1988] to their data. Within their model the ultimate scour depth (where scour refers to the removal of dye, not sediment) is split into the scoured depth, i.e. that depth of sediment that has had the tracer removed, and the residual scourable depth, that depth that could be scoured but has not been. This is the reverse process to maximum penetration of solute from the overlying water into the bed. The exchange coefficient changes abruptly within the model, which is a feature seen in most of their tests.

Elliott and Brooks [1997b]

Elliott and Brooks [1997b] conducted a series of tests exploring the effect of bed-forms on hyporheic exchange. They used a 5.0 by 0.15m flume with a fine sand bed. Two fluorescent dyes (Amino G Acid and Lissamine FF) were used. The dye was fully mixed within the overlying flow and the decrease in concentration recorded at the outlet weir. The tests ran for up to 14 days and provided the validation for the pumping model described in Section 2.3.1. This study was the first to investigate the effects of bed-forms; all previous studies had used flat beds.

Marion, Bellinello, Guymer, and Packman [2002]

Marion *et al.* [2002] continued the study of bed-form affected hyporheic exchange. They use a tilting flume with a 18.4 by 0.65m channel, a 0.4m thick bed of sand (0.85mm diameter), and re-circulated the tracer over different bed-forms. Five different bed-forms were tested, flat, naturally formed ripples, naturally formed dunes and ripples, artificial sinusoidal dunes and artificial triangular dunes. The surface water was allowed to become fully mixed for 30 minutes before sampling mid way along the channel was undertaken at 10 minute intervals. Salt was used as the tracer and tests were conducted for up to 10 hours. The results from Marion *et al.* [2002] showed that for smaller bed-forms the pumping model provided a good approximation to the observed data, however for more extreme bed-forms the pumping model

failed to predict the observed behaviour. This was attributed to storage in the part of the bed-form that protrudes above the mean bed elevation, which is not taken into account by the Elliott and Brooks [1997a] pumping model.

Packman, Salehin, and Zaramella [2004]

Packman *et al.* [2004] investigated the effect of bed-forms on hyporheic exchange in gravel beds and was mainly used to provide extra laboratory data for their scaling relationship proposed in 2003 [Packman and Salehin, 2003] described in Section 2.3.3. The tests were conducted in a 2.5 by 0.2m recirculating channel, with a course gravel bed ranging in thickness from 0.2 to 0.3m. Sodium chloride (salt) was used as the tracer and once added the flow was re-circulated until the system reached equilibrium. Flat and dune topographies were tested under different flow conditions.

Packman, Brooks, and Morgan [2000]

Packman *et al.* [2000] conducted a series of tests in a 12.0 by 0.265m recirculating flume to study colloid transport and exchange, and aimed to validate the colloid transport model. The results present the exchange rate of colloids (kaolinite clay) and a conservative tracer (lithium) for a stream with a sand bed covered with stationary natural bed-forms. Kaolinite was observed to be more extensively trapped in the stream bed than lithium owing to non-conservative processes, with essentially all added kaolinite taken up by the streambed by the end of most experiments. The colloid pumping model predicts particle exchange based on pumping hydraulics, particle settling in the bed, and filtration by the bed sediments. Packman *et al.* [2000] state the observed colloid and solute exchange was successfully predicted by the process-based models without the use of fitting coefficients. The successful prediction of experimental results validates the modelling approach of combining a fundamental hydraulic exchange model with a physicochemical model for colloid transport and filtration in the streambed.

Packman and MacKay [2003]

Packman and MacKay [2003] conducted a study to examine the relationship between stream subsurface exchange fluxes, the delivery of suspended sediments to the hyporheic region, fine particle accumulation in the streambed, and alteration of sedimentary properties. They used a 10.0 by 0.2m recirculating flume with a sand bed covered with stationary bed-forms. The experiments observed kaolinite clay deposition in a sand bed and the resulting alteration of hyporheic exchange fluxes.

As in Packman *et al.* [2000] the colloid pumping model was used to predict solute and suspended sediment exchange. The model worked well for clean beds. However, substantial accumulation of clay in the bed causes an alteration of the pore water flow environment, which reduces both fluid flux across the sediment water interface and subsequent particle deposition. Their measurement of bulk solute exchange and direct observations of clay accumulation in the bed both indicated that transported fine particles were preferentially removed near the sediment water interface. Packman and MacKay [2003] also state the clogging of inflow regions produces heterogeneous subsurface clay deposits even when the bed is initially homogeneous and that this behaviour is predicted by the fundamental colloid pumping model. They state that their results contradict the accepted view that suspended sediments will generally deposit in the deepest regions of the bed and thus clog the bed from the bottom upward and indicate that clogging of the streambed surface will often isolate deeper regions of the bed from the stream flow.

Ren and Packman [2004]

Ren and Packman [2004] investigated how fine suspended particles of kaolinite and silica affected the exchange of a zinc solution ($ZnCl_2$) being used as a tracer. The tests were conducted in a 2.5m long by 0.2m wide recirculating flume, with a sand bed and naturally sculpted artificial bed-forms. The bed thickness varied between tests, as did the velocity and water depth. Zinc was chosen as a tracer because it is non-toxic, has a single oxidation state under their experimental conditions, and is a common pollutant in streams [Ren and Packman, 2004]. They found that reactive colloids can substantially mediate the exchange of contaminants, that zinc immobilisation in the bed was significantly greater in the presence of kaolinite than colloidal silica and that colloid deposits can provide a mechanism of contaminant immobilisation that is generally not considered in field studies. In their discussion they state that for this case, a simple model that predicts colloidal-phase contaminant deposition based simply on a mean particle settling velocity and an effective partitioning coefficient would have greatly over predicted the actual zinc immobilisation [Ren and Packman, 2004].

Rehg, Packman, and Ren [2005]

Rehg *et al.* [2005] continued the investigation into the effect of suspended sediment on hyporheic exchange, using a 7.5 by 0.2m recirculating channel to study the effects of clogging on hyporheic exchange. The bed consisted of sand to a depth of

approximately 0.1m with naturally sculpted bed-forms. Salt was used as the conservative tracer and kaolinite as the clogging material. Two tests were undertaken; the first with no sediment transport and the second with some bed sediment transport. For both tests the facility was prepared and once a steady state was reached the first tracer injection was conducted. Another injection was undertaken after each two injections of kaolinite, by which time the previous tracer injection had reached an equilibrium state due to hyporheic exchange. The first test was conducted over 14 days with 5 injections of kaolinite of 350-450mg/l. The second test was conducted over 29 days and consisted of 6 injections of 350mg/l and three of 600mg/l. Rehg *et al.* [2005] found that in the first test, without sediment movement, kaolinite formed a thick near-surface clogged layer that greatly reduced hyporheic exchange. In contrast the second test, with sediment movement, showed little change in the hyporheic exchange over the 29 days of testing, as the clogging layer of kaolinite could not form.

Tonina and Buffington [2007]

Tonina and Buffington [2007] investigated the effect of 3D pool-riffle formations with a heterogeneous gravel bed that ranged between course gravel and fine sand, representing a natural headwater stream. Fluorescene was used as the conservative tracer and sampled from the recirculating flow using a Turner Designs 10-AU in flow through mode. Micro-piezometers were used to obtain the pressure distribution across the bed as described at the end of the pumping model section (Section 2.3.1). These data were used to verify the three-dimensional modified Elliott pumping model described in Section 2.3.1. This model was shown to have good agreement with the observed experimental data and gave a much better fit than the conventional two-dimensional model.

Analysis Techniques

A measured value of effective diffusion over a sediment bed can be obtained directly from the use of a conservative tracer [O'Connor and Harvey, 2008]. This is easily demonstrated by considering a closed system, such as a recirculating laboratory flume, where the concentration (C) is initially zero in the bed sediment and the concentration in the overlying water (C_{wc}) is equal to an initial concentration (C_0) (well-mixed system). Once the experiment starts, hyporheic exchange will drive the tracer into the sediment pore water releasing bed fluid of zero concentration, resulting in a decrease of concentration in the overlying water with time. Modelling

hyporheic exchange as an effective diffusion process means the flux of tracer into the sediment is described by Fick's second law (2.58).

For a well-mixed system approximation the boundary conditions for (2.58) are; the concentration at the sediment water interface is equal to C_0 and $\partial C/\partial y = 0$ deep in the sediment. A solution for (2.58) can be obtained for C assuming a semi-infinite domain in the vertical axis and using Laplace transforms as described by Crank [1975], giving

$$C = C_0 \left(1 - \operatorname{erf}\left(\frac{y}{2\sqrt{Dt}}\right)\right). \tag{2.92}$$

The term erf represents the error function, which is a standard mathematical function. It is usually defined as (2.93), and is related to the cumulative distribution which is the integral of the standard normal distribution.

$$\operatorname{erf}(x) = \frac{2}{\sqrt{\pi}} \int_0^x e^{-t^2} \, \mathrm{d}t \tag{2.93}$$

The flux of solute (J) from the overlying water into the sediment is governed by Fick's first law (2.1), however the molecular diffusion coefficient is replaced by an effective diffusion coefficient (2.94).

$$J = -D \left.\frac{\mathrm{d}C}{\mathrm{d}y}\right|_{y=0} \tag{2.94}$$

Taking the derivative of equation (2.92) at the sediment water interface and inserting it into (2.94) gives the expression for the solute flux, (2.95), given by O'Connor and Harvey [2008].

$$J = C_0 \sqrt{\frac{D}{\pi t}} \tag{2.95}$$

This is different from equation (2.96) presented by Packman and Salehin [2003] and in Packman *et al.* [2004] by a factor of $\sqrt{\pi}$, caused by an error in the grouping of terms in the derivation [O'Connor and Harvey, 2008]. A check of the mathematics shows that O'Connor and Harvey [2008] are correct and Packman and Salehin [2003] are out by a factor of $\sqrt{\pi}$.

$$J = \frac{C_0}{\pi} \sqrt{\frac{D}{t}} \tag{2.96}$$

The net solute flux can also be obtained from the expression for the conservation of mass

$$J = -\frac{V_w}{A_s} \frac{\mathrm{d}C_{wc}}{\mathrm{d}t} \tag{2.97}$$

where: V_w is the volume of overlying water in the recirculating system, A_s is the sur-

face area of the bed sediment and $C_{wc}(t)$ is the solute concentration in the overlying water as a function of time.

Equating (2.95) and (2.97), rearranging terms and integrating the resulting function gives

$$C_{wc} = -2C_0 \frac{A_s}{V_w} \sqrt{\frac{Dt}{\pi}} \tag{2.98}$$

Equation (2.98) describes the linear decrease in solute concentration with respect to $t^{1/2}$. Experimental tracer data usually shows this linear decrease over the initial time period, however the decrease in C_{wc} eventually decays over long periods of time [Marion *et al.*, 2002]. The initial slope of C_{wc} versus $t^{1/2}$ can be used to quantify D through rearranging equation (2.98) to give

$$D = \left(\frac{\sqrt{\pi}}{2} \frac{V_w}{A_s} \frac{\mathrm{d}C^*}{\mathrm{d}(t^{1/2})} \right)^2 \tag{2.99}$$

where: $C^* = C_{wc}/C_0$ is the normalised solute concentration in the overlying water. The error in the expression for J, (2.96), used by Packman and Salehin [2003] and in Packman *et al.* [2004] now propagates through into their formula for D, which differs from (2.99) by a factor of π.

For experiments similar to Marion *et al.* [2002] where the tracer was placed in the water column and samples were taken from the water column (i.e. decrease in concentration with time) equation (2.99) can be used. Experiments like those described by Richardson and Parr [1988] and Lai *et al.* [1994] where bed sediment was saturated with tracer concentration $C_{0,s}$ and the mass accumulation within the overlying flow was measured equation (2.100) was used.

$$D = \left(\frac{\sqrt{\pi}}{2C_{0,s}} \frac{\mathrm{d}M_w}{\mathrm{d}(t^{1/2})} \right)^2 \tag{2.100}$$

Where: M_w is the accumulative mass of dye transferred from the sediment to the overlaying water.

Elliott and Brooks [1997b] placed tracer in the water column and converted the decrease in concentration measured in the water column into effective depth of solute penetration (M'/θ). First the mass accumulation in the bed, M_s, is calculated using

$$M_s = \frac{V_w(C_0 - C_{wc})}{a} \tag{2.101}$$

where: V_w is the volume of overlaying fluid in the flume (i.e. excluding interstitial fluid), C_0 is the initial concentration in the water column, C_{wc} is the measured

concentration in the water column and a is the plan area of the sediment bed.

M_s is divided by the initial concentration C_0 of the water column to give M', which is then divided by the porosity θ to give the effective depth of solute penetration. Elliott and Brooks [1997b] showed that a plot of M'/θ versus $t^{1/2}$ initially has a linear increase and the slope can be used to quantify D using

$$D = \left(\frac{\sqrt{\pi}}{2} \frac{\mathrm{d}(M'/\theta)}{\mathrm{d}(t^{1/2})} \right)^2 \tag{2.102}$$

which is a rearrangement of (2.35).

The equations presented above are in the same form as that used by O'Connor and Harvey [2008] to analyse all the experimental data used to derive their scaling relationship (2.51) except the data from Nagaoka and Ohgaki [1990]. The use of these equations and the method of taking the initial slope of a concentration profile to calculate D is referred to in the remainder of this thesis as the O'Connor and Harvey [2008] methodology.

Equation (2.99) and (2.100) can be directly related to each other, as the conversion of normalised concentration to accumulated mass incorporates the V_w/A_s and C_0 terms. Equation (2.102) is related to the others but the comparison is not as straight forward. However if there were no sediment present, then the porosity would be 1, making (2.102) the same as the others.

The relationship between the three equations can be shown by analysing the water column data from a model 4 simulation with a constant diffusion coefficient ($1.55 \times 10^{-7}\mathrm{m}^2/\mathrm{s}$, Figure 2.14). Table 2.3 gives the different initial slopes and corresponding diffusion coefficients obtained from the first 1.0×10^4s of water column concentration profile. There is a slight difference in the coefficient calculated using (2.102), but as stated above it takes a slightly different form to the other equations. The values calculated using the O'Connor and Harvey [2008] methodology are not exactly the same as that specified in the model simulation. However, they are close, with a difference of 10% or less.

Equation	Initial slope	Calculated D ($10^{-7}\mathrm{m}^2/\mathrm{s}$)
(2.99)	0.000616	1.38
(2.100)	0.041907	1.38
(2.102)	0.000452	1.61

Table 2.3: Comparison of diffusion coefficients calculated from different O'Connor and Harvey [2008] analysis equations, showing the similarity between them

In their paper O'Connor and Harvey [2008] state that the trace data exhibits a linear decrease (or increase) for initial periods of time. However they do not define what the initial time period might be. The three simulations with model 4 presented earlier (Figure 2.14 - constant diffusion coefficient, 2.16 - 7 zone and 2.17 - exponential depth dependent function) have been used to asses what percentage of the end concentration (equilibrium if the simulation has been run for long enough) gives a calculated interface exchange coefficient closest to that used in the simulation. Table 2.4 gives the percentage of the maximum concentration taken (as the last point included in the initial slope), the slope, calculated diffusion coefficient (using (2.100)) and the percentage difference from the specified coefficient. The specified interface coefficients for the three models are 1.55×10^{-7}, 2.0×10^{-6} and $9.0 \times 10^{-7}\mathrm{m}^2/\mathrm{s}$ for the constant diffusion coefficient, 7 zone and the exponential depth dependent function simulations respectively.

%	Constant			7 zone			Exponential		
max. con.	Slope (10^{-8})	D_{calc} ($10^{-7}\mathrm{m}^2/\mathrm{s}$)	Diff. (%)	Slope (10^{-7})	D_{calc} ($10^{-6}\mathrm{m}^2/\mathrm{s}$)	Diff. (%)	Slope (10^{-8})	D_{calc} ($10^{-8}\mathrm{m}^2/\mathrm{s}$)	Diff. (%)
1	4.05	1.01	−35						
2	4.27	1.12	−27				10.6	69.0	−23
5	4.77	1.40	−10	1.63	1.63	−19	**12.1**	**90.7**	**1**
10	**4.88**	**1.47**	−5	1.69	1.75	−13	11.8	85.3	−5
20	4.80	1.42	−8	**1.73**	**1.84**	−8	10.0	62.0	−31
30	4.70	1.36	−12	1.72	1.81	−9	7.85	37.9	−58
40	4.59	1.30	−16	1.66	1.70	−15	6.01	22.2	−75
50	4.48	1.23	−20	1.55	1.48	−26	4.46	12.2	−86
60	4.36	1.17	−24	1.39	1.19	−40	3.20	6.29	−93
70	4.22	1.10	−29	1.18	0.86	−57	2.22	3.03	−97
80	4.00	0.98	−37	0.95	0.55	−72	1.49	1.37	−98
90	3.57	0.78	−49	0.72	0.32	−84	0.97	0.58	−99
100	1.30	0.11	−93	0.52	0.16	−92	0.62	0.23	−100

Table 2.4: Effect of using different percentages of a concentration profile on calculated diffusion coefficient from model 4 water column simulated data using equation (2.100)

The bold text indicates the closest match to the specified coefficient. This is between 5 and 20% of the maximum concentration. The constant coefficient and 7 zone simulations are likely to be a better guide for the experimental data than the exponential function, based on the results presented in Chandler *et al.* [2010], summarised in Section 3.2. If the percentage of the maximum concentration is converted into a percentage of the equilibrium concentration (not affecting the constant diffusion simulation as it ran to equilibrium) then the constant coefficient and 7 zone simulations suggest that taking 15% of the equilibrium concentration would give the most accurate exchange coefficient. However the difference in the coefficients

calculated for percentages less than 40% is negligible, particularly given the spread of coefficients from repeat experiments presented by O'Connor and Harvey [2008] (Figure 2.9). It is interesting to note that all the coefficients, except one (5% of the exponential simulation) give values lower than those specified in the simulations. The O'Connor and Harvey [2008] methodology seems to under estimate the interface exchange coefficient, but only slightly for slopes including concentrations less than or equal to 40% of the equilibrium concentration.

Figure 2.18(a) gives the water column concentration profiles for the three model simulations analysed above (Table 2.4). Figure 2.18(b) shows the variation in the calculated diffusion coefficient with the percentage of the equilibrium concentration taken to define the end of the slope. The diffusion coefficients have been normalised using the coefficient specified in the model simulation. Therefore, 1 is an exact match. Figure 2.18(b) shows the same result as Table 2.4 that the most appropriate percentage to use is 15%, although the exponential model simulation suggests a lower percentage.

This analysis can be expanded further to incorporate previously published work. Marion *et al.* [2002] is one of the data sets analysed by O'Connor and Harvey [2008], so it provides a useful reference for what they may have taken as the initial slope. Figure 2.19 uses the same axis as O'Connor and Harvey [2008] adopted to present their scaling relationship (Figure 2.9), but focuses in on the Marion *et al.* [2002] data set. There is a slight discrepancy between the x-axis values used by O'Connor and Harvey [2008] and those calculated in this analysis, however the differences are slight. The important outcome from Figure 2.19 is the diffusion coefficients (y-axis values) used by O'Connor and Harvey [2008] generally match the highest values obtain from this analysis of the Marion *et al.* [2002] data, which correspond to 100% of the concentration profiles in all but one run (S5, second from right). Run S5 (artificial triangular dunes) is the only test where the measured concentration profile reached an equilibrium plateau. For this run the highest coefficient corresponds to 50% of the of the change in concentration being used to define the end of the initial slope. The value used by O'Connor and Harvey [2008] is generally between 90 and 100% of the change in concentration during a test. This may be because the data shows a strong linear trend until the equilibrium concentration is neared.

From the analysis above, this methodology is suitable for analysing the water column data generated by the erosimeter experimental setup (Chapter 3). From the model data analysis, taking between 20-30% of the equilibrium concentration to define the end of the initial slope is appropriate. However this will need to be

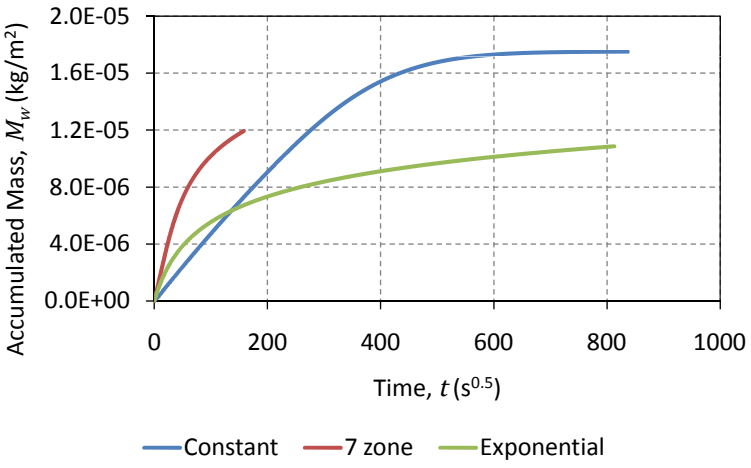

(a) Water column concentration profiles

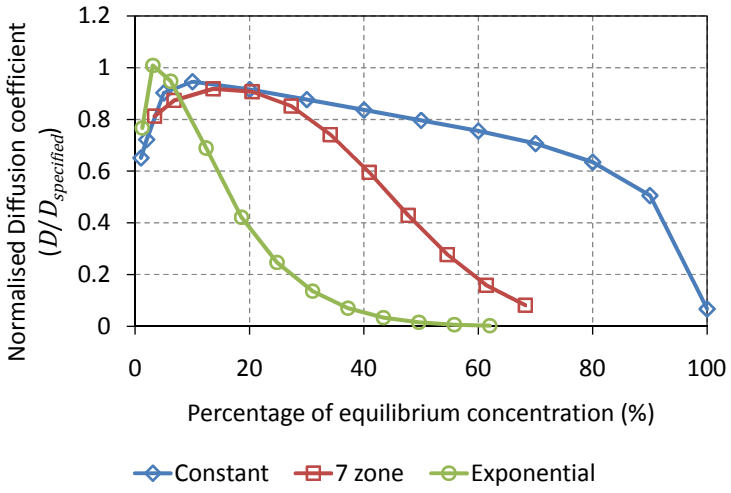

(b) Change in calculated coefficient

Figure 2.18: Effect of using different percentages of a concentration profile on calculated diffusion coefficient from model 4 water column simulated data using equation (2.100)

validated for the main series of experimental tests. The comparison of the analysis of Marion *et al.* [2002] data with that conducted by O'Connor and Harvey [2008] indicates that they took the largest exchange coefficient obtainable from the data. In the case of the Marion *et al.* [2002] data, this corresponded to using 100% of the measured concentration profile in all but one case.

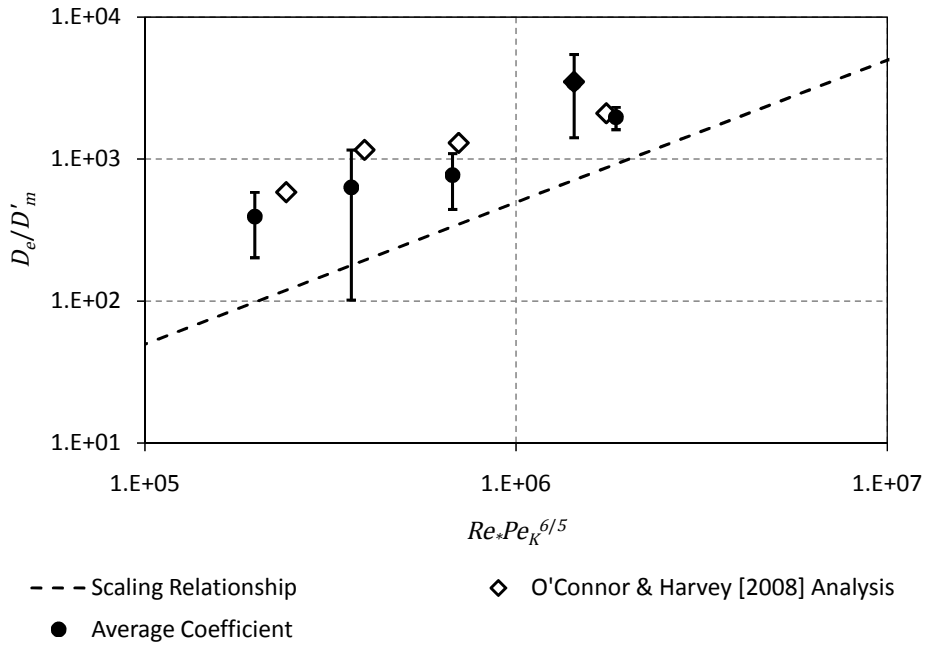

Figure 2.19: Comparison of different percentages of the data taken to represent the initial slope on Marion *et al.* [2002] data

2.4.2 In-bed Measurements

There are fewer studies that have measured tracer concentrations within bed sediments in laboratory conditions. The three main studies are Elliott and Brooks [1997b], Shimizu *et al.* [1990] and Nagaoka and Ohgaki [1990]. Details of their investigations are given below along with a discussion of the analysis techniques employed.

Elliott and Brooks [1997b]

Elliott and Brooks [1997b] conducted in-bed measurements concurrently with water column measurements in some of their experiments detailed above in Section 2.4.1. They installed a vertical array of sampling ports at several longitudinal locations within the flume. The vertical spacing was 10mm centre to centre. 100μl of interstitial fluid was removed using a needle and syringe. The samples were all measured ex-situ in a Shimadzu RF-540 fluorospectrophotometer. Although the spatial resolution of the measurements is high the temporal resolution is not. Samples were only taken from some traces and at irregular intervals. The vertical concentration profiles were used to map the evolution of the dye front as is descends into the bed sediment.

Shimizu, Tsujimoto, and Nakagawa [1990]

Shimizu *et al.* [1990] conducted a series of tracer experiments where in-bed profiles were measured at three different depths below the sediment water interface. They used a highly permeable bed consisting of 17 and 30mm diameter glass spheres, giving an permeability of 6.9×10^{-8} and $2.8 \times 10^{-7}\mathrm{m}^2$ respectively. The spheres were arranged in the 'most packed tetragonal-spheroidal' pattern, giving a layer of constant thickness along the 8m long by 0.21m wide channel. Velocity measurements were conducted within the water column using a Pitot tube (2mm diameter) and in the porous bed using conductivity probes with a slug injection of salt water tracer at the same height as the probes. This method gave a measure of the longitudinal seepage velocity within the porous media. The hyporheic exchange experiments were conducted with salt water as the tracer. Tracer was continuously injected at the sediment water interface and measured 50mm downstream, at 0, 5 and 25mm below the interface. Temporal concentration profiles were not given in the paper, but the continuous nature of the injection would suggest that the concentration (salinity) rose from zero at $t = 0$ to an equilibrium value.

Nagaoka and Ohgaki [1990]

Nagaoka and Ohgaki [1990] studied mass transfer mechanisms in porous riverbeds, with a view enhancing the quality of urban rivers within Tokyo through self-purification by the micro organisms attached to the bed sediment. They used two flumes, the larger 3.7 by 0.18m and the smaller 2.25 by 0.18m. Two different diameter ceramic balls were used, with the smaller balls (diameter 19mm) in the smaller flume and the larger, 40.8mm diameter balls, in the larger flume. The beds consisted of organised layers of spheres, with conductivity probes placed at the water-sediment interface and between the next four layers. Salt was used as the tracer, and was introduced into the downstream sump once steady state conditions had been reached. The system was recirculating and it is possible to see the salt plume recirculating throughout the experimental data. These tests were not left until the salt was fully mixed within the system and an equilibrium state reached. From this work Nagaoka and Ohgaki [1990] proposed the diffusion coefficient was affected by different parameters, depending on the vertical position within the sediment. For the near surface region they proposed that the turbulent intensity was the most influential factor, whereas the time average velocity and void scale was the most influential in deeper regions. However, they did not attempt to quantify the variation in diffusion coefficient with depth.

Analysis Techniques

The O'Connor and Harvey [2008] methodology used in the water column studies cannot be applied to in-bed data. This is because the technique assumes that the concentration profile being used is representative for the volume in which the measurements are made, i.e. that the volume is well-mixed. This is not the case within the bed sediment as shown by the measurements taken spatially by Elliott and Brooks [1997b]. However Elliott and Brooks [1997b] did not use their measured concentrations profiles from the bed sediment to determine a diffusion coefficient within the bed. Both Shimizu *et al.* [1990] and Nagaoka and Ohgaki [1990] did calculate diffusion coefficients from measurements within the bed sediment.

Shimizu, Tsujimoto, and Nakagawa [1990]

Shimizu *et al.* [1990] began with Ficks second law (2.58) and solved it using the following initial and boundary conditions.

$$C(y,0) = 0 \qquad (0 < y < -H_s) \tag{2.103}$$

$$C(0,t) = C_0 \ (= \text{const.}) \qquad (t > 0) \tag{2.104}$$

$$C(-H_s,t) = 0 \qquad (t > 0) \tag{2.105}$$

Where: C is tracer concentration, t is time and H_s is the depth of the sediment bed (from the sediment water interface to the bed of the flume). The third condition, (2.105), corresponds to the case $H_s \to \infty$, which Shimizu *et al.* [1990] take to be a valid assumption because they assume the sediment bed is thicker than the turbulence affected region. Using these boundary and initial conditions, Shimizu *et al.* [1990] derive the following expressions for the concentration profile, $C(y,t)$.

$$C(y,t) = C_0 \left\{ 1 + \frac{y}{H_s} + \frac{2}{\pi} \sum_{j=1}^{\infty} \frac{(-1)^j}{j} \exp\left(-\frac{j^2 \pi^2 D}{H_s^2} t \right) \sin\left[\frac{j\pi(y + H_s)}{H_s} \right] \right\} \tag{2.106}$$

Where: D is the vertical diffusion coefficient and the steady, equilibrium, solution at y is given by

$$C(y,\infty) = C_0 \left(1 + \frac{y}{H_s} \right) \tag{2.107}$$

Shimizu *et al.* [1990] appreciate that a perfect line source was not accomplished in their experiments, so the convection term could not be neglected against the theoretical solution, (2.106), meaning $C(y,\infty)$ was not independent of longitudinal position x. However they assume that the temporal asymptotic behaviour of

the concentration would be similar along x. Having made this assumption Shimizu *et al.* [1990] state; "When the time scale at which the concentration reaches $1/e$ of the equilibrium concentration ($C(y,\infty)$) is represented by T_e, the following relation is valid:"

$$C(y,T_e) = \frac{C_0}{e}\left(1+\frac{y}{H_s}\right). \tag{2.108}$$

By equating (2.108) and (2.106),

$$\frac{C_0}{e}\left(1+\frac{y}{H_s}\right) = C_0\left\{1+\frac{y}{H_s}+\frac{2}{\pi}\sum_{j=1}^{\infty}\frac{(-1)^j}{j}\exp\left(-\frac{j^2\pi^2 D}{H_s^2}T_e\right)\sin\left[\frac{j\pi(y+H_s)}{H_s}\right]\right\} \tag{2.109}$$

The vertical diffusion coefficient, D, can be estimated using (2.109) by obtaining experimental values of T_e. Once T_e is known, D can be optimised so that (2.109) becomes true. This method only uses one temporal concentration measurement ($C(y,T_e)$) to obtain D. The methodology assumes that the theoretical profile (2.106) fits the measured profile.

In order to test this methodology model 4 simulations were analysed and the theoretical concentration profiles, calculated using (2.106), from the diffusion coefficient obtained. These theoretical profiles are then compared with the original model profiles. The same model 4 constant coefficient simulation (Figure 2.14) used to assess the O'Connor and Harvey [2008] methodology was analysed. The coefficients obtained from analysing temporal profiles taken from six depths below the sediment water interface are presented in Table 2.5.

Depth (m)	Specified (10^{-7}m^2/s)	Analysis (10^{-7}m^2/s)
-0.025	1.55	5.43
-0.050	1.55	1.38
-0.075	1.55	1.13
-0.125	1.55	0.784
-0.150	1.55	0.729
-0.175	1.55	0.656

Table 2.5: Output from Shimizu *et al.* [1990] analysis of constant coefficient model 4 simulation showing the coefficient specified in the model simulation and that obtained from the analysis

The diffusion coefficients from the analysis are not the same as those specified in the model (1.55×10^{-7}m^2/s). Analysis of the lower profiles produces coefficients that are smaller than those specified, whilst near the interface the coefficients are larger. Figure 2.20 shows the model simulation profile at -0.025m below the sedi-

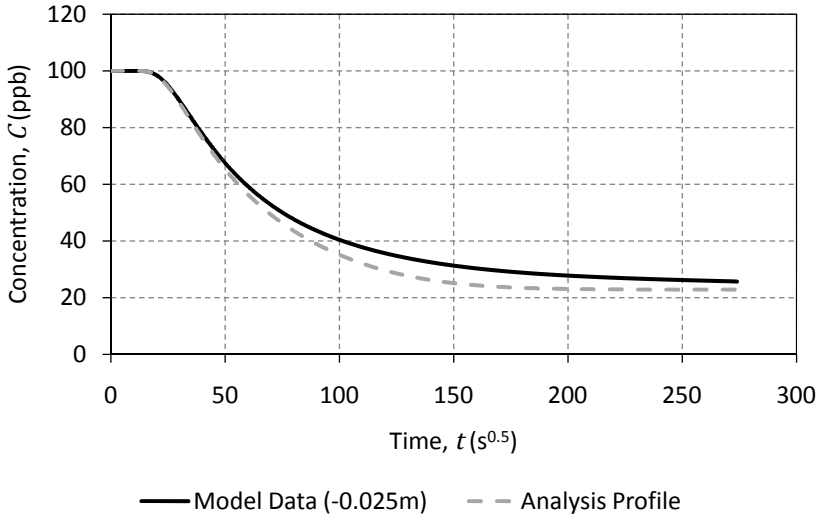

Figure 2.20: Comparison of Shimizu *et al.* [1990] analysis profile (generated using (2.106)) against model 4 simulation profile used in analysis (-0.025m)

ment water interface and theoretical profile calculated by (2.106), using the analysis coefficient. The theoretical profile appears to over predict the diffusion, and reaches the equilibrium concentration much sooner than the simulation.

Despite the differences between the theoretical profiles generated by (2.106) and the data analysed so far, the technique is producing diffusion coefficients that are similar, if not exactly the same, as those specified in the constant coefficient model simulation. The analysis methodology has been applied to the 7 zone variable diffusion coefficient model 4 simulation, Figure 2.16. The specified coefficients, for the region directly above the depths given, and those obtained from the analysis are presented in Table 2.6.

Depth (m)	Specified (10^{-7}m^2/s)	Analysis (10^{-7}m^2/s)
-0.025	20.0	70.2
-0.050	20.0	23.7
-0.075	6.00	14.7
-0.100	2.00	7.42
-0.125	0.60	2.98
-0.150	0.20	0.86

Table 2.6: Output from Shimizu *et al.* [1990] analysis of 7 zone variable coefficient model 4 simulation showing the coefficient specified in the model simulation and that obtained from the analysis

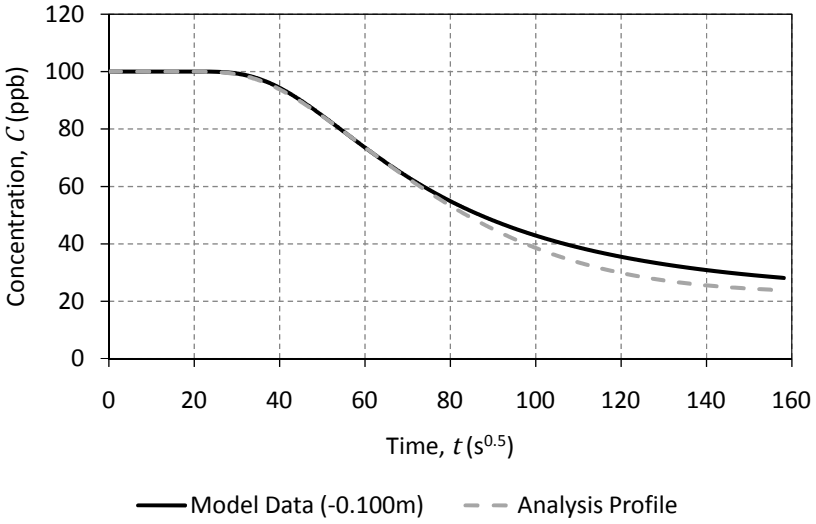

Figure 2.21: Comparison of Shimizu *et al.* [1990] analysis profile (generated using (2.106)) against 7 zone variable coefficient model 4 simulation profile used in analysis (-0.100m)

The analysis coefficients are approximately half an order of magnitude larger than those specified. They are closer to the coefficients for the region above that adjacent to the profile analysed. For example -0.125m profile analysis coefficient is close to that specified in the region above -0.100m. This is a result of (2.106), and the assumption within the equation that the coefficient is the same throughout the domain above the profile being analysed. This will lead to higher analysis coefficient that those specified, because the higher coefficient region nearer the surface within the simulation will affect the concentration profile. This is not accounted for in this analysis methodology. Although it is more sophisticated than the O'Connor and Harvey [2008] methodology, it is still only using one profile and assuming that it is representative of the whole region.

Figure 2.21 shows the simulated temporal concentration profile at -0.100m below the sediment water interface, with the theoretical profile calculated using the analysis coefficient. As with the constant coefficient simulation, the theoretical profile still reaches the equilibrium concentration quicker than the model simulation. The theoretical profile describes the first portion, up to the $C(y, T_e)$ (used for the analysis) well, However after this concentration the profiles diverge. This demonstrates the problem of assuming a single diffusion coefficient in a variable coefficient system.

The methodology used by Shimizu *et al.* [1990] has many assumptions, and the comparison with the model simulations suggests that relying on one single concentration measurement, and assuming that the rest of the profile matches can give misleading results. Another consideration is that this methodology is applied by Shimizu *et al.* [1990] in the turbulence affected region, which would not necessarily be the case deep within the sediment bed in the erosimeter experiments.

Nagaoka and Ohgaki [1990]

Nagaoka and Ohgaki [1990] used the initial increasing portion of their measured concentrations profiles and optimised the equations described below to obtain a diffusion coefficient between each of their profiles. This procedure is similar to the routing procedure that has been applied to the advection diffusion equation (ADE) model [Fischer, 1968; Rutherford, 1994].

As with the other analysis methodologies, this method starts with Fick's second law (2.58). Nagaoka and Ohgaki [1990] experimental method resulted in a concentration profile that started at zero and rose to a peak concentration. They solved (2.58) using the following initial and boundary conditions.

$$C(0, y) = 0 \tag{2.110}$$

$$C(t, 0) = f(t) \tag{2.111}$$

$$C(t, -L^-) = C(t, -L^+) \tag{2.112}$$

$$\lim_{y \to -\infty} C(t, y) = 0 \tag{2.113}$$

$$D = D_1 (0 < y < -L) \tag{2.114}$$

$$D = D_2 (-L < y < -\infty) \tag{2.115}$$

$$D_1 \frac{\partial C}{\partial y}\bigg|_{y=-L-} = D_2 \frac{\partial C}{\partial y}\bigg|_{y=-L+} \tag{2.116}$$

Where: L is the vertical distance between sensors.

The boundary conditions correspond to the scenario where two different layers, with different diffusion coefficients (D_1 in the upper and D_2 in the lower), are acting at $y = -L$. The upper layer is from $y = 0$ to $y = -L$ and the lower layer is from $y = -L$ to $y = -\infty$. By substituting $y = -L$ into the analytical solution to (2.58), Nagaoka and Ohgaki [1990] obtained the concentration change at the

interface between the two layers, defined as the function $C_A[f(t), D_1, D_2]$.

$$C_A[f(t), D_1, D_2] = C(t, L) = \frac{L}{(b+1)\sqrt{\pi D_1}} \times \int_0^t \frac{f(\varepsilon)}{(t-\varepsilon)^{3/2}} \sum_{j=0}^{N} c^j (2j+1) \exp\left(-\frac{(2j+1)^2 L^2}{4D_1(t-\varepsilon)}\right) \, \mathrm{d}\varepsilon \quad (2.117)$$

Where

$$b = \sqrt{\frac{D_2}{D_1}} \quad (2.118)$$

$$c = \frac{b-1}{b+1} \quad (2.119)$$

Equation (2.117) expresses how the concentration at the interface between the two layers changes when the concentration at the upper edge of the upper layer, $f(t)$, changes. This equation can be applied if the change in concentration at the top of the upper layer and both diffusion coefficients are known. The first is true if we have a concentration profile from an instrument above the position that we are interested in, i.e. one at -0.200m and another at -0.100m. The profile from -0.100m can be used to estimate the profile from -0.200m given the correct diffusion coefficients. To reduce the number of parameters that require optimisation, it is preferable to know one of the coefficients. If the analysis starts with the lowest instrument pair and works up then D_2 is known from the previous analysis, leaving only D_1 to be optimised so that the profile generated from (2.117) matches the measured profile from -0.200m.

This does leave a problem with analysing the lowest pair, because D_2 is not known. However taking the limit $D_1 \to D_2$, then another function $C_B[f(t), D_1]$ can be defined.

$$C_B[f(t), D_1] = \frac{L}{2\sqrt{\pi D_1}} \int_0^t \frac{f(\varepsilon)}{(t-\varepsilon)^{3/2}} \exp\left(-\frac{L^2}{4D_1(t-\varepsilon)}\right) \, \mathrm{d}\varepsilon \quad (2.120)$$

Here the assumption is the diffusion coefficient for the upper layer (between the two profiles) is the same as that in the lower layer (below the bottom profile). The methodology starts by optimising D_1 in (2.120) so that the closest match is found between the predicted profile $C_B[f(t), D_1]$ and the lowest instrument position measured concentration profile. Once D_1 is obtained between the lowest pair of instruments, it can be used as D_2 in (2.117), and D_1 can be optimised between the next lowest instrument pair.

The Nagaoka and Ohgaki [1990] methodology is evaluated below against model simulations in the same manner as the Shimizu *et al.* [1990] methodology above. Further evaluation of this technique is conducted with experimental data in the results chapter (Chapter 4). The preliminary evaluation of this methodology was conducted by optimising the 2D correlation coefficient, calculated using the in built MATLAB® function `corr2` between the measured and calculated profiles. Further details on this function and a comparison of different goodness of fit parameters is given later in this section (Parameter Optimisation).

The initial evaluation was conducted on simulations using a two zone version of model 4. In this model the diffusion coefficient can be varied in each half of the bed region, i.e. one coefficient between the base (-0.200m) and -0.100m, and a second between -0.100m and the sediment water interface (0m). The first simulation has the same coefficient in both regions ($2 \times 10^{-6}\text{m}^2/\text{s}$) and the second has a different coefficient in the lower region ($2 \times 10^{-8}\text{m}^2/\text{s}$ between -0.200 and -0.100m). Table 2.7 gives the output from the Nagaoka and Ohgaki [1990] analysis of the constant coefficient simulation, with the depths of the profile pairs (upper used as $f(\varepsilon)$ in the equation and the lower compared with this calculated profile to obtain a goodness of fit value), the coefficient specified between those depths and that obtained from the analysis. For both this simulation analysis and that following on the variable coefficient simulation, the optimisation started with the specified interface coefficient ($2 \times 10^{-6}\text{m}^2/\text{s}$) and ran to a tolerance level of ($1 \times 10^{-10}\text{m}^2/\text{s}$).

Upper profile depth (m)	Lower profile depth (m)	Specified ($10^{-6}\text{m}^2/\text{s}$)	Analysis ($10^{-6}\text{m}^2/\text{s}$)
-0.025	-0.050	2.00	1.24
-0.050	-0.075	2.00	1.48
-0.075	-0.100	2.00	2.09
-0.100	-0.125	2.00	3.25
-0.125	-0.150	2.00	4.76

Table 2.7: Output from Nagaoka and Ohgaki [1990] analysis of constant coefficient model 4 simulation showing the two profiles used in the analysis, the coefficient specified in the model simulation and that obtained from the analysis

The analysis coefficients are of the same order of magnitude as the specified coefficients, but only between -0.075 and -0.100m does the analysis coefficient equal that specified. However the coefficients are much closer to the specified coefficients that those obtained from the Shimizu *et al.* [1990] methodology, when used to analyse a constant coefficient simulation.

The analysis of the variable coefficient simulation (Table 2.8) demonstrates an even better agreement between the specified model coefficients and those obtained from the analysis, particularly in the lower coefficient region, between −0.200 and −0.100m. The coefficients obtained nearer the interface are not as close to those specified in the simulation and if the predicted profile is compared with the model simulation there is a marked difference, not evident for the lower profiles. This is shown in Figure 2.22, which shows the output profiles from the analysis between −0.050 to −0.075m and −0.125 and −0.150m.

Upper profile depth (m)	Lower profile depth (m)	Specified (10^{-7}m^2/s)	Analysis (10^{-7}m^2/s)
−0.025	−0.050	20.0	40.9
−0.050	−0.075	20.0	46.4
−0.075	−0.100	20.0	19.4
−0.100	−0.125	0.20	0.20
−0.125	−0.150	0.20	0.20

Table 2.8: Output from Nagaoka and Ohgaki [1990] analysis of 2 zone variable coefficient model 4 simulation showing the two profiles used in the analysis, the coefficient specified in the model simulation and that obtained from the analysis

The Nagaoka and Ohgaki [1990] methodology gives better results when the specified coefficient is varied. This methodology was applied to the 7 zone model 4 simulation (Figure 2.16), which was used to evaluate the Shimizu *et al.* [1990] methodology. The optimisation starting point was 2×10^{-6}m^2/s (the interface coefficient) and the tolerance was again 1×10^{-10}m^2/s. Table 2.9 gives the output of the analysis. The depths used previously have been retained, which correspond to the changes in diffusion coefficient within the simulation.

Upper profile depth (m)	Lower profile depth (m)	Specified (10^{-7}m^2/s)	Analysis (10^{-7}m^2/s)
−0.025	−0.050	20.0	18.9
−0.050	−0.075	6.00	5.36
−0.075	−0.100	2.00	1.85
−0.100	−0.125	0.60	0.60
−0.125	−0.150	0.20	0.20

Table 2.9: Output from Nagaoka and Ohgaki [1990] analysis of 7 zone variable coefficient model 4 simulation showing the two profiles used in the analysis, the coefficient specified in the model simulation and that obtained from the analysis

The Nagaoka and Ohgaki [1990] methodology has produced coefficients that almost exactly match those specified in the model simulation. However the model

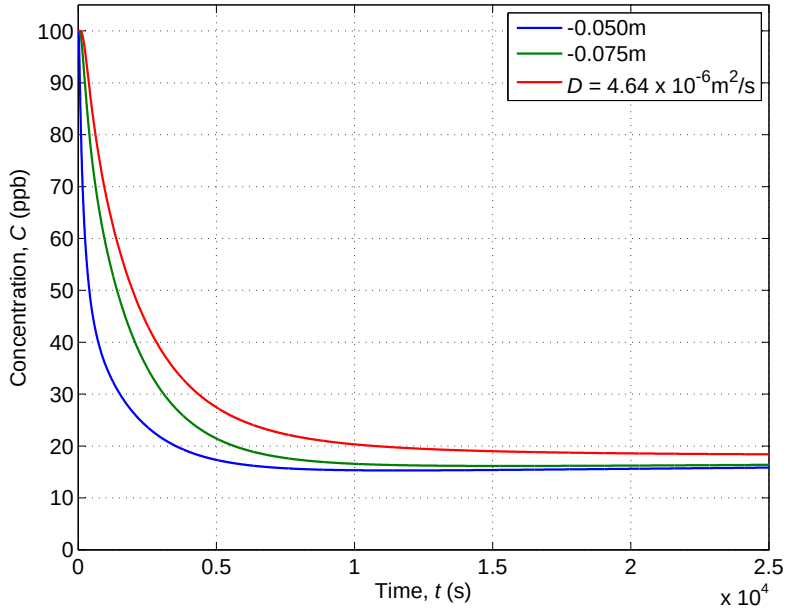

(a) Analysis between -0.050 and -0.075m, coefficient specified in simulation $2 \times 10^{-6}\mathrm{m}^2/\mathrm{s}$

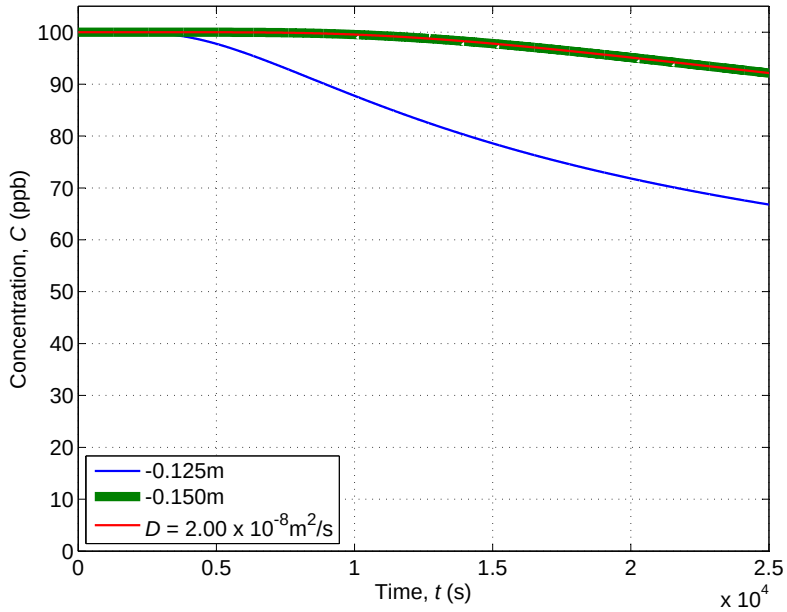

(b) Analysis between -0.125 and -0.150m, coefficient specified in simulation $2 \times 10^{-8}\mathrm{m}^2/\mathrm{s}$

Figure 2.22: Example analysis of 2 zone variable coefficient model 4 simulation, showing the simulation profiles used in the analysis and the result of the optimisation (red line) including the coefficient used to generate the profile (legend entry)

data is 'perfect', with no experimental noise. The simulation was analysed again, but with the addition of random noise. This procedure utilised the MATLAB® function `rand` which produces a random number between zero and one. This value was doubled to increase the effect of the random number. A random value is added and subtracted because doing one or the other would shift the profile either up or down, which was not desired. In retrospect this slightly arbitrary choice of randomisation generated somewhat unrealistic noise because the distribution of noise is uniform. The noise should have had a higher variance and perhaps used a normal distribution rather than a uniform one.

$$C = C + 2(\texttt{rand}(\texttt{size}(C)) - 2(\texttt{rand}(\texttt{size}(C)) \tag{2.121}$$

Where: C is a matrix of concentration values from a model simulation and `rand` and `size` are in-built MATLAB® function.

The analysis was conducted with the same interface coefficient and tolerance level as previously. Table 2.10 gives the analysis output along with the specified coefficients and those from the analysis of the original, no noise data. An example output plot is given in Figure 2.23. There are some small differences between the coefficients obtained from the noisy data and those from the original, clean, data. However the noise does not seem to have affected the optimisation process significantly and the coefficients obtained are still very close to those specified in the model simulation.

Upper profile depth (m)	Lower profile depth (m)	Specified coefficient (10^{-7}m^2/s)	Analysis, no noise (10^{-7}m^2/s)	Analysis, noise (10^{-7}m^2/s)
−0.025	−0.050	20.0	18.9	18.8
−0.050	−0.075	6.00	5.36	5.33
−0.075	−0.100	2.00	1.85	1.85
−0.100	−0.125	0.60	0.60	0.599
−0.125	−0.150	0.20	0.20	0.197

Table 2.10: Output from Nagaoka and Ohgaki [1990] analysis of 7 zone variable coefficient model 4 simulation with noise showing the two profiles used in the analysis, the coefficient specified in the model simulation and that obtained from the analysis with and without noise

The Nagaoka and Ohgaki [1990] methodology has produced coefficients that closely match those specified in the model simulations. The technique is more robust than that of Shimizu *et al.* [1990] and allows for variation in the exchange coefficient within the bed. The section below investigates the optimisation process implemented

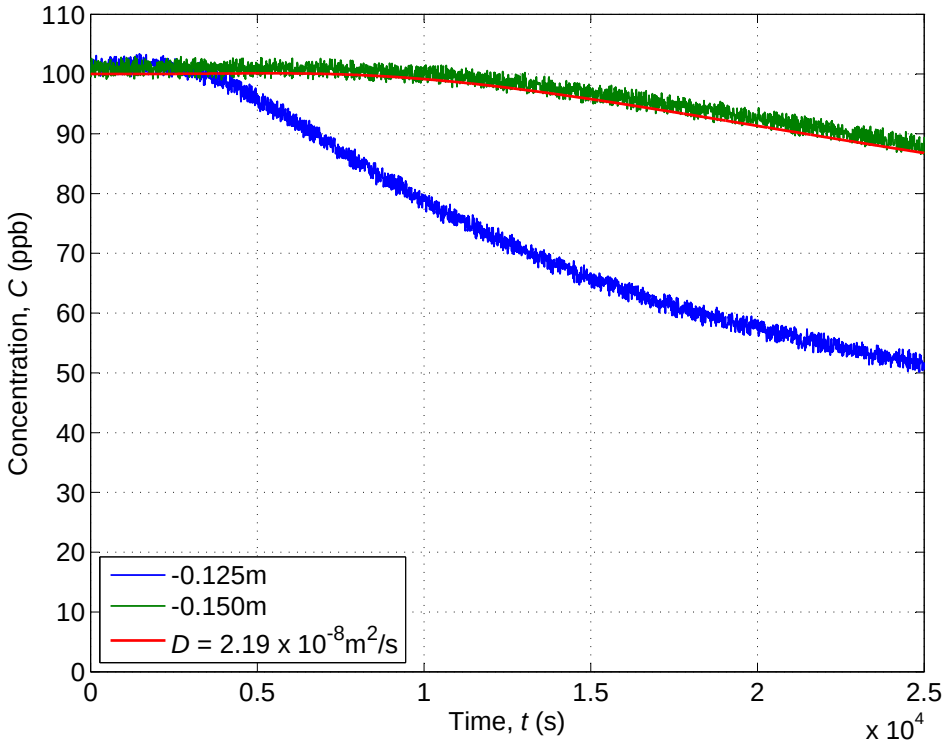

Figure 2.23: Example output from Nagaoka and Ohgaki [1990] analysis of 7 zone variable coefficient model 4 simulation with noise for the region between −0.125 and −0.150m, showing the simulation profiles used in the analysis and the result of the optimisation (red line) including the coefficient used to generate the profile (legend entry)

with the Nagaoka and Ohgaki [1990] methodology in this study.

Parameter Optimisation

The Nagaoka and Ohgaki [1990] methodology involves optimising D_1 in either (2.117) or (2.120), so that the calculated profile gives the closest match to a measured profile. The advantage of using MATLAB® (or any other computational maths program) is the optimisation process can be automated. A procedure similar to that used by Dennis [2000] and Dutton [2004] was implemented. A vector of possible diffusion coefficients is specified, initially based on the sediment water interface coefficient, either known for a model simulation or from analysis of the water column data using the O'Connor and Harvey [2008] methodology. A calculated profile is generated for all the coefficients within this vector and a goodness of fit parameter, such as the coefficient of determination (R_t^2), is obtained between the measured and calculated profiles. The coefficient that gives the best fit is then used to specify a

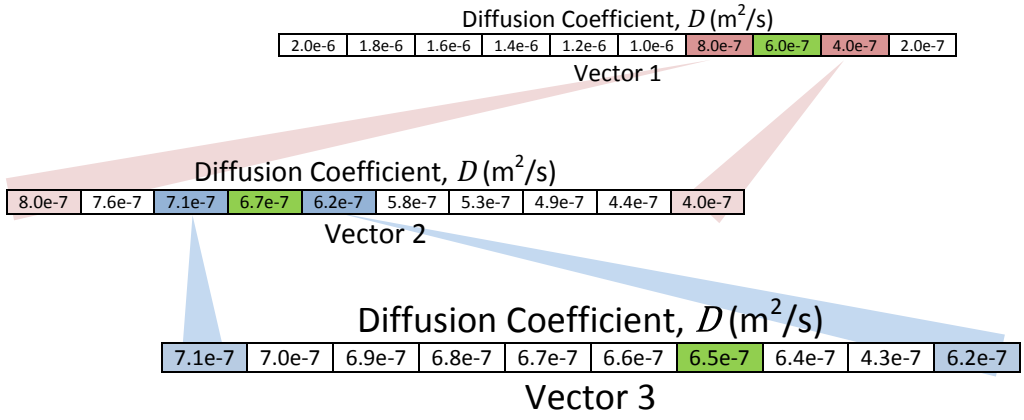

Figure 2.24: Pictorial representation of optimisation process indicating the 'best' coefficient (green) at each stage of the optimisation and how the next vector of possible diffusion coefficients is defined

new vector of diffusion coefficient, but covering a narrower range. In this manner the code iterates towards the coefficient that gives the best calculated profile when compared with the measured (or model simulated) profile. This is shown graphically in Figure 2.24. The optimisation stops when the difference between the highest and lowest diffusion coefficients within the vector is less than a specified tolerance level.

Figure 2.25 shows the outputs from the first three stages of an optimisation routine. Figure 2.25(a) shows the first stage, with the two measured (or model simulated) profiles (-0.075 and -0.100m) and the theoretical analysis profile generated by a vector of possible diffusion coefficients, such as the first row in Figure 2.24. Here the vector contains 20 possible diffusion coefficients that range from 4×10^{-6}m^2/s to 4×10^{-7}m^2/s. As stated above, this initial vector is based on the sediment water interface coefficient, which in this case is significantly higher than that between the profiles used.

The diffusion coefficient that gives the best fit to the -0.100m profile is the lowest and is then used to generate a second vector of possible coefficients. The resultant profiles are shown in Figure 2.25(b). The range of diffusion coefficients now includes the coefficient between the two profiles, indicated by the theoretical profiles overlying the lower -0.100m profile. The optimisation now focusses the next vector of possible coefficients around the value that gives the best fit against the -0.100m Figure 2.25(c), where the 20 theoretical analysis profiles are concentrated around the 'correct' value. The optimisation continues until the desired tolerance level is

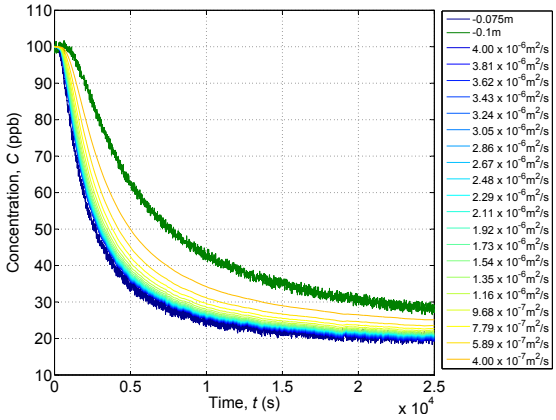

(a) First iteration

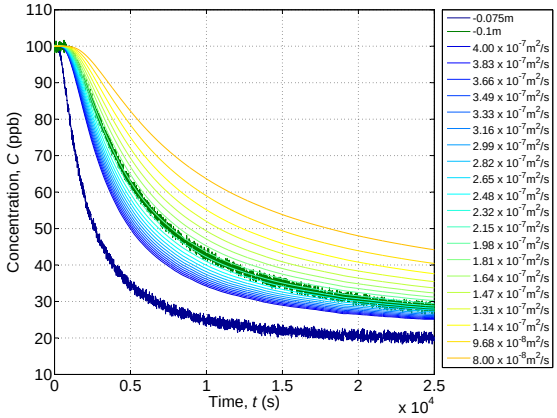

(b) Second iteration

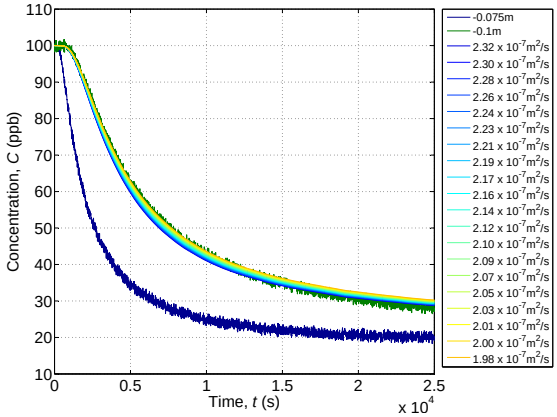

(c) Third iteration

Figure 2.25: Example optimisation from Nagaoka and Ohgaki [1990] analysis methodology, showing the different profiles generated by the vector of diffusion coefficients and the focussing of the optimisation on the 'correct' diffusion coefficient (-0.075 and -0.100m, 7 zone model 4 simulation with noise added)

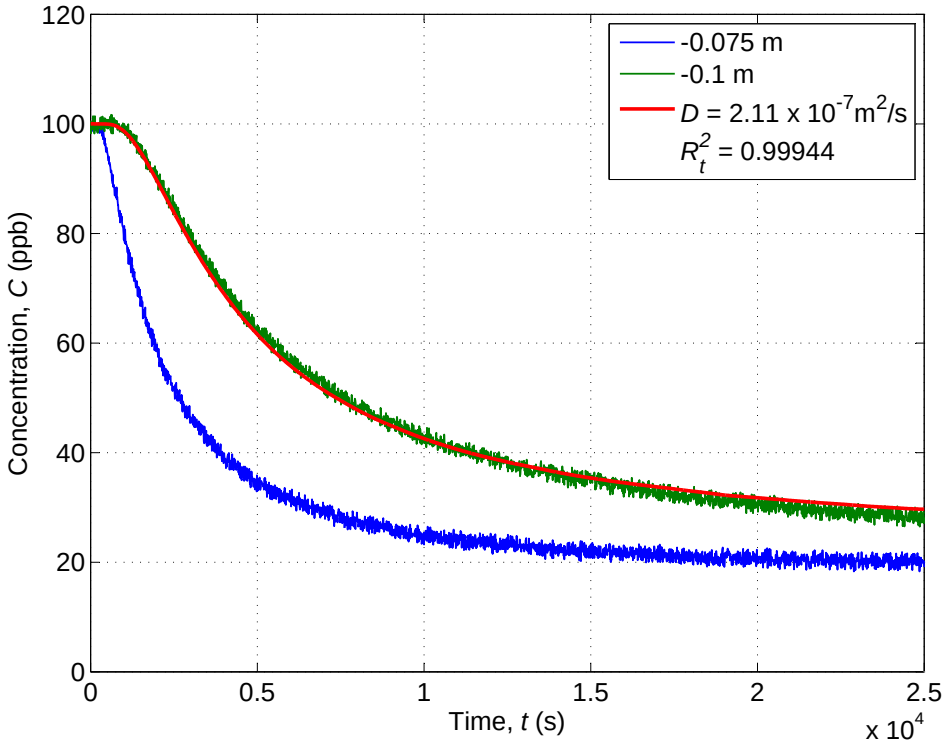

Figure 2.26: Example output from the optimisation used in the Nagaoka and Ohgaki [1990] analysis methodology, conducted with profiles from 7 zone model 4 simulation with noise added (-0.075 and -0.100m), showing the two profiles and the optimised analysis profile (red) (legend gives the profile positions, the diffusion coefficient obtained by the analysis and the R_t^2 value between the model simulation and the optimised analysis profiles

reached. Figure 2.26 shows an example final output plot from the optimisation with the two measured (or model simulated) profiles and the theoretical analysis profile, with the diffusion coefficient used to calculate it as its legend entry.

As stated at the start of this section all the analysis detailed currently has optimised for the best `corr2` value. This is an in-built MATLAB® function that calculates the 2D correlation coefficient (r) between two matrices or vectors (of the same length) A and B according to

$$r = \frac{\sum_m \sum_n (A_{mn} - \bar{A})(B_{mn} - \bar{B})}{\sqrt{\left(\sum_m \sum_n (A_{mn} - \bar{A})^2\right)\left(\sum_m \sum_n (B_{mn} - \bar{B})^2\right)}}. \tag{2.122}$$

Where: $\bar{A} = \texttt{mean2}(A)$ and $\bar{B} = \texttt{mean2}(B)$, where `mean2` is an in built MATLAB® function to calculate the mean value of a matrix's elements.

There are several different goodness of fit parameters that could be used. Based on a study by Sonnenwald *et al.* [Unpublished] there are two other parameters worth investigating further. The first is the coefficient of determination (R_t^2) [Young *et al.*, 1980] and the other is average percent error (APE) [Kashefipour and Falconer, 2000]. R_t^2 has traditionally been used in longitudinal dispersion studies when upstream profiles are used to predict downstream profiles using various models including the aggregated dead zone (ADZ) and advection diffusion equation (ADE) models [Guymer *et al.*, 2005]. R_t^2 gives a value between zero and one depending on the correlation between measured and calculated profile using (2.123). APE is less commonly used and gives a value between zero and 100% (0% indicating that there is no error or difference between the measured and calculated profiles) and is given by (2.124).

$$R_t^2 = 1 - \frac{\sum_{t=1}^{N}(C_t - P_t)^2}{\sum_{t=1}^{n} C_t^2} \tag{2.123}$$

$$APE = \frac{\sum_{t=1}^{N}(C_t - P_t)}{\sum_{t=1}^{n} C_t} \times 100 \tag{2.124}$$

Where: C_t is the measured concentration profile and P_t is the predicted concentration profile.

The same 7 zone model 4 simulation with noise added was analysed using R_t^2 and APE as the optimisation criteria, with the same inputs used previously. Table 2.11 gives the different coefficients obtained using the different goodness of fit parameters. There is very little difference between the different goodness of fit parameters, particularly between R_t^2 and APE. The biggest difference is closer to the sediment water interface, where `corr2` gives a closer match. However the difference is so slight that it is not possible to determine which fit parameters should be used purely from the model simulation data. This analysis is repeated in Section 4.3.2 with experimental data to determine which goodness of fit parameter should be used in the optimisation process.

There are several different parameters that can affect the optimisation process such as the sampling interval of the data (dt) and the initial starting point of the op-

Upper profile depth (m)	Lower profile depth (m)	Specified (10^{-7}m^2/s)	`corr2` (10^{-7}m^2/s)	R_t^2 (10^{-7}m^2/s)	APE (10^{-7}m^2/s)
-0.025	-0.050	20.0	18.8	29.0	36.7
-0.050	-0.075	6.00	5.33	7.28	7.72
-0.075	-0.100	2.00	1.85	2.11	2.10
-0.100	-0.125	0.60	0.599	0.60	0.60
-0.125	-0.150	0.20	0.197	0.20	0.20

Table 2.11: Comparison of diffusion coefficients obtained using different goodness of fit parameters with those specified in the 7 zone model 4 simulation

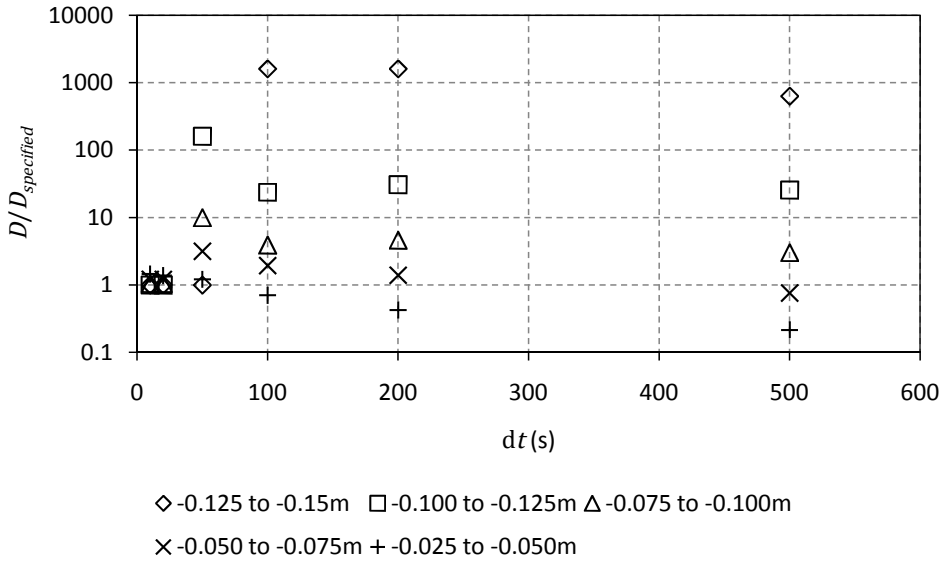

Figure 2.27: Effect of sampling interval, dt, on Nagaoka and Ohgaki [1990] analysis of 7 zone model 4 simulation (optimisation starting point $D_{wc} = 2 \times 10^{-6}$m^2/s)

timisation. The 7 zone model 4 simulation with noise added has been analysed using six different dt values, 20, 30, 50, 100, 200 and 500s. The goodness of fit parameter was R_t^2 and initially the starting point for the optimisation, D_{wc}, was the interface coefficient 2×10^{-6}m^2/s, with a tolerance limit of 1×10^{-10}m^2/s. Figure 2.27 shows the variation in diffusion coefficients obtained with different dt values. The y-axis gives the analysis coefficients non-dimensionalised by the coefficient specified in the model. Due to the large variation at high dt values the axis has a log scale. It is clearly visible that above dt of 20s the optimisation is giving much higher coefficients than those specified. This is because the optimisation is finding other local maxima within the spread of possible diffusion coefficients. The structure of (2.117) and (2.120) result in two or three very different coefficients giving calculated profiles

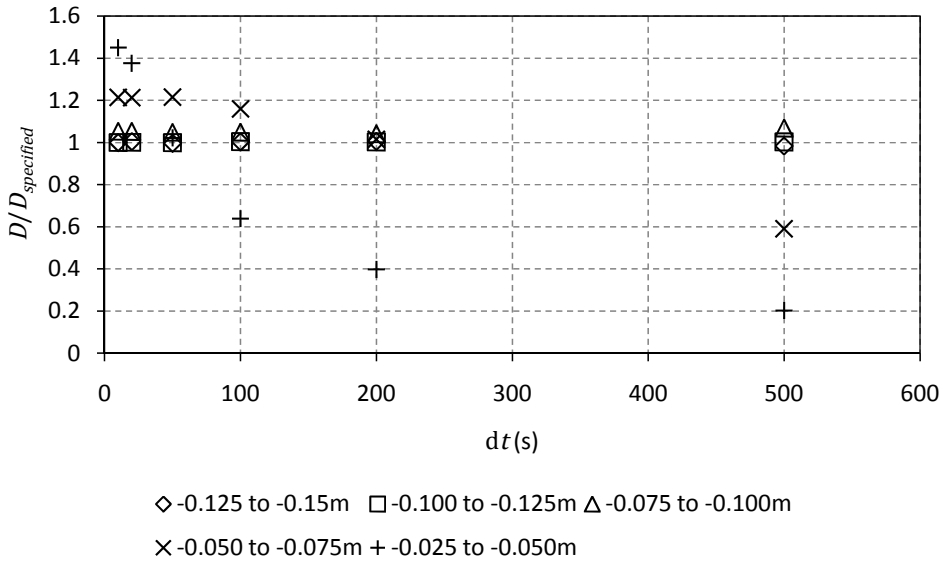

Figure 2.28: Effect of sampling interval, dt, on Nagaoka and Ohgaki [1990] analysis of 7 zone model 4 simulation (optimisation starting point $D_{wc} = 2 \times 10^{-7}\mathrm{m}^2/\mathrm{s}$)

that are a 'good' fit to the measured profile. This phenomenon is discussed further below.

The effect of dt analysis was repeated with a lower D_{wc} value of $2\times10^{-7}\mathrm{m}^2/\mathrm{s}$. This resulted in the optimisation routing focussing in on the 'correct' coefficients which are given in Figure 2.28. Here the y-axis is linear because the difference between the specified and analysis coefficients is much smaller. There is a clear trend in the figure, with the lower profiles pairs (-0.125 to -0.150m, -0.100 to -0.125m and -0.075 to -0.100m) giving accurate analysis coefficients over the full range of dt values. However the profiles closer to the sediment water interface (-0.050 to -0.075m and -0.025 to -0.050m) show a distinct variability with dt. At lower values of dt, 10 and 20s, the analysis near the interface gives higher coefficients than specified, where as at higher values of dt, 200 and 500s, the analysis gives lower coefficients than specified. The difference between the specified and analysis coefficients is greatest for d$t = 500$s, which may be caused by the number of points that make up the profiles (only 51 points). With a large dt there are not enough points at the start of the profile for the calculated analysis profiles to react and match the model simulation profiles, demonstrated in Figure 2.29. The large dt means the measured profiles drop instantly from C_0 and there are not enough points within the slope to accurately describe it. A dt value of between 10 and 50s is the most appropriate. The effect dt has on the optimisation process, by changing which

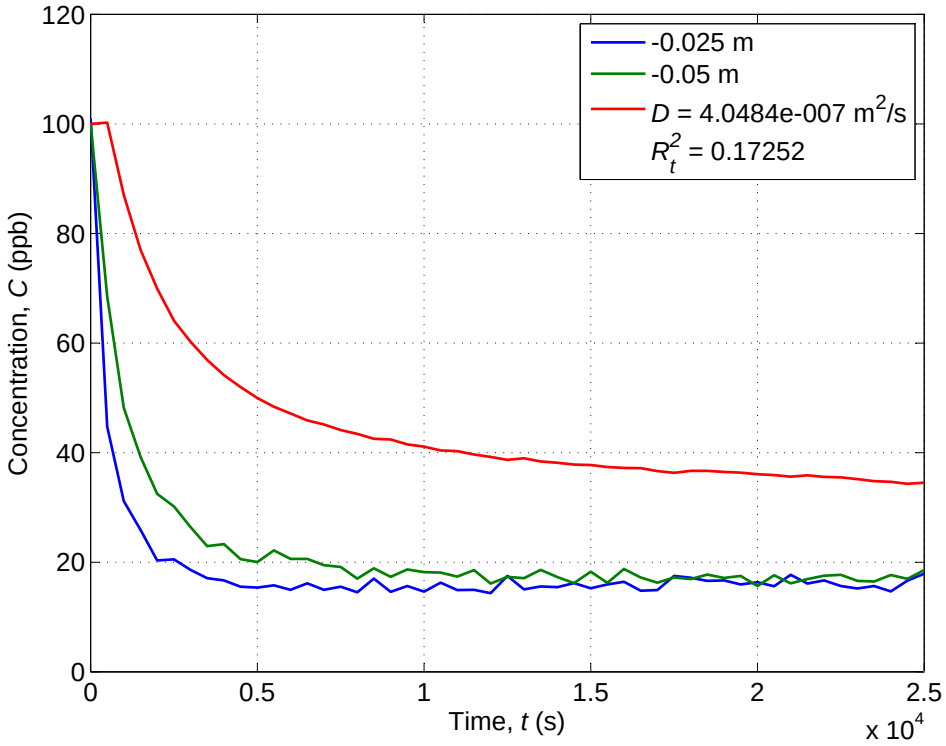

Figure 2.29: Effect of a large sampling interval on Nagaoka and Ohgaki [1990] analysis of 7 zone model 4 simulation (dt = 500s), showing the two profiles and the optimised analysis profile (red) with the legend giving the profile positions, the diffusion coefficient obtained by the analysis and the R_t^2 value between the model simulation and the optimised analysis profiles

route the optimisation takes, was unexpected and will need to be monitored during experimental data analysis. The effect of dt on the optimisation could also be due to the optimisation routine not always identifying the 'correct'/best parameter. This could be caused by local minima/maxima or the choice of best fit parameter.

The analysis on the effect dt has on the optimisation demonstrated that the starting value of the optimisation, D_{wc}, has an impact on the coefficients obtained. This is due to the behaviour of (2.117) and (2.120). It has already been established that the equations are a balance between their two different parts. The same 7 zone model 4 simulation with noise added was used to compare a series of set diffusion coefficients through their R_t^2 goodness of fit between their calculated profiles and the model simulation profiles. Following the same order as the normal optimisation process (2.120) was investigated first with the lowest profile pair (-0.125 and -0.150m). A logarithmically varying diffusion coefficient from 1.0×10^{-12} to 10.0m^2/s was used (Table 2.12). The R_t^2 values between the calculated profiles and

Column	Diffusion Coefficient (m^2/s)				
1 to 9	1.0×10^{-12}	2.0×10^{-12}	...	8.0×10^{-12}	9.0×10^{-12}
10 to 18	1.0×10^{-11}	2.0×10^{-11}	...	8.0×10^{-11}	9.0×10^{-11}
⋮	⋮	⋮	⋮	⋮	⋮
55 to 63	1.0×10^{-6}	2.0×10^{-6}	...	8.0×10^{-6}	9.0×10^{-6}
⋮	⋮	⋮	⋮	⋮	⋮
9 to 117	1.0	2.0	...	8.0	9.0
118	10.0				

Table 2.12: Diffusion coefficients used to investigate the behaviour of (2.117) and (2.120)

the model profile at -0.150m are shown in Figure 2.30(a).

There is a clear minimum and two maxima in the R_t^2 values. The minimum occurs at 9.0×10^{-6}m^2/s and the maxima at 1.0×10^{-3} and 2.0×10^{-8}m^2/s (the specified coefficient). The R_t^2 values for these coefficients are 0.9372, 0.9995 and 0.9999 respectively. The profiles generated with these coefficients are shown in Figure 2.30(b) along with other intermediate coefficients. The calculated profile moves from a horizontal line (no change, 1.0×10^{-12}m^2/s), through the best fit (2.0×10^{-8}m^2/s), towards the upper profile (9.0×10^{-6}m^2/s) and then back towards the lower profile as the diffusion coefficient keeps increasing. The interplay of the two parts of (2.120) can clearly be seen where two very different coefficients, several orders of magnitude apart, give similar profiles. The single minimum with two maxima is the reason that very high coefficients were obtained with $D_{wc} = 2.0 \times 10^{-6}$m^2/s in the d$t$ analysis. For large dt values the highest R_t^2 values in the initial optimisation matrix were around the starting value. The next optimisation step used this as its start and moved towards the maxima at 1.0×10^{-3}m^2/s, rather than the 'correct' solution (2.0×10^{-8}m^2/s). This shows the importance of the starting point in the optimisation procedure. With a smaller dt value there are enough points to accurately represent the distribution and the optimisation moves towards the 'correct' solution.

The same procedure was applied to (2.117) between -0.100 and -0.125m. Figure 2.31(a) demonstrates the more complex nature of (2.117), with three maxima and two minima. In Figure 2.31(a), D_2 has been set to 2.0×10^{-8}m^2/s, the specified coefficient in the model simulation. The maxima are at 6.0×10^{-8}, 1.0×10^{-4} and 4.0×10^{-2}m^2/s and the primary minima at 1.0×10^{-5}m^2/s, with R_t^2 values of 0.9999, 0.9954, 0.9885 and 0.8285 respectively. Figure 2.31(b) shows profiles from selected coefficients and like Figure 2.30(b) the movement of the calculated profile

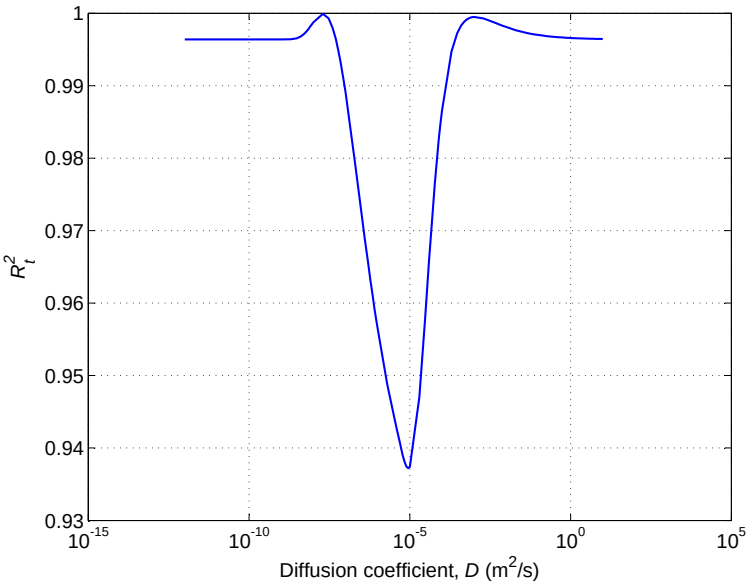

(a) Variation in R_t^2 values between model simulation profile -0.150m and Nagaoka and Ohgaki [1990] analysis profile

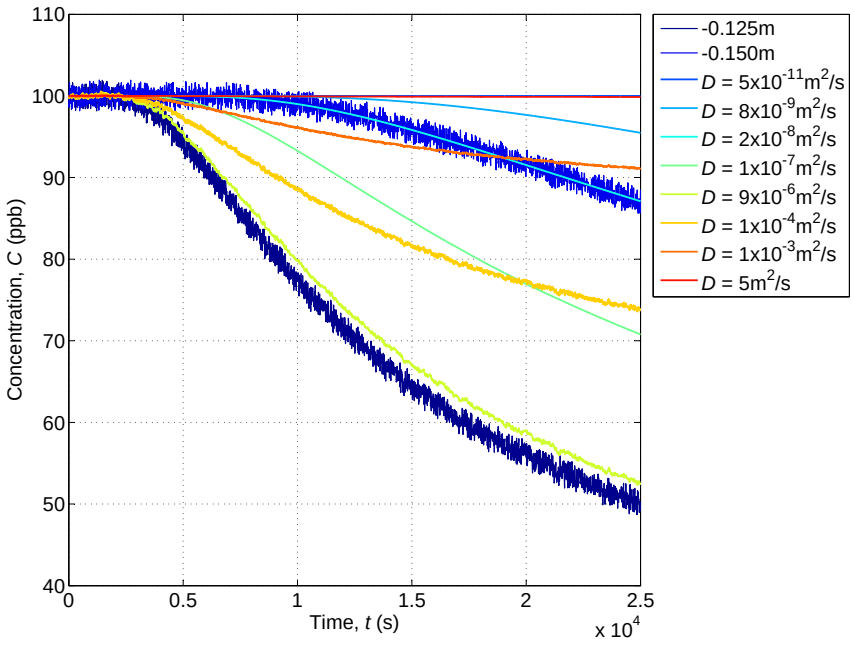

(b) Variation in Nagaoka and Ohgaki [1990] analysis profiles showing the profiles generated from different diffusion coefficients

Figure 2.30: Variation in R_t^2 values and Nagaoka and Ohgaki [1990] analysis profiles with different diffusion coefficients between -0.125 and -0.150m profiles from 7 zone model 4 simulation (Equation (2.120))

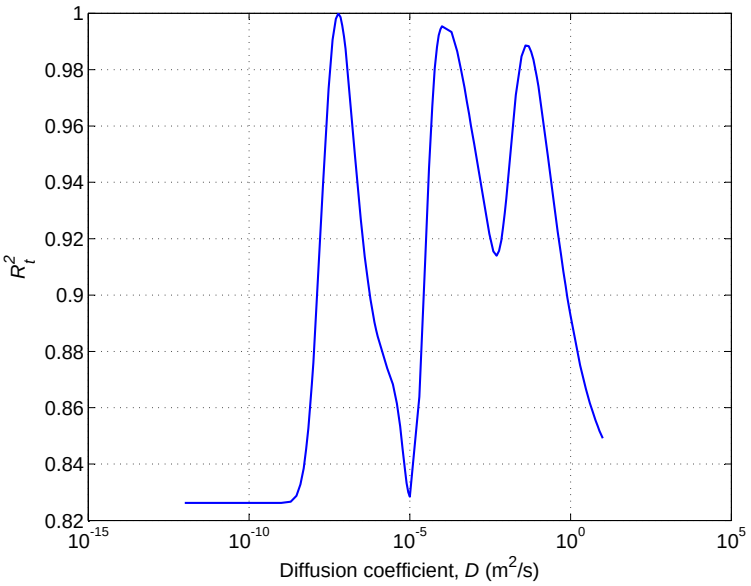

(a) Variation in R_t^2 values between model simulation profile -0.150m and Nagaoka and Ohgaki [1990] analysis profile

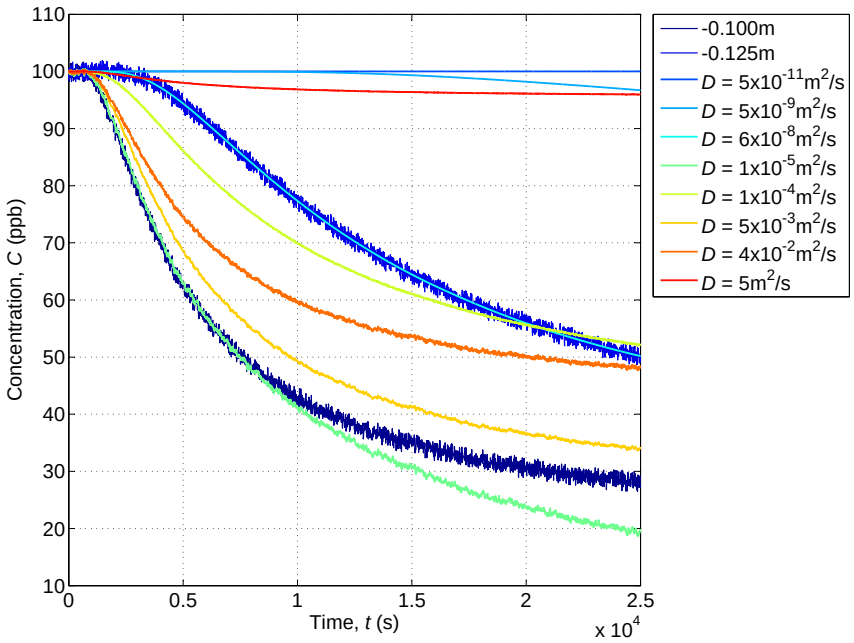

(b) Variation in Nagaoka and Ohgaki [1990] analysis profiles showing the profiles generated from different diffusion coefficients

Figure 2.31: Variation in R_t^2 values and Nagaoka and Ohgaki [1990] analysis profiles with different D_1 diffusion coefficients between -0.100 and -0.125m profiles from 7 zone model 4 simulation (Equation (2.117), $D_2 = 2.0 \times 10^{-8}\text{m}^2/\text{s}$)

is clear as the coefficient is increased, moving from C_0 towards the lower profile and then bouncing away and back again. The primary minimum is further from D_{wc} than the analysis on (2.120) showed, which increases the likelihood of the optimisation moving towards the 'correct' value. The current optimisation starts with the interface coefficient, which as this analysis has shown is close to the minimum (for both equations). To reduce the risk of the optimisation routine working towards the 'wrong', local maxima, the optimisation could start with a lower coefficient. The problem then becomes which coefficient to use as it needs to be universally applicable. The obvious choice would be the molecular diffusion coefficient, however both Figure 2.30(a) and 2.31(a) show that if the coefficient is too low then there is no difference in the R_t^2 values. This would halt the optimisation process and give an output equal to the starting coefficient. On balance the best coefficient to start the optimisation with appears to be the interface coefficient, which for the experimental data can be calculated using the O'Connor and Harvey [2008] methodology and the water column data. This allows a consistent method to be applied to all experimental and model simulation data.

The relationship between D_1 coefficient and R_t^2 value demonstrated in Figure 2.31(a) is repeated for the other profiles taken from the 7 zone model 4 simulation with noise added. They all show three maxima, but the 'correct' coefficient always gives the highest overall R_t^2 value. There is variation in the location of the primary (lowest) minimum, with the minima between the 'correct' solution and the next maximum reducing with proximity to the sediment water interface. This could result in the optimisation process finding the 'wrong' solution and needs to be monitored during the analysis of the experimental data. Figure 2.32 shows a similar analysis to Figure 2.31(a), but with D_2 varying and D_1 fixed as the coefficient specified in the model simulation ($6.0 \times 10^{-8}\mathrm{m}^2/\mathrm{s}$). There is only one maximum and it is at the 'correct' value ($2.0 \times 10^{-8}\mathrm{m}^2/\mathrm{s}$), however if D_1 changes then the highest R_t^2 value does not occur at $2.0 \times 10^{-8}\mathrm{m}^2/\mathrm{s}$. This indicates that the combination of D_1 and D_2 coefficients can give similar R_t^2 values, but with very different coefficients.

This illustrates the importance of correct D_2 coefficients from the previous profile pair analysis and the impact this could have on the optimisation of the next profile pair. Equation (2.117) could be treated as a two parameter optimisation problem, with both D_1 and D_2 allowed to vary. Instead of allowing both to be optimised within a code, a matrix of possible combinations of D_1 and D_2 can be created, using the same coefficients as the analysis above (Table 2.12). If these possible combinations of D_1 and D_2 is compared with the model simulation profiles at -0.100 and -0.125m (as the analysis above) then there is no obvious best parameter

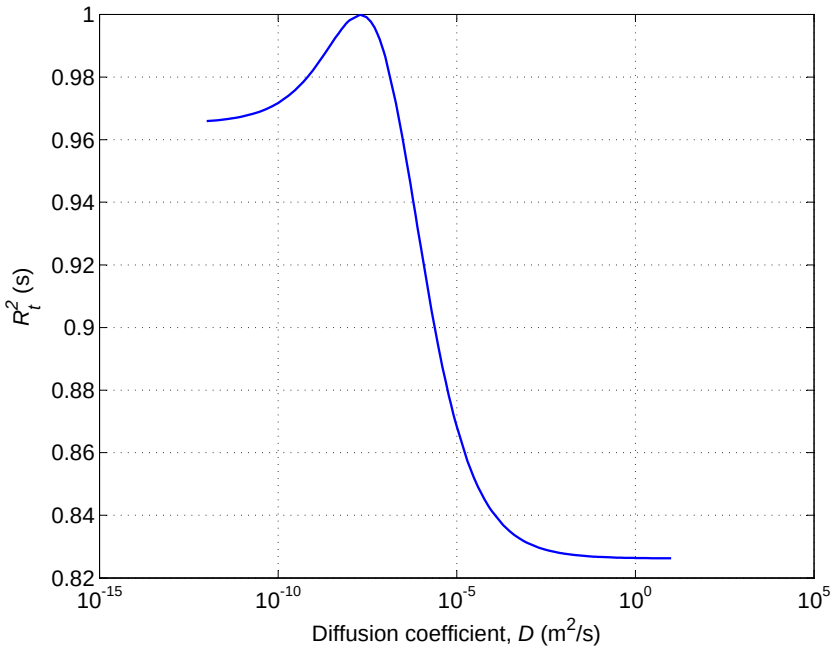

Figure 2.32: Variation in R_t^2 values with different D_2 diffusion coefficients between -0.100 and -0.125m profiles from 7 zone model 4 simulation (Equation (2.117), $D_1 = 6.0 \times 10^{-8}\text{m}^2/\text{s}$)

combination. This is shown in Figure 2.33. The x-axis and y-axis indicate the D_1 and D_2 coefficient used and the z-axis gives the R_t^2 value obtained for each combination. Almost 14000 profiles were calculated and compared to generate Figure 2.33. It demonstrates that varying D_2 would reduce the certainty of the analysis. The 'correct' solution ($D_1 = 6.0 \times 10^{-8}\text{m}^2/\text{s}$ and $D_2 = 2.0 \times 10^{-8}\text{m}^2/\text{s}$) can be picked out in Figure 2.33, but the difference between the R_t^2 value compared to some other D_1, D_2 combinations is negligible. The conclusion from Figure 2.33 is that D_2 should be fixed, as it was in Nagaoka and Ohgaki [1990] original analysis.

From the evaluation conducted above the in-bed data will be analysed using the Nagaoka and Ohgaki [1990] methodology. However, further evaluation with experimental data is required before the best goodness of fit parameter can be determined (Section 4.3.2).

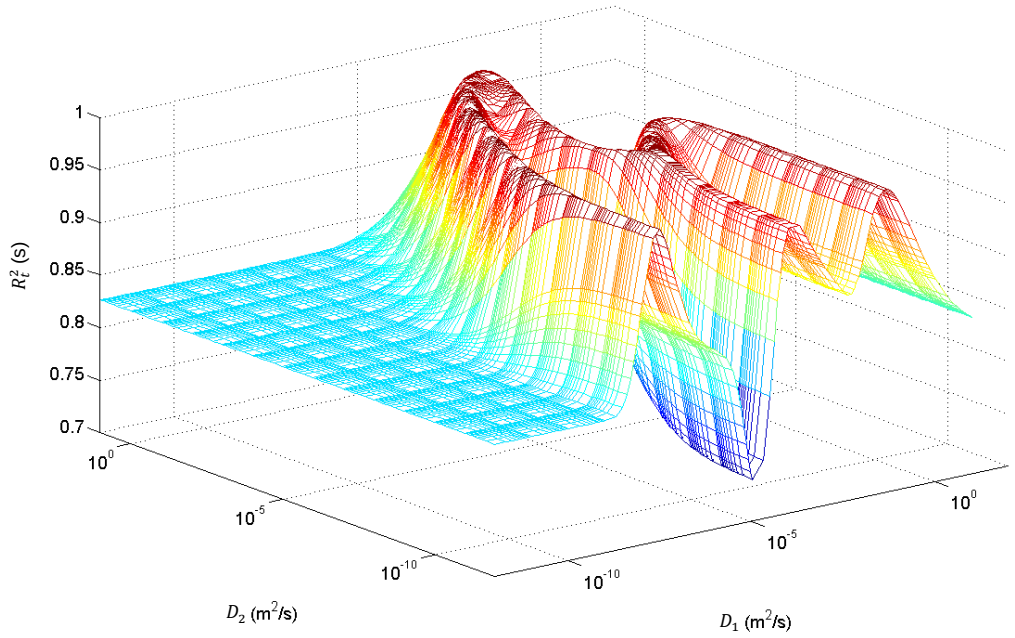

Figure 2.33: Variation in R_t^2 values with different D_1 and D_2 diffusion coefficients between -0.100 and -0.125m profiles from 7 zone model 4 simulation (Equation (2.117))

2.5 Field Studies

There have been fewer field investigations into hyporheic exchange than laboratory studies. This is primarily due to the difficulty in quantifying the parameters that influence the exchange and in reliably measuring it. The majority of studies have used transient storage models to determine both hydraulic parameters and mixing coefficients, including hyporheic exchange.

West Fork of Walker Branch

Hart [1995] and Hart *et al.* [1999] used data from a 70m reach of the West Fork of Walker Branch situated in the US Department of Energy's Oak Ridge National Environmental Research Park in the Ridge and Valley Province of eastern Tennessee. Conservative tracer injections were conducted between November 1991 and May 1994 to investigate the affect of seasonality and flow conditions on several hydraulic parameters including hyporheic exchange. Either Cl (as NaCl) or ^{3}H (as ^3H_2O) were injected for periods typically between 1.5 and 2 hours. Concentrations were measured 8 and 70m downstream from the injection at 0.5 to 5 minute intervals. A

transient storage model was used to analyse the data and determine the hydraulic parameters. The stream had been previously characterised by Mulholland *et al.* [1985] and Mulholland [1993].

St. Kevin Gulch

Two separate studies used reaches of St. Kevin Gulch in Colorado. Kimbal *et al.* [1994] used data from a tracer study conducted in 1987 on a 2km section. The study injected lithium chloride (LiCl) for 36 hours and recorded the concentrations at seven sites, ranging from 26 to 1804m downstream of the injection. They also investigated the transport of SO_4, Mn, Fe and Al and the effect that the acidic inflow from mine drainage had on the sorption of each metal. The trace data was analysed using a transient storage model to determine the hydraulic properties of the stream. Harvey *et al.* [1996] chose a smaller 36m reach, but employed much more intensive sampling, both in-stream and sub-surface through a selection of the 60 wells on site. Again LiCl was used as a tracer and was injected for 4 days. Two approaches for calculating hyporheic exchange were compared, one based on the trace study and the other on the sub-reach-scale measurements of the hydraulic conductivity, gained from head measurements in all the wells and at all staff gauges during the trace.

Säva Stream

Several papers [Johansson *et al.*, 2001; Wörman *et al.*, 2002; Forsman *et al.*, 2002; Jonsson *et al.*, 2003] have used the data from a trace conducted in 1998 on a 30km reach of the Säva Stream in Sweden. Simultaneous injections of the tracers tritium, ^3H_2O (conservative), and chromium, ^{51}Cr(III) (sorptive), were conducted. The tracers were injected for 5 hours with manual sampling occurring at eight sites. Core samples were taken from two sites for the next few months to study the vertical and horizontal variation in tracer concentrations within the bed sediment. All the papers that use this data have looked at the effect of sorption on the movement of solutes within streams, including the effect on hyporheic exchange. This data formed the basis for the model developed by Forsman *et al.* [2002] detailed in Section 2.3.4.

Uvas Creek

Tracer experiments were conducted in a 619m reach of Uvas Creek in Sierra Nevada, California, by Bencala and Walters [1983]. LiCl was injected over a three hour period with concentrations measured at three site. Both the cross-section and the discharge varied throughout the reach. The bed consisted of a series of ripples and pools from

which they infer that hyporheic exchange is dominating the solute transport. This is quantified using a transient storage model. The same data was also analysed by Wörman [2000] and the output compared with a second experiment conducted in Lenna Brook.

Lenna Brook

Wörman *et al.* [1998] conducted trace experiments on Lenna Brook, Skara County, Sweden. A sorbing tracer (CrCl) was injected over a 5.5 hour period and measured at five sites over a 11.2km reach. The aim of the study, as with much of the field work summarised here, was to investigate the impact of sorption on hyporheic exchange. As mentioned above this study was also used by Wörman [2000].

Ipswich River

Briggs *et al.* [2009] conducted a series of trace experiments in different reaches or tributaries of the Ipswich River, north shore of Massachusetts. NaCl was used as a conservative tracer and injected into both first and fourth-order streams, Lockwood Brook and upper Ipswich River main stem respectively. A constant rate injection was used in Lockwood Brook, whilst a slug injection was used in the upper Ipswich River main stem. Conductivity was recorded at several sites along each reach and the data were used to develop a two-zone transient storage model approach.

2.6 Sediment Parameters

This section details the calculation of several sediment parameters, either because they are known to affect hyporheic exchange or to conduct calibrations within the experimental equipment described in Chapter 3.

2.6.1 Sediment Motion

This section gives the background theory required for the erosimeter bed shear calibration (described in detail in Section 3.3.2). Sediment begins to move when the bed shear stress (τ) exceeds a critical value (τ_{cr}) which depends on the particle size, density, shape and cohesiveness of the bed material [Rutherford, 1994]. For the calibration this critical shear stress is linked to the bed shear velocity (u_*) and the propeller speed of the erosimeter through the following series of equations. The bed sediment is characterised by the dimensionless particle parameter (d_*) which

expresses the particle diameter in relation to the overlying fluid properties and is given by van Rijn [1984] as

$$d_* = d_{ch} \left(\frac{\rho_r g}{\nu^2} \right)^{\frac{1}{3}} \tag{2.125}$$

where: d_* is the dimensionless particle parameter, d_{ch} is the characteristic particle diameter, g is gravity, ν is the kinematic viscosity, and ρ_r is the relative density of sediment particle to fluid $((\rho_s - \rho_w)/\rho_w)$ where ρ_s is the density of the sediment particle and ρ_w is the density of the fluid.

van Rijn [1984] relates the dimensionless particle parameter to a critical sediment mobility parameter (d_{cr}), given by (2.126), through Table 2.13.

$$d_{cr} = \frac{u_*^2}{\rho_r g d_{ch}} \tag{2.126}$$

Table 2.13 is based on the Shields curve, which gives the variation in constants and powers seen below.

Dimensionless particle parameter	Critical sediment mobility parameter
$d_* \leq 4$	$d_{cr} = 0.24(d_*)^{-1}$
$4 < d_* \leq 10$	$d_{cr} = 0.14(d_*)^{-0.64}$
$10 < d_* \leq 20$	$d_{cr} = 0.04(d_*)^{-0.1}$
$20 < d_* \leq 150$	$d_{cr} = 0.013(d_*)^{0.29}$
$d_* > 150$	$d_{cr} = 0.055$

Table 2.13: van Rijn [1984] d_* to d_{cr} conversion table

For the calibration, equation (2.126) was rearranged into (2.127) so u_* could be related to propeller speed.

$$u_* = \sqrt{d_{cr} \rho_r g d_{ch}} \tag{2.127}$$

There are four identifiable states of sediment motion, which are important in deciding what propeller speed is causing sediment motion. These four stages are given below and are taken from Jubb [2001]. For the calibration, stage three is the definition used for sediment motion.

Stages of Motion

1. *Initialisation*: The individual grains start moving and shaking without leaving their location in the sediment bed.

2. *Stabilisation*: Grains occasionally leave their location and move to places of shelter in the sediment bed. There they remain, protected from the current flow.

3. *Erosion*: The grains roll over the sediment surface, being moved a significant distance.

4. *Transport*: By increasing the shear stress, it is possible to increase the rate at which grains move, both temporally and spatially.

2.6.2 Permeability

Previous studies investigating hyporheic exchange [Richardson and Parr, 1988; Lai *et al.*, 1994; O'Connor and Harvey, 2008; Packman and MacKay, 2003] have shown that permeability (K) is an important parameter affecting hyporheic exchange. There are several formulae available to predict permeability. Equation (2.128) is the Kozeny-Carman equation [Carman, 1937], given by [Freeze and Cherry, 1979] as

$$K_c = \left(\frac{\rho_w g}{\mu}\right)\left(\frac{\theta^3}{1-\theta)^2}\right)\left(\frac{d_g^2}{180}\right) \tag{2.128}$$

where: K_c is the hydraulic conductivity, ρ_w is the density of the fluid, g is gravitational acceleration, μ is dynamic viscosity, θ is porosity and d_g is the mean grain diameter.

Hydraulic conductivity can be converted to permeability through equation (2.129), which results in (2.130), a formula that can predict the permeability of a sediment [O'Connor and Harvey, 2008].

$$K = \frac{K_c \nu}{g} \tag{2.129}$$

Where: K is the permeability, ν is the kinematic viscosity ($\nu = \mu/\rho_w$).

$$K = 5.6 \times 10^{-3} \frac{\theta^3}{(1-\theta)^2} d_g^2 \tag{2.130}$$

Equation (2.128) is derived from Darcy's law and the packing of spheres, with the addition of an experimentally derived constant [Bear, 1972]. Carman [1937] states that (2.128) is valid for non-spherical particles in the streamline (laminar)

flow region with an error of 10-20%. Equation (2.130) is used by O'Connor and Harvey [2008] when the permeability is not stated in the studies they used to derive their scaling relationship (2.51) and in this study to validate the in-situ permeability measurements (Section 3.3.3).

2.6.3 Roughness Height

The roughness height k_s is a function of both the sediment grain diameter and any bed-forms that are present. It allows comparison, through a single parameter, of experiments that have flat beds with those where bed-forms were used. van Rijn [1984] defined the roughness height as

$$k_s = 3d_{90} + 1.1\Delta(1 - e^{-25\Delta/\lambda}) \tag{2.131}$$

where: k_s is the roughness height, d_{90} is the particle size such that 90% of the particles are finer, Δ is the bed-form amplitude and λ is the bed-form wavelength. For flat bed experiments the second part of the equation is ignored resulting in

$$k_s = 3\,d_{90}. \tag{2.132}$$

2.7 Summary and Hypothesis

The preceding chapter has covered the different driving forces for hyporheic exchange and several different techniques for modelling or predicting it. A review of the current laboratory and field investigations has been undertaken and an evaluation of the analysis techniques employed for the different types of trace data that are generated. The erosimeter has been introduced, along with various sediment parameters. The majority of studies have concentrated on the bulk or interface exchange coefficient. The two studies that have calculated coefficients from in-bed data suggest a variation with depth below the sediment water interface. However, depths of only a few grain diameters were investigated and the variation is not quantified. The majority of modelling assumes a constant diffusion coefficient within the bed region [Ruff and Gelhar, 1972; Habel *et al.*, 2002], even when a variable velocity distribution is applied.

2.7.1 Hypothesis

Of the techniques available to predict hyporheic exchange the scaling relationship proposed by O'Connor and Harvey [2008] shows the closest agreement with exper-

imentally derived coefficients. The relationship provides the coefficient across the sediment water interface and is higher than molecular diffusion in the majority of cases. Studies by Ruff and Gelhar [1972], Nagaoka and Ohgaki [1990], Shimizu *et al.* [1990] and others have shown that the velocities reduce within a porous media with depth below the interface. It seems reasonable to assume that if the driving force for exchange reduces with depth below the interface, then so should the exchange. This would ultimately reduce the diffusion coefficient to the level of molecular diffusion.

The aim of this thesis is to record the reduction in the magnitude of diffusion coefficient with depth below the sediment water interface and to derive a mathematical relationship to describe it. In-bed concentration measurements will be required, and these can be compared to a 1D vertical diffusion model in order to validate the relationship derived.

Chapter 3

Experimental Setup

3.1 Synopsis

This chapter describes the experimental setup used to study the vertical variation in hyporheic exchange coefficients. It describes development work initially undertaken to investigate the use of the erosimeter in studying hyporheic exchange. Details are given of the re-designed erosimeter, based on the initial testing, which includes an in-situ permeability test and a fibre optic measurement system used to capture in-bed temporal concentration profiles. Particle image velocimetry (PIV) measurements taken within the erosimeter to understand the flow field are presented and details of the experimental procedure provided.

3.2 Experimental Development

Initial experimental work was undertaken to evaluate the use of the EROSIMESS-system (shortened to erosimeter) in studying hyporheic exchange. The majority of previous laboratory studies (detailed in Section 2.4) used re-circulating flumes. These systems usually require large volumes of sediment and extensive setup times. Using a smaller system would reduce these problems, but generating realistic scale turbulence driven hyporheic exchange becomes difficult.

The erosimeter is an instrument originally developed at The Institute of Hydraulic Engineering and Water Resources Management, Aachen University of Technology, Germany. Originally used for determining the critical bed shear stress of sediments deposited in small hydropower plant reservoirs [Liem *et al.*, 1997]. It has also been used extensively to determine the stabilising effect of benthic algae on cohesive sediments [Spork *et al.*, 1997].

The original design, shown in Figure A.1, has been investigated using laser doppler velocimetry (LDV) to ensure that the propeller and baffles were placed in optimum locations, ensuring uniform horizontal velocities [Liem *et al.*, 1997]. The instrument has been altered on several occasions; notably to study, in-situ, the effects of erosion on dissolved oxygen (DO) concentration [Jubb, 2001; Jubb *et al.*, 2001]. This saw the introduction of a DO probe into the top of the main erosimeter measurement cylinder and several outlets at different heights down the side of the cylinder (main section).

A base section, also shown in Figure A.1, can be fitted to the open bottom of the main section allowing calibration of the propeller speed to bed shear stress to be conducted in the laboratory [Jubb, 2001; Jubb *et al.*, 2001]. Jubb [2001] conducted trace experiments to investigate the mixing times within the main section. She found that complete mixing occurred between 2 and 4 minutes, depending on the propeller speed.

It is assumed that turbulence generated by the propeller and baffles can drive hyporheic exchange. Trace experiments were conducted with a sediment bed saturated with tracer (Rhodamine WT), and clean water filling the main section. A Turner Designs Cyclops 7 fluorometer (details in Section 3.5.1 below) was placed in the dissolved oxygen (DO) measurement port added by Jubb *et al.* [2001] and was used to measure concentrations within the water column (main section). In four experiments a second Cyclops 7 was placed in the sediment bed, with a mesh hat creating a measurement volume for the instrument. The experiments were presented at the 6$^{\text{th}}$ International Symposium on Environmental Hydraulics, 2010, Athens [Chandler *et al.*, 2010]. A copy of the paper is given in Appendix B where more information on the experimental setup is given. Figure 3.1 shows the erosimeter setup used in the initial experimentation and Table 3.1 gives the experimental parameters used.

Test No.	u_* (m/s)	d_g (10^{-3}m)	k_s (m)	K (10^{-9}m^2)	D'_m (10^{-11}m^2/s)	V_s (ml)
1	0.0171	2	0.00708	2.55	5.61	300
2	0.0171	2	0.00708	2.55	5.61	245
3	0.0175	2	0.00708	2.55	5.61	300
4	0.0176	2	0.00708	2.55	5.61	300
5	0.0162	2	0.00708	2.55	5.61	300
6	0.0278	7.5	0.03	94.9	5.71	300
7	0.0280	7.5	0.03	94.9	5.71	275
8	0.0099	1	0.00354	0.64	6.65	300

Table 3.1: Initial experimental parameters [Chandler *et al.*, 2010]

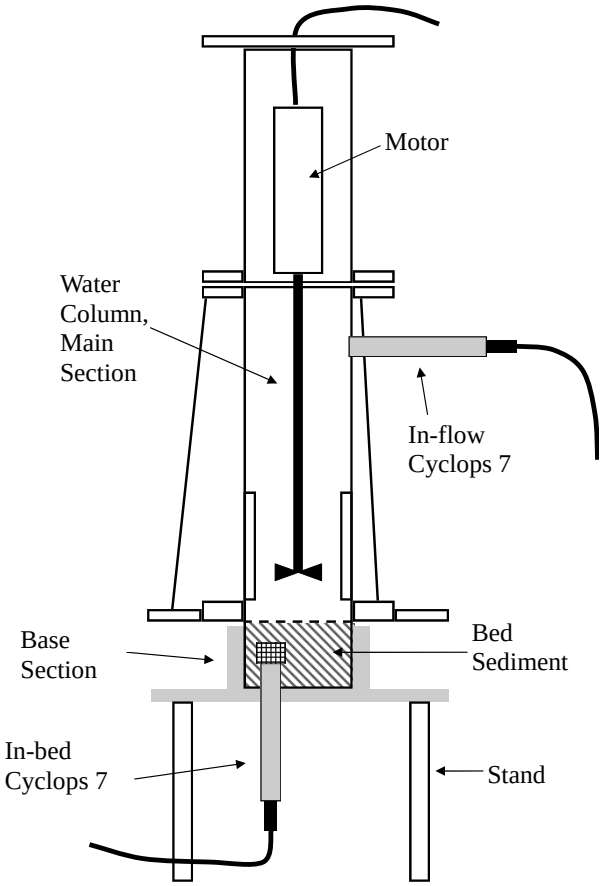

Figure 3.1: Schematic of the erosimeter used in the initial experimental work [Chandler *et al.*, 2010]

Example water column and in-bed concentration profiles are given in Figure 3.2. The initial gradients used to calculate the hyporheic exchange coefficients are indicated together with the equilibrium concentration on the water column trace. The axis correspond to those required by the analysis methodology.

Both the water column and in-bed concentration profiles are analysed using the O'Connor and Harvey [2008] methodology (Section 2.4.1). The technique is not strictly valid for the in-bed profiles as the bed is not well-mixed. However the large volume generated by the mesh hat relative to the volume of the bed means that the technique can be applied to give a guide as to the magnitude of the hyporheic exchange.

The diffusion coefficients obtained from the concentration profiles were compared to the O'Connor and Harvey [2008] scaling relationship (2.51), Figure 2.9. Figure 3.3 shows the coefficients from the initial testing plotted alongside the O'Connor

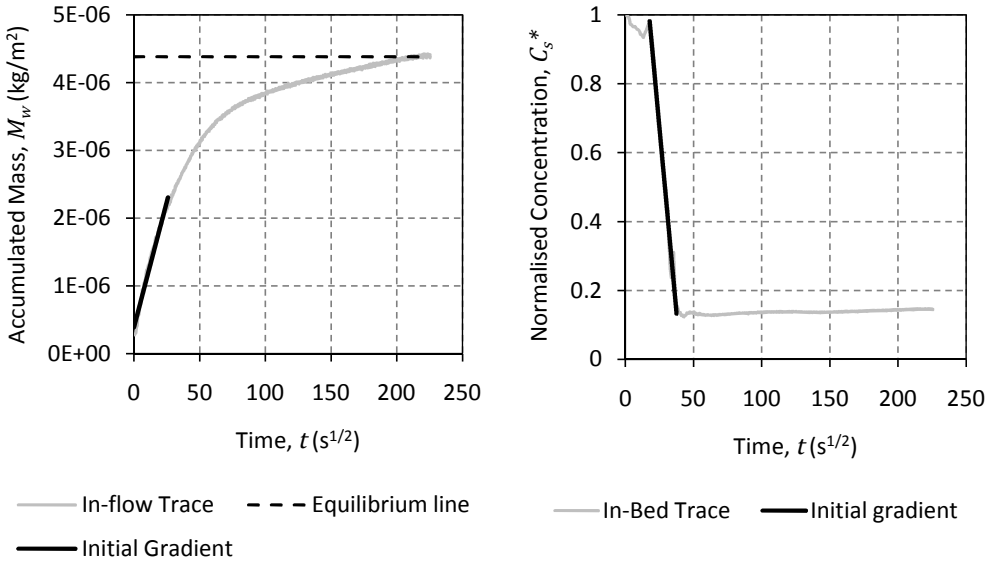

(a) Water column

(b) In-bed

Figure 3.2: Example concentration profile from test 5 from Chandler *et al.* [2010], showing water column and in-bed traces with the portion of the trace used in calculating the diffusion coefficient indicated

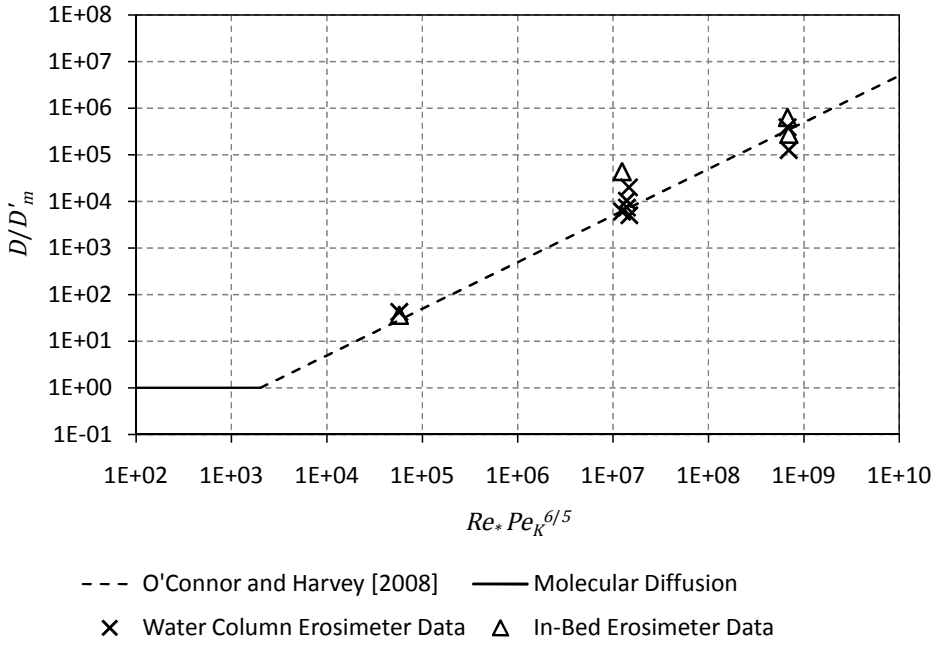

Figure 3.3: Initial erosimeter experimental results plotted against the O'Connor and Harvey [2008] scaling relationship (2.51) [Chandler *et al.*, 2010]

and Harvey [2008] scaling relationship. There is good agreement between the experimental coefficients and the scaling relationship, particularly the water column coefficient. The in-bed coefficients are further from the relationship but are still within the scatter of previous laboratory tests used to derive the relationship (Figure 2.9).

The initial testing presented in Chandler *et al.* [2010] and summarised above indicate that the erosimeter can be used to study hyporheic exchange. It provides repeatable data using much smaller volumes of material than are required by laboratory flumes. There are, however, several improvements to the system that could be made based on the experience gained during initial testing.

The main improvement from initial testing would be to the base section, with a flanged connection between it and the main section at the sediment water interface. This would improve sediment placement and allow access through the sides of the base section for in-bed instrumentation. If the base section were to be lengthened then deeper sediment depths could be tested and an in-situ permeability test incorporated. The other main recommendation is reducing the size of the instruments used to measure concentrations within the bed. The disturbance caused by the Cyclops 7 is significant given the small volume of sediment used. Using fibre optics would give the required reduction in size of measurement head.

3.3 Re-designed Erosimeter

The aims of the re-design were to adapt the erosimeter for laboratory use, to improve sediment placement, instrument access to the sediment bed and to include an in-situ permeability measurement system. Figure 3.4 shows the final experimental setup, with the re-designed erosimeter and instrumentation, all within a wooden box to exclude background light (Section 3.5). Each of these features will be described in the following sections.

The only component that remains unchanged between the current setup and that described in Section 3.2 is the propeller and motor (including the housing and control box). The dimensions of the re-designed erosimeter are detailed in Figure 3.5. The average internal diameter is 96.2mm measured with a Tesa three point bore micrometer. The new main and base sections have a flanged connection at the sediment water interface to allow easier and more accurate placement of sediment. The main section remains 300mm long, but the base section has been extended to 200mm deep to allow greater sediment depths to be studied and the necessary length to diameter ratio for the permeability tests (length:diameter $\geq$ 2:1

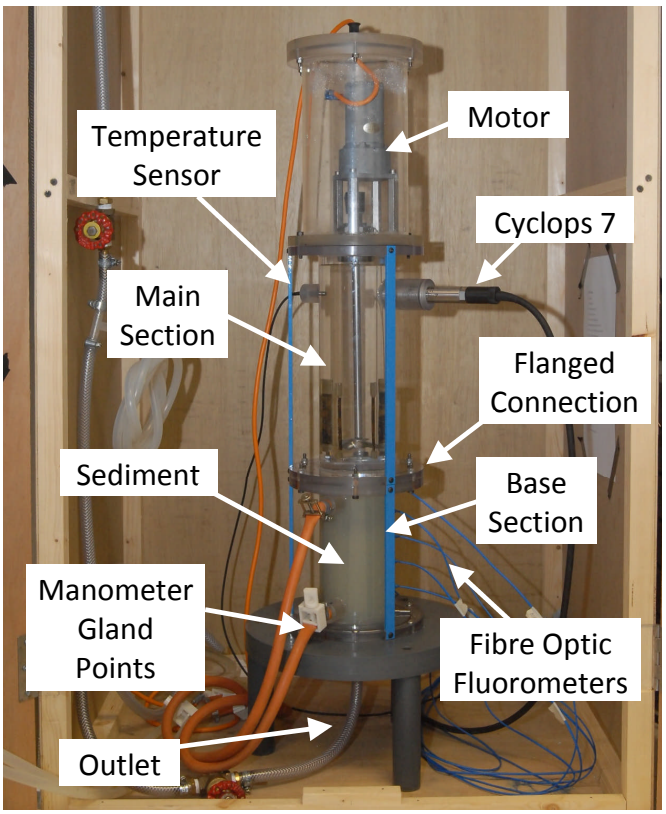

Figure 3.4: Photograph of the complete erosimeter laboratory experimental setup

[BS1377-5, 1990]). The new base section also incorporated manometer gland points and draining capacity to allow in-situ permeability tests to be conducted (detailed in Section 3.3.3).

As in the initial experimental setup (Figure 3.1) a Cyclops 7 fluorometer is positioned 60mm below the top of the main section. This is measured to the centre of the instrument, which is approximately to the centre of the measurement volume. Opposite the Cyclops position is a temperature sensor, the head of which penetrates 13.5mm into the erosimeter main section. Details of the temperature sensor a given below in Section 3.3.4.

The new base section design allows placement of fibre optic fluorometers, developed during this study (details in Section 3.5.2), at different vertical locations within the bed sediment. Six fibre optic fluorometers were used during testing, although problems with one instrument resulted in only five instruments (those on the right hand side of Figure 3.5) being used initially. The sixth instrument (FOF3) was added during the later tests on the opposite side of the erosimeter 32mm below the sediment water interface.

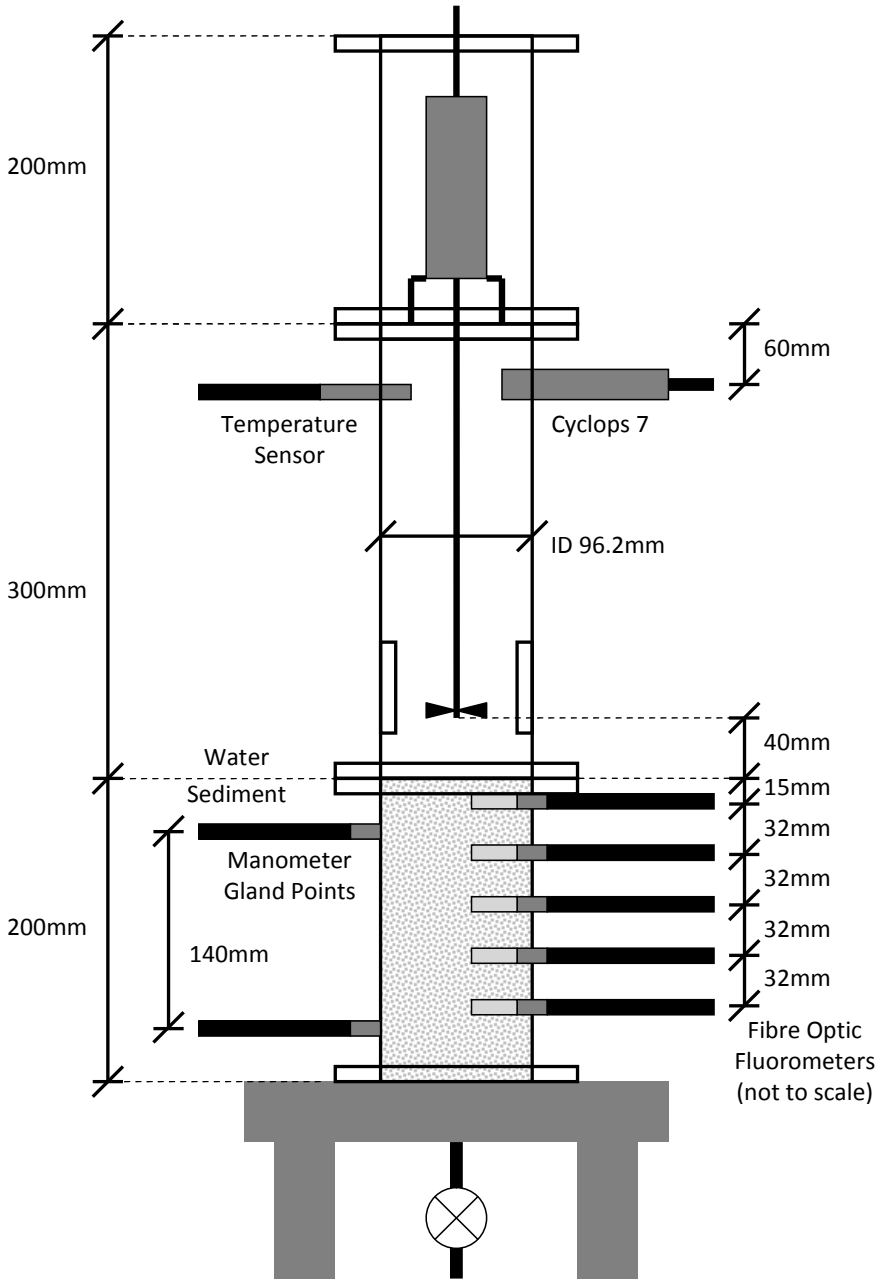

Figure 3.5: Schematic of the re-designed erosimeter detailing instrument positions marked

3.3.1 Motor and Control System

The motor and motor control unit remain unchanged from the original erosimeter described in Section 3.2. The control unit (Figure 3.6) allows the motor to be powered directly from mains electricity (via a standard three pin plug) or by a 12V

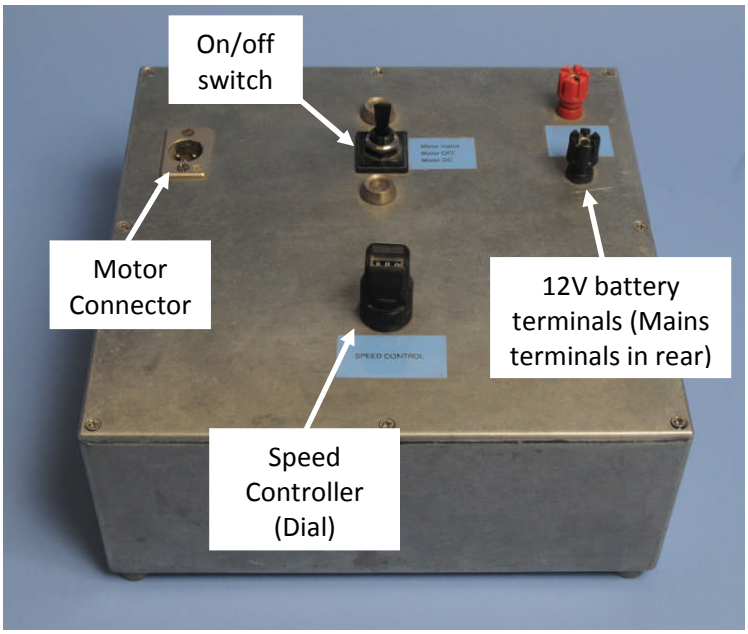

Figure 3.6: Photograph of the motor control unit

battery. All the experiments were conducted under mains power. The speed of the motor is controlled by a variable potentiometer which has a three digit counter, ranging between 999 and 000, and is equipped with a locking feature. To measure the speed in revolutions per minute (rpm) of the propeller reflective tape was attached to the shaft within the motor housing and two Veeder-Root hand held tachometers in non contact mode were used. They have an accuracy of ±1rpm (in the range of 60 to 4000rpm) at a distance of 50 to 300mm from the target to the photo head.

The first aspect of the control system investigated was the long term stability. To check the stability of the motor and control electronics, the dial was set to 300 and the propeller speed measured over six days. This test showed that the erosimeter motor was stable to ±2rpm. However the test did show a significant warm up time on the motor, where the propeller speed increased significantly before plateauing. This phenomenon was investigated further by measuring the propeller speed at 30s intervals starting from cold, after it had been run at the maximum speed for 10 minutes and after the gearing and bearings had been oiled and the motor run on maximum for 30 minutes. The results of this test are shown in Figure 3.7. It is clear that after a longer run (and oiling) the warm up time is significantly reduced.

A second test was conducted to determine the maximum length of time that the motor could be switched off without resulting in a significant increase in warm up time. For this test the motor was run on maximum for 20 minutes, then stopped

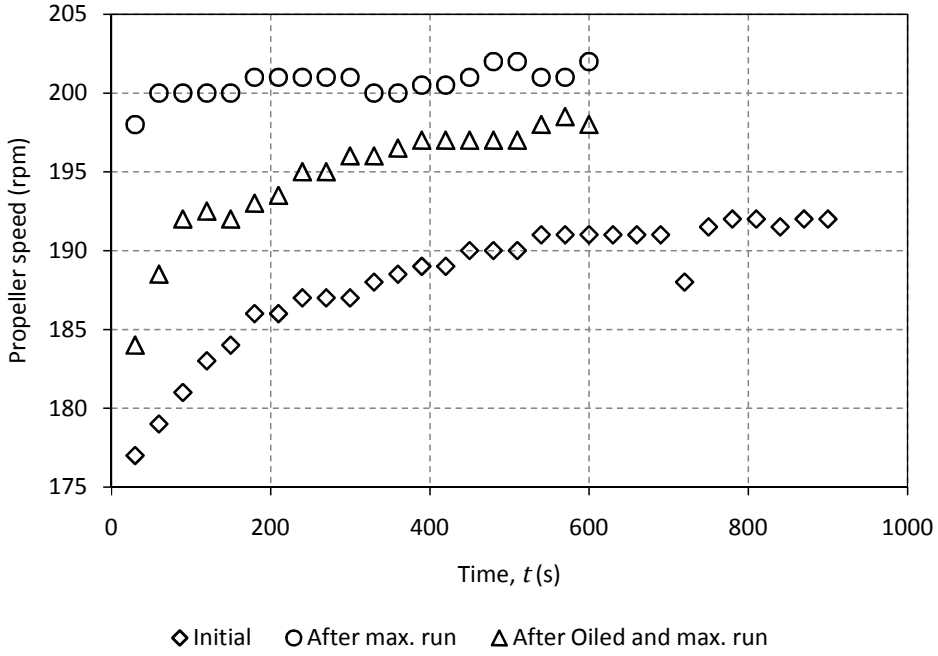

Figure 3.7: Change in propeller speed as the motor warms up (Dial = 300)

for different lengths of time, starting with the shortest (2 minutes), before restarting. The speed was recorded every 30s for 5 minutes after re-starting. Figure 3.8 shows the results of this test and indicates that the motor can be left for up to 10 minutes without affecting the warm up time (approximately 2 minutes). Therefore the motor will be left running between tests, only being switched off to transfer it into and out of the main section at the start and end of each test to prevent a significant change in propeller speed during a test.

Figure 3.9 shows a calibration relating the dial reading on the control box to the speed of the propeller (rpm). The plot contains data from several different calibration runs and also data taken during the initial experimental work [Chandler *et al.*, 2010] and the first bed shear calibration (Section 3.3.2). An initial calibration showed a linear increase in speed with dial reading up to a reading of 800, after which there was little increase to the maximum setting of 999. Several repeat calibrations were conducted within this linear region, 100 to 800. Below dial setting 70 (approximately 45rpm) the motor does not rotate smoothly, and below dial setting 50 does not rotate.

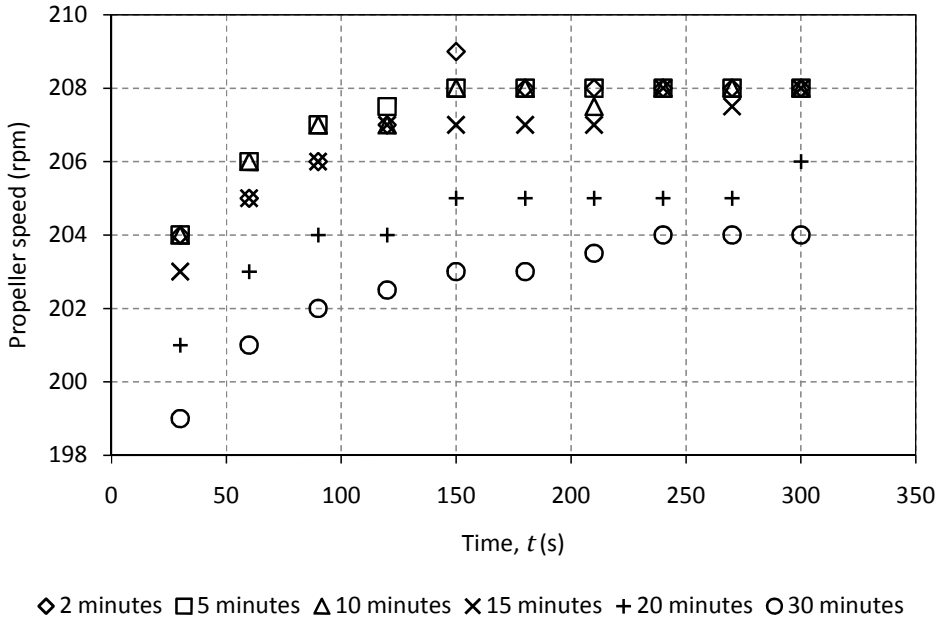

Figure 3.8: Change in motor warm up time depending on length of time switched off (Dial = 300)

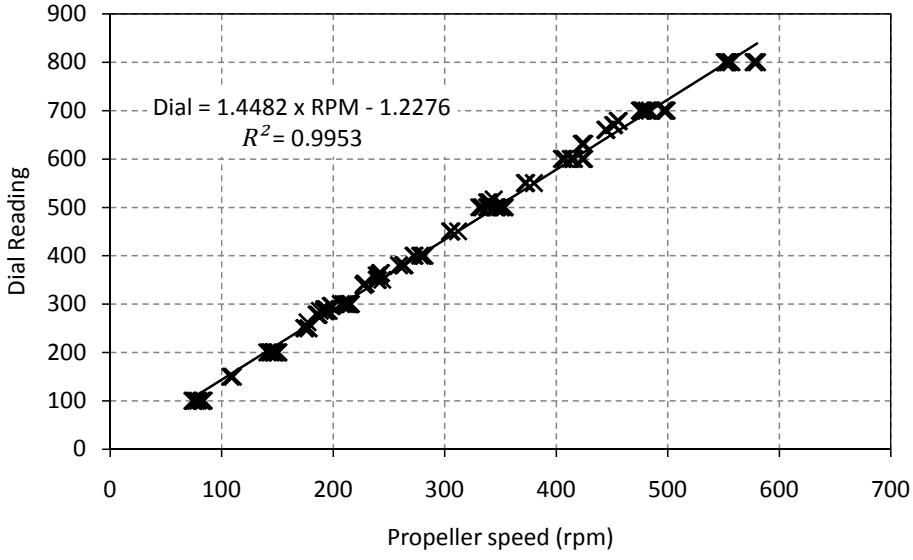

Figure 3.9: Calibration of dial reading to propeller speed (rpm)

There is some scatter on the data presented in Figure 3.9, with a variation of ±10rpm for a given dial reading. The relationship shown has been used in the experimental setup to set the motor to the approximate speed required for a given test, but then the tachometers are used to set the speed precisely. The reading from the dial is not relied upon as the speed is measured directly during each test (Section 3.8).

3.3.2 Bed Shear Velocity Calibration

There is a need to relate the rotation speed of the propeller within the erosimeter to the velocity in a channel to allow comparison with previous studies (Sections 2.4 and 2.5). The propeller speed can be related to a critical bed shear stress through a sediment motion calibration. This can then be related to a bed shear velocity, which has been used in previous work on hyporheic exchange as the representative velocity/turbulence term. Because of the different flow field (discussed in Section 3.4) the standard open channel flow approximation for calculating u_*, (2.15), cannot be used. The calibration described below is based on that employed by Jubb [2001] and Jubb *et al.* [2001]. The background theory for the calibration is described in Section 2.6.1, particularly (2.127) which was used to calculate the bed shear velocity required to cause sediment motion.

Two different calibrations were conducted, one with natural sediments and another with glass spheres, 16 months apart. The first calibration used four natural sediments, the same as used in the preliminary experiments [Chandler *et al.*, 2010], that were manually sieved to achieve close to uniform sizing. They have an angular, elongated nature, which could affect the calibration as the equations for motion (Section 2.6.1) are based on spherical particles. Starting with the smallest diameter sediment, it was placed in the base of the erosimeter and the propeller speed was increased until sediment motion (stage three, Section 2.6.1) occurs. The onset of motion was determined visually and is therefore subject to human error and differences of opinion about when motion has occurred. When motion occurs the propeller speed was recorded with two tachometers (detailed in Section 3.3.1). The procedure is repeated three more times with the same sediment. The whole procedure was repeated from the other sediments in ascending order of diameter. The results of the calibration with natural sediments are given in Table 3.2.

A second calibration, conducted 16 months later, used glass spheres instead of natural sediment. The same procedure was followed except each sediment was repeated twice not four times. The glass spheres used are the same ones used in the trace experiments, although the largest diameter ($d_g = 5$mm) was not included

Diameter range (10^{-3}m)	Critical bed shear stress, τ_{cr} (N/m^2)	Critical bed shear velocity, u_* (m/s) (2.127)	Average propeller speed (rpm)	σ propeller speed (rpm)
0.60 - 0.30	0.194	0.014	193	4.3
1.18 - 0.60	0.298	0.017	235	7.0
2.00 - 1.18	0.653	0.026	339	4.1
2.36 - 2.00	1.289	0.036	444	12.1

Table 3.2: Results from bed shear velocity calibration with natural sediments, relating propeller speed to the bed shear velocity within the erosimeter

because even at the maximum propeller speed, motion did not occur. More information on the glass spheres is given below in Section 3.6. This second calibration was conducted to check the original calibration. The results from the second calibration are given in Table 3.3 and both calibrations are plotted in Figure 3.10.

Diameter range (10^{-3}m)	Critical bed shear stress, τ_{cr} (N/m^2)	Critical bed shear velocity, u_* (m/s) (2.127)	Average propeller speed (rpm)	σ propeller speed (rpm)
0.20 - 0.10	0.158	0.013	173	1.4
0.30 - 0.40	0.195	0.014	211	4.9
0.75 - 0.50	0.288	0.017	248	16.3
2.00 - 1.70	1.068	0.033	415	7.2

Table 3.3: Results from bed shear velocity calibration with glass spheres, relating propeller speed to the bed shear velocity within the erosimeter

Figure 3.10 shows the good agreement between the two calibrations conducted despite the different sediments used and the time between them. Because of the close agreement between the two calibrations, the data has been combined to provide the calibration equation between propeller speed (rpm) and bed shear velocity (m/s), given below. Equation (3.1) is used to relate the propeller speed to the bed shear velocity throughout this study.

$$u_* = 8.67 \times 10^{-5}(\text{Propeller speed}) - 3.27 \times 10^{-3} \tag{3.1}$$

Where: u_* is bed shear velocity (m/s) and propeller speed is in revolutions per minute (rpm).

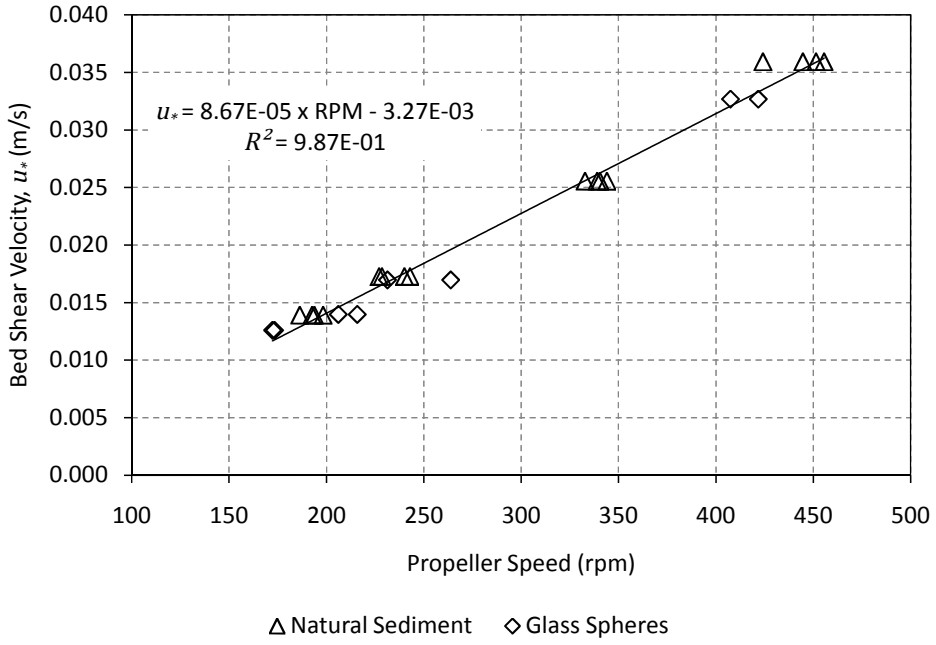

Figure 3.10: Results of bed shear velocity calibration relating propeller speed to bed shear velocity

3.3.3 In-Situ Permeability Test

The erosimeter was re-designed to allow in-situ permeability tests to be conducted on the sediments after hyporheic exchange dye tracing experiments were complete. Figure 3.11 shows the erosimeter setup used to conduct permeability testing.

The erosimeter permeability test system requires commissioning to ensure that it is providing accurate permeability readings. The system has been designed to BS1377-5 [1990] and the test method described below is also based on BS1377-5 [1990]. The method below was used in the permeability tests conducted to commission the erosimeter permeability test system. The method is slightly different when tests are conducted after a trace experiments because the sediment will already be in place and the system full (details in Section 3.8).

- Base section filled with water
- Sediment is placed into the base section with water being drained through base valve, C, to prevent overflowing and the side of base section tapped to help sediment settle (which would occur over the duration of the test if not done prior)
- Temperature logger started, sensor in water column (Figure 3.5)

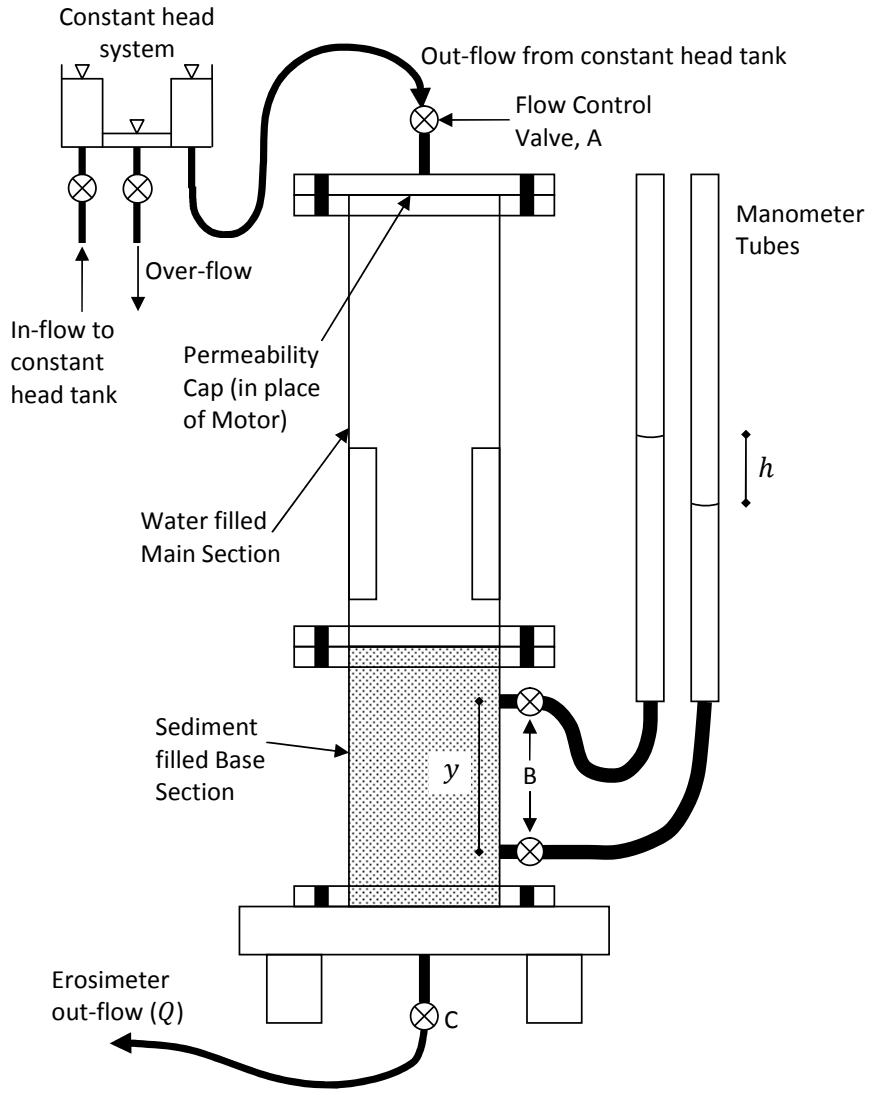

Figure 3.11: Erosimeter permeability test setup

- Main section placed and filled with water
- Manometer tubes connected (initially with the valves, B, shut to prevent air bubbles travelling into the sample) and air removed from tubes
- Permeability cap fitted and remainder of the main section filled (ensuring no air in the system).
- Top flow control valve, A, opened fully
- Bottom valve, C, opened fully

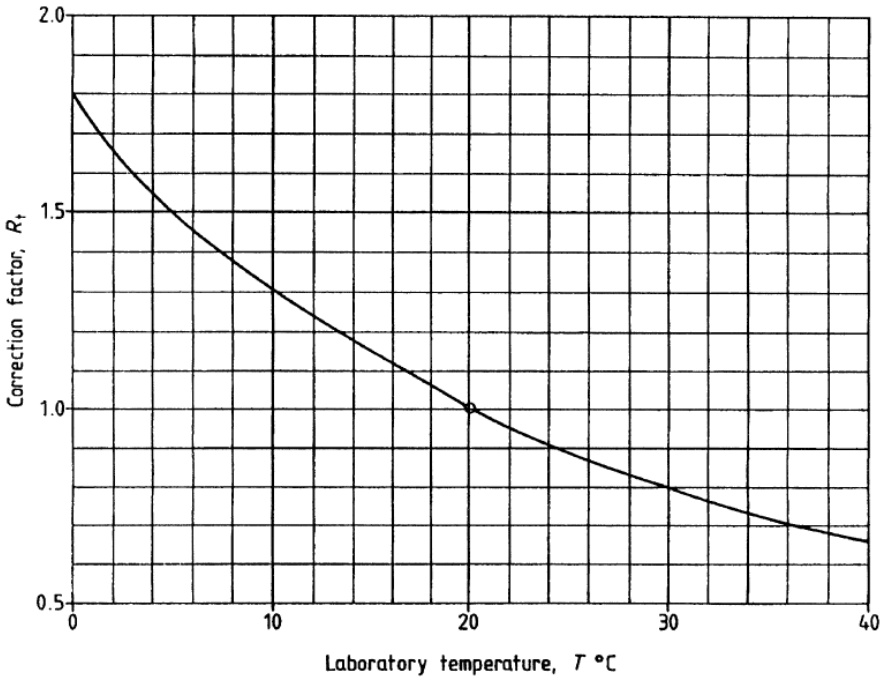

Figure 3.12: Temperature correction curve for permeability test [BS1377-5, 1990]

- Top valve, A, closed until the desired hydraulic gradient is reached
- Leave the system for 10-20 minutes to stabilise before taking discharge and manometer readings
- Discharge readings repeated at least three times and the average taken, with the manometer and temperature readings checked each time

To calculate the permeability the following equations are used. Equation (3.2) is taken from BS1377-5 [1990] and calculates the hydraulic conductivity of the sediment. This is converted to a permeability using (2.129).

$$K_c = \left(\frac{Q}{i}\right)\left(\frac{R_T}{A_s}\right) \tag{3.2}$$

Where: K_c is the hydraulic conductivity (m/s), Q is flow rate (ml/s), i is hydraulic gradient (h/y) where h is the difference in manometer level (mm) and y is the distance between manometer gland points (mm), R_T is the temperature correction factor, to account for the effect temperature has on viscosity, obtained from Figure 3.12 and A_s is the cross-sectional area of the sample (mm^2).

Three different natural sediments were tested and the measured permeability

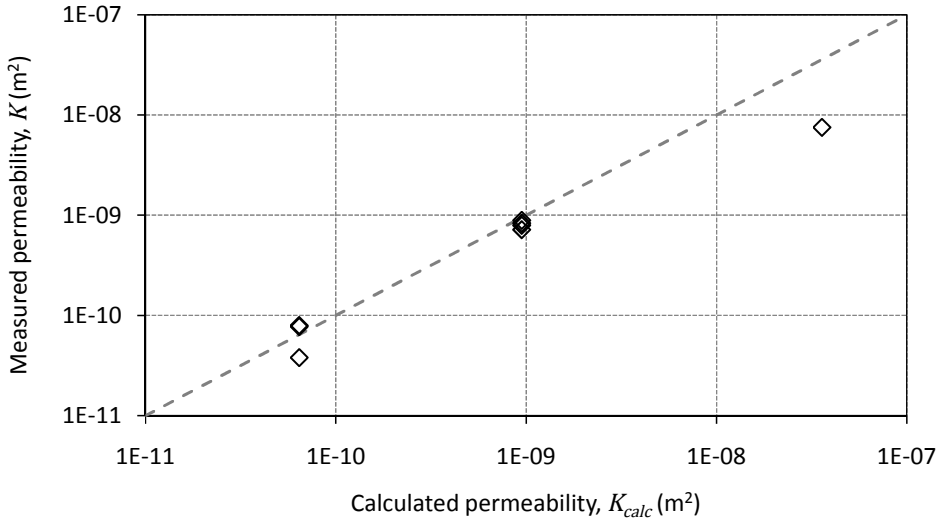

Figure 3.13: Comparison of calculated (2.130) and measured permeability for natural sediment using erosimeter

compared to those calculated using (2.130). The results are presented in Table 3.4. The results of the first three tests are given in Table 3.4. Three different diameter sediments were used. The next three tests (with the 2mm gravel) and the last two (with 0.3mm sand) were conducted on the same samples but with decreasing hydraulic gradients. It is interesting that the test under the smallest gradients give the result closest to the prediction formula. This is because the flows in the other tests, with larger hydraulic gradients, are either in or close to the turbulent region, which will result in a lower measured permeability [BS1377-5, 1990]. The results from Table 3.4 are shown graphically in Figure 3.13.

d_g (10^{-3}m)	θ	K_c (10^{-3}m/s)	K (10^{-10}m^2)	K_{calc} (10^{-10}m^2)	Difference (%)
7.5	0.36	65.2	75.1	359	−377.5
2.0	0.28	6.88	7.93	9.49	−19.6
0.3	0.37	0.33	0.38	0.64	−69.4
2.0	0.28	6.23	7.17	9.49	−32.3
2.0	0.28	7.23	8.33	9.49	−13.9
2.0	0.28	7.72	8.89	9.49	−6.7
0.3	0.37	0.69	0.79	0.64	19.0
0.3	0.37	0.67	0.77	0.64	16.9

Table 3.4: Comparison of calculated (2.130) and measured permeability for natural sediment using erosimeter

The test using the largest sediment was conducted with top valve fully open

in order to get a measurable hydraulic gradient over the sample. This probably explains the −377.5% deviation from the predicted value, as the flow is likely to be turbulent. The value used for the porosity also has a degree of uncertainty associated with it. This is because the diameter of the sediment is close to a tenth the diameter of the container used in the porosity tests. This is the smallest ratio that should be used in porosity testing [Carman, 1937]. The second and third series of tests demonstrate the repeatability of the permeability tests, but also the importance of staying within the laminar (Darcy flow) region.

Carman [1937] gives the expected deviation from the theoretical value of permeability to that measured for non spheres as 10-20%. The majority of the tests are within this bound, only three tests show a difference greater than 20%. In all but the last two tests, the measured permeability was lower than the predicted value. Apart from the reasons already stated, small amounts of air in the sample (from the normal tap water used) may have reduced the permeability. BS1377-5 [1990] suggests using de-aired water to negate this, but states that tap water is adequate in most instances.

The permeability test incorporated into the erosimeter measures values that compare favourably with accepted theoretical values. The majority of the errors between the predicted and measured values are within the bounds given by Carman [1937], and the largest error was seen with the 7.5mm gravel, which was probably too large for this permeability test due to the high discharges required to generate a hydraulic gradient. There is further evaluation of the permeability test system in the results chapter (Section 4.2.1), where the permeabilities obtained during testing are compared with (2.130).

3.3.4 Temperature Sensor

The temperature sensor used is a Tempatron NTC (thermistor) sensor in a stainless steel sheath (6mm diameter and 50mm long). The effective range of the sensor is −50°C to +110°C and is based on a 10KΩ resistance (±1%) at 25°C. The sensor is connected to a Wheatstone bridge, shown in Figure 3.14, with the power supplied by a 'plug in the wall' 12V DC power supply. The voltage, V_g, is measured across the bridge and is then related to the temperature.

The data sheet for the sensor gives maximum and minimum resistance value at specific temperatures. Using the mid-point of this resistance range for each temperature within the range 10°C to 30°C (the expected range of temperatures in the erosimeter), the values of the other resistors in the bridge were optimised to give

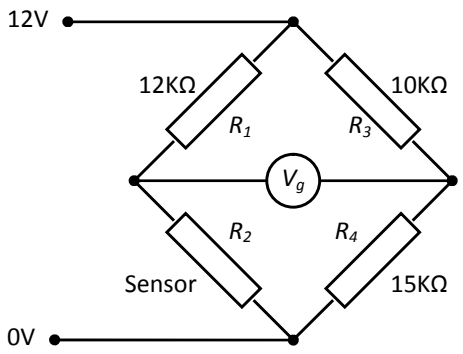

Figure 3.14: Wheatstone bridge used with temperature sensor

the greatest variation in V_g, over the range 10°C to 30°C. This was calculated using

$$V_g = V_{sup}\left(\frac{R_4}{R_3 + R_4} - \frac{R_2}{R_1 + R_2}\right) \tag{3.3}$$

where: V_{sup} is the supply voltage and the positions of resistors R_1 to R_4 are given in Figure 3.14.

The temperature sensor was calibrated within a Julabo F25 water bath. The bath had been purchased shortly before the temperature sensor calibration was conducted and had itself been calibrated in the factory. The bath has a working temperature range of −28°C to +200°C, with a stability of ±0.01°C. The absolute temperature calibration (ATC) was ±3°C and the resolution of the temperature display was 0.1°C.

The bath was set to the lowest temperature used in the calibration, 8°C, and allowed to stabilise for 5 to 10 minutes. Three voltage readings were taken at 30s intervals, along with the temperature reading from an un-calibrated thermometer (Kane-May KM220, accuracy ±1°C and resolution 0.1°C). The thermometer was used to provide an independent check on the temperature of the water bath. Once the lowest temperature readings had been taken the temperature of the bath was increased and allowed to stabilise before the measurements were taken again. This procedure was followed until the highest temperature of 35°C was reached.

Figure 3.15 shows the temperature sensor voltage readings against the water bath temperature, as well as the linear best fit equation used to convert the voltage output from the sensor into a temperature. Figure 3.16 shows the response of the un-calibrated thermometer, and indicates that the thermometer has retained its calibration. The calibration shown in Figure 3.15 has been used in all the subsequent experimental work, as well as the in-situ permeability test detailed above

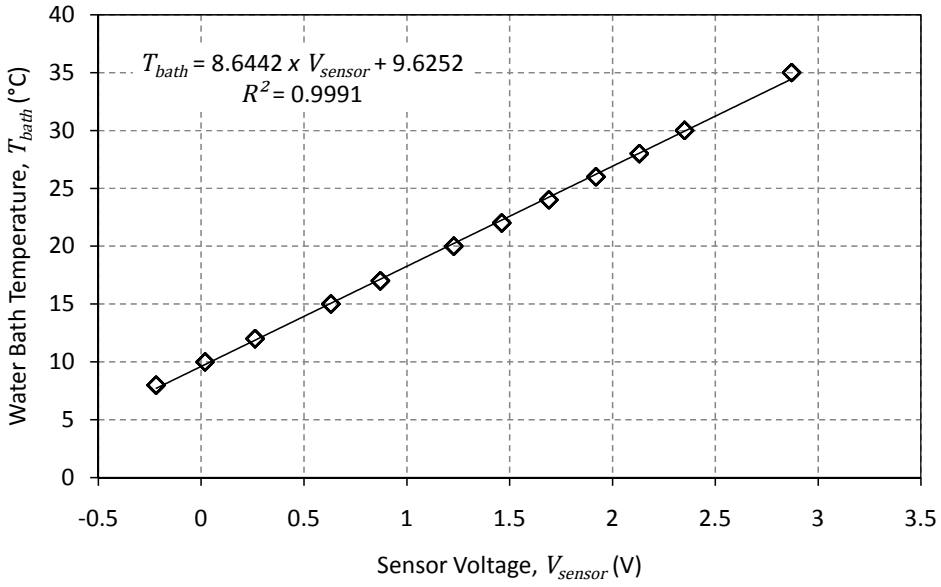

Figure 3.15: Temperature sensor calibration

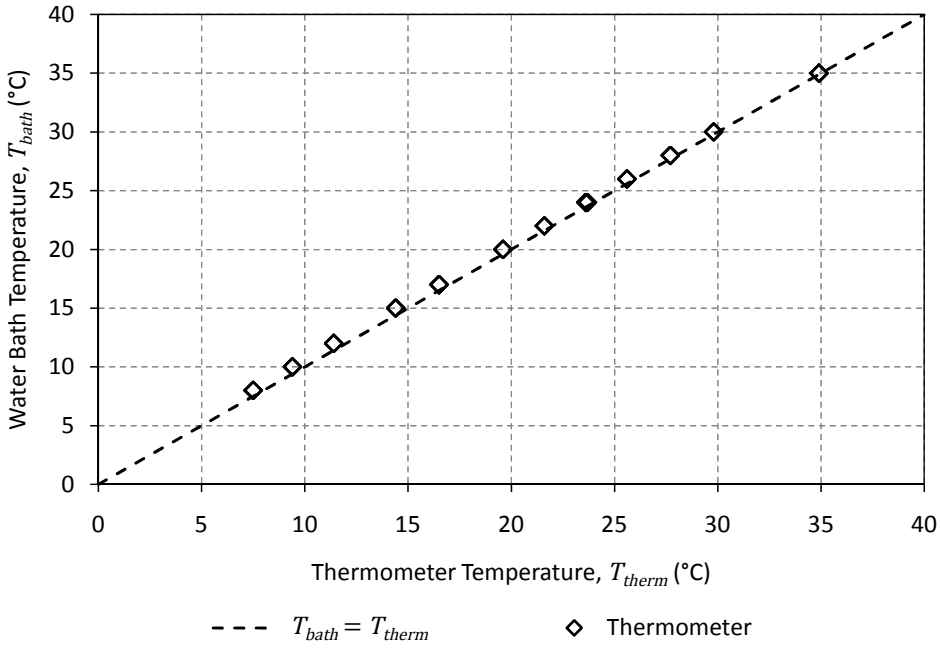

Figure 3.16: Comparison of temperatures measured using an un-calibrated laboratory thermometer and that given by the water bath

(Section 3.3.3).

3.4 Flow Visualisation

The erosimeter does not have a conventional open channel velocity profile, like a laboratory flume. To understand the flow field within the erosimeter, particle image velocimetry (PIV) measurements were undertaken. The aims were to qualitatively asses the flow field within the system, to establish the uniformity of the flow field at the sediment water interface and to relate the velocity field to the bed shear velocity (u_*) obtained during the sediment motion calibration, Section 3.3.2. Both vertical and horizontal light sheets were used to study the flow field in three-dimensions. This work also allows comparisons to be made with previous velocity measurements taken in the erosimeter using two-dimensional laser doppler velocimetry (LDV) [Liem *et al.*, 1997].

3.4.1 Experimental Setup

Initially experiments were conducted using a Point Grey Firefly MV-03M2M 640 by 480 pixel grey scale camera with a maximum frame rate of 60fps. However the flow speed within the erosimeter, even at the slowest propeller speed of 112rpm, was too high to be captured by 60fps and the PIV analysis software (DaVis 7.2), would not correlate the images and create vector fields. To obtain the required frame rate for the flow speed within the system a high speed camera was used instead of the Firefly.

The high speed camera used was a Photron Fastcam 1024 PCI, capable of 1000fps at full resolution (1024 by 1024 pixels). The lens used was a Nikon 55mm f/2.8 Micro-Nikkor, focused manually. After some experimentation with different frame rates and shutter speeds, 1000fps with a shutter time of 0.5ms was used for the following experiments. 1000fps was chosen because of the unknown velocity magnitudes within the system and the limited time available with the camera prevented a lengthy investigation into the most appropriate frame rate. This gave a recording length of 3.2s, 3200 images, which are recorded into a buffer and then transferred to hard drive once the recording is complete. Only one record was conducted for each dial setting in each configuration. On reflection this was not adequate to obtain a true ensemble average. The implications of this are discussed further in the Section 3.4.3.

Two different experimental setups were employed. The first with a vertical light sheet (VLS) and the second with a horizontal light sheet (HLS). Both experi-

mental setups used a CNI MRL-III-655, 1W continuous wave 655nm red diode laser and 50mm focal length Edmund Optics cylindrical lens, 25mm wide, to generate a 4mm thick light sheet. The flow was seeded with talisman particles, with a mean diameter of 0.1mm. This is the same equipment used by Vlaskamp [2011], except for the high speed camera. During the vertical light sheet experiments the light sheet was set at 90° to the camera with the laser set to produce a vertical light sheet through the center of the main section, illuminating the area between the bed and the propeller, Figure 3.17.

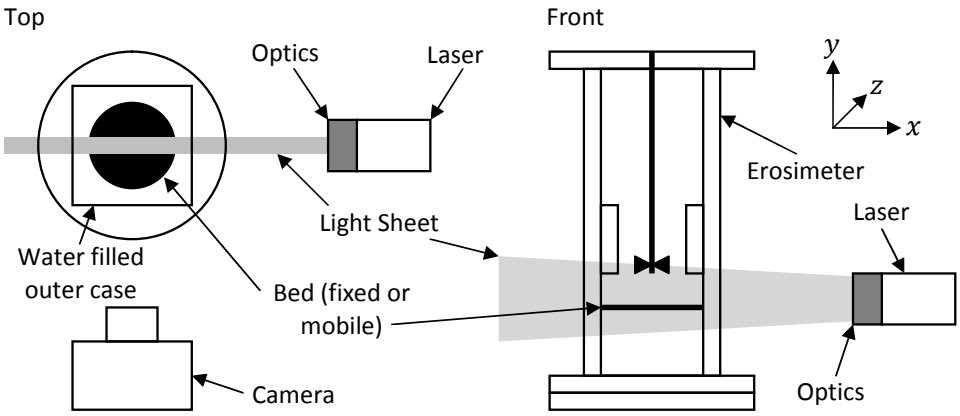

Figure 3.17: Initial vertical light sheet PIV setup

A new main section was constructed for the PIV experiments, with the same internal dimensions and baffle arrangement as that used the tracer experiments (Section 3.3). A square box was added around the cylindrical core and filled with distilled water to give a flat surface for both the camera and the laser, which reduces the distortion caused by the circular main section, Figure 3.18.

Both mobile and fixed beds were used with the vertical light sheet. The mobile bed consisted of 1.7-2mm diameter glass spheres, used because they are large enough not to undergo sediment motion at all but the highest flow speed and are approximately in the middle of the size range used in the tracer experiments. At the highest flow speed some motion occurs. However it is limited to the first two stages of sediment motion (Section 2.6.1), so does not affect viewing of the flow field. The fixed bed tests used a polycarbonate plate set at the same height as the sediment water interface when a mobile bed is used. This series allows comparison of the fixed bed, needed to view the horizontal light sheet used later, with the more realistic mobile bed. Five different propeller speeds, indicated by the dial reading from the speed controller (Figure 3.6) were investigated. These speeds correspond

Figure 3.18: Photograph of the modified main section used in PIV experiments

to the bed shear velocities investigated in the dye tracing experiments and are given in Table 3.5 with the measured propeller speed (rpm). The mobile bed was installed first, followed by the fixed bed once all the propeller speeds had been tested.

Dial Setting	Mobile Bed (rpm)	Fixed Bed (rpm)	Average (rpm)
190	109	109	109
270	162	161	162
340	208	206	207
490	308	312	310
640	419	426	423

Table 3.5: Propeller speeds used with vertical light sheet, mobile and fixed beds

The second experimental setup utilised the same laser, optics and camera as the vertical light sheet setup, but the light sheet is rotated 90° so it lies horizontally between the fixed bed and propeller. The camera set below the erosimeter, viewing the light sheet through a 45° mirror positioned directly below the erosimeter (Fig-

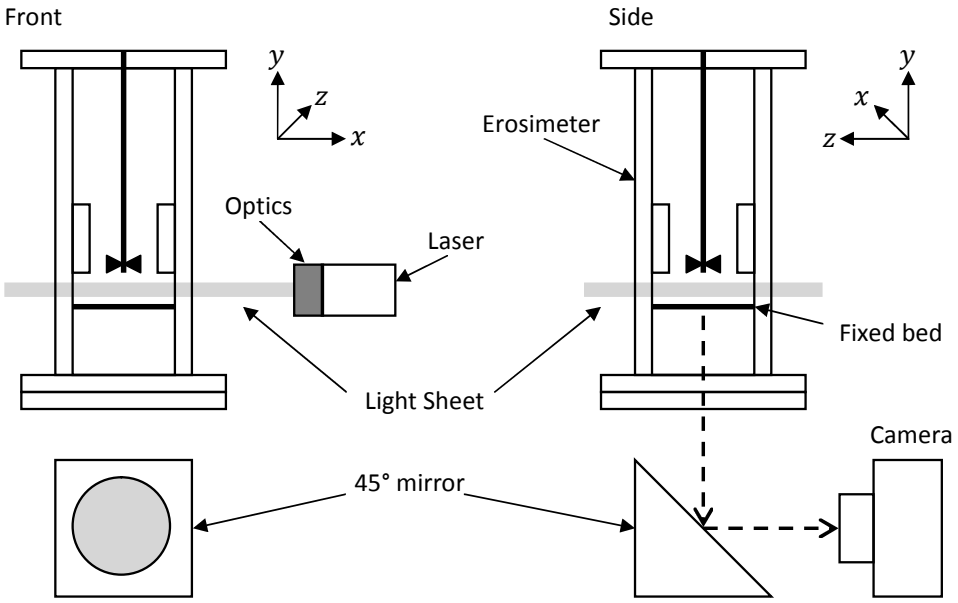

Figure 3.19: Horizontal Light Sheet Setup

ure 3.19). This arrangement inverts the image so the rotation direction is reversed in the camera relative to the straight view underneath. However the images do not need to be reverted but simply interpreted as if the camera was above the light sheet, rather than below.

Three different heights of light sheet (3mm, 13mm and 23mm) above the fixed bed were used and the same range of dial settings as above (Table 3.6). These heights were chosen due to the thickness of the light sheet and the distance between the baffles and the bed. The distances above the bed are to the centre of the light sheet and were measured in front of and behind the erosimeter using a ruler and a camera. The beam could not be seen with the eye whilst wearing safety goggles, but the intense light saturates the camera sensor and produces a visible white line on the screen, allowing alignment.

The difference between the measured speed of the propeller at the same dial setting between the horizontal and vertical light sheet tests (Table 3.5 and Table 3.6) is due to the warm up of the motor after it has been left running, as discussed in Section 3.3.1 above. However, the increase in speed does not significantly increase the number of propeller revolutions within the time frame recorded, adding an extra one or two revolutions in the horizontal light sheet data compared to the vertical light sheet data.

For all the different camera or light sheet positions a calibration image was

Dial Setting	3mm HLS (rpm)	13mm HLS (rpm)	23mm HLS (rpm)	Average (rpm)
190	124	125	128	126
270	179	178	180	179
340	226	225	227	226
490	329	327	330	329
640	440	438	439	439

Table 3.6: Propeller speeds for different heights of horizontal light sheet above fixed bed

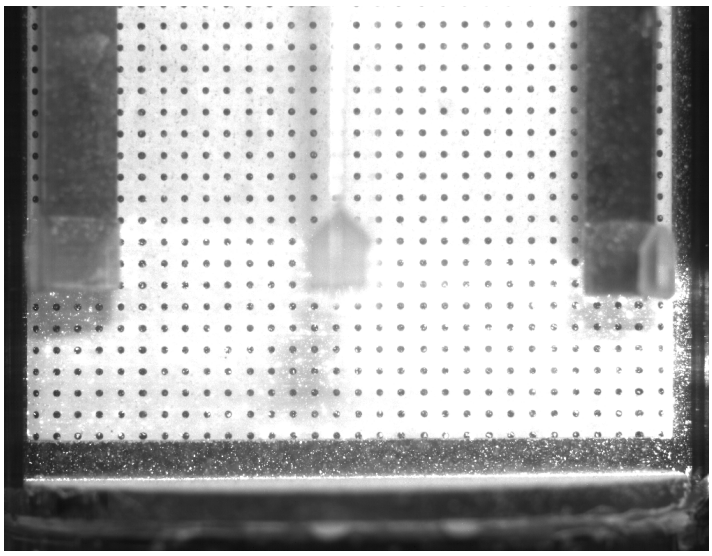

Figure 3.20: Example vertical light sheet calibration image showing the calibration plate, with regular grid of dots, used by image processing software (DaVis 7.2) to convert pixel displacements to physical distance

taken. This showed a calibration plate, aligned with the light sheet, that presented a grid of 1mm dots at a spacing of 3mm (centre to centre) to the camera (Figure 3.20). These calibration images were used to relate the pixels in the image to distances in physical space, so that pixel displacements obtained from image processing could be converted into velocities (m/s).

3.4.2 Analysis

This section gives a description of the image processing used to generate vector fields from the particle images, and then describes the post processing that has been conducted on those vector fields.

Image Analysis

PIV has developed since the 1930's from analogue (film based) to digital techniques used most commonly today [Raffel *et al.*, 1998]. The setup described above uses multiple frame, single exposure digital PIV which is analysed using cross correlation, (3.4), of the intensity fields generated from image pairs [Skeen, 2006; Raffel *et al.*, 1998]. The software used to analyse the particle images in this study was DaVis 7.2, produced by LaVision. The technique essentially tracks the movement of patterns of particles between two images, giving the pixel displacements, which combined with the image separation gives a velocity vector. This is shown graphically in Figure 3.21.

$$S(\mathrm{d}x, \mathrm{d}y) = \sum_{x=0}^{x<N} \sum_{y=0}^{y<N} I_1(x, y) I_2(x + \mathrm{d}x, y + \mathrm{d}y) \tag{3.4}$$

Where: $S(\mathrm{d}x, \mathrm{d}y)$ is the correlation strength at a displacement $\mathrm{d}x, \mathrm{d}y$, which are in the range $\pm 0.5N$, N is the size of the interrogation window and I_1 and I_2 are the image intensity of the first and second interrogation windows.

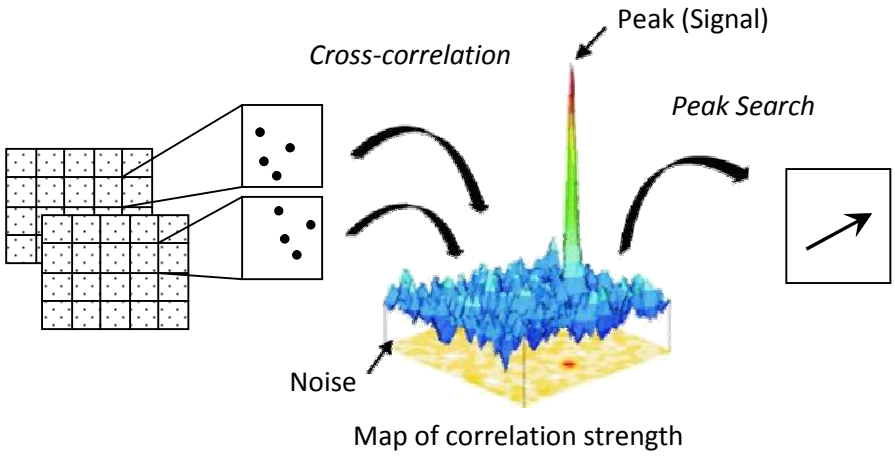

Figure 3.21: Evaluation of PIV image pair (left) using cross correlation resulting in velocity vector (right) [LaVision, 2006]

Each image is sub divided into interrogation windows, the size of which determines the maximum spatial resolution of the velocity field, i.e. the smallest eddies that can be seen. The size of the interrogation window is a balance between the number of particles within the window and that there should be no significant velocity gradients within the window [Raffel *et al.*, 1998]. Keane and Adrian [1992] state that for single exposure a particle density of 7 (i.e. 7 particles per interrogation

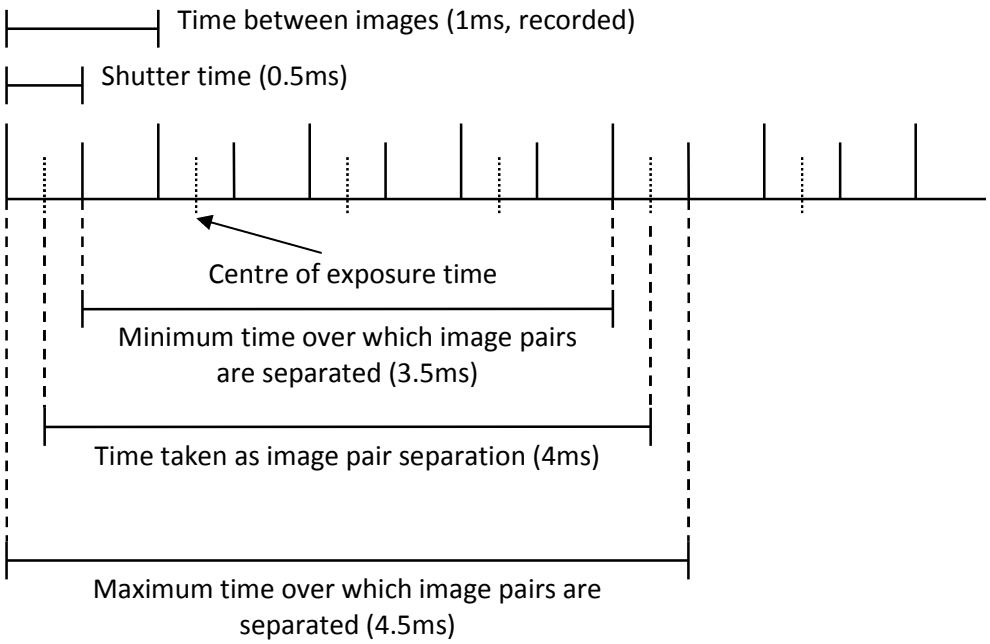

Figure 3.22: Graphical representation of the possible error in image pair timing

window) or greater should be used, otherwise there is a significant drop in the probability of valid detection, which would cause missing or spurious vectors. A window size of 12 by 12 pixels was used in this analysis with an overlap of 25%, giving the greatest spatial density of vectors whilst maintaining a particle density of 7. The ratio of physical to image distance is approximately 0.1mm/px (pixel) for all the experimental setups, which means that an interrogation window is approximately 1.4mm^2.

The image pairs used in the analysis were set three frames apart, meaning the time between images was 4ms not 1ms. This was done to decrease the error with respect to the time step and to allow enough particle movement to occur. The time step error is illustrated in Figure 3.22. This error occurs between the particle position in the physical flow at the beginning of the exposure and the end of the exposure, relative to the position in the second image in the pair. If the image pair separation is close to that of the exposure time, then there is a greater chance of an error in the physical time step relative to that displayed by the image.

There is also reference in the literature [Gray *et al.*, 1991], that the image separation should be greater than or equal to 20 times the exposure. However this relationship was originally published as part of a lecture series, [Meynart and Lourenco, 1984], and was for optical speckle velocimetry systems, where the particles

had to move by more than their diameter between frames. With modern digital PIV sub-pixel displacement algorithms are employed [LaVision, 2010], resulting in the value of 20 now being an over estimate. However, there has not been any detailed research into error created with ratios less than 20 using modern analysis techniques. The ratio of image separation to exposure time used for this study was 8, which is less that 20, but is better than other studies [Vlaskamp, 2011] that have produced good data from DaVis 7.2. If the time between frames was increased then the window size would also have to be increased to accommodate the greater movement of particles, which in turn would reduce the size of the smallest structures that could be detected. This led to the choice of parameters used in this study and described above.

Post Processing

Two main processes have been applied to the individual data sets. The first was to generate temporal average vector fields and the second was to calculate a bed shear velocity (u_*) to compare with that obtained through the bed shear calibration (Section 3.3.2). The velocity components for each point within the vector fields were averaged using

$$\bar{u} = \frac{1}{N} \sum_{i=1}^{N} u_i \tag{3.5}$$

where: $\bar{u}$ is the temporally average velocity in the x-direction and N is the number of vector fields. *The vector fields already account for the time step between images, so time is not explicitly used in the averaging, only the number of vector fields.* The same equation was also used for the vertical velocities (v) and the other horizontal component in the z-direction (w).

The vertical light sheet data contains components u and v, whilst the horizontal light sheet data contains components u and w. As discussed in Section 2.2.2 the bed shear velocity can be calculated from the velocity fluctuations. In the co-ordinate system imposed here, and given the flow field discussed below in Section 3.4.3, equation (2.17) becomes

$$u_* = \sqrt{\overline{w'v'}}. \tag{3.6}$$

This requires velocity components from both the horizontal and vertical light sheets, at the line across the erosimeter where the sheets would intersect. However, the measurements were not conducted simultaneously so the instantaneous fluctuations in the z and y directions are not concurrent.

Bed shear velocity is often used as a measure of turbulent intensity and is taken as indicative of turbulence in all directions because the turbulence is assumed to be homogenous (Section 2.2.2). Given the flow field above the bed in the erosimeter (detailed below in Section 3.4.3), the wall shear around the edge of the erosimeter should be equal to the bed shear, assuming that the turbulence is homogeneous. Therefore, the assumption was made that the bed shear velocity can be calculated from the velocity fluctuations in the x and z directions using the horizontal light sheet data from 3mm above the bed using

$$u_* = \sqrt{\overline{u'w'}}. \tag{3.7}$$

3.4.3 Results

The first section of the results focusses on the time averaged vector fields. Figure 3.23 shows example time averages vertical light sheet plots for both fixed and mobile bed at dial setting 640 (the fastest propeller speed). Plots from the other propeller speeds are given in Appendix C for both the vertical and horizontal light sheet data. In all the plots the colour indicates the magnitude and the arrow the directions of the velocity.

There is an asymmetry in the flow field, visible in both the fixed and mobile bed vector fields. The propeller is rotating anti-clockwise, (moving out of the page in the left half of the plot and into the page on the right). This may help to explain the asymmetry, as could a slight miss alignment of the light sheet to the central axis of rotation. The bottom of the baffles are approximately 35mm above the sediment water interface and the bottom of re-circulating cells between the baffles can be seen at the top of the plots. The velocities at the bed are significantly lower than those near the propeller. The velocities are similar at the bed in both the fixed and mobile cases, but there are much clearer vertical velocities, into and out of the bed, in the mobile bed vector field (Figure 3.23(b)). The close agreement between the fixed and mobile bed cases indicates that the horizontal light sheet data, conducted with a fixed bed, will be representative of the horizontal flow field with a mobile bed.

Figure 3.24 shows example horizontal light sheet vector fields, starting closest to the propeller (23mm above the fixed bed) and moving downwards towards the bed (3mm above the fixed bed). The bottom of the six vertically re-circulating cells between the baffles can be seen in Figure 3.24(a), along with a general anti-clockwise circulation. The velocities are generally higher than at the other heights above the bed, which agrees with the vertical light sheet data (Figure 3.23). The time average plots do not show the transient nature of the re-circulations between the baffles.

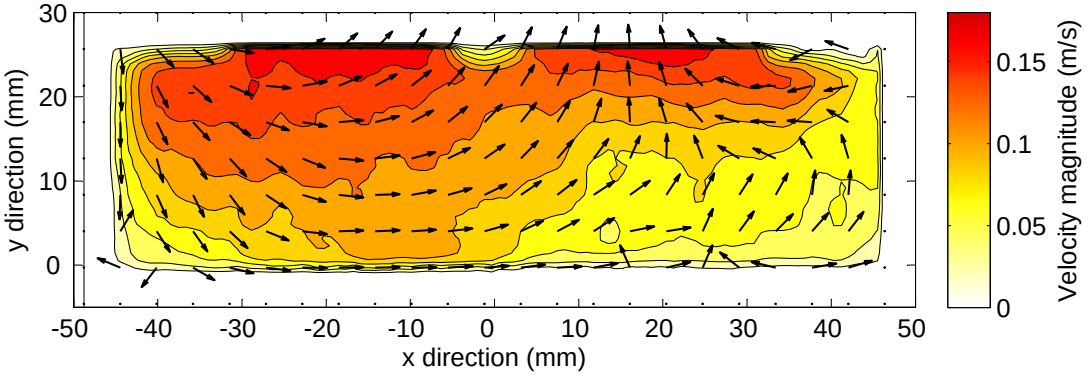

(a) Fixed bed, 426rpm

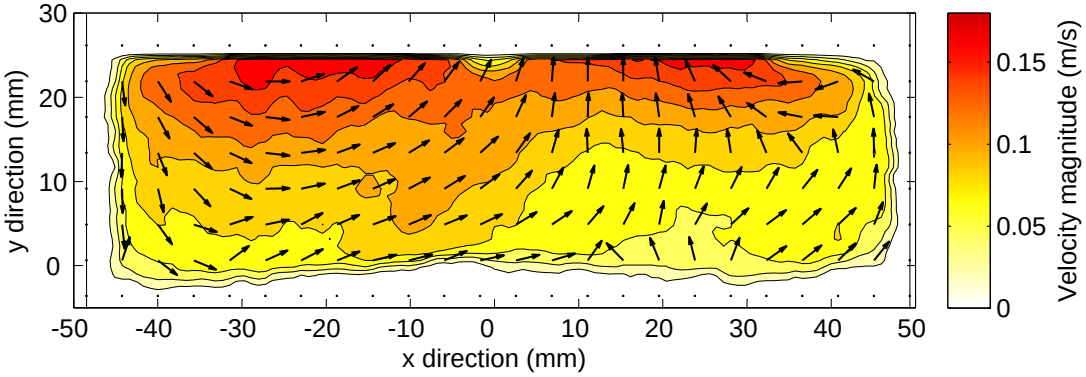

(b) Mobile bed, 419rpm

Figure 3.23: Time averaged VLS vector fields, Dial = 640

Observation during experiments and of the unprocessed images shows an increase in velocity as one of the propeller's three blades passes an area between the baffles. There is also an increase in movement towards the bed in the form of a down welling.

The velocity field closest to the bed (3mm, Figure 3.24(c)) shows a very different flow field to that just below the propeller. The flow is circular, without the inward motion. It is not possible to see the effects of the baffles and the flow is reasonably uniform. There are higher velocities in the centre and lower ones around the edge. The mean velocity is 0.11m/s, with most velocities within ±40% of the mean. Figure 3.24(c) suggests a fairly uniform circulating flow field at the bed, which has similar velocities at the wall to those seen at the bed in Figure 3.23(a). This suggests that the assumption made in the Post Processing section above is valid and the velocity fluctuations from horizontal light sheet 3mm above the bed can be used to estimate the bed shear velocity.

At 13mm above the fixed bed (Figure 3.24(b)), half way between the baffles

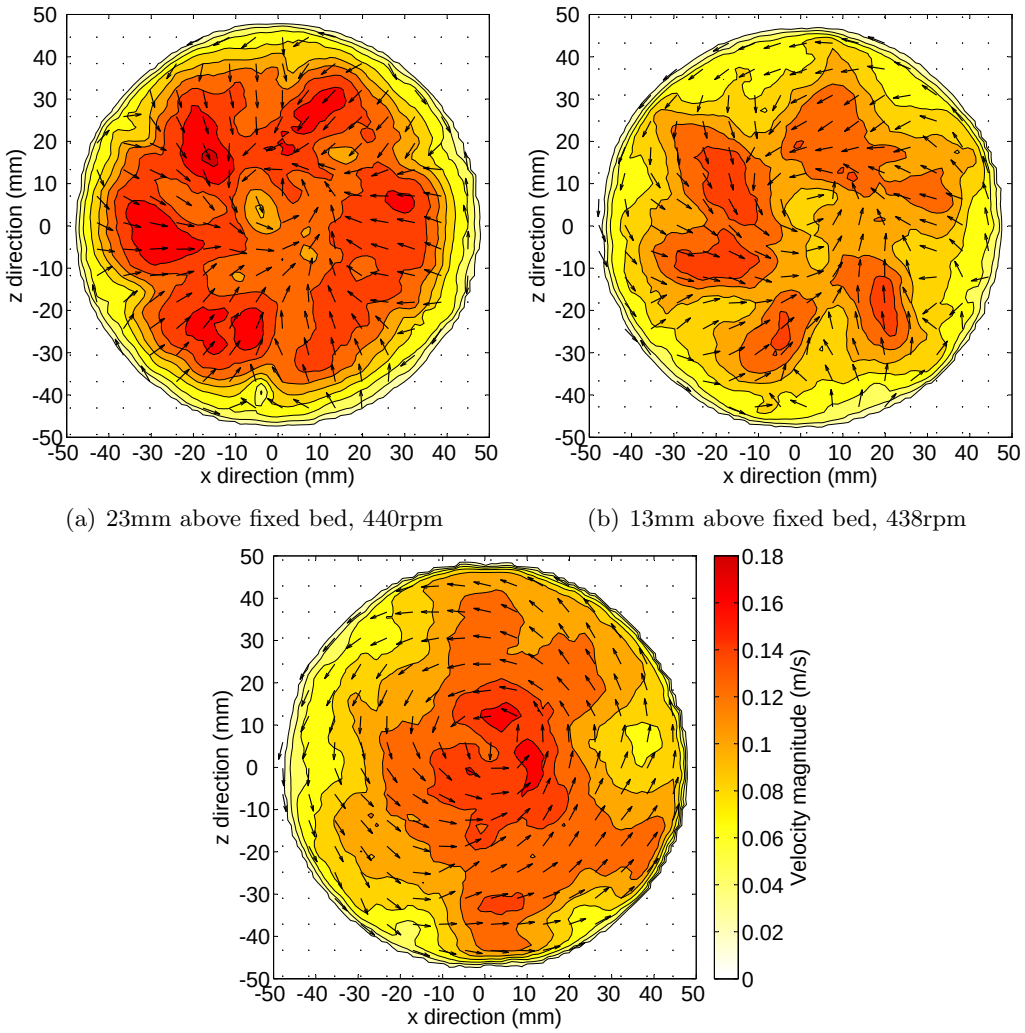

(a) 23mm above fixed bed, 440rpm

(b) 13mm above fixed bed, 438rpm

(c) 3mm above fixed bed, 440rpm

Figure 3.24: Time averaged HLS vector fields showing change in flow field at three heights above a fixed bed, Dial = 640

and the bed, the flow field is in transition from the six predominantly inward flowing regions at 23mm to the circular motion seen at 3mm above the bed. The flow is generally circular, but still with a strong normal component towards the centre. The time average plots smooth the chaotic nature of this region observed during testing and in the unprocessed images. Areas of high velocity exist, showing the regions between the baffles, but the rest of the flow has more uniform velocities, closer to those seen 3mm above the bed.

The flow field described above, shown in Figures 3.23 and 3.24, is consistent with propeller speed as can be seen in Appendix C. The flow field is clearest at

the fastest propeller speed because more revolutions are captured in the 3.2s of recording. This has the same effect as increasing the temporal averaging compared to slower propeller speeds, making the flow field clearer. The short recording time and lack of repeat recordings creates an uncertainty in the time averaged velocities calculated. Particularly at the slower propeller speeds, there is a suggestion in the flow fields (Appendix C) that the recording time is not adequate to remove temporal fluctuations. The slowest propeller speed contains 6 revolutions, whilst the fastest contains 23 revolutions. Comparison of different propeller speeds shows the velocity magnitudes increase with propeller speed, as would be expected. The variation from the mean velocity, 3mm above the bed, for the propeller speeds presented in Appendix C is between ± 40 and $\pm 50\%$, indicating consistency in flow field with propeller speed.

To check that the vertical and horizontal light sheet velocities were comparable the u component from the portion of both light sheets were compared at the intersecting point just above the bed. The region is a strip 4 by 4 by 96.2mm across the erosimeter just above the bed, using data from the vertical light sheet fixed bed tests and the horizontal light sheet 3mm above the bed. Figure 3.25 gives a comparison of the u velocities for dial setting 640. Despite the slight difference in propeller speed (426rpm for the VLS and 440rpm for the HLS) there is good agreement between the two data sets. The shape of the profiles is similar with the vertical light sheet showing slightly reduced velocities as would be expected with the slower propeller speed. The similarity shown in Figure 3.25 is repeated in the data from the other propeller speeds and proves that the velocities are comparable in both orientations of light sheet.

The u' and w' velocity components from the horizontal light sheet positioned 3mm above the fixed bed were analysed using (3.7) to give an indication of the bed shear velocity for a given propeller speed (u_{*PIV}). The spatially averaged values are given in Table 3.7, along with the bed shear velocity calculated from the bed shear calibration (Section 3.3.2), $u_{*BedShear}$. There is good agreement between the two calculations, with only one propeller speed showing greater than 10% difference. The good agreement validates both the bed shear calibration conducted in Section 3.3.2 and the assumptions made in using (3.7).

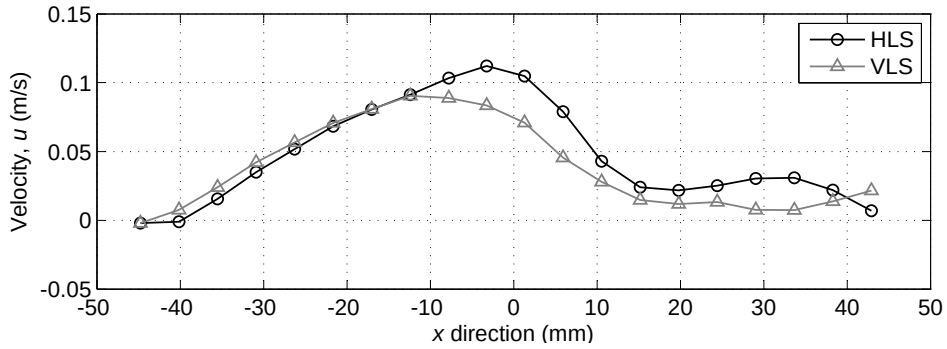

(a) Velocity profiles

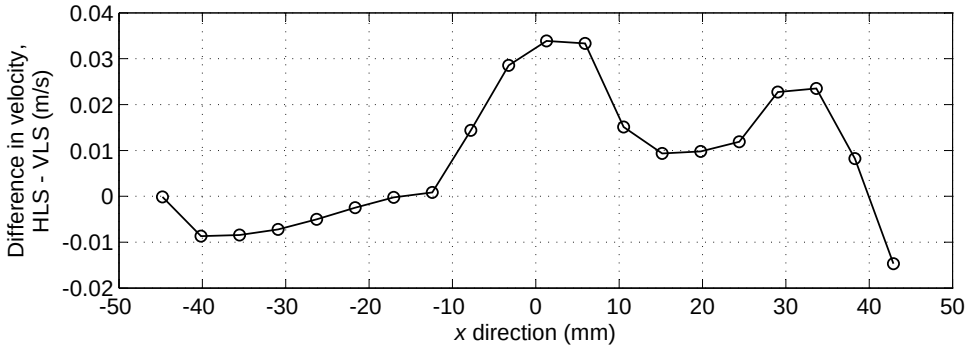

(b) Difference in velocities

Figure 3.25: Comparison of horizontal u velocities across the centre of the erosimeter 3mm above the bed from vertical (VLS) and horizontal (HLS) light sheet tests

Dial Setting	Propeller Speed (rpm)	$u_{*BedShear}$ (m/s)	u_{*PIV} (m/s)	Difference (%)
190	124	0.0093	0.0091	−1.7
270	179	0.0147	0.0147	0
340	226	0.0194	0.0166	−14
490	329	0.0296	0.0266	−10
640	440	0.0406	0.0427	5

Table 3.7: Comparison of u_* calculated from bed shear calibration and HLS PIV data at 3mm above the fixed bed

3.4.4 Conclusion

There is good agreement between the bed shear velocity calculated from the PIV data and those calculated from the bed shear calibration (Section 3.3.2). The flow field within the erosimeter is complex and changes with height above the bed, how-

ever the field shape is independent of propeller speed, with only the magnitude of the velocities varying. The field is relatively uniform at the bed with slightly higher velocities in the centre and lower velocities around the outside near the wall. The velocities obtained from the PIV data are comparable to those reported by Liem *et al.* [1997], however direct comparison is not possible because different propeller speeds were used in the two studies.

The length of time that images were recorded for (3.2s) is too short to calculate a true ensemble average. Multiple recordings should have been used to increase the number of pairs available for averaging at each propeller speed, however the data obtained is representative of both the magnitudes and directions, particularly at the higher propeller speeds.

3.5 Fluorometry

The tracer adopted for this study is Rhodamine WT, a pink fluorescent dye, developed in the 1960's specifically as a tracer (US patent 3, 367.946). Maximum excitation occurs at an incident wavelength of 555nm, with peak emissions of 580nm [Smart and LaidLaw, 1977]. Rhodamine WT has been chosen for a number of reasons including the fact that it has low levels of photochemical decay (typically 2-4% per day) [Smart and LaidLaw, 1977], which allows studies lasting several days to be conducted. Also it has low potential to sorb to sediments, which is a serious problem with other tracers. This allows accurate measurement of free hyporheic exchange to be studied [Smart and LaidLaw, 1977].

Rhodamine WT has temperature dependent fluorescence, which means the apparent concentration (when measured using fluorescence) will vary with temperature. Smart and LaidLaw [1977] give the temperature correction formula for Rhodamine WT as

$$C_T = C_{T0} \exp(-0.027T) \tag{3.8}$$

where: C_{T0} is the apparent concentration at 0°C, T is temperature (°C) and C_T is the apparent measured concentration at temperature T.

This approximately equates to a 2% reduction in fluorescence per degree increase in temperature. With this in mind the erosimeter system was placed inside a wooden box, to prevent any photochemical decay and the wooden box inside an air conditioned laboratory, typically 21°C, to reduce the temperature change during tests. Placing the erosimeter inside a wooden box had the added advantage of preventing photo-driven bio-film growth, which was seen in some initial testing.

3.5.1 Cyclops 7 Fluorometer

Turner Designs Cyclops 7 fluorometers use a green LED as an excitation light source and a photodiode to measure the fluoresced light. Three gain settings are available and provide a linear calibration between 0 and 1000 parts per billion (ppb) (gain X1), 0 and 100ppb (gain X10) and 0 to 10ppb (gain X100), although the linear range has been found to extend beyond these values. The middle (X10) gain setting was used, because a lower concentration within the bed will show a greater proportional difference when mixed with the water column, but is still easily mixed in the small quantities required for each experiment.

A control box was constructed to allow the gain to be easily changed and so the instruments could be powered by a 5V DC 'plug in the wall' transformer. The control box also allowed the instrument to be grounded, reducing noise problems. Figure 3.26 shows a Cyclops 7 fluorometer with the green LED illuminated. The instrument is 110mm long, 22mm diameter with a signal voltage output between 0 and 5V.

Figure 3.26: Turner Designs Cyclops 7

Two different instruments (SN2101038 and SN2100669) were used during testing due to a malfunction of instrument SN2101038 part way through. This prevented the water column trace from test 30_1850_1 being used (Section 4.4). De-aired water was used during testing to prevent air bubbles forming on the measurement head of the Cyclops. These can obscure either the LED or photodiode which will alter the reading given by the Cyclops. This was found to be a problem during initial testing.

3.5.2 Fibre Optic Fluorometer

One of the draw backs of using Cyclops 7's in the bed sediment is their relatively large size compared to the sediment grain diameter, and the large measurement volume compared to the sediment pore size (Section 3.2). This led to the development of a fibre optic fluorometer. The essence of the instrument is to take the excitation and detection away from the measurement head. This is done using a fibre optic cable, which has a much smaller size than the Cyclops 7, therefore affecting the in-situ flow fields less.

Development

The instrument was developed in house, originally by Dr. P Dunkley (RA) and latterly through this study. A number of options were tried. The best results were achieved using a 532nm, 5mW green laser diode as an excitation source (Photop Suwtech Inc. GDL-6005) and a photo multiplier tube (PMT) with appropriate filter as the detector (Hamamatsu H5784). Figure 3.27 shows the original prototype fibre optic fluorometer developed by Dr. P Dunkley. The laser diode and PMT are separate from the main box and this version requires three different power supplies to operate. The PMT has in-built amplification with the gain controlled using an external variable potentiometer. A 10KΩ variable potentiometer with a two digit display was used giving a range of gains from 00 to 99.

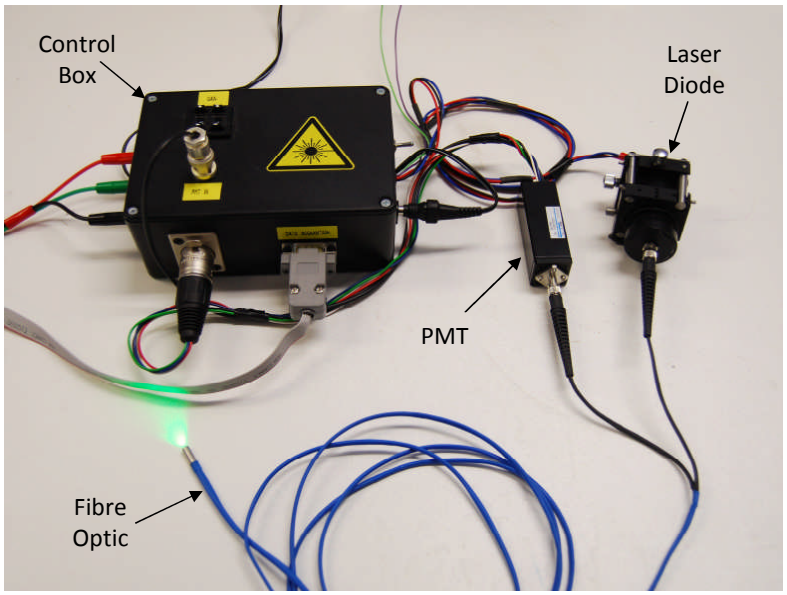

Figure 3.27: Prototype fibre optic fluorometer

Banner PBF26U fibres were chosen, which are two core (one from the laser diode and the other to the PMT) plastic fibres with a 16mm long, 4mm diameter steel cap at the measurement end (Figure 3.28). A lower power laser diode and a less sensitive PMT could be used if higher quality glass fibre optics were used. However, the original intention was to take these instruments into the field where the fibres would be treated as disposable, therefore lower quality cheeper fibres were used.

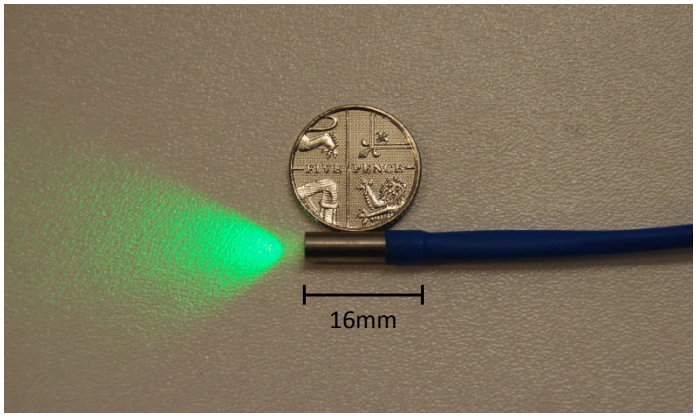

Figure 3.28: Fibre optic head with 5 pence piece

The prototype fibre optic fluorometer was tested to ensure it gave a linear response with dye concentrations like the commercial Cyclops 7 fluorometer. Figure 3.29 shows a calibration conducted with the prototype fibre optic fluorometer. The response from the prototype is linear and of the same order as the Cyclops 7 (Section 3.5.3 below).

Having demonstrated that the prototype fluorometer works and gives a linear response similar to the commercial Cyclops 7, the control and power circuitry were developed and all the components placed in one box. This version of the fibre optic fluorometer used a singe 12V AC power supply and contained a 555 timer circuit which allowed the laser to be pulsed. This was in preparation for use in the field as the fluorescence caused by background light could be assessed whilst the laser was off and subtracted from the reading when the laser was on.

However stability problems with the power supply circuitry forced a move back to a simpler system where the laser was continuously on and the fluorometer powered by laboratory power supplies. This was another reason for putting the erosimeter inside a wooden box during testing, to prevent background light from interfering with the fibre optic fluorometer measurements.

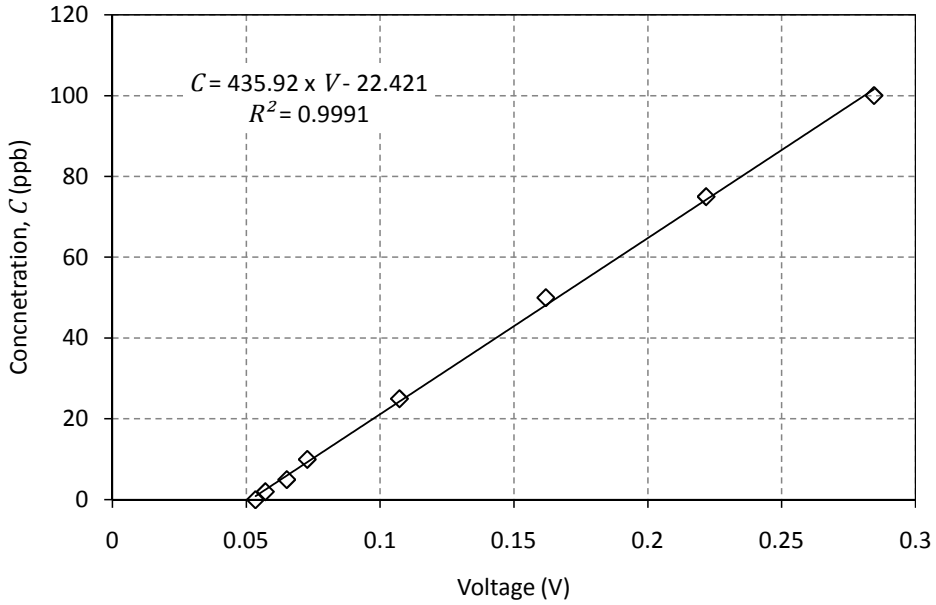

Figure 3.29: Example trace from Prototype fibre optic fluorometer (Gain 51)

Final Design

The final version of the fibre optic fluorometer, and which was used in this study, is shown in Figure 3.30. It uses the same laser diode and PMT as the prototype and is powered using laboratory power supplies. The fibres are the same as those described above with the addition of mesh hats to create a measurement volume within the sediment. The mesh hats are cylinders of approximately 200μm stainless steel mesh, 30mm long and 4mm diameter. There is a 3mm solid plug in the end, creating a measurement volume of approximately 0.23ml.

After initial testing a low pass filter was added just before the signal passed into the data logger (Section 3.7). This prevented the amplified high frequency noise from the PMT from masking the concentration change being measured. A cutoff frequency of 30Hz was chosen because of the slow nature of exchange within the bed and to exclude any mains noise at 50Hz. The frequency could be changed if faster exchange processes were being investigated in the future. Figure 3.31 shows the low pass filter circuit, which utilises an 8^{th} order Butterworth filter.

The circuit was prototyped and tested with a signal generator and oscilloscope before being connected to the fibre optic fluorometer. Figure 3.32 shows two traces from the fibre optic fluorometer, the first (Figure 3.32(a)) without the filter and the second (Figure 3.32(b)) with the filter. The reduction in high frequency noise is clear. The peak to peak noise is reduced by approximately half.

Figure 3.30: Final design of fibre optic fluorometer

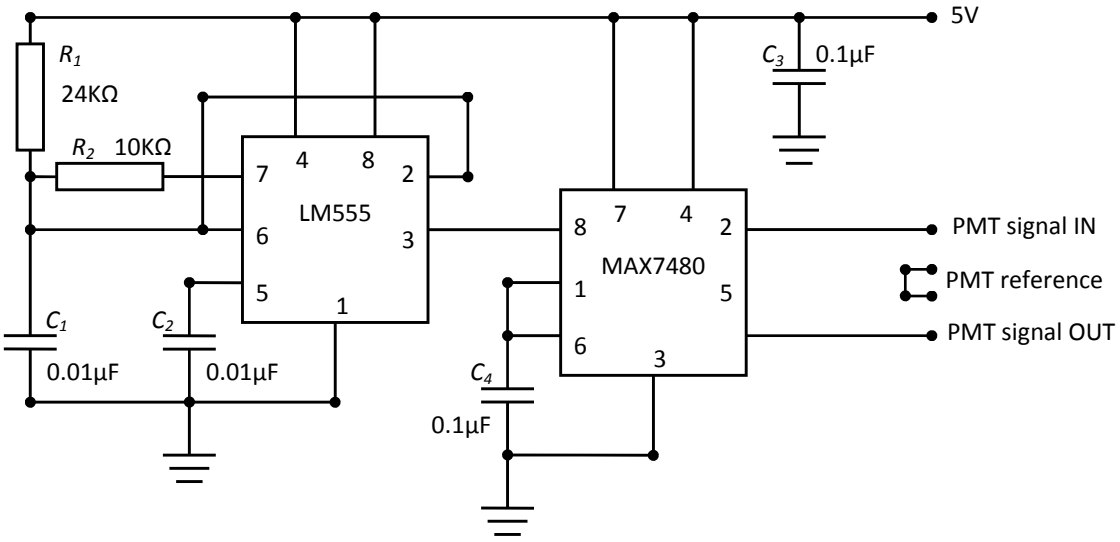

Figure 3.31: Low pass filter circuit

Six fibre optic fluorometers (FOF's) were manufactured, and are referred to as FOF1 to FOF6. Each instrument has a corresponding fibre optic cable and mesh hat which remained constant throughout testing. All the instruments give slightly different voltage outputs, because of slight variations in components, however the voltages are similar enough to allow all instruments to be set to gain 60. There were

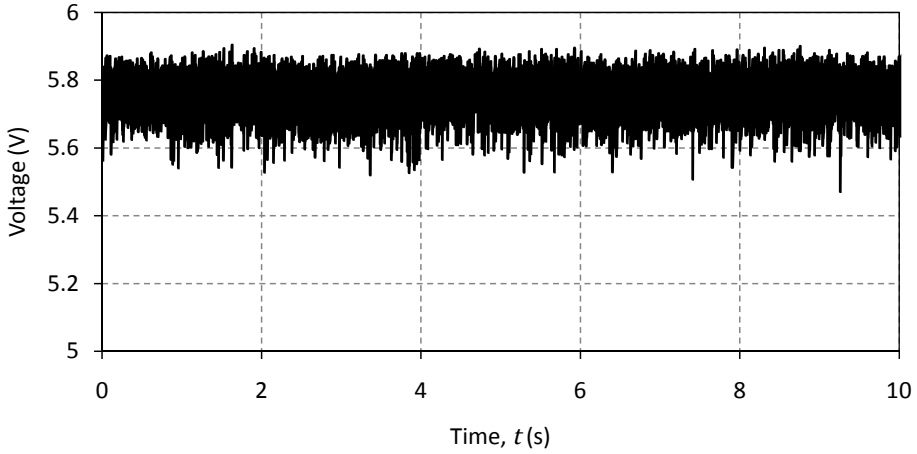

(a) Without low pass filter

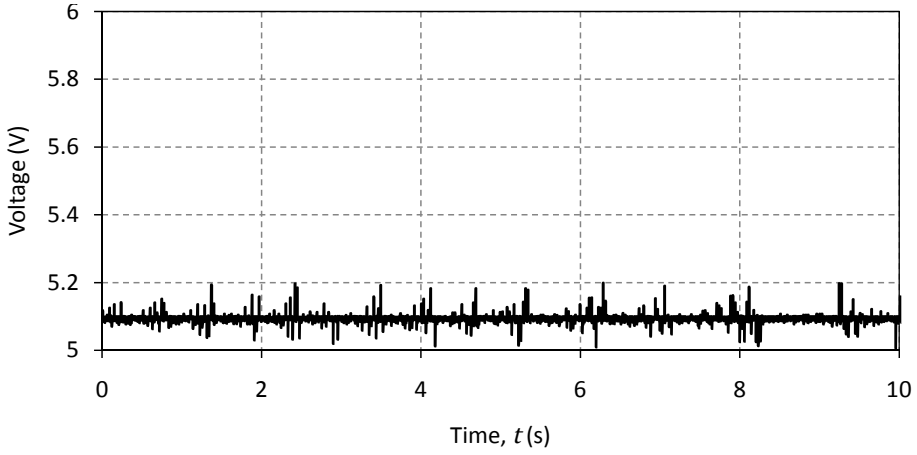

(b) With low pass filter

Figure 3.32: Comparison of fibre optic fluorometer (FOF4) output signal with and without low pass filter (sampling frequency 1kHz)

technical problems with FOF3 during the initial phase of testing and were only resolved for the last five experiments. This is covered in more detail in Chapter 4.

3.5.3 Calibration

Both the Cyclops 7 and the fibre optic fluorometers indicate the concentration of Rhodamine WT via the voltage they output. This is converted into a concentration, measured in parts per billion (ppb), through an in-situ calibration. The method used is detailed below.

- Clean erosimeter and equipment
- Mix stock solution and fill erosimeter with clean water

- Start logging and switch on motor (to ensure complete mixing)
- Close box and leave for 5 minutes
- Inject stock solution to raise concentration to required level
- Close box and leave for 5 minutes, then repeat previous step until final concentration level is reached
- 5 minutes after the final injection, stop logging and switch off motor, drain and clean erosimeter

An average of the minute preceding the next injection is taken as the voltage that corresponds to the concentration within the erosimeter. Water at the same temperature as that used in testing reduces the effects of temperature on the calibration. Figure 3.33 shows the raw data from a calibration. The increase in voltage output when the boxes doors are opened can be seen and the step change in output with each injection of stock solution.

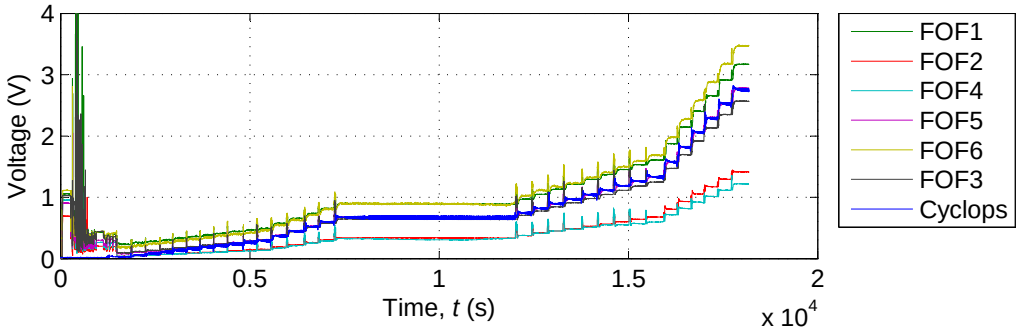

Figure 3.33: Example raw calibration trace

Figure 3.34(a) shows a calibration conducted in 2011 before testing began with five fibre optic fluorometers and the Cyclops 7. All instruments show a linear response, however a bubble in the mesh hat on FOF4 caused the reduction in voltage output at 20ppb. Figure 3.34(b) gives another in-situ calibration conducted in 2012 after the completion of testing. On both the responses are linear, but the fibre optic fluorometers give a very different response, while the Cyclops calibration is very similar. This is highlighted for FOF1, but is similar for all the fibre optic fluorometers.

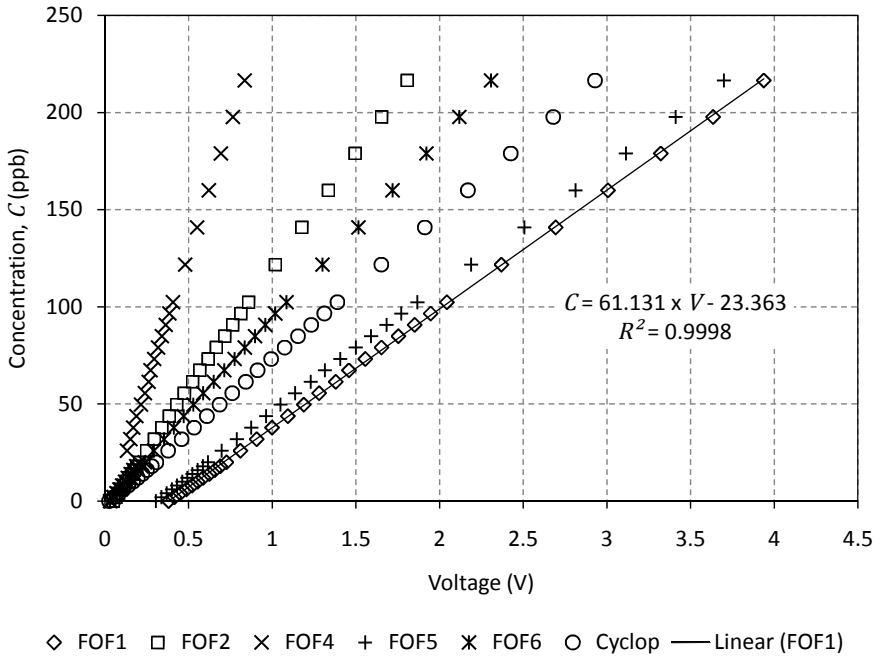

(a) Calibration with 5 fibre optic fluorometers and Cyclops (2011)

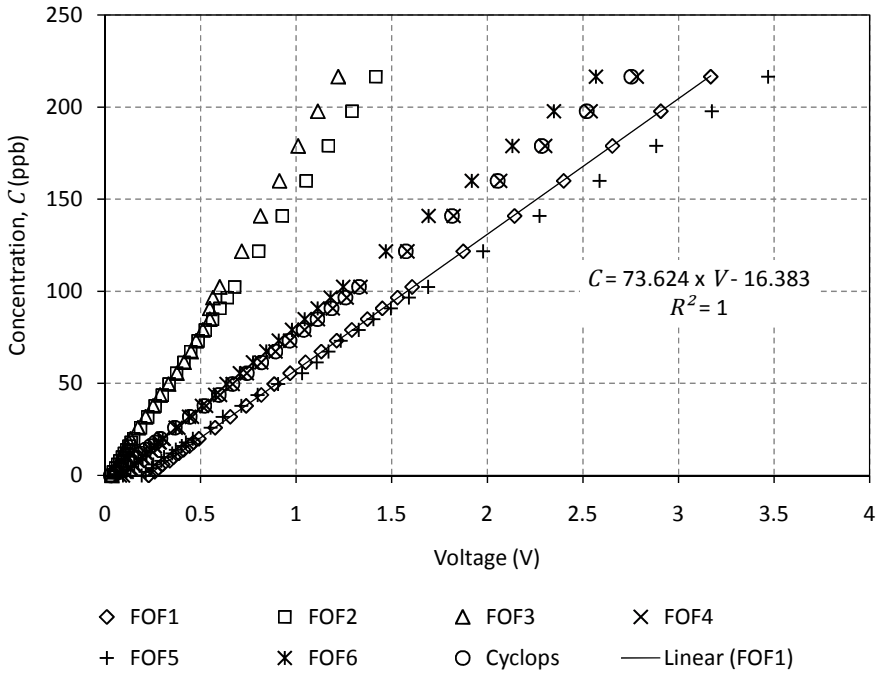

(b) Calibration with 6 fibre optic fluorometers and Cyclops (2012)

Figure 3.34: Comparison of fluorometer calibrations conducted in 2011 and 2012, demonstrating the changing in fibre optic calibration

The difference in the fibre optic fluorometer calibrations is caused by changes in fibre optic and mesh hat position. Each time the fibres are disconnected from the laser diode and PMT the calibration changes slightly. The orientation of the mesh hat and how far it is pushed onto the fibre optic head also affects the calibration as the light reflects differently within the hat. Once the instruments are setup the response is linear. As Figure 3.34 shows, however each setup produces a different response.

This presented a problem during testing because the mesh hats needed to be removed during the cleaning and setup process, although the fibre optics can be left for the duration of the experimental series. The solution was to employ a two point calibration for each test, similar to that used with commercial instruments such as Turner Designs SCUFA® fluorometers. At the start of each test the bed was saturated with tracer (Section 3.8), which allows the measurements of a known concentration (100ppb). At the end of the tracer experiment a permeability test was conducted which will flush out and mix any tracer that has not been mixed during the trace experiment. After the permeability test was complete, a recording was taken and the concentration recorded by the Cyclops 7 was assumed for all other instruments, since its calibration was always consistent.

The concentration was recorded for 5 minutes in each case and an average was taken. Although the second point was based of the reading from another instrument the concentration was very low, only a few parts per billion, so any slight inaccuracies or variations in the calibration of the Cyclops will not significantly impact the calibration of the fibre optic fluorometers. Figures 3.35 and 3.36 show the start and end of a test with the 5 minutes, used in the calibration. This method has produced reliable calibrations, shown by the almost identical concentrations between instruments after the calibration was applied.

3.6 Sediments

To reduce the uncertainty in sediment parameters and eliminate sorption from the experiments, glass spheres were adopted for the bed material. The spheres are made from solid soda glass with a density of 2530kg/m^3. Five different particle diameters were used covering a range of diameters usually associated with river sediment and used by previous experimental studies (Sections 2.4 and 2.5). The size range was also governed by the operational parameters of the erosimeter discussed in Section 3.3 and the requirements of the permeability test setup. The largest diameters must be less than a twelfth the diameter of the erosimeter and the sample containing not

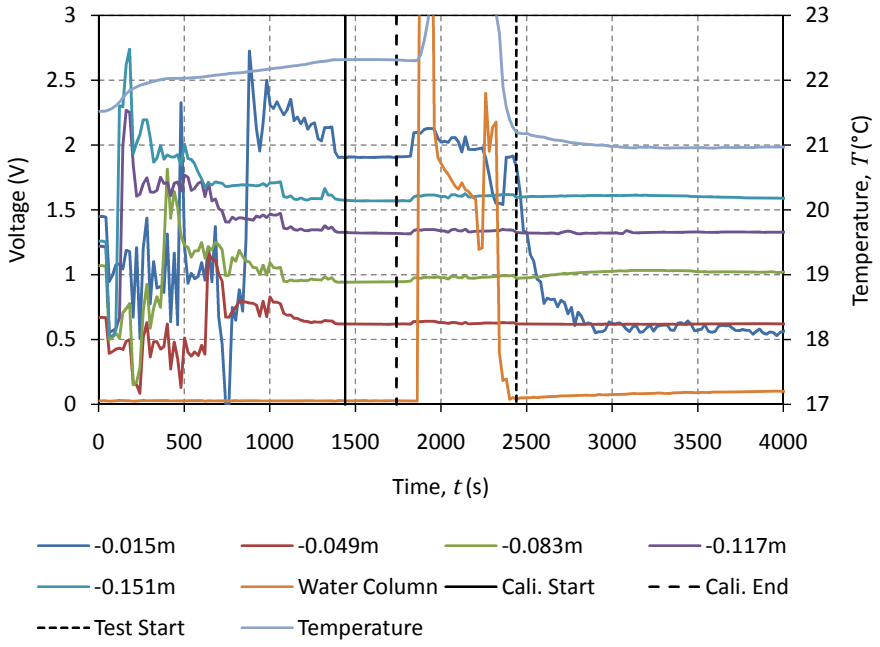

Figure 3.35: First 4000s of example raw trace showing the part used in calibration, taken from test 15_1850_2 ($K = 1.96 \times 10^{-9}\mathrm{m}^2$, $u_* = 0.015\mathrm{m/s}$)

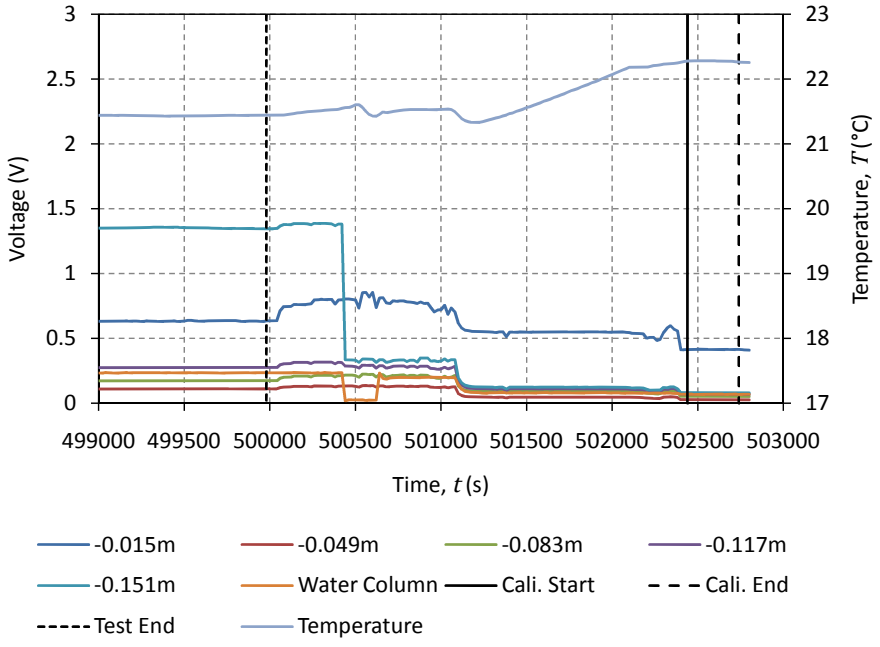

Figure 3.36: Last 4000s of example raw trace showing the part used in calibration, taken from test 15_1850_2 ($K = 1.96 \times 10^{-9}\mathrm{m}^2$, $u_* = 0.015\mathrm{m/s}$)

more that 10% particles passing a 63μm sieve [BS1377-5, 1990]. Table 3.8 gives the diameters of the spheres used in testing. The sediments are generally referred to by their mean particle diameter (d_g) throughout the rest of this document.

Grade	90% larger, d_{10} (mm)	90% smaller, d_{90} (mm)	Mean particle diameter, d_g (mm)
5011	4.70	5.30	5
4507	1.70	2.00	1.85
4502	0.50	0.75	0.625
5223	0.30	0.40	0.35
5214	0.10	0.20	0.15

Table 3.8: Diameter range of glass spheres

3.6.1 Porosity

Porosity is the ratio of volume of voids (V_v) in a sediment to the total volume (V_T), (3.9). However the volume can be substituted for mass if the same substance is used, e.g. water. If both the total volume and the volume of voids is measured with water then the density of the fluid can be neglected as the ratio will remain the same. This is the method used to obtain the porosity of the glass spheres, placed under the same conditions as those in the tracer experiments.

$$\theta = \frac{V_v}{V_T} \tag{3.9}$$

The electronic balance used for the porosity measurements was an AND Electronic Balance, F-2000, with a maximum weight of 2100g and a sensitivity of 0.01g. The balance is calibrated every 12 months by Avery Weigh-Tronix and had been calibrated 2 months before the tests. A purpose built container of a similar diameter to the erosimeter was used in the porosity measurements and has a diameter greater than ten times the largest diameter sphere, the smallest ratio that should be used in porosity testing [Carman, 1937]. The method used in the porosity measurements is summarised below.

- Level balance and zero with empty, dry porosity test container on
- Fill container with water to get the total volume, V_T, in mass of water
- Remove container from balance and fill with sediment, displacing the water as the sediment is placed
- Level the sediment off at the top of the container, removing excess

- Dry the outside of the container and remove any sediment from the outside
- Weigh the sediment and water filled container
- Empty the sediment from the container and dry in geotechnics drying oven (100°C)
- Weigh dry sediment

The dry weight of the sediment is subtracted from the wet weight to give the mass of water filling the voids. This is divided by the mass of water needed to fill the container to give the porosity. Table 3.9 gives the average porosity measured for each diameter of glass sphere. The porosities measured are slightly higher than the theoretical value of 0.37 for randomly placed spheres [Richardson and Parr, 1988], probably because some consolidation is achieved through gentle tapping of the container, needed ensure even placement and done as part of the experimental setup procedure in the erosimeter.

Mean particle diameter (mm)	Average porosity (θ)
5	0.39
1.85	0.39
0.625	0.38
0.35	0.38
0.15	0.38

Table 3.9: Porosity of glass spheres

3.7 Data Acquisition

The voltage signal from the fluorometers and temperature sensor were recorded using a National Instruments (NI) PCIe-6323 logging card with two SCB-68 connection blocks. The analogue voltage signals were digitised and stored in text files using NI LabView software. The PCIe-6323 has a maximum sampling frequency of 250kHz, a timing resolution of 10ns and a 16 bit analogue to digital converted (ADC). The voltage range of the logger was set from zero to +5V, as reducing the voltage range from the default ±10V increase the signal to noise ratio in the analogue to digital conversion, and increases the absolute accuracy to around 500μV.

All channels were logged differentially at 120Hz to reduce noise and aliasing with mains frequency. The data were then averaged over 120 or 240 readings giving an output value every 1 or 2 seconds, depending on the length of test. Channel 5

was initially left blank so FOF3 could be added, once repaired, for the later tests (Section 3.5.2).

3.8 Experimental procedure

This section details the experimental procedure followed during testing. The volume of water used to fill the main section varied in the first few experiments. Initially 2000ml was used, then 1800ml and finally 1900ml, which was used for 60% of the tests. A table (Table 4.1) of the test parameters is given at the start of Chapter 4, which indicates the number of repeat tests conducted for each parameter combination and the combinations that could not be tested without causing sediment motion.

To prevent mixing of interstitial fluid with the water column occurring during setup cling film was placed across the sediment water interface, and up one side of the main section. This was slowly removed once the main section had been filled. Although this method is not perfect it was tested extensively during initial testing (Section 3.2) and was the least intrusive. Thin ice disk and sliding plates were all considered, but the design of the erosimeter, with the baffles and trying to seal a moving plate whilst maintaining the cylindrical shape prevented these methods being used. The ice disk would have altered the temperature at the sediment water interface, affecting the fluorescence.

The experimental procedure was:

- De-air water and leave to reach room temperature
- Set propeller speed (rpm) using tachometers
- Mix 1000ml of 100ppb tracer solution
- Take and record tachometer readings of propeller speed
- Start data logging and record time using computers clock
- Fill base with tracer solution, fit mesh hats and place sediment, measuring the leftover tracer solution to know volume used in test
- Shut doors and log system for 5 minutes for initial calibration point
- Place cling film inside main section
- Place main section and slowly fill with 1900ml clean de-aired water

- Carefully remove cling film creating as little disturbance as possible
- Stop motor and place on top of main section
- Shut door
- Start motor recording 'start' time, initial voltages and check initial tracer concentration using 10-AU fluorometer

  Allow test to run.

- Record 'end' time and voltages
- Open doors and take tachometer readings of propeller speed
- Turn off and remove motor and take reference concentrations from base using 10-AU fluorometer
- Turn on re-circulating pump connected to header tank
- Connect permeability test cap and fill main section to top
- Connect and open manometer tubes
- Open top and bottom valves
- Reduce top valve to desired flow rate
- Leave for 10-20 minutes to stabilise
- Take discharge measurements
- Shut doors and log system for 5 minutes for end calibration point
- Stop logging
- Empty and clean the system

Chapter 4

Experimental Results and Analysis

4.1 Synopsis

Experimental results and analysis are presented in this chapter. Example raw data are given and both the water column and in-bed concentration profiles are analysed. The water column data are compared to previous experimental data [O'Connor and Harvey, 2008], and the vertical variation of the in-bed diffusion coefficient is examined using the in-bed data. The relationships between bed shear velocity, permeability and other experimental parameters with diffusion coefficient are also shown.

4.2 Raw Data

Example outputs from the erosimeter experimental system described in Chapter 3 are presented below, along with a summary table of the tests conducted. Table 4.1 shows the number of repeat tests conducted for each parameter combination. For this study, measurements were restricted to conditions below the sediment motion threshold. A '−' indicates that the test could not be conducted without causing sediment motion. In the following analysis and discussion the tests will be named using the bed shear velocity in mm/s, the mean sediment particle diameter in μm and the repeat number. This system produces the name 10_350_2 for a tests conducted with a bed shear velocity (u_*) of 0.010m/s, 0.35mm mean diameter glass spheres and is the second test for this parameter combination.

As described in Section 3.5 the fibre optic and Cyclops fluorometers produce

u_*		d_g	(mm)			u_*
(m/s)	5.000	1.850	0.625	0.350	0.150	(mm/s)
0.040	3	–	–	–	–	40
0.030	2	2	–	–	–	30
0.020	2	2	–	–	–	20
0.015	2	2	2	1	–	15
0.010	2	2	2	1	1	10
	5000	1850	625	350	150	
		d_g	(μm)			

Table 4.1: Number of tests preformed for each combination of u_* and d_g

a voltage output that is converted into concentration through a linear calibration equation. Figure 4.1 shows the calibrated concentration profiles from test 20_1850_2, which is the second test with the 1.85mm sediment (measured permeability, K, of $2.06 \times 10^{-9}\text{m}^2$) and a u_* of 0.020m/s. The effect of instrument position below the sediment water interface is clearly visible, with the instruments closer to the interface showing much more rapid mixing than those further away. The effect of temperature on the apparent concentration measurements (Section 3.5) is clearly visible in both Figure 4.1(a) and (b), particularly in the profiles at (-0.117 and -0.151m). Throughout the next three chapters concentration is used to describe calibrated trace data, which has not been temperature corrected. When the effect of temperature on concentration is discussed, it refers to the effect temperature has on fluorescence which will affect the apparent measured concentration, and not the actual concentration of the solute. The data was not temperature corrected because the temperature sensor was positioned at the top of the water column and may not necessarily give representative temperatures for positions within the bed sediment. The temperature changes effect some instruments more than others which may indicate that the electronics within some instruments were affected by temperature changes, as well as the fluorescence of the tracer. This would have to be corrected in addition to the effects of temperature on fluorescence.

Once the in-bed concentration at each depth has reached that of the water column, the in-bed profile shows an increase in concentration with time, the same as the water column profile exhibits and is most clearly shown in Figure 4.1(a). This drop to a minimum and then slight rebound, most visible for the instruments close to the interface, is entirely expected. The reason for the rise in concentration after a region has mixed is that tracer from deeper within the bed is raising the 'well-mixed' concentration within the system. The well-mixed concentration will be higher when 3/4 of the tracer has mixed than when only 1/4 has mixed. This is illustrated in

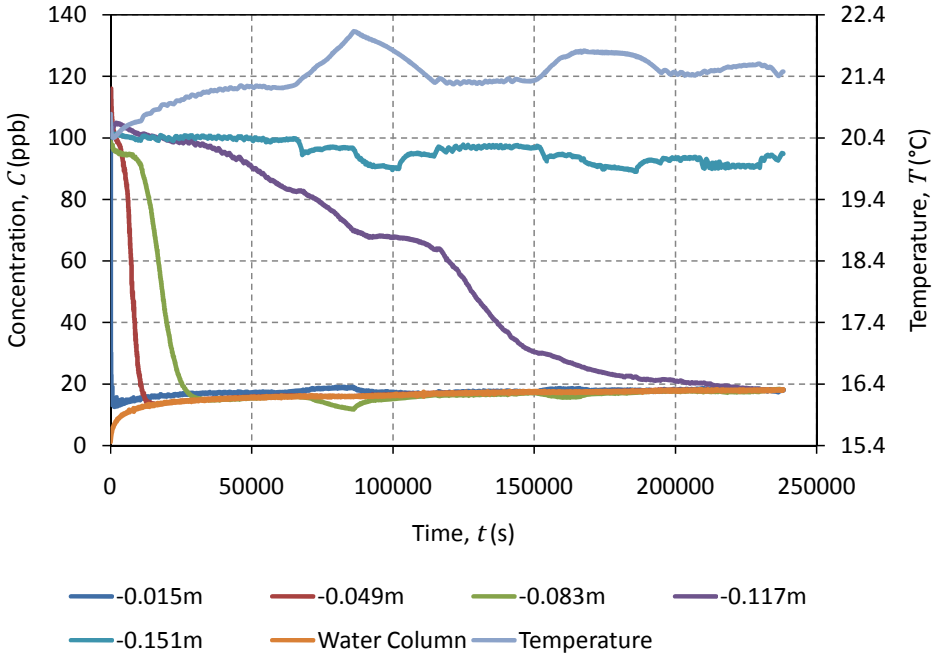

(a) Full trace (66hrs)

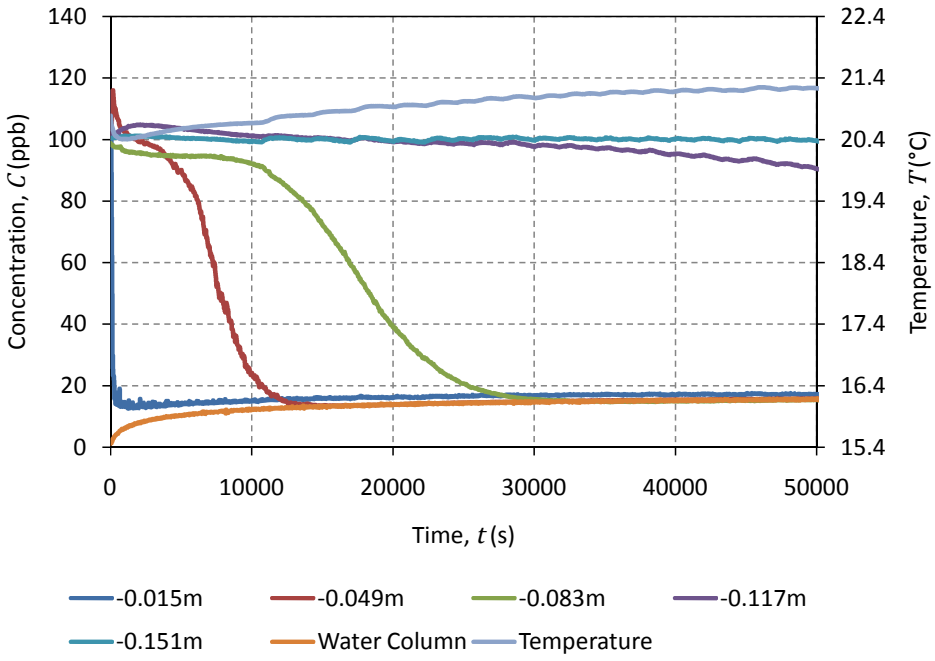

(b) First 50000s (14hrs)

Figure 4.1: Example calibrated, non-temperature corrected, trace data from test 20_1850_2 ($K = 2.06 \times 10^{-9}\mathrm{m}^2$, $u_* = 0.020\mathrm{m/s}$)

Figure 4.2. If the process of mixing/exchange is thought of in terms of discrete layers of tracer, then it becomes obvious that a layer of tracer can not exchange/mix until the layers above have done so. However, this analogy is not strictly true because the tracer will start to mix slowly as soon as there is a concentration gradient.

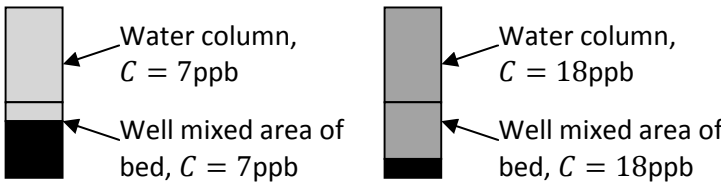

(a) 1/4 tracer mixed (b) 3/4 tracer mixed

Figure 4.2: Increase in 'well-mixed' concentration with time during test

The test (20_1850_2) shown in Figure 4.1 does not reach the expected equilibrium concentration of 23ppb by the end of the test. This is because the test was not run for long enough to allow all the tracer to mix within the system and is demonstrated by the small change in concentration at -0.151m below the sediment water interface throughout the test. The length of time required for the system to reach equilibrium conditions for the tests conducted with finer sediments and lower bed shear velocities would have been prohibitive, as the diffusion coefficient throughout lower portions of the bed is likely to be dominated by molecular diffusion. Therefore realistic time scales had to be adopted for each test, governed by the time available and the stability of the fibre optic fluorometers (Section 3.5.2). This particular test was one of the first to be conducted and in hindsight should have been run for longer, although it had already been run for 3 days. There is further discussion on the effects of not running all the tests to equilibrium later in this chapter.

4.2.1 Sediment Permeability

Permeability has been shown to be an important factor when studying hyporheic exchange (Section 2.6.2), thus the in-situ permeability was measured after each trace experiment, as described in Section 3.8. The in-situ permeability test system and procedure had previously been evaluated using natural sediments (Section 3.3.3). The measured permeability was compared with that calculated using (2.130). As discussed in Section 2.6.2 this equation is based on the packing of spheres, so the results from the experimental in-situ measurements should match the assumptions made in deriving (2.130), allowing a direct comparison, and the use of (2.130) to

validate the system and methodology. The mean measured permeability (K) for each sediment, along with the standard deviation, σ, (for those sediments which were tested more than twice) and the calculated permeability (K_{calc}), using (2.130), are given in Table 4.2.

There is good agreement between the calculated permeability and those measured, as demonstrated in Figure 4.3. There is good repeatability between different tests with the same diameter glass spheres. This is due to the behavior of randomly packed spheres, the equipment and the test methodology.

d_g (mm)	K_{calc} (10^{-10}m^2)	K (10^{-10}m^2)	σ (%)
5.000	223	107	5.5
1.850	30.6	20.4	2.0
0.625	3.12	3.18	0.8
0.350	0.98	1.38	
0.150	0.18	0.46	

Table 4.2: Comparison of calculated (2.130) and average measured permeability for a range of glass sphere diameters

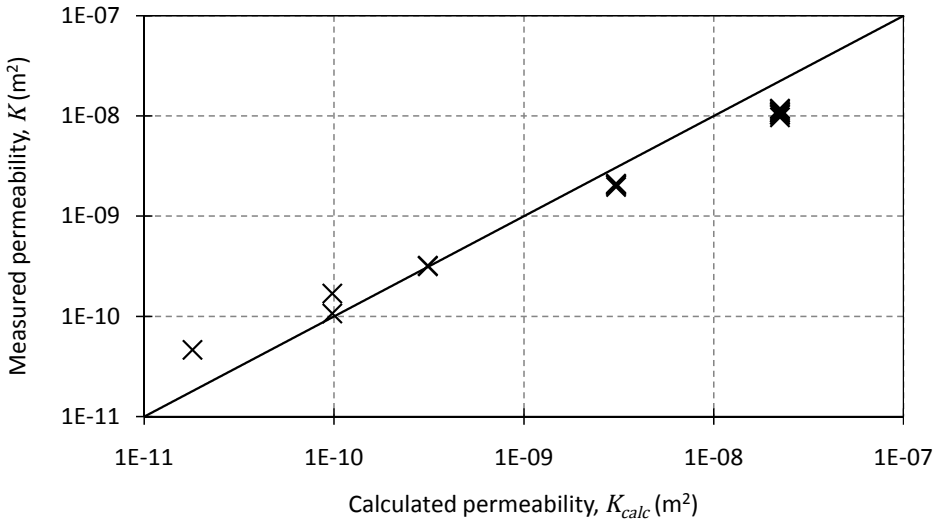

Figure 4.3: Comparison of calculated (2.130) and measured permeability for glass spheres

There is a general trend within Figure 4.3, where the calculated permeability is higher than measured for large diameter spheres, whereas for small diameter spheres the reverse is true, and the calculated permeability is lower than that measured. There are fewer tests conducted on fine (small diameter) spheres so there

is less certainty in this portion of the trend. The trend is the same, although less pronounced, as that seen with natural sediments in Section 3.3.3. The lower than expected permeability for large diameter spheres could be due to non-laminar flow conditions within the permeability tests. This would invalidate the assumption of Darcy flow in the derivation of (2.130) and lead to the discrepancy.

The difference between measured and predicted permeability shown in Figure 4.3 should have a relatively small impact on the prediction of a hyporheic exchange coefficient using the O'Connor and Harvey [2008] scaling relationship (2.51). A sensitivity analysis was conducted and a 10% change in permeability results in only a 6% change in the calculated diffusion coefficient.

4.3 Evaluation of Analysis Techniques

Three different analysis techniques were introduced in Section 2.4, and evaluated using model simulation data. Based on this, the water column data was analysed using the O'Connor and Harvey [2008] methodology (Section 2.4.1) and the in-bed data using the Nagaoka and Ohgaki [1990] methodology (Section 2.4.2). Both methodologies have aspects which needed further investigation with experimental data, rather than model simulation data.

4.3.1 Water Column

The model simulation data suggested that 20 to 30% of the equilibrium concentration should be used to define the maximum value included in the initial slope (Section 2.4.1). Because the porosities of the different size glass spheres are so similar, there is little difference in the amount of fluid (including tracer) placed within the system during each test. Therefore the calculated equilibrium concentrations for the experiments conducted varies between 24.4 and 22.0ppb. The average equilibrium concentration is 23.1ppb and has been adopted as the equilibrium concentration for all experiments, as the difference is only slightly larger than the noise on the water column experimental data. This reduces the variation in analytical method applied to different traces.

The trace data, as stated in Section 4.2, is calibrated into ppb, whereas (2.100) requires it in accumulated mass of tracer. The process first requires the conversion from ppb into l/l, by dividing by 10^9. This assumes that the neat tracer is 100% Rhodamine WT, which in reality is a concentrated solute. l/l is the ratio of the volume of tracer to water, which will be the same for any units of volume, e.g. m^3/m^3. This concentration is then multiplied by the volume of the water in

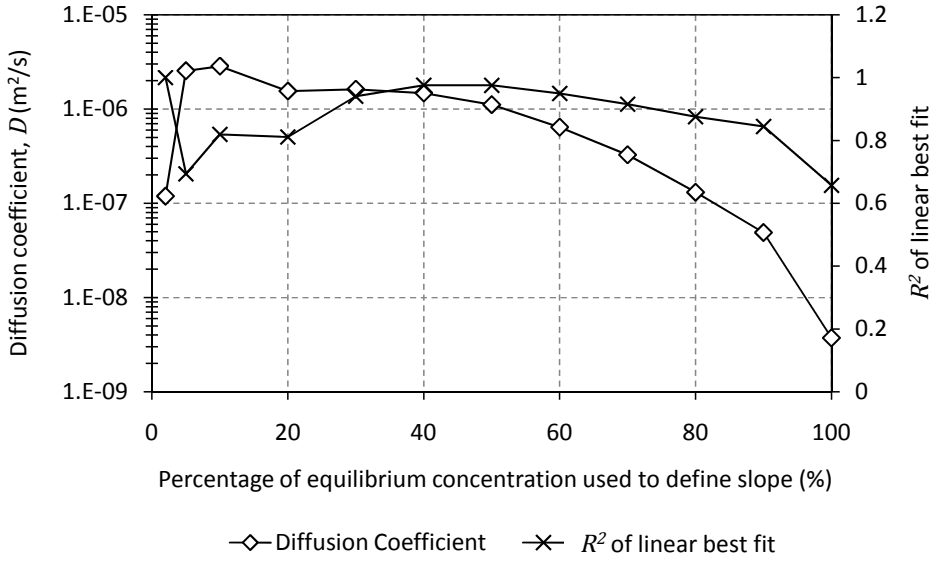

Figure 4.4: Effect of different initial slopes on calculated diffusion coefficient from test 30_5000_2

which the concentration measurement was taken (V_w) to give a volume of tracer that results in the original ppb concentration measurement. This volume is multiplied by the density of Rhodamine WT, ρ_{Rhod}, (1130 kg/m^3, taken from the MSDS) to give the mass of tracer. This is finally divided by the cross-sectional area (A_s) to give the accumulated mass of tracer per unit area within the water column (M_w, kg/m^2). This process is given by

$$M_w = \frac{C_{ppb}\rho_{Rhod}V_w}{A_s 10^9}. \tag{4.1}$$

The equilibrium concentration of 23.1ppb becomes 6.71kg/m^2 when converted into accumulated mass.

This value has been used to analyse three different water column traces (30_5000_2, 20_1850_2 and 15_625_2) to help confirm which percentage of the equilibrium concentration to use in the analysis. Figures 4.4, 4.5 and 4.6 show the calculated diffusion coefficients against the percentage of the equilibrium concentration used to define the top of the initial slope. The secondary axis shows the R^2 coefficient from the linear best fit line used to obtain the gradient of that initial slope. The R^2 value indicates how well the concentration data is represented by a straight line. This is the best measure available to asses which percentage is best, because unlike model data, the exact coefficient is not known, so there is no 'correct'

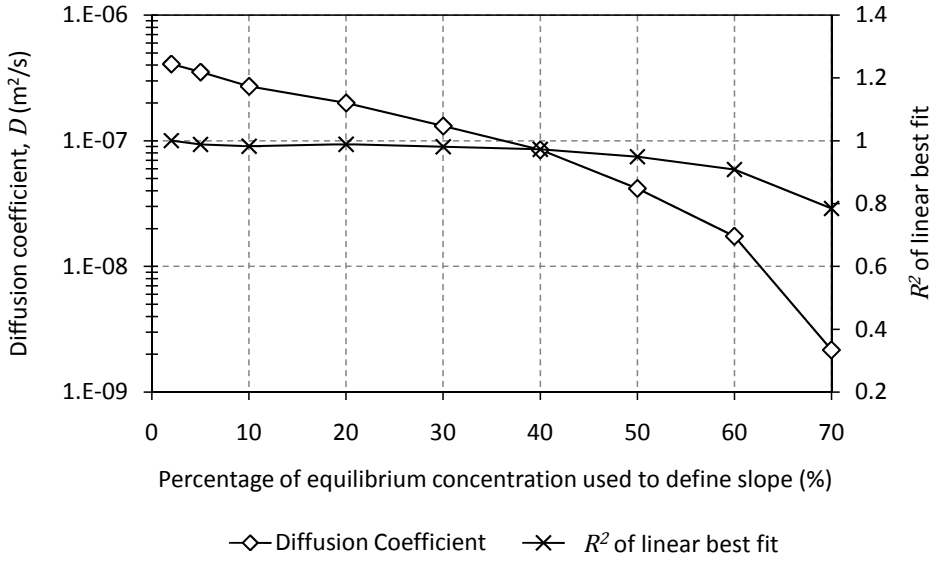

Figure 4.5: Effect of different initial slopes on calculated diffusion coefficient from test 20_1850_2

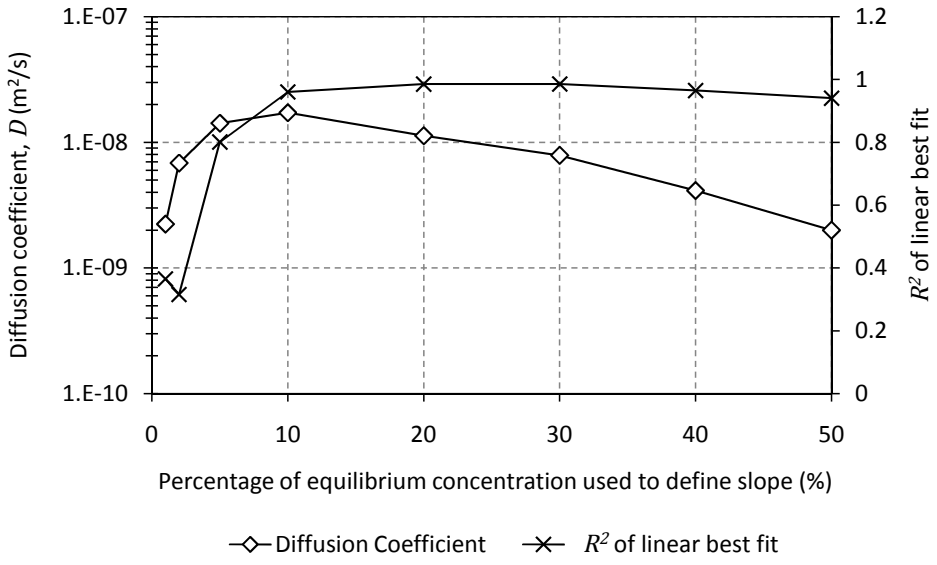

Figure 4.6: Effect of different initial slopes on calculated diffusion coefficient from test 15_625_2

answer to compare the calculated coefficients against.

Figure 4.4 shows the effect of varying the percentage on a high exchange test, using 5mm spheres ($K = 1.02 \times 10^{-8}\text{m}^2$) and u_* of 0.03m/s. The percentages with the best R^2 values are between 60 and 30%, with the best R^2 at 50%. The R^2

value then reduces until only a few points are being included in the slope (1%). The difference in the diffusion coefficient obtained between 50 and 30% changes is small (maximum of 1.62×10^{-6} and minimum of $1.11\times10^{-6}\mathrm{m}^2/\mathrm{s}$), but the coefficient starts to reduce for 60% and higher ($6.42\times10^{-7}\mathrm{m}^2/\mathrm{s}$). The highest diffusion coefficients are obtained with 10%, a value of $2.85\times10^{-6}\mathrm{m}^2/\mathrm{s}$, but an R^2 of only 0.82. For this trace the best percentage of the equilibrium concentration to take as the last value included in the initial slope is between 30 and 50%, which is higher than suggested by the model data analysis.

Figure 4.5 shows the same analysis for the example trace 20_1850_2 given above (Figure 4.1, $K = 2.06\times10^{-9}\mathrm{m}^2$, $u_* = 0.020\mathrm{m/s}$). As mentioned above this test did not run until equilibrium conditions were reached. This means that the the same range of percentages used to examine 30_5000_2 could not be applied. 70% of the equilibrium concentration included all the trace data, and is the highest percentage that can be examined. There is much less variation in the R^2 values for different percentages of the equilibrium concentration used to define the top of the initial slope, than in Figure 4.4, all are much closer to 1. However the best R^2 value, that does not include only a few data points, occurs when using 20% of the equilibrium concentration. The calculated diffusion coefficient continuously rises as the percentage taken drops, with the highest calculated coefficient corresponding with the fewest data points. As mentioned previously there is no 'correct' answer to compare the calculated values with, unlike the model simulation data, therefore R^2 must be used as a guide. For this data set a value of 20% would seem to be appropriate, which differs from that suggested by the 30_5000_2 trace.

The final trace that has been used to determine what percentage of the equilibrium concentration to use is 15_625_2 ($K = 3.18\times10^{-10}\mathrm{m}^2$, $u_* = 0.015\mathrm{m/s}$). Figure 4.6 again shows the percentage of the equilibrium concentration used to define the initial slope, the diffusion coefficients calculated from a best straight line fit to that data, and the R^2 value from the linear best fit line. Here the tests again did not reach equilibrium, only reaching 50% of the calculated equilibrium concentration. As with 20_1850_2 the R^2 values are high (above 0.9) between 50 and 10%, however here there is a significant decrease in the R^2 at lower percentages. This is because there are more data points in the lower percentages than the others, however not enough to reduce the effects of noise present within the data. The reduction in R^2 value coincides with a drop in calculated diffusion coefficient, which rises from $1.99\times10^{-9}\mathrm{m}^2/\mathrm{s}$ and 50% to $1.67\times10^{-8}\mathrm{m}^2/\mathrm{s}$ at 10%. The best R^2 value occurs when 30% of the equilibrium concentration is taken to define the initial slope. This is similar to the percentage for 20_1850_2 and the model simulation analysis

(Section 2.4.1).

It is interesting to note that for all three traces studied above the R^2 coefficient from the linear best fit is high (greater than 0.9) between 50 and 30% of the equilibrium concentration. 15_625_2 and 20_1850_2 also show a high R^2 value down to 10%. The best R^2 value coincided with taking 50, 20 and 30% for 30_5000_2, 20_1850_2 and 15_625_2 respectively. However there is a clear increase in the calculated coefficient with a lower percentage, and a lower percentage could be said to be more representative of an *initial* slope. The model simulation data suggested taking between 20 and 30% of the equilibrium concentration to define the initial slope. Given the analysis above and that previously on the model data, a value of 25% of the equilibrium concentration has been chosen to define the maximum value included in the initial slope.

Given the small (2.4ppb) difference between the highest and lowest calculated equilibrium concentrations, it has already been stated that a single uniform value has been assumed for the equilibrium concentration for all tests (23.1ppb). It is therefore possible to use a consistent 25% of this to define the initial slope of all the tests. In accumulated mass (M_w) this becomes 1.68×10^{-6}kg/m^2. The difference between 25% of the highest and lowest calculated equilibrium concentrations is 0.6ppb or 1×10^{-7}kg/m^2, which is about the same as the noise on the experimental data.

4.3.2 In-bed Data

The aspects needing further investigation for the Nagaoka and Ohgaki [1990] methodology, Section 2.4.2, are the goodness of fit parameter that should be used in the optimisation process (`corr2`, R_t^2 or APE) and whether a sampling interval, dt, of 10s is appropriate (as suggested by the model simulation data).

Test 20_1850_2 (Figure 4.1, $K = 2.06 \times 10^{-9}$m^2, $u_* = 0.020$m/s) was analysed using the three different goodness of fit parameters discussed in Section 2.4.2 (`corr2`, R_t^2 or APE) to optimise D_1. For this test, five fibre optic fluorometers were available, resulting in four profile pairs. Table 4.3 gives the diffusion coefficients obtained for each profile pair using the different goodness of fit parameters. The coefficient obtained between -0.117 and -0.151m is used in the analysis between -0.083 and -0.117m, and so on up to the final profile pair -0.015 and -0.049m.

R_t^2 and APE give almost identical diffusion coefficients for the lower two profile pairs, however `corr2` gives a much higher coefficient for the lowest pair (-0.117 to -0.151m). This then has a impact on the optimisation of the next pair (-0.083 to -0.117m), which is much lower than the other two goodness of fit parameters suggest, in order to compensate for the over large, D_2, coefficient below the pair.

Upper profile depth (m)	Lower profile depth (m)	D values for `corr2` (10^{-8}m^2/s)	D values for R_t^2 (10^{-8}m^2/s)	D values for APE (10^{-8}m^2/s)
−0.015	−0.049	22.3	38.5	160
−0.049	−0.083	7.12	12.1	73.3
−0.083	−0.117	0.36	1.02	0.90
−0.117	−0.151	15.4	0.23	0.23

Table 4.3: Comparison of different goodness of fit parameters with experimental data

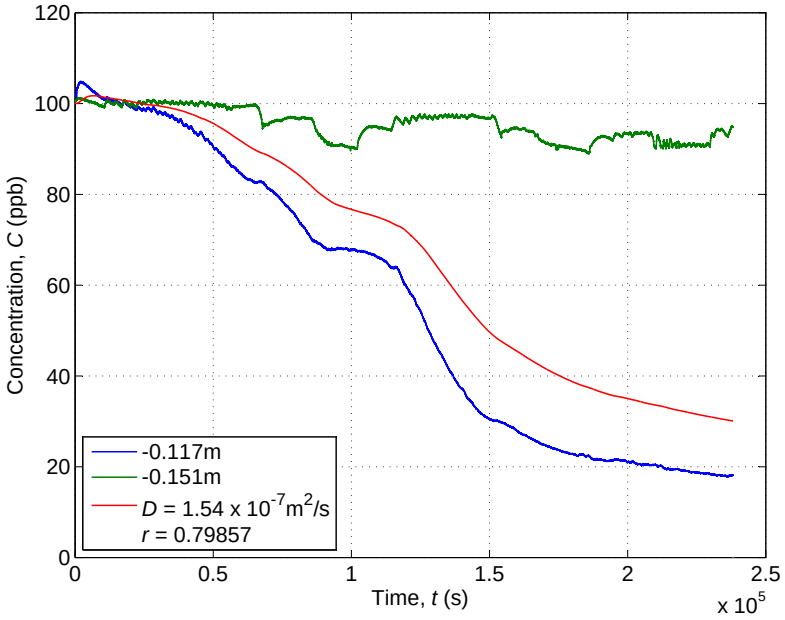

Figure 4.7: Example optimisation using `corr2` between −0.117 and −0.151m for 20_1850_2, showing the poor fit between the red (analysis) and the green (measured) profiles

The output plots for the lowest pair (−0.117 to −0.151m) for each of the goodness of fit parameters are given in Figures 4.7, 4.8 and 4.9. All represent the global maxima (or minima) for each goodness of fit parameter, and have been checked by applying a range of coefficients in the same manner as Figure 2.120 (Section 2.4.2). It is clearly visible that the output profiles from R_t^2 and APE match the experimental profile from −0.151m much better than `corr2`. This is because `corr2`, Equation (2.122), takes more account of the relative shape of the profiles than the absolute value (or difference in value) between the two profiles. This results in the fluctuations, caused by temperature changes during the test, affecting the `corr2` optimisation. Which results in the best `corr2` value giving a coefficient much higher than realistically

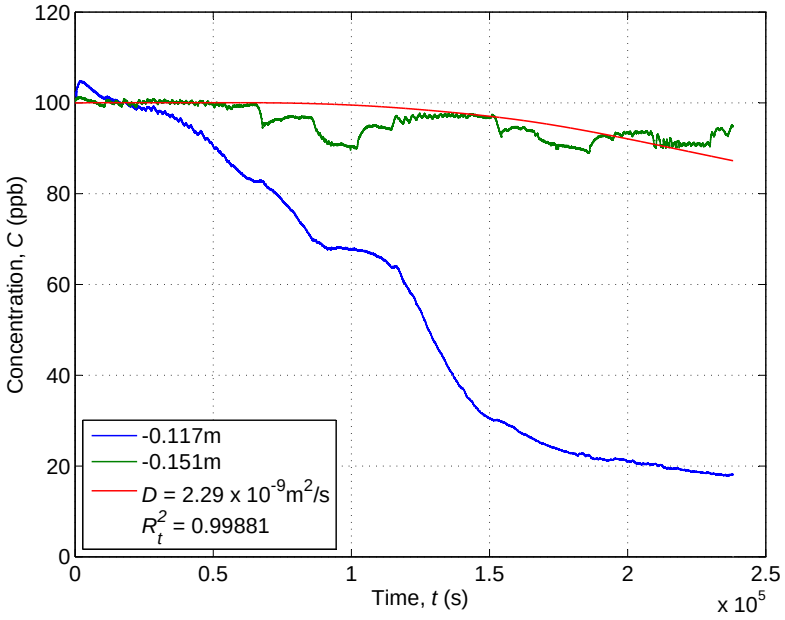

Figure 4.8: Example optimisation using R_t^2 between -0.117 and -0.151 for 20_1850_2, showing the good fit between the red (analysis) and the green (measured) profiles

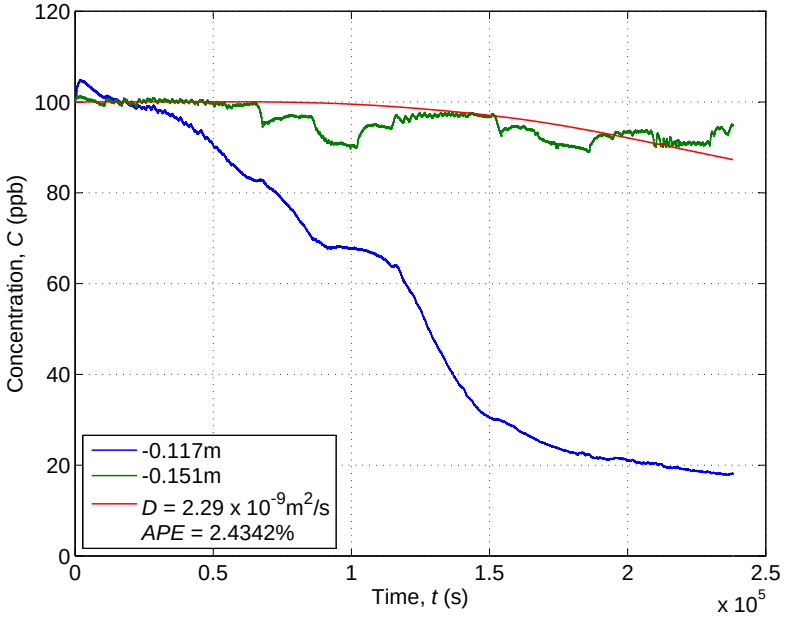

Figure 4.9: Example optimisation using APE between -0.117 and -0.151 for 20_1850_2, showing the good fit between the red (analysis) and the green (measured) profiles

possible, given the coefficients obtained closer to the interface, those obtained using R_t^2 and APE and the water column data derived coefficient of $1.86 \times 10^{-7}\mathrm{m}^2/\mathrm{s}$.

The problem that an unrealistically high diffusion coefficient from the first profile pair (or a 'wrong' coefficient from any of the optimisations except the last) can be seen in the `corr2` optimisation between -0.083 and -0.117m. As stated above, the coefficient is significantly lower than that obtained using R_t^2 or APE. The effect of this poor optimisation at the start of the process influences the optimisation of all of the other profile pairs.

The problems demonstrated here with `corr2` finding unrealistic coefficients has been seen in other optimisations using `corr2`, so it has been ruled out as a possible goodness of fit parameter for use in the optimisation process. This leaves R_t^2 or APE, which start to deviate in their output for the profile pairs closer to the sediment water interface. APE gives slightly higher coefficients than R_t^2 between -0.049 and -0.083m, but then much higher (almost by an order of magnitude) for the highest profile pair (-0.015 to -0.049m). In both these cases the output plots from the APE optimisation show that the calculated profiles are very close to the upper profile used in their calculation, like that shown in Figure 4.7 for `corr2`. The R_t^2 analysis profiles are much closer to the lower profile, which the analysis is trying to match. This, along with the fact that the coefficient obtained for the highest pair using APE is an order of magnitude higher than the water column derived interface coefficient, suggests that R_t^2 is the most appropriate goodness of fit parameter to use in the analysis of the in-bed data. All further in-bed analysis presented was conducted using R_t^2 as the goodness of fit parameter optimised during the analysis.

From the analysis of model simulation data (Section 2.4.2) a sampling interval, dt, of 10s was decided. However, there are many experimental tests that ran for much longer times than the current model simulations and are expected to have much lower diffusion coefficients, supported by the water column data analysis. The importance of the sampling interval is to insure that there are enough points to describe the shape of the profile adequately for analysis. It is therefore plausible that for a longer, lower exchange test, a larger sampling interval (greater than 10s) will still allow for an adequate number of points to describe the profile. The number of data points within a profile has a direct impact on the length of time it takes to analyse the data.

The results of test 15_625_2 ($K = 3.18 \times 10^{-10}\mathrm{m}^2$, $u_* = 0.015\mathrm{m/s}$), shown in Figure 4.10, was chosen as representative of a long, slow exchange test. The water column data gave an interface coefficient of $9.57 \times 10^{-9}\mathrm{m}^2/\mathrm{s}$ and the test ran for 7.65 days (183.6hrs). Figure 4.10 shows the effect temperature fluctuations have on the

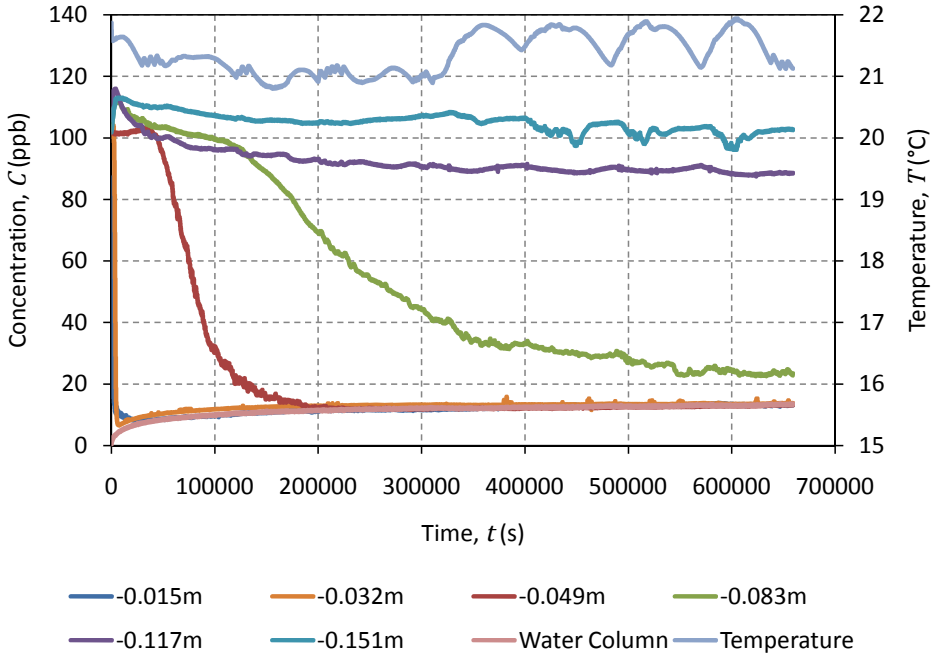

Figure 4.10: Test 15_625_2 used to evaluate the effect dt has on optimisation ($K = 3.18 \times 10^{-10}\text{m}^2$, $u_* = 0.015\text{m/s}$)

fibre optic fluorometer data, and that there is a problem with the lowest instrument (-0.151m). The concentration rises and remains high during the entire trace, which could have been caused by a poor calibration (although the trace starts at 100ppb) or a malfunction with either the laser or photo multiplier (PMT). The trace from -0.151m has therefore been excluded from the analysis detailed below.

Table 4.4 gives the diffusion coefficients obtained from analysing 15_625_2 with a sampling interval of 10s. These values have been used to normalise the diffusion coefficients obtained using a sampling intervals of 50, 100, 200, 500 and 1000s. The normalised coefficients are plotted against the sampling interval in Figure 4.11. There is very little difference between the sampling intervals except when analysing the highest profile pair (-0.015 to -0.032m). Here much lower coefficients are obtained with a larger sampling interval.

Upper profile depth (m)	Lower profile depth (m)	$D_{dt=10s}$ (10^{-8}m^2/s)
−0.015	−0.032	10.5
−0.032	−0.049	0.881
−0.049	−0.083	0.516
−0.083	−0.117	0.103

Table 4.4: Diffusion coefficients obtained from 15_625_2 using a sampling interval, dt, of 10s

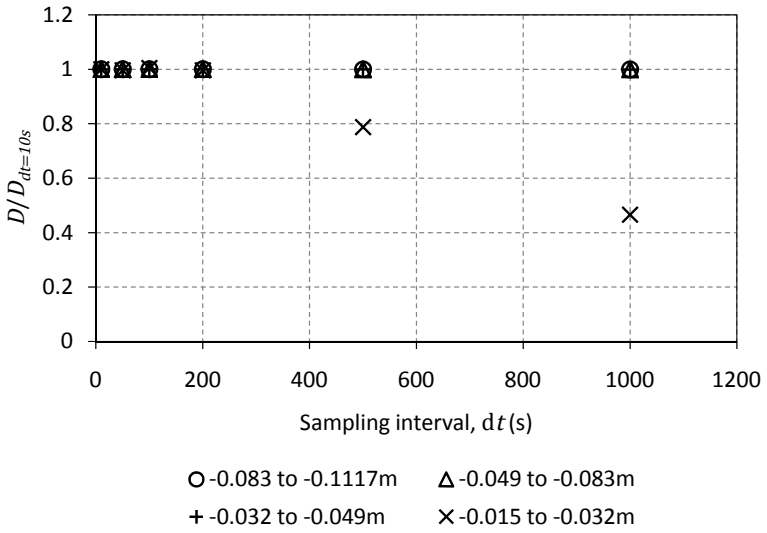

Figure 4.11: Effect of sampling interval, dt, on Nagaoka and Ohgaki [1990] analysis of experimental data

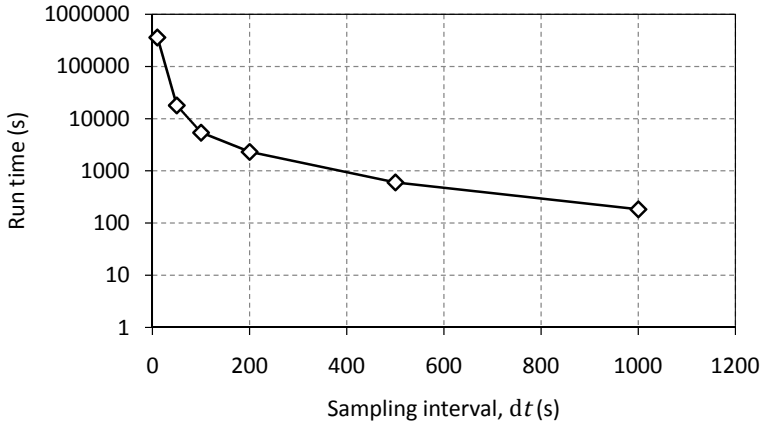

Figure 4.12: Effect of sampling interval, dt, on computational time required for analysis of all profiles in a single test

Figure 4.12 shows the increase in run time of the analysis code with a reduction in dt. All the analysis was conducted on the same machine, running the same code, with no other programs running. With a dt of 10s the run time is 4 days (100hrs), over half the time the experiment took. Whereas increasing dt to 200s reduces the run time to 39 minutes. Taking into account the variability between tests and the advantages even a small increase in dt has on the run time a sampling interval of 50s was used for the longer, lower exchange tests (15_625_1, 15_625_2, 10_625_1, 10_625_2, 15_350_1, 10_350_1, 10_150_1), and dt of 10s used for the rest.

4.4 Water Column Data

The water column data has been analysed using the O'Connor and Harvey [2008] methodology (Section 2.4.1). From the evaluation conducted above (Section 4.3.1) and on the model simulation data (Section 2.4.1) 25% of the equilibrium concentration (1.68×10^{-6}kg/m^2) was used to define the initial slope of the concentration profile used in (2.100). Figures 4.13, 4.14 and 4.15 show the output from the water column data analysis for the tests used above (30_5000_2, 20_1850_2 and 15_625_2 respectively). The experimental data is shown in blue and the straight red line is the linear best fit line for the initial slope.

The test with a high bed shear velocity and large sediment diameter (Figure 4.13, 30_5000_2) reached equilibrium conditions by the end of the test, indicated by the flattening of the last portion of the profile. There is also more noise at the start of the test than the slower velocity, finer sediment tests. This is probably due to the rapid mixing that is occurring. There is a slight lag between the start of the test and the first arrival of tracer at the instrument position. This is not as significant as it appears on the plots because the x-axis is the square root of time ($t^{1/2}$) so the profile appears stretched, with greater spacing between points at the start than the end. The delay is actually only 35s, rising to 100s in 15_625_2 (Figure 4.15), which is insignificant given the length of time included in the initial slope. The delay shows that the water column is not instantaneously well-mixed, but that the time scale for mixing within the water column is very quick compared to the change in concentration caused by hyporheic exchange.

Figure 4.14, shows the results from test 20_1850_2. The measured data have a different overall shape than Figure 4.13. The trace does not reach equilibrium, however the profile flattened out significantly towards the end of the test, indicating that the mixing coefficient at the depth the exchange has reached is significantly lower than that at the surface.

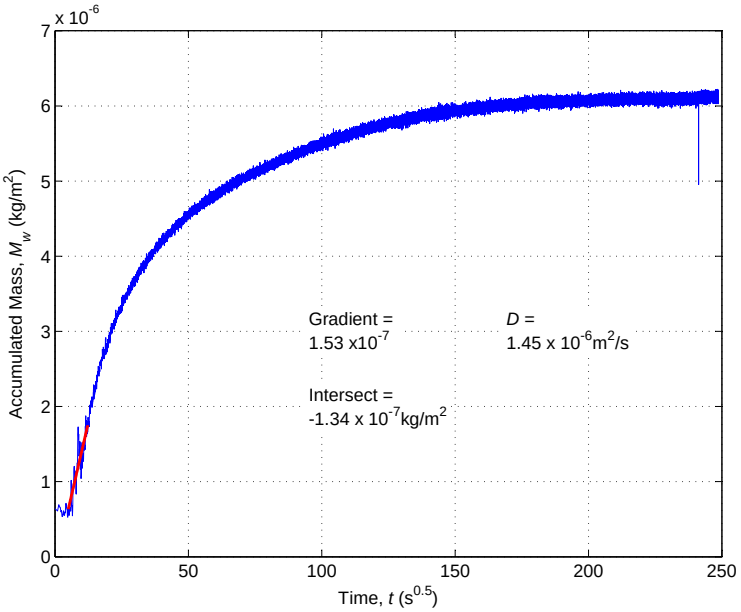

Figure 4.13: Water column data analysis of 30_5000_2 ($K = 1.02 \times 10^{-8}\text{m}^2$, $u_* = 0.030\text{m/s}$), red line showing the linear best fit line used to obtain the gradient of the initial slope

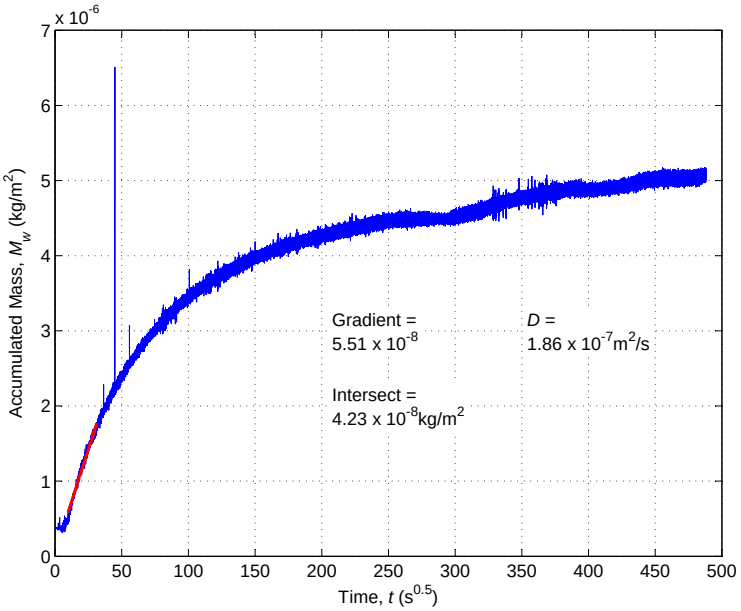

Figure 4.14: Water column data analysis of 20_1850_2 ($K = 2.06 \times 10^{-9}\text{m}^2$, $u_* = 0.020\text{m/s}$), red line showing the linear best fit line used to obtain the gradient of the initial slope

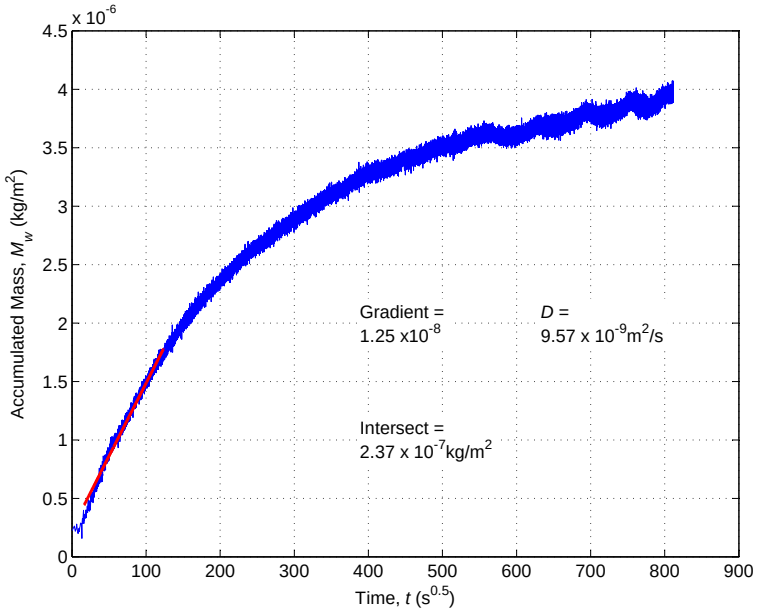

Figure 4.15: Water column data analysis of 15_625_2 ($K = 3.18 \times 10^{-10}$m^2, $u_* = 0.015$m/s), red line showing the linear best fit line used to obtain the gradient of the initial slope

The final example water column analysis, Figure 4.15 (15_625_2), is indicative of the tests with a low bed shear velocity and small sediment diameter. The increase in concentration is much slower, indicated by the lower gradient obtained for the initial slope.

The hyporheic exchange coefficients obtained from all the water column data are presented in Figure 4.16. The coefficients are non-dimensionalised using molecular diffusion and plotted against $Re_* Pe_K^{6/5}$, the same axis used by O'Connor and Harvey [2008], Figure 2.9. The different sediment diameters are given by the marker colour and the different bed shear velocities by the shape. The repeatability between tests is clear in Figure 4.16. There is some variation in the x-axis between repeats, caused by slight variations in the permeability (probably due to slight differences in the packing of the glass spheres) and the propeller speed (from which the bed shear velocity is inferred). The variation on the y-axis is also small for repeat tests, with most repeats lying on top of each other (e.g. 30_5000, 20_1850 and 15_1850).

The repeatability of the erosimeter tests is much better than that shown in previous experimental studies used by O'Connor and Harvey [2008] (Figure 2.9). Repeat tests (in the O'Connor and Harvey [2008] data) are indicated by the same (or very similar) position on the x-axis. The erosimeter water column coefficients lie

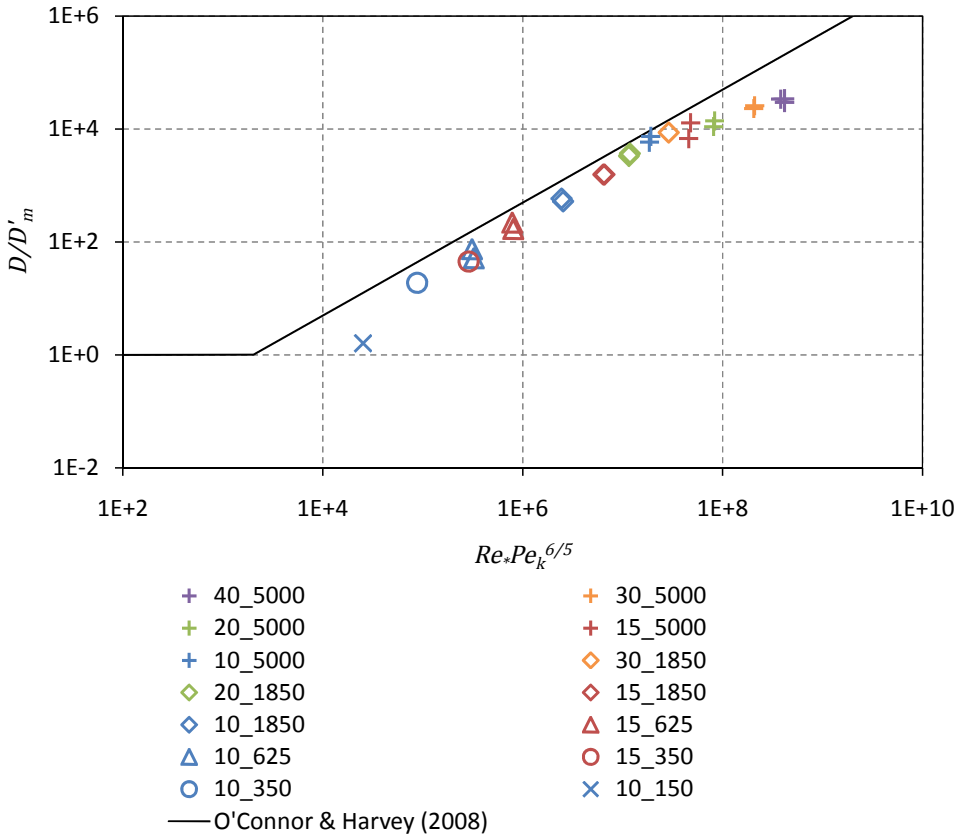

Figure 4.16: Comparison of water column coefficients against previous experimental data through O'Connor and Harvey [2008] scaling relationship

within the scatter of the previous experimental data, however they are consistently lower than the scaling relationship. This is most pronounced at the extremes, where either a large diameter sediment and a high bed shear velocity or a small diameter and a low bed shear velocities have been used (40_5000 or 10_150). Possible reasons for this and the consistently lower coefficients than the scaling relationship would suggest are considered in the Chapter 5.

4.5 In-bed Data

The in-bed data has been analysed using the Nagaoka and Ohgaki [1990] method, described in Section 2.4.2. The method allows the diffusion coefficient between two profiles to be obtained. The previous evaluation work on the model simulation data (Section 2.4.2) and some experimental data above (Section 4.3.2) has provided a consistent methodology that can be used to analyse all the in-bed experimental

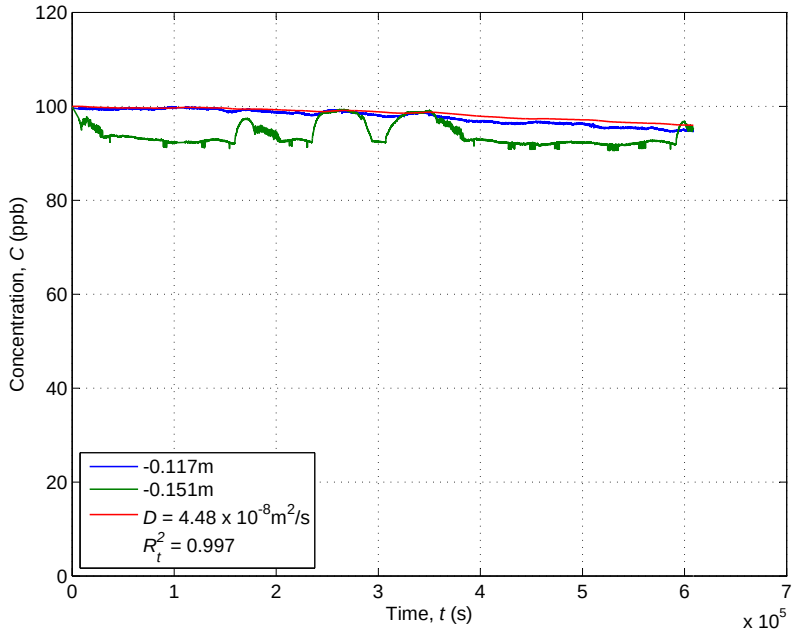

Figure 4.17: Example of inaccurate optimisation due to test length which resulted in little or no concentration change in lower regions of the bed (15_350_1, −0.117 to −0.151m), green and blue are measured profiles and red is the analysis profile generated with the diffusion coefficient specified in the legend

data.

However, during analysis there were various challenges encountered, which ultimately reduced the number of profile pairs that could be analysed successfully. The first problem involved the initial tests within the experimental series. The experimental setup, particularly the removal of the cling film separator caused the instrument closest to the bed to give erroneous profiles. The concentration would drop immediately (sometimes to negative values) or would be very noisy. The tests most affected were the shorter, high bed shear and permeability tests. It is possible that this parameter combination was also a factor. However, repeat tests, conducted later in the test program, did not show the same problems, so setup was the most likely cause of the unreliable data.

The second challenge was the length of run time for some tests. This affected the low bed shear velocity and low permeability tests. Here the tests were not run to equilibrium conditions, as stated in the raw data and water column data analysis sections, 4.2 and 4.4, which meant that some instruments further from the interface saw no significant change in concentration during the test. This presents a problem when optimising a calculated profile to the measured profile because there

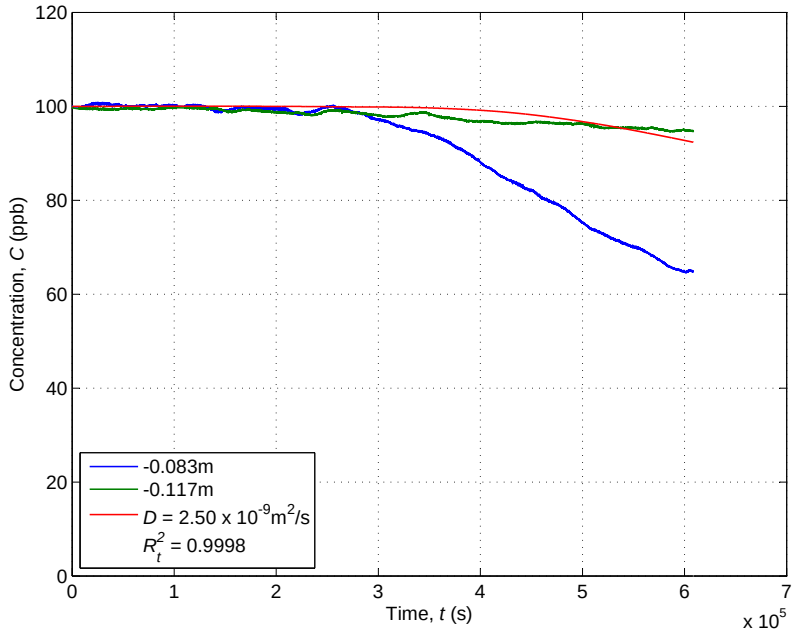

Figure 4.18: Example of inaccurate optimisation due to test length which resulted in little or no concentration change in the measured profile being optimised to in the analysis (15_350_1, −0.083 to −0.117m), green and blue are measured profiles and red is the analysis profile generated with the diffusion coefficient specified in the legend

was no change to fit to. Figure 4.17 shows the output from analysing the lowest pair of profiles from 15_350_1 ($K = 1.69 \times 10^{-10}\text{m}^2$, $u_* = 0.015\text{m/s}$). The trace from −0.151m has been affected much more by the temperature changes during the test than the data from −0.117m. However, neither show a significant change in concentration (overall) during the test. This results in a very high coefficient, $4.48 \times 10^{-8}\text{m}^2/\text{s}$, which is 18 times larger than the interface coefficient obtained from the water column data ($2.53 \times 10^{-9}\text{m}^2/\text{s}$) and much higher than coefficients obtained from profile pairs nearer the interface. Any coefficient will give a reasonable approximation to the measured profiles, so profiles like this where no significant change occurs cannot be used in the analysis.

Figure 4.18 shows the analysis output from the next profile pair up (−0.083 to −0.117m) from 15_350_1. The analysis was conducted with equation (2.120), because the coefficient from the lower profile pair cannot be used, so the assumption has to be made that the coefficient between these two profiles is the same as below them. As stated above there is no significant change in the profile from −0.117m. The optimisation process has produced a coefficient of $2.50 \times 10^{-9}\text{m}^2/\text{s}$, which is

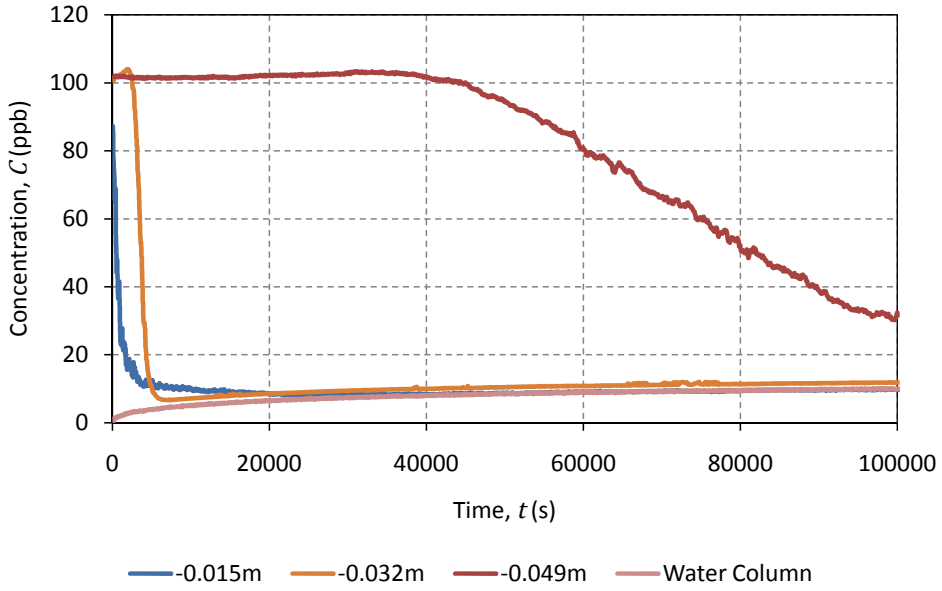

Figure 4.19: First 1×10^5s of 15_625_2 for the three instruments closest to the interface showing the different shape of the concentration profile from -0.032m

equal to the interface coefficient and higher than coefficients obtained from profile pairs closer to the interface. The optimisation is fitting to the slight, steady drop in concentration (5ppb) throughout the test. This could have been caused by molecular diffusion or, perhaps, sorption of the tracer to the sediment or erosimeter. If there is no significant change in the profile due to mixing processes a diffusion coefficient cannot be obtained. This phenomenon affected the low permeability and low bed shear velocity tests and reduced the number of coefficients that could be obtained from the experimental data.

The third and unexpected challenge was the difference in profiles obtained when a fibre optic fluorometer was inserted at -0.032m below the interface, but on the opposite side of the erosimeter to all the other instruments. These profiles, generally dropped much quicker than the profiles either side (-0.015 and -0.049m) and often rebounded to follow the water column profile quicker than the -0.015m profile which was closer to the interface, shown in Figure 4.19, which is a closeup taken from Figure 4.10. The coefficients obtained between -0.015 and -0.032m were generally two orders of magnitude higher than the water column data derived coefficient, so have been excluded from the plots below. This can be seen in Table 4.4, where the profile from -0.032m was included. The coefficients between -0.032 and -0.049m have been included, but separate to the main series that uses the coefficient between -0.015 and -0.049m, which is the same as the tests without the

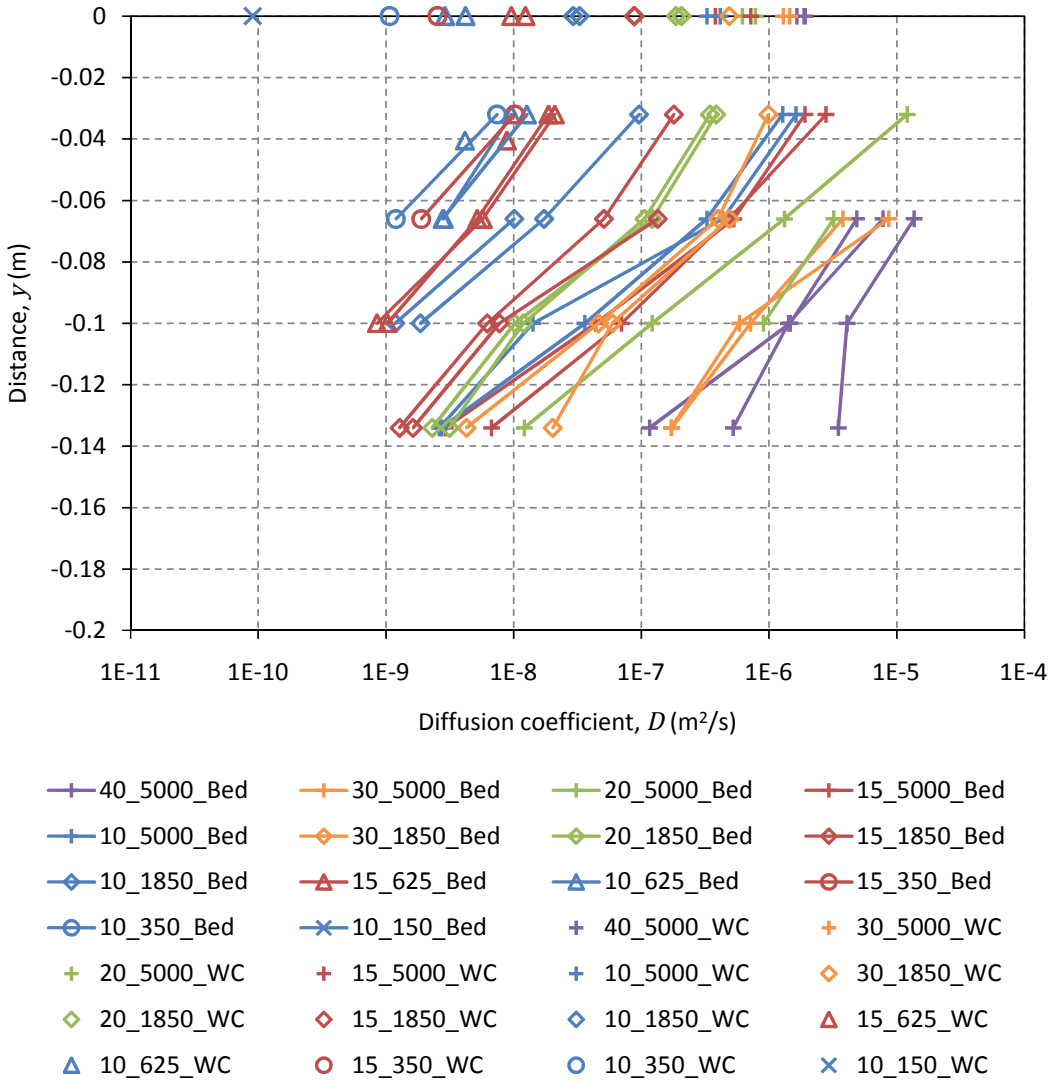

Figure 4.20: All diffusion coefficients obtained from the experimental data plotted against the mid-point between the two profiles used

instrument at -0.032m. There is more discussion on the difference in the profiles in Section 5.2.2.

Figure 4.20 shows all the diffusion coefficients obtained from the in-bed and water column data, plotted (for the in-bed data) at the mid-point between the two profiles used to obtain that coefficient. Within the figure there is good correlation between repeat tests and there is a clear variation of the diffusion coefficient with depth below the interface, also with permeability (sediment diameter) and bed shear velocity. The variation in diffusion coefficient with permeability, bed shear velocity

and other experimental parameters are discussed in more detail in the next sections. A full table of results and experimental parameters is given in Appendix D. The table also shows which tests were affected by the problems described above.

There is more variation in the high permeability, high bed shear velocity experiments (on the right hand side of Figure 4.20), which is probably due to the higher coefficients and the slight variability in setup during these initial experiments. The most striking feature is the difference in the water column data derived coefficients and those obtained from the profile pair closest to the interface. There is between half and almost one order of magnitude difference between them. Possible reasons for this are considered in Section 5.2.1.

4.5.1 Effects of Bed Shear Velocity

This section takes the data presented in Figure 4.20 and presents it according to sediment diameter so the effect of bed shear velocity (u_*) can be seen. Figures 4.21, 4.22 and 4.23 show the results from tests with different bed shear velocities, but the same sediment diameter. Within all three there is a clear relationship between the magnitude of the diffusion coefficient and the bed shear velocity. This is most clearly demonstrated with the 1.85mm diameter sediment (Figure 4.22).

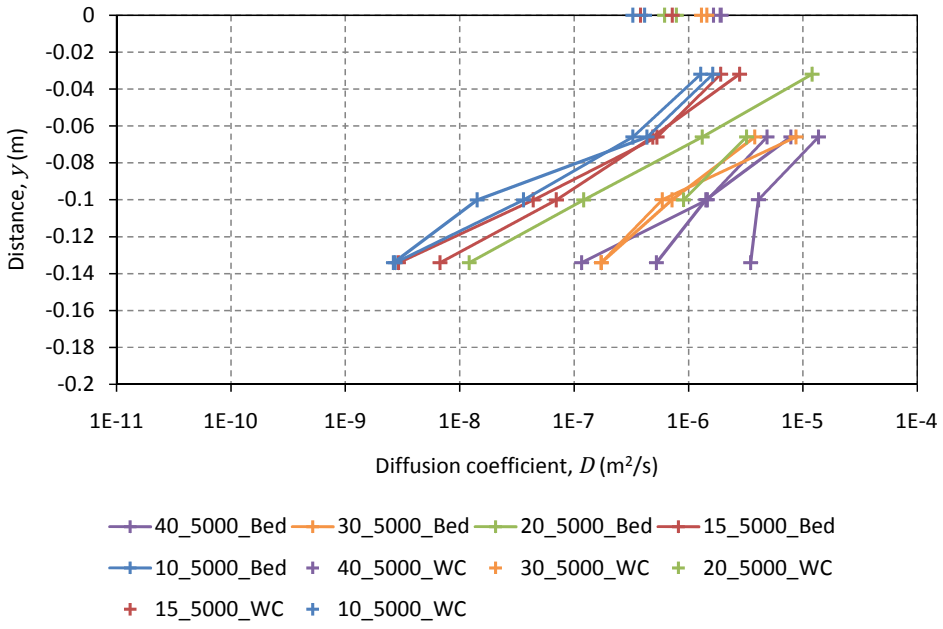

Figure 4.21: Diffusion coefficients obtained from 5mm diameter sediment tests with different bed shear velocities

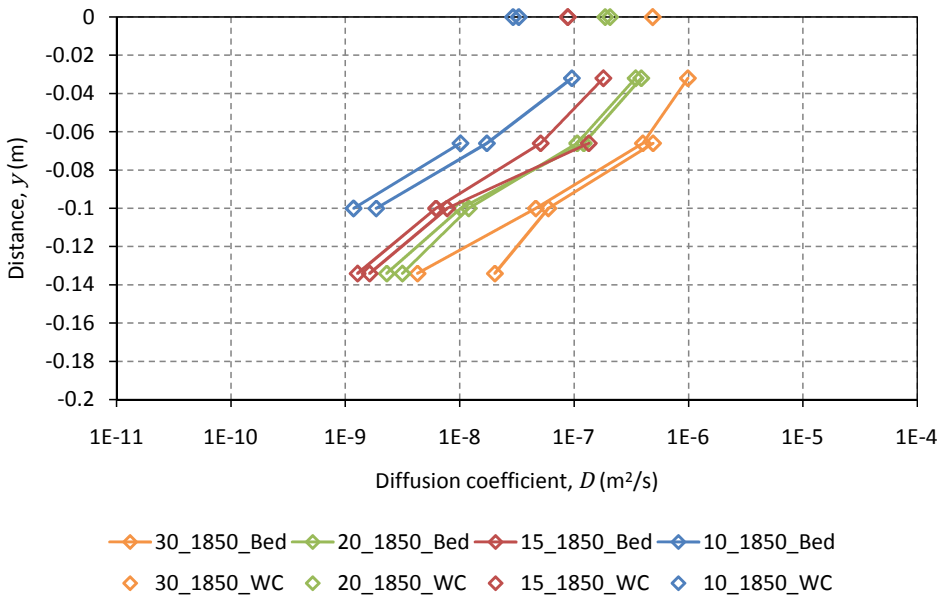

Figure 4.22: Diffusion coefficients obtained from 1.85mm diameter sediment tests with different bed shear velocities

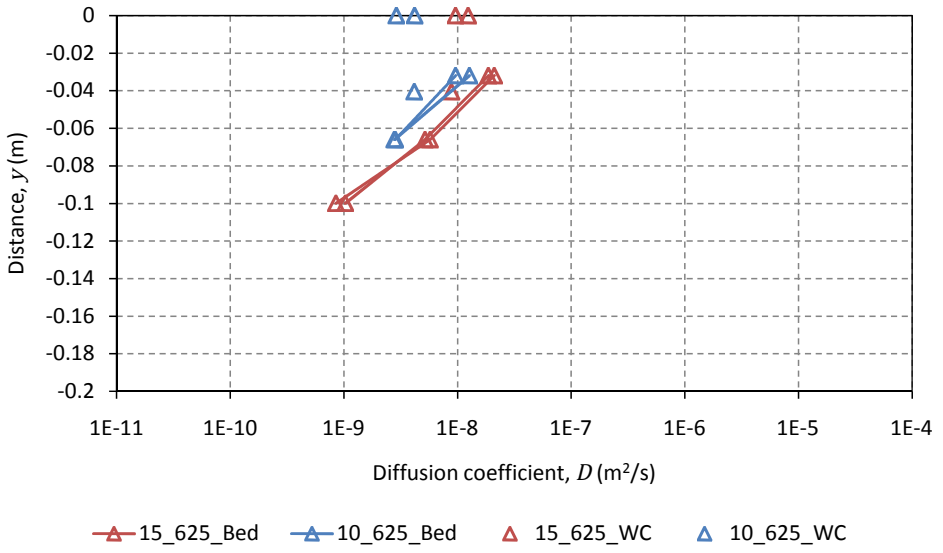

Figure 4.23: Diffusion coefficients obtained from 0.625mm diameter sediment tests with different bed shear velocities

Figure 4.24 shows all the diffusion coefficients plotted against bed shear velocity for each depth below the sediment water interface. This is similar to Figure 1(b) in O'Connor and Harvey [2008]. There is a general trend as the bed shear velocity increases so does the diffusion coefficient. The relationship between bed shear

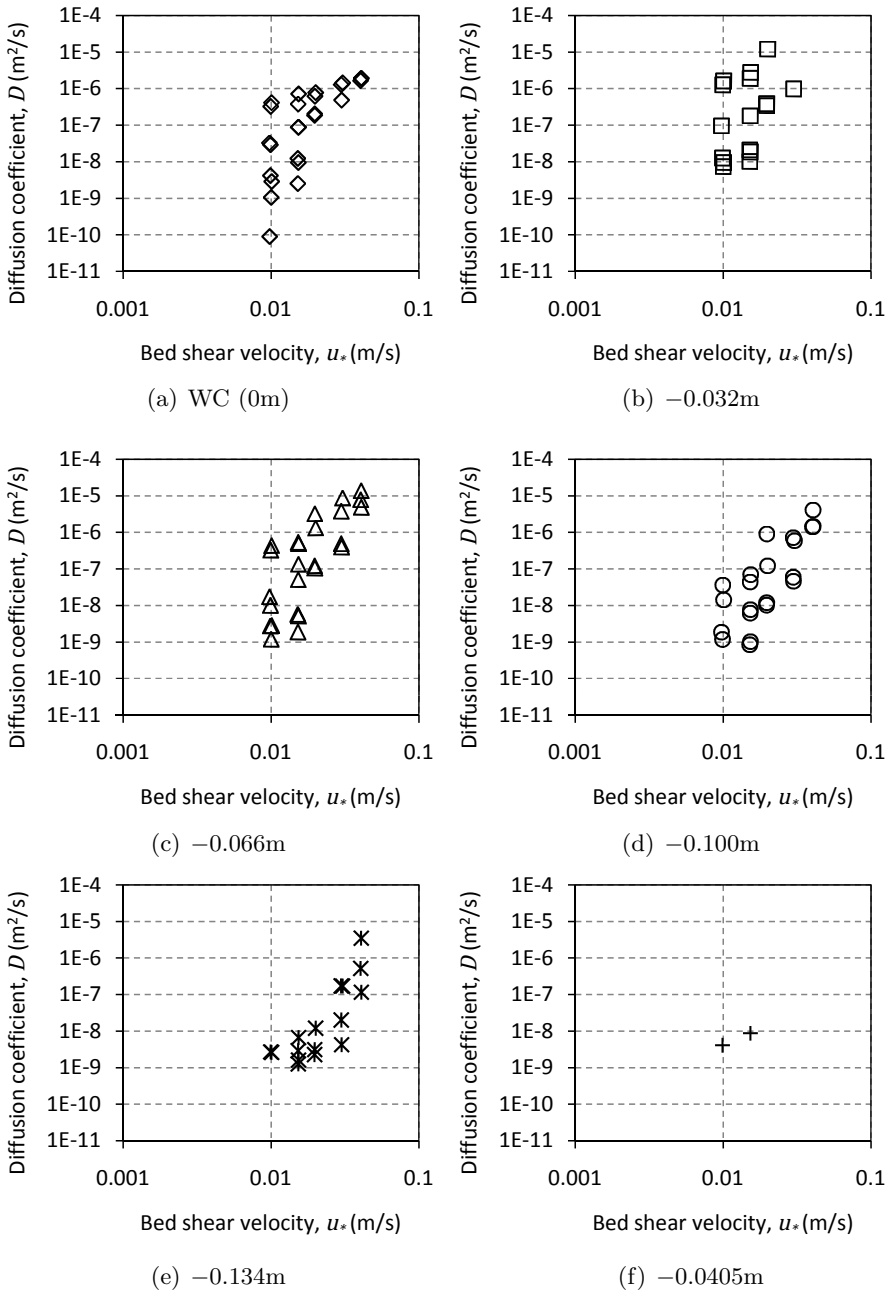

(a) WC (0m) (b) −0.032m

(c) −0.066m (d) −0.100m

(e) −0.134m (f) −0.0405m

Figure 4.24: Comparison of diffusion coefficients against bed shear velocity (u_*) from the water column (WC) and different depths below the sediment water interface

velocity and diffusion coefficient is not as clear as it is in O'Connor and Harvey [2008] because the range of velocities is much smaller in this study, covering less than half an order of magnitude (0.01 to 0.04m/s) instead of almost two. The effect of the other test parameters is clear at each depth below the interface, particularly

the sediment diameter (permeability). In Figure 4.24(c) four distinct groups are visible, each with the same gradient. These correspond to four of the five different sediment diameters (0.350, 0.625, 1.85 and 5.00mm).

Figure 4.25 gives a comparison between the variation in diffusion coefficient with depth and mean surface flow velocity found by Nagaoka and Ohgaki [1990] and the variation in diffusion coefficient with depth and bed shear velocity found from this study. There are significant differences between the two studies, particulary in the sediment diameters used. Nagaoka and Ohgaki [1990] used 40.8 and 19mm glass spheres, whereas the data presented in Figure 4.25(b) is for 1.85mm spheres. If the crude approximation that bed shear velocity is a tenth of the mean surface velocity (Section 2.2.2) is made, then the bed shear velocities of the two studies cover a similar range, between 0.01 and 0.04m/s. Therefore to allow an easier comparison a bed shear velocity of 0.01m/s is equivalent to a mean surface flow velocity of 10cm/s, and a diffusion coefficient of $1 \times 10^{-4}\mathrm{m}^2/\mathrm{s}$ is equal to $1\mathrm{cm}^2/\mathrm{s}$.

Because the sediment diameters are over an order of magnitude different, which will result in a large difference in permeability, the diffusion coefficients from this study are much smaller than those obtained by Nagaoka and Ohgaki [1990]. However, the same general trend with depth is visible in both data sets. The labels K1 to K4 in Figure 4.25(a) refer to the number of particle diameters below the interface the lower of the two profiles used to obtain the coefficient was. K1 uses an instrument at the surface and one particle diameter down, whereas K3 uses instruments two and three diameters below the interface. Therefore the maximum absolute depth below the interface studied by Nagaoka and Ohgaki [1990], if the mid-point between the profiles is used as in this study, was -0.1428m below the interface. This distance is comparable to this study, but the depth relative to the grain diameters used is much greater in this study.

It is interesting to note that by increasing the number of grain diameters, the relationship with depth has become clearer. There is more scatter in the Nagaoka and Ohgaki [1990] data. The relationship shown in Figure 4.25(b) is repeated for the other sediment diameters used. Figure 4.25(b) also shows what was not clear from Figure 4.24, which is the variation in depth and bed shear velocity. However by removing the influence of permeability (by choosing only one sediment diameter instead of showing all as in Figure 4.24) it demonstrates that bed shear velocity alone cannot describe the variation in diffusion coefficients.

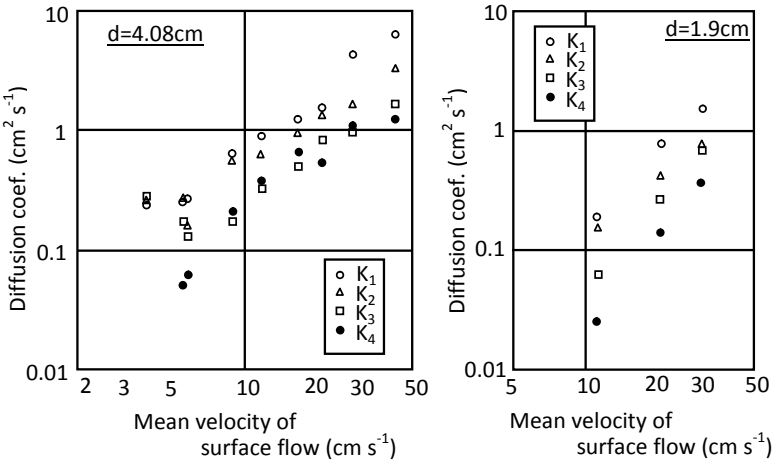

(a) Figure 12 from Nagaoka and Ohgaki [1990], where K refers to the number of grain diameters below the sediment water interface

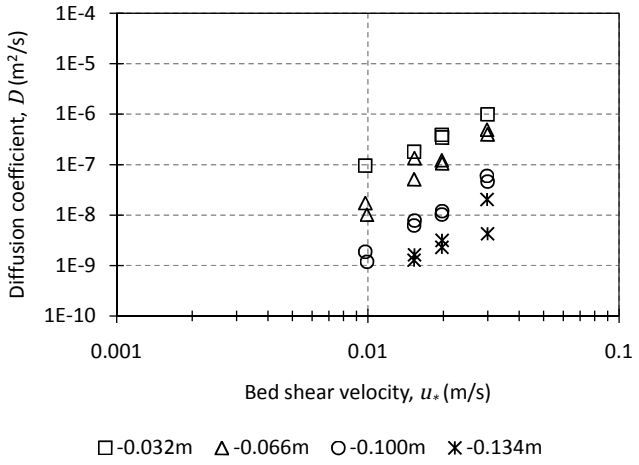

(b) $d_g = 1.85$mm (This study)

Figure 4.25: Comparison of experimental diffusion coefficients (this study) and Nagaoka and Ohgaki [1990] diffusion coefficients against mean or bed shear velocity

4.5.2 Effects of Permeability

Like the previous section the data presented below is the same as that given in Figure 4.20, however grouped according to bed shear velocity so the effect of sediment diameter, and through this permeability (K), can be seen. Figures 4.26, 4.27 and 4.28 show the variation that changing the permeability has for a given bed shear velocity. The effect is most clearly demonstrated in Figure 4.27. It also shows the greater influence of particle diameter on the magnitude of the diffusion coefficient compared with bed shear velocity. This is seen in the greater distance between dif-

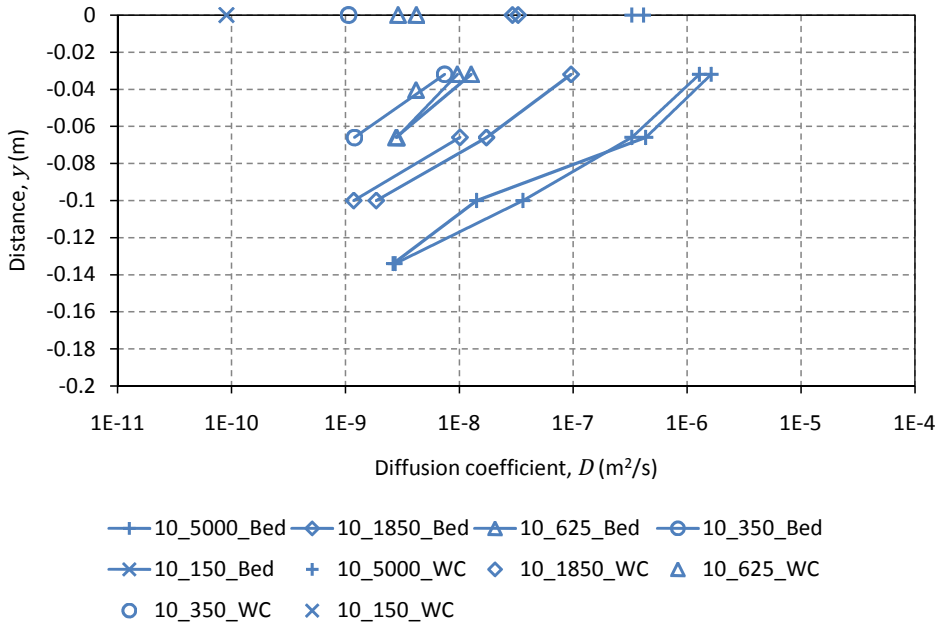

Figure 4.26: Diffusion coefficients obtained from 0.01m/s bed shear velocity tests with different sediment diameters

ferent sediment diameter tests than the different bed shear velocities in Figures 4.21, 4.22 and 4.23.

Figure 4.29 also supports the greater influence of permeability than bed shear velocity in this study. It shows a much stronger relationship between permeability and diffusion coefficient than that shown in Figure 4.24 for bed shear velocity. This may be because the range of permeabilities is much greater than bed shear velocities in this series of tests. However Figure 1(d) in O'Connor and Harvey [2008] also shows a stronger relationship between permeability and diffusion coefficient than bed shear velocity. The influence of bed shear velocity is not as visible in Figure 4.29 as the influence of permeability was in Figure 4.24. The plot where the influence of bed shear velocity is clearest is Figure 4.29(d) at 1×10^{-8}m^2 (5mm diameter), where the five bed shear velocities can be identified.

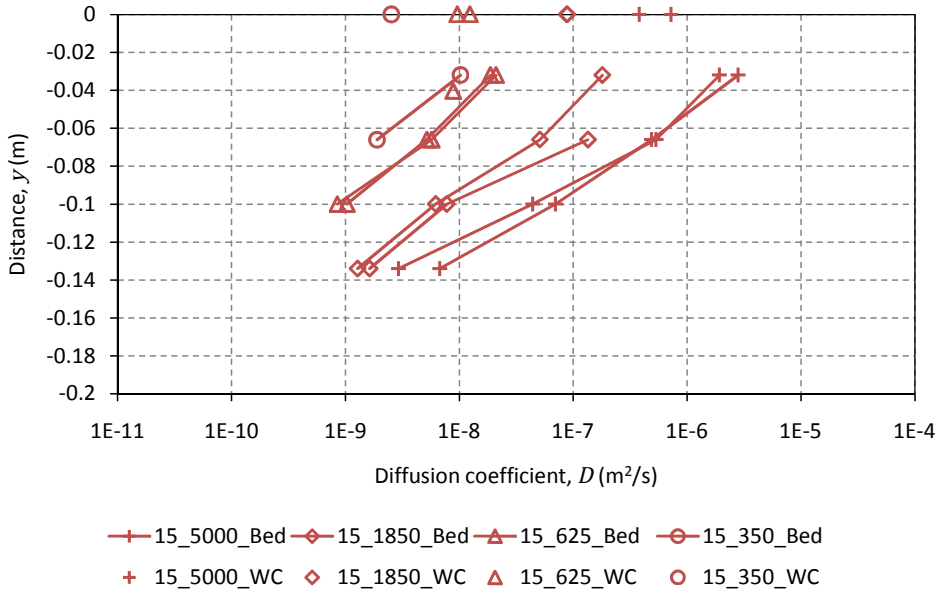

Figure 4.27: Diffusion coefficients obtained from 0.015m/s bed shear velocity tests with different sediment diameters

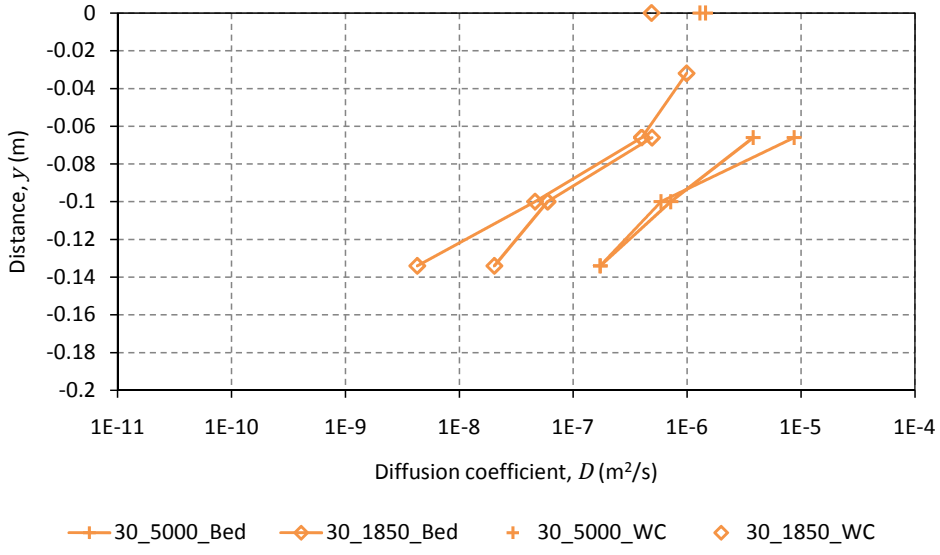

Figure 4.28: Diffusion coefficients obtained from 0.03m/s bed shear velocity tests with different sediment diameters

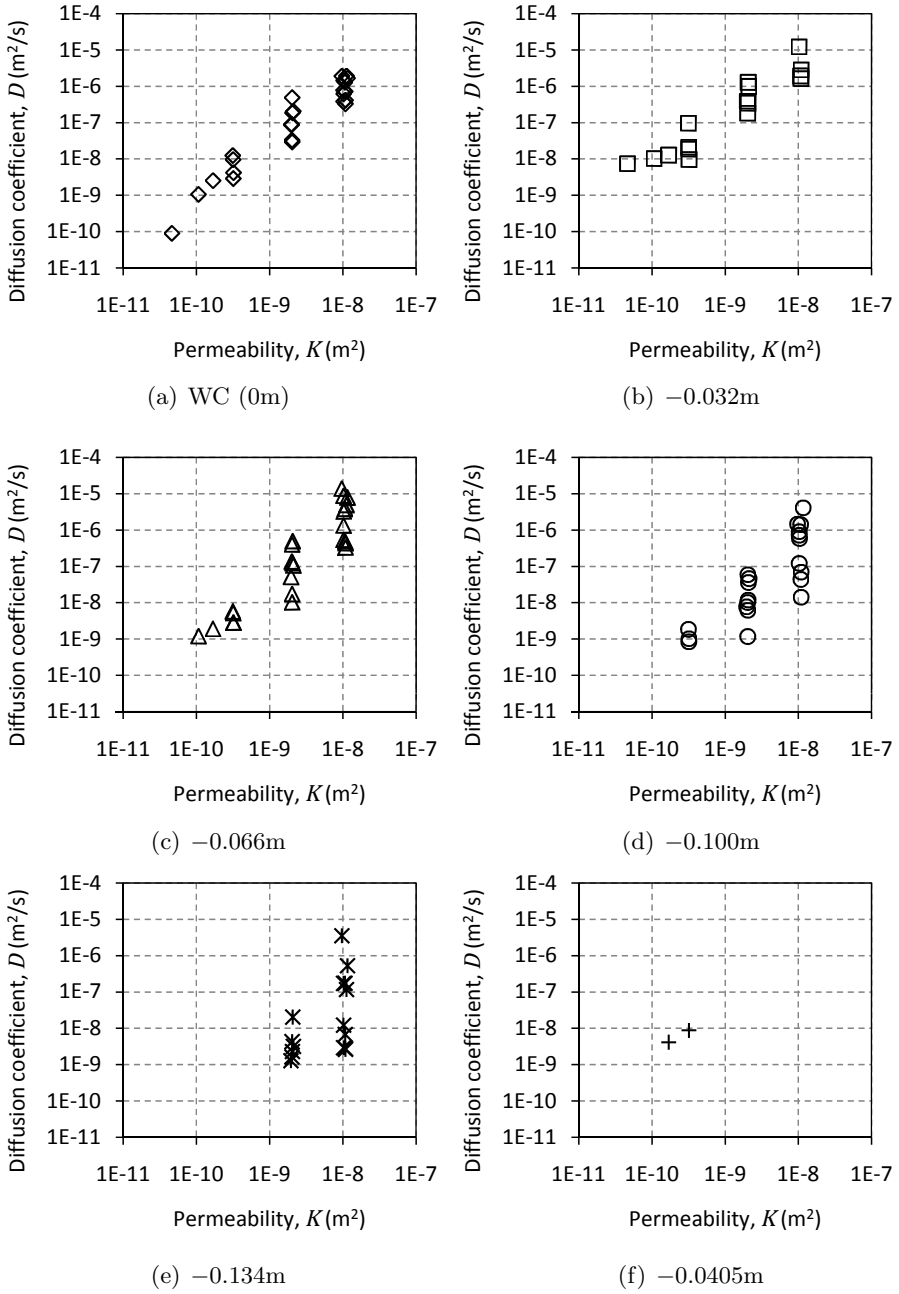

(a) WC (0m)

(b) −0.032m

(c) −0.066m

(d) −0.100m

(e) −0.134m

(f) −0.0405m

Figure 4.29: Comparison of diffusion coefficients against measured bed permeability (K)

4.5.3 Effects of Other Experimental Parameters

The experimental data presented in Figure 4.20 has been compared with other experimental parameters in a similar manner to Figures 4.24 and 4.29. These parameters are the mean particle diameter (d_g) and the roughness height (k_s). Both these parameters show the same trend as that between permeability and diffusion coefficient (Figure 4.29), which is expected. Both the permeability and the roughness height are a function of the sediment diameter, given the lack of bed-forms to affect the roughness height and the consistent porosity of glass sphere sediments (Table 3.9). Both these parameters are used in the O'Connor and Harvey [2008] scaling relationship (2.51), and have been shown by other studies to influence hyporheic exchange.

4.5.4 Dimensionless Groups

O'Connor and Harvey [2008] and others have demonstrated that relationships exist between several dimensionless groups and effective diffusion coefficients. The groups identified by O'Connor and Harvey [2008], and discussed in Section 2.3.3, were the Chézy resistance coefficient (C_z), shear Reynolds number (Re_*) and permeability based Péclet number (Pe_K). Of these, Re_* and Pe_K showed the strongest correlations, forming the basis for the scaling relationship, (2.51), proposed by O'Connor and Harvey [2008]. Figures 4.30 and 4.31 show all the diffusion coefficients obtained from the experimental data plotted against Re_* and Pe_K respectively.

There is a strong relationship shown in both figures, which is expected given the strong relationships shown in Figures 4.24 and 4.29 between diffusion coefficient and bed shear velocity or permeability respectively. There is a clear distinction with depth below the sediment water interface in both figures. The coefficients from each depth display a similar gradient but with lower values further below the interface.

A third dimensionless group, the number of sediment grain diameters below the interface (y/d_g), is compared with the diffusion coefficients. In Figure 4.32 the water column data derived coefficients are plotted at $y/d_g = 1$ and are only included for completeness. There is a general trend within Figure 4.32, however it is not as strong as that seen in Figures 4.30 and 4.31. There is no clear pattern between the change in diffusion coefficient and the number of grain diameters below the interface, the general reduction in diffusion coefficient with increased number of diameters is evident, but the relationship is not as clear as simply depth below the interface shown in Figure 4.20.

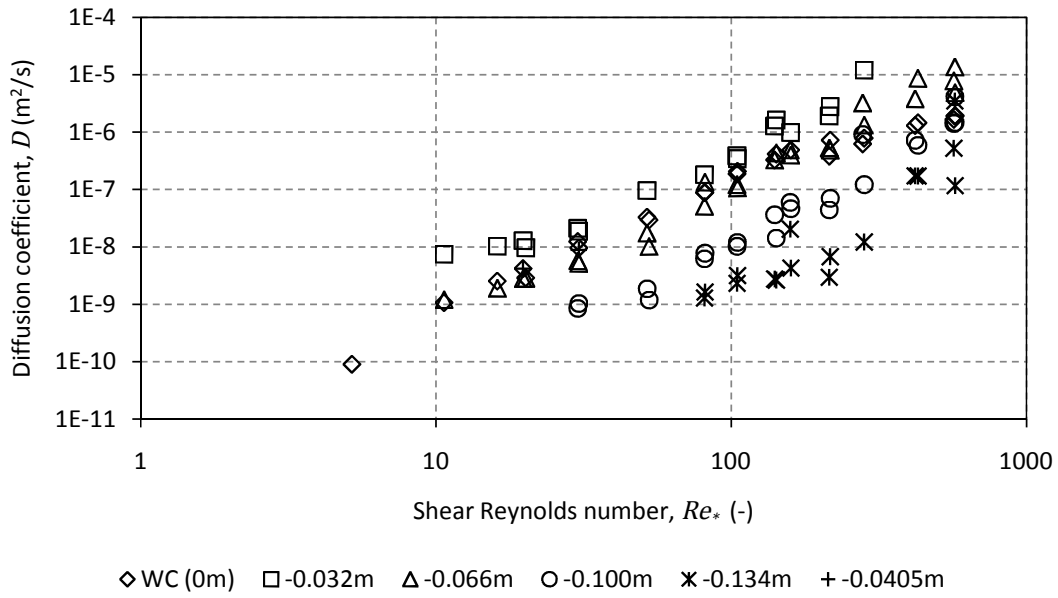

Figure 4.30: Comparison of diffusion coefficients against shear Reynolds number (Re_*)

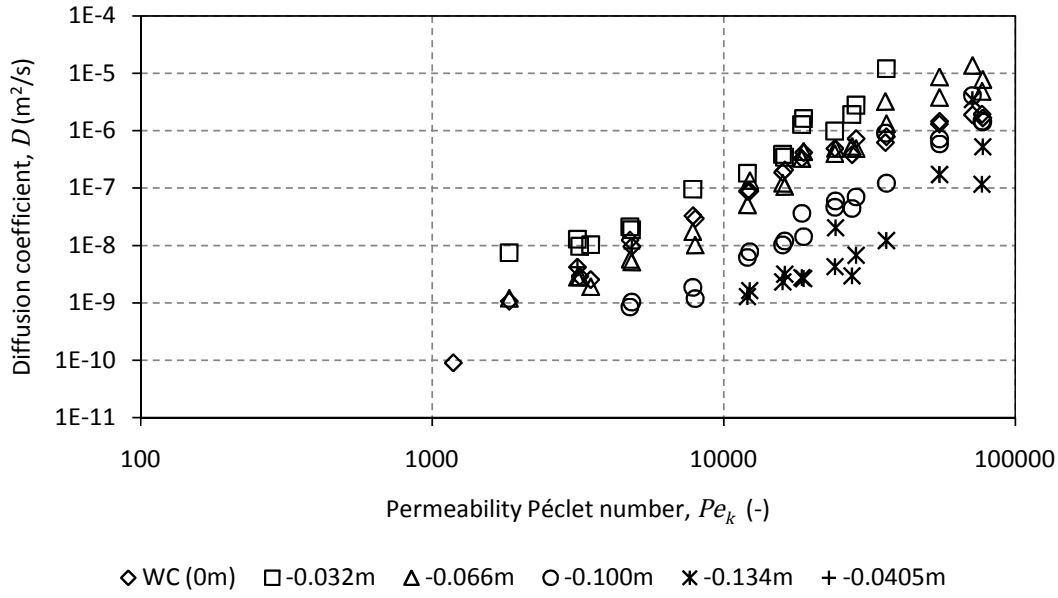

Figure 4.31: Comparison of diffusion coefficients against permeability Péclet number (Pe_k)

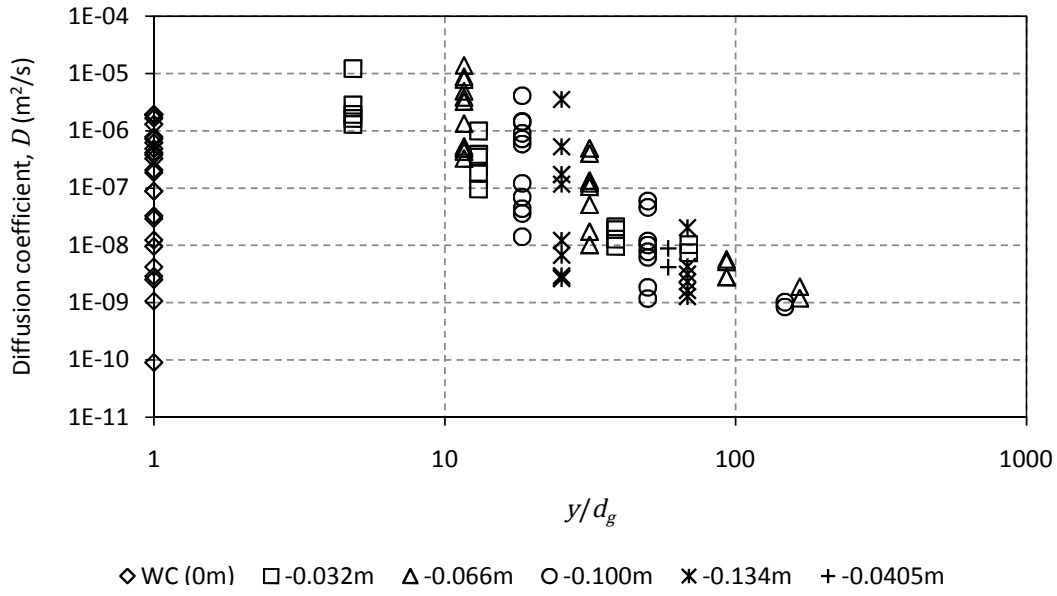

Figure 4.32: Comparison of diffusion coefficients against the number of sediment grain diameters below the interface (y/d_g)

Figure 4.33 shows all the diffusion coefficients obtained from the experimental data non-dimensionalised using molecular diffusion and plotted against $Re_* Pe_K^{6/5}$, the same axis used by O'Connor and Harvey [2008], Figure 2.9, in the same manner as Figure 4.16. The coefficients from each depth display a similar gradient to the scaling relationship (2.51), with lower y-axis values further below the sediment water interface. There is a cut off in the in-bed data at approximately $D/D_m = 10$, which corresponds to a diffusion coefficient of $1.0 \times 10^{-9}\text{m}^2/\text{s}$ however the relationship is expected to continue as the water column data does. The O'Connor and Harvey [2008] scaling relationship predicts the coefficients close to the interface well, with those from -0.032m just above the scaling relationship and within the scatter of the coefficients from other studies shown in Figure 2.9. Further discussion on the significance of Figure 4.33 is given in Chapter 5

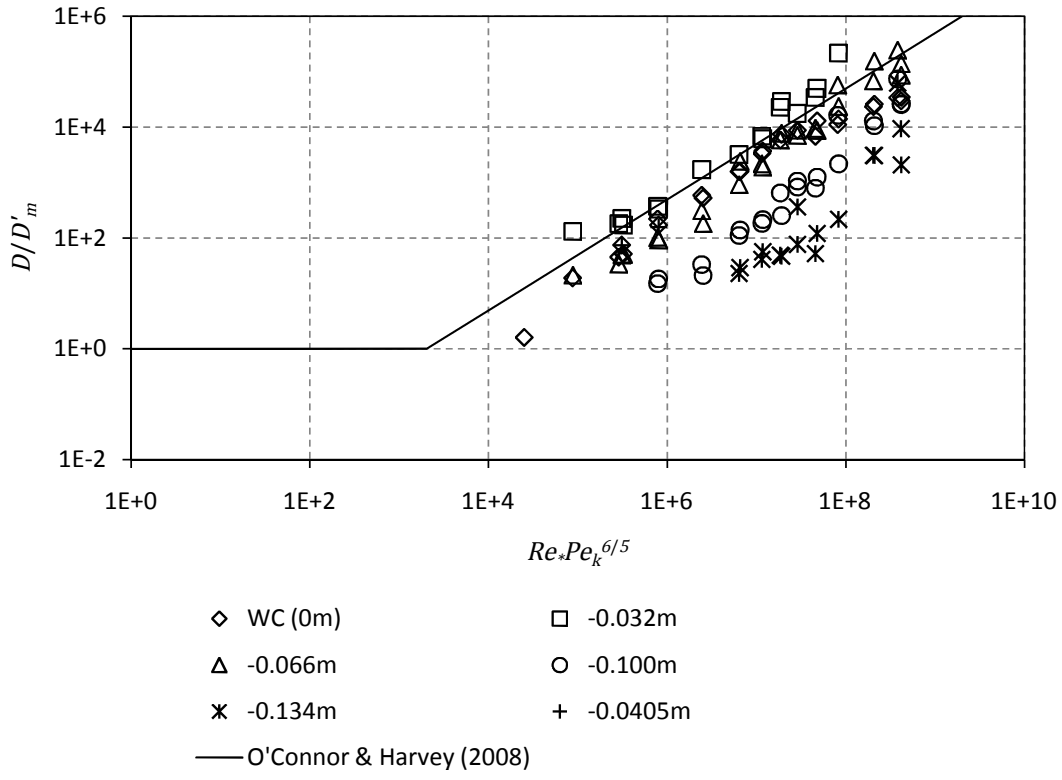

Figure 4.33: Comparison of diffusion coefficients against O'Connor and Harvey [2008] scaling relationship (2.51)

4.6 Summary

In this chapter example raw data has been presented and the permeability data from the test series examined. The diffusion coefficients calculated from the water column and in-bed data have been presented and the challenges encountered in the analysis process discussed. The relationship between the diffusion coefficient and depth below the interface has been observed and will be discussed further in the next chapter (Chapter 5). The influence of bed shear velocity and sediment diameter/permeability on the magnitude of the diffusion coefficients has been shown. The coefficients have been compared with three dimensionless groups and previous work by O'Connor and Harvey [2008]. This showed a strong correlation with the scaling relationship (2.51) and depth below the interface.

Chapter 5

Discussion

5.1 Synopsis

This chapter summarises the discussions from the previous chapters. The experimental data and analysis is reviewed and a function relating the diffusion coefficient to depth below the sediment water interface is derived. A comparison is made between the experimental data and a model simulation based on the depth dependent diffusion coefficient function. Finally applications for the findings of this study are discussed.

5.2 Experimental Data

Several areas regarding the experimental data were highlighted in Chapter 4 that require further discussion. These have been split into two broad sections, water column and in-bed, below.

5.2.1 Water Column

Figure 4.16 that shows the diffusion coefficients obtained from the water column data are all lower than those predicted by the O'Connor and Harvey [2008] scaling relationship (2.51). As stated in Section 4.4 the experimental coefficients from this study lie within the scatter of coefficients used by O'Connor and Harvey [2008]. There is a general non-linear trend in the data plotted on Figure 4.16, with the coefficients from tests with either very low permeability and bed shear velocity (e.g. 10_150_1) or very high permeability and bed shear velocity (e.g. 40_5000_2), furthest away from the scaling relationship.

The trend seen in the data from this study is similar to that of O'Connor and

Harvey [2008] (Figure 2.9). The data points at the extremes are further from the relationship than points in the middle. There are also more data points below the scaling relationship than above, although 95% are within 95% confidence intervals [O'Connor and Harvey, 2008]. Despite more than half the data points plotted by O'Connor and Harvey [2008] lying below the scaling relationship, the points around x-axis values of 10^6 to 10^8 are above the line, which is not seen in the data from this study (Figure 4.16).

This may be because the exchange process within the erosimeter is purely turbulence driven, without the other driving forces, such as pumping, that occur in laboratory flumes. This would reduce the hyporheic exchange within the erosimeter relative to a laboratory flume for a test with the same parameters. Another reason may be the definition of initial slope used in the analysis (Section 4.3.1). In order for there to be a change in the water column concentration, tracer must exchange from the bed across the sediment water interface. This process is progressive, with removal of tracer from near the sediment water interface first. Tracer from deep within the bed cannot exchange with the water column until the tracer above, nearer the interface has exchanged. This results in an interface between tracer that is exchanging and that which has not. This concept was proposed by Elliott and Brooks [1997a] and was shown by their in-bed measurements. In their study the tracer was initially located in the water column, resulting in an increasing concentration in the sediment with time, rather than the decrease with time seen in this study.

Using the same assumptions as Elliott and Brooks [1997a], the water column concentrations can be related to an effective depth of penetration, used in (2.35). Taking 25% of the equilibrium concentration within the erosimeter corresponds to an effective depth of -0.042m. Therefore the diffusion coefficient calculated from the water column data will be a function of the exchange across this region and not strictly the coefficient at the interface. This is true of all the coefficients calculated using the O'Connor and Harvey [2008] method, for this and previous studies, as a change in concentration is required to get an initial slope. However taking too small a percentage of the equilibrium concentration (e.g. 5%) results in few data points being included, which reduces the statistical significance and therefore the confidence in the coefficient calculated. Taking a smaller percentage will also increase the effect of experimental noise on the coefficient calculated.

The suggestion that the water column coefficient is a function of the diffusion coefficients within the first 42mm of the sediment bed, is supported by the in-bed data. The coefficients obtained from the instruments at -0.015 and -0.049m are

higher than the water column coefficients. This can be seen in both Figure 4.20 and 4.33. The coefficients obtained from the instruments at -0.049 and -0.083m are lower than the water column coefficients. The lower water column coefficients compared to those in-bed near the interface, may also be due to the analysis techniques themselves. In evaluating the O'Connor and Harvey [2008] method, Section 2.4.1 (used on the water column data), the technique consistently under predicted the diffusion coefficient used in the model simulations, even with a constant coefficient throughout the sediment region. The Nagaoka and Ohgaki [1990] method (used for the in-bed data) was not consistent in either under or over predicting the coefficients used in model simulations (Section 2.4.2). However with a constant coefficient or one that does not vary greatly near the interface, the technique generally gives an over estimate of the coefficient. This could explain the difference between the water column and in-bed derived diffusion coefficients near the sediment water interface. Using a consistent analysis technique, such as optimising the 1D model to fit the data, may reduce difference between the in-bed and water column derived diffusion coefficients.

5.2.2 In-bed

The main challenges encountered whilst analysing the in-bed data were discussed Section 4.5, however the different response shown from the fluorometer -0.032m below the sediment water interface (FOF3), on the opposite side of the erosimeter to the others, was not elaborated on. An instrument was placed in this position for 5 tests, indicated in Table D.1 column -0.0405m, with either a diffusion coefficient or by an 'S'. For tests 15_625_2 and 10_625_2 the profile from -0.032m could be used to calculate a diffusion coefficient, however this coefficient is higher than that expected from the coefficients calculated from the other profiles (Figure 4.20). Because the coefficients calculated using profiles from -0.032m do not show the same relationship as the others and because the instrument is on the opposite side of the erosimeter to all the others, the coefficients have been plotted separately from, or after, the other coefficients in all the figures in Chapter 4.

Profiles were obtained from tests 15_350_1, 10_350_1 and 10_150_1. However they showed complete mixing at -0.032m below the interface on one side of the erosimeter before it had fully mixed at -0.015m on the other. An example of this is given in Figure 5.1, and in these cases the profile from -0.032m was not incorporated in the analysis. The most likely cause of the apparent increase in mixing on one side of the erosimeter is an inconsistent flow field, that has higher turbulence levels on one side relative to the other. The PIV data presented in Section 3.4 suggests

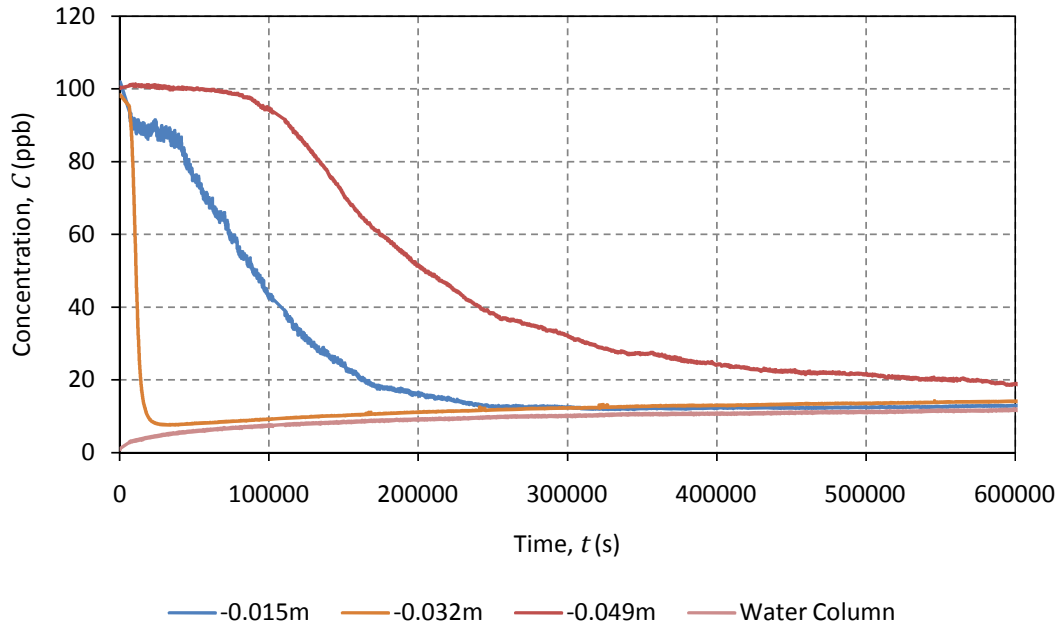

Figure 5.1: Selected concentration profiles from 15_350_1 showing faster mixing at −0.032m

that the flow field is uniform at the sediment water interface, although some areas of higher velocity are visible in Figure 3.24(c). Although it is difficult to be sure that these are not caused by the short recording time used in the PIV measurements (Discussed in Section 3.4.3).

Despite the uniformity in flow field suggested by the PIV data, Figure 5.2 shows the re-arrangement of the sediment bed during test 15_350_1. Particles have been moved from one side (the side where the −0.032m fluorometer is positioned) and deposited on the opposite side, where the other fluorometers are positioned. This suggests a higher bed shear stress (and velocity) on one side than the other, which could explain the difference in profile seen in Figure 4.19, and would result in the higher diffusion coefficients from tests 15_625_2 and 10_625_2.

The sediment motion observed in Figure 5.2 would explain the mixing at −0.032m before −0.015m seen in Figure 4.19. Initially both the instruments recorded a similar reduction in concentration, however as sediment is deposited above the instrument at −0.015m the effective depth below the interface increases, causing the tracer to exchange slower in that region. Conversely the instrument at −0.032m is now closer to the interface, showing faster exchange.

This may mean that the exchange within the erosimeter is not purely vertical and that there is some lateral component, as mixing occurs faster on one side

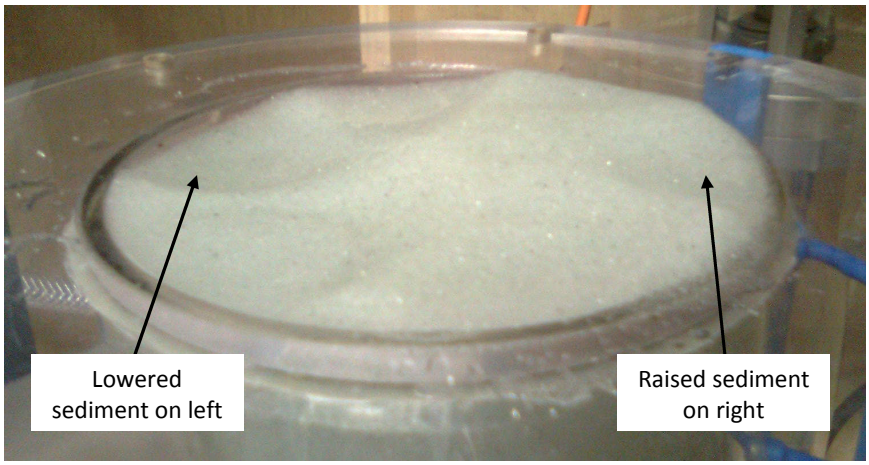

Figure 5.2: Photograph taken after 15_350_1 showing re-arrangement of the sediment bed

than the other. The variation in diffusion coefficient seen in Figure 4.20 and others will still be representative because all the instruments (except that at −0.032m) are placed on the same side, vertically aligned so experience the same level of turbulence. The motor and main section were placed in the same position relative to the instruments in all tests, so any variation in the flow field was consistent for all tests. The sediment motion seen in Figure 5.2 was not observed in any other test.

In column −0.0405m of Table D.1, tests 15_350_1, 10_350_1 and 10_150_1 are designated 'S' because either the setup, with the instrument on the opposite side of the erosimeter or an instrument malfunction prevented a coefficient from being calculated. Test 10_150_1, the smallest sediment diameter test did not yield any in-bed coefficient, due to an instrument malfunction at −0.049m and the lack of concentration change at the other depths. The malfunction may have been caused by ingress of sediment into the mesh hat, which has a mesh size close to that of the sediment diameter, so has been designated 'S' in Table D.1.

5.3 Depth Dependent Diffusion Coefficient Function

The analysis in Chapter 4 shows a strong vertical variation in diffusion coefficient with depth below the sediment water interface. Figure 4.20 suggests that the vertical variation in diffusion coefficient is exponential and that the gradient of the exponential is consistent for all the tests conducted. Figure 4.33 supports Figure 4.20 in the variation being a function of depth below the interface as a length and not as number of grain diameters or other dimensionless number. Figure 5.3 shows diffusion

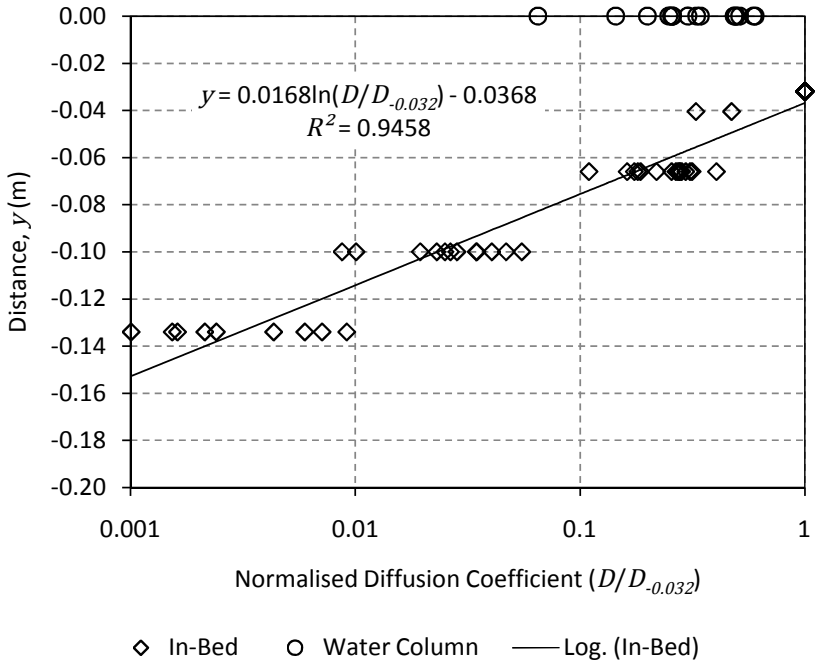

Figure 5.3: Vertical variation in diffusion coefficient normalised with in-bed coefficient closest to the sediment water interface ($D_{-0.032}$)

coefficients from all tests where a diffusion coefficient could be calculated nearest to the sediment water interface (column -0.032m Table D.1). The coefficients are normalised using this coefficient and are plotted, as in Chapter 4, at the mid-points between the instrument positions. A logarithmic best fit line through the in-bed data is shown along with the equation and R^2 value.

Figure 5.3 shows the consistent variation in diffusion coefficient with depth. Rearranging the logarithmic equation to give the dependency of D on y produces

$$D = D_{-0.032} \exp(60y + 2) \tag{5.1}$$

where: D is diffusion coefficient at a particular depth (m^2/s), $D_{-0.032}$ is the measured diffusion coefficient closest to the sediment water interface (m^2/s) and y is vertical distance (m).

To make a prediction, without conducting measurements, would require $D_{-0.032}$ to be predicted. This coefficient is close to the sediment water interface, and as discussed previously the best method currently available is the O'Connor and Harvey [2008] scaling relationship (2.51). The relationship is a good approximation of the diffusion coefficient near the sediment water interface, as can be seen

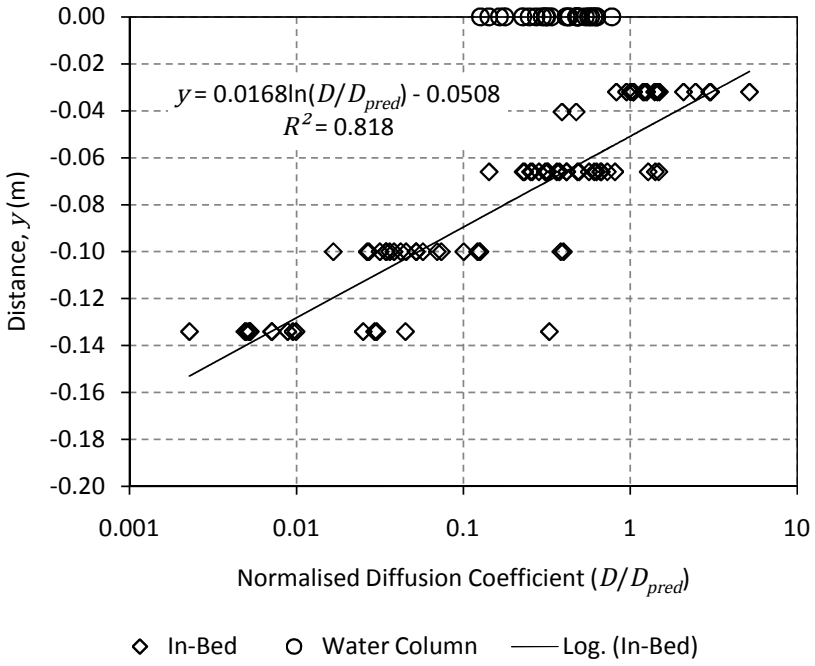

Figure 5.4: Vertical variation in diffusion coefficient normalised with coefficient predicted by O'Connor and Harvey [2008] scaling relationship (2.51) (D_{pred})

in Figure 4.33. Figure 5.4 shows all the diffusion coefficients obtained from the experimental data normalised by the coefficient predicted by (2.51), D_{pred}. A logarithmic best fit line through the in-bed data is shown, again with the equation and R^2 value.

As expected, there is a greater scatter in the data, reducing the R^2 value of the best fit compared to Figure 5.3 because the normalisation is based on a predicted, not a measured coefficient. the gradient of the logarithmic line is the same, only the offset has changed from -0.0368 to -0.0508. Rearranging the equation in the same manner as (5.1) gives

$$D = D_{pred} \exp(60y + 3) \tag{5.2}$$

where: D_{pred} is the diffusion coefficient predicted using O'Connor and Harvey [2008] scaling relationship (2.51) (m^2/s).

The assumption made in both Figure 5.3 and 5.4 is that the average coefficient between the two instrument positions used to obtain it occurs at the mid-point between the two profiles. This would be true if the variation in coefficient between the instrument positions was linear, however the analysis above indicates that the variation is exponential. The assumption is valid because of the small distance between instruments, which results in a 2 to 3mm error in the position of the average

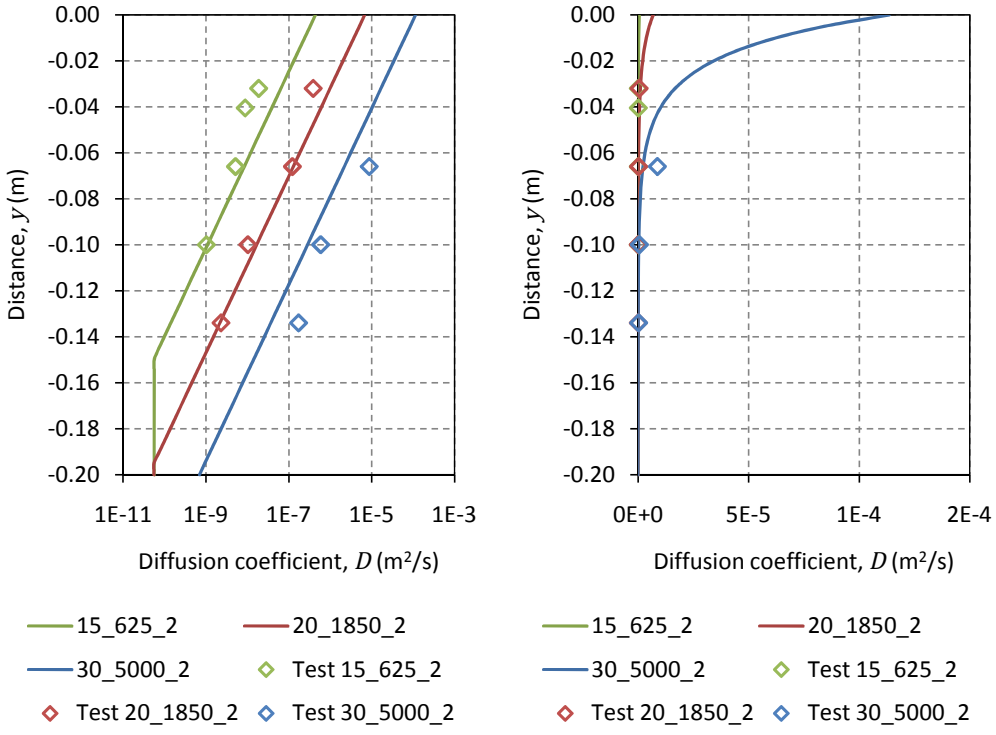

(a) Log axis scale

(b) Linear axis scale

Figure 5.5: Comparison of predicted vertical variation in diffusion coefficient (solid line) with experimental coefficients (points)

coefficient over 32mm (the spacing between instruments). Therefore plotting the in-bed diffusion coefficients at the mid-point, as has been adopted throughout this study, does not influence the outcome of the analysis conducted.

Equation (5.2) is derived from diffusion coefficients covering four orders of magnitude. However the reduction in the coefficient to molecular diffusion was not captured within the experimental data. Based on the strength of the relationship to within 1.5 orders of magnitude of molecular diffusion it has been assumed that it holds until molecular diffusion is reached. After this, there is assumed to be no further reduction in the diffusion coefficient. This assumption produces a relationship of a similar form to (2.51), (5.3), which has been used to produce predicted diffusion coefficient profiles with depth for three different tests (15_625_2, 20_1850_2 and 30_5000_2). Figure 5.5 shows these predicted profiles with the corresponding experimental coefficients plotted on both a log and linear scale.

$$D = \begin{cases} D_{pred}\exp(60y+3) & \text{for } D_{pred}\exp(60y+3) > D'_m \\ \\ D'_m & \text{for } D_{pred}\exp(60y+3) \leq D'_m \end{cases} \tag{5.3}$$

Equation (5.3) allows a prediction of the vertical variation in diffusion coefficient within a sediment bed based on bed shear velocity (u_*), sediment permeability (K), roughness height (k_s), molecular diffusion coefficient (D'_m), kinematic viscosity (ν) and depth below the sediment water interface (y). It has been validated to a depth of 0.134m below the sediment water interface, over a sediment diameter range of 5 to 0.15mm (permeabilities from 1.16×10^{-8} to $4.63 \times 10^{-11}\text{m}^2$) and bed shear velocities of 0.04 to 0.01m/s. Equation (5.3) can be used to predict the temporal and spatial concentrations within the erosimeter or a similar natural aquatic system.

5.4 1D model comparison

The finite difference model (model 4) discussed in Section 2.3.5 has been used in conjunction with (5.3) and (2.51) to predict the concentrations within the erosimeter for different sets of experimental parameters. The first test modelled was 20_1850_2 (Figure 4.1). The input parameter for the simulation are given in Table 5.1, along with the temporal and spatial resolution used.

Parameter	Value
u_*	0.020m/s
K	$2.06 \times 10^{-6}\text{m}^2$
k_s	0.006m
D'_m	$5.61 \times 10^{-11}\text{m}^2/\text{s}$
ν	$1.13 \times 10^{-6}\text{m}^2/\text{s}$
$\text{d}x$	0.001m
$\text{d}t$	0.05s

Table 5.1: Input parameters used to simulate test 20_1850_2 in the 1D finite difference model (model 4)

Figures 5.6 and 5.7 show a comparison between the model simulation profiles and the experimental data, with R_t^2 values for all the profiles given on Figure 5.7. The model profiles have not been optimised to fit the experimental data. The increase in water column concentration is captured well by the model simulation, showing the same steep initial increase, which then flattens towards the end of the test. The model and experimental profiles from -0.015m below the sediment water interface also compare well. However, the model starts decreasing before

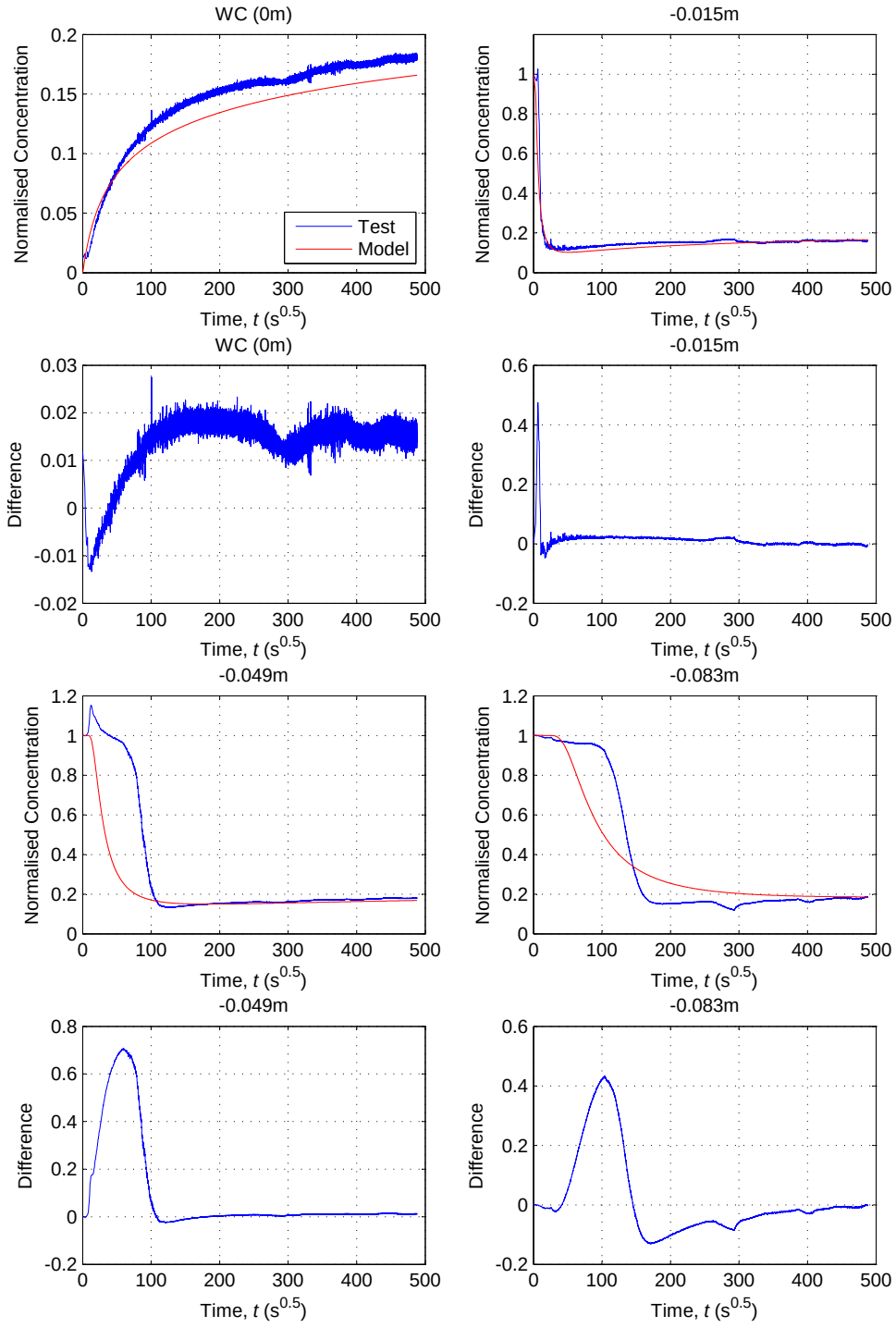

Figure 5.6: Comparison of model simulation and experimental data for test 20_1850_2 (WC, −0.015, −0.049 and −0.083m profiles)

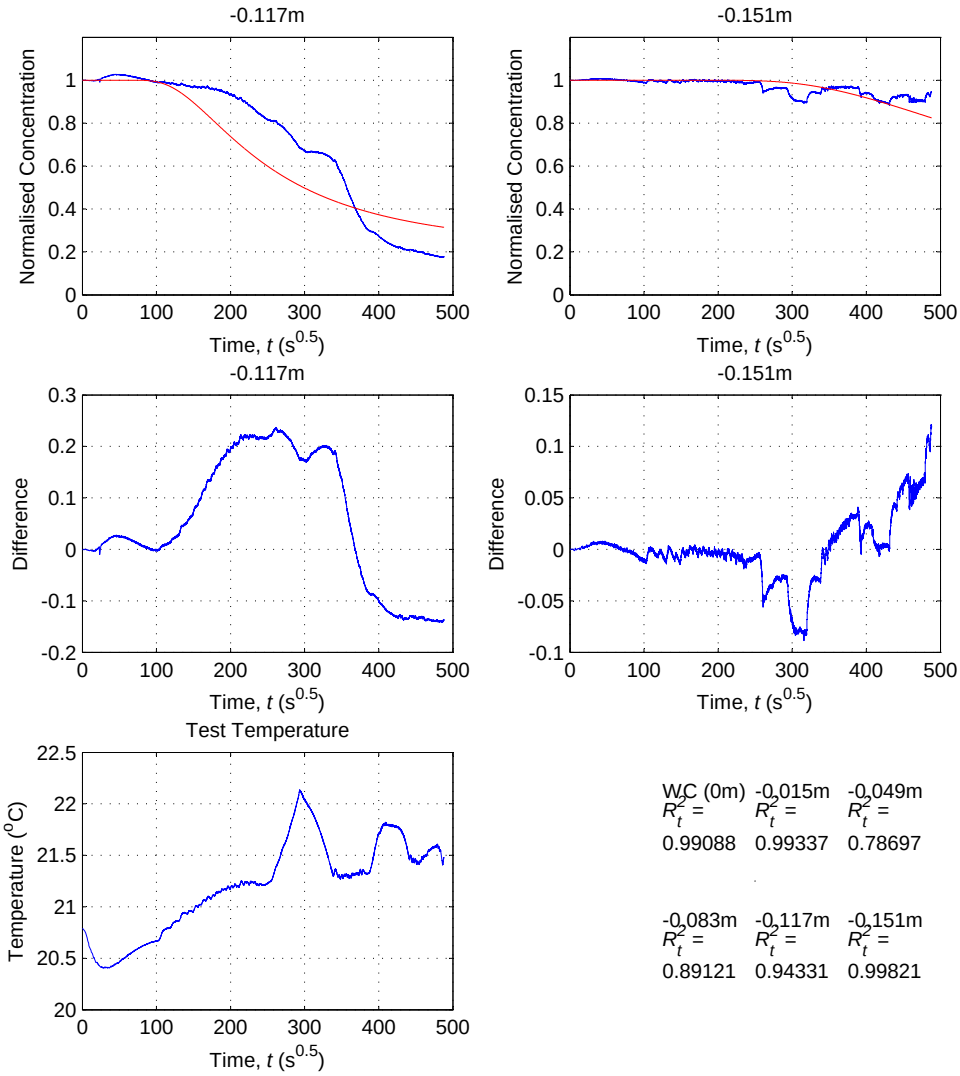

Figure 5.7: Comparison of model simulation and experimental data for test 20_1850_2 (-0.117 and -0.151m profiles) and R_t^2 coefficients for all profiles

the experimental data, and at a slightly slower rate, highlighted in the plot of the difference between the two.

The comparison between the profiles at -0.049, -0.083 and -0.117m are not as good as the water column or at -0.015m. The model concentrations start reducing much sooner than the experimental data and at a slower rate, which results in a much longer time for complete mixing to occur at a particular depth. This is most evident at -0.083m and is suggested at -0.151m as well, but the change in concentration is small during the test making comparison difficult.

The premature start and subsequent extended mixing time is due to the na-

ture of the mathematical model. Although the analogy is not strictly true, parallels can be drawn with a Gaussian profile produced by the analytical solution to Fick's second law for a plane injection in an infinite domain (2.65). The analytical solutions suggests that some particles spread very quickly resulting in the tails seen in Figure 2.10. In the model simulation some tracer mixes quicker (resulting in the early start) and some takes longer (the slower rate of concentration decrease), which is not seen in the experimental data.

The behaviour shown in Figures 5.6 and 5.7 is consistent when other experimental data is compared to model simulations. Tests 30_500_2 and 15_625_2 have also been compared and the model consistently shows significant mixing occurring before the experimental data and then taking longer for mixing to occur at a particular depth. Several different simulations have been considered including varying the exponential function, and using a zoned model (similar to Figure 2.16) with the experimental coefficient obtained at each depth used, which demonstrate similar characteristics. A selection of different model simulation comparisons to experimental data is given in Appendix E. The best R_t^2 values obtained using a continuous function were with (5.3) governing the variation in diffusion coefficient with depth. The zoned simulation using the experimentally derived coefficients (Figures E.1 and E.2) gave slightly better R_t^2 values to the in-bed data, but could not be used as a predictive tool.

The 1D model is not capturing the in-bed concentration profiles at particular depths as accurately as the water column concentrations. The mixing processes may not be a true vertical 1D processes. This is supported by the evidence of an non-uniform flow field and mixing within the erosimeter presented in Section 5.2.2. Another option is the complexity of the processes cannot be accounted for by a single diffusion coefficient. The idea of an effective diffusion coefficient, used in a 1D model, is that it is describing both the sediment and flow conditions as well as the the behaviour of the tracer. If concentration measurements were undertaken throughout the entire sediment bed and averaged at each level then there may be a better comparison between the experimental and model simulation data.

The model is providing an accurate representation of the overall exchange within the erosimeter, as shown by the close correlation between the water column profiles. However at a particular depth within the bed sediment the model is less accurate. The model can still provide useful insights into pollutant transport, which are discussed in the next section.

5.5 Application

The main application of the relationship derived above between diffusion coefficient and depth below the sediment water interface (5.3) is in pollutant transport modelling. As discussed in Chapter 2, current models often assume a constant coefficient within the sediment [Fries, 2007], if they consider mixing within the sediment at all. The experimental data demonstrate the variation which is quantified above. Equation (5.3) could be used to produce a 'lookup' chart showing the depth to which the diffusion coefficient is greater than molecular diffusion, or some multiple of molecular diffusion. This would indicate an 'active layer' within the sediment bed in which pollutants are more likely to mix because of the higher diffusion coefficient. This would allow a quick analysis based on a bed shear velocity and a mean particle diameter to be conducted. The permeability could be estimated using (2.130) from the mean particle diameter and an assumed porosity. An example table is shown in Figure 5.8.

Depth of active ($D > D'_m$) layer (m)

Mean particle diameter, d_{50} (m)	0.01	0.015	0.02	0.025	0.03	0.035	0.04
0.0051	-0.208	-0.223	-0.234	-0.242	-0.248	-0.254	-0.259
0.0046	-0.204	-0.219	-0.230	-0.238	-0.245	-0.250	-0.255
0.0041	-0.200	-0.215	-0.226	-0.234	-0.240	-0.246	-0.251
0.0036	-0.195	-0.210	-0.221	-0.229	-0.236	-0.241	-0.246
0.0031	-0.190	-0.205	-0.215	-0.223	-0.230	-0.236	-0.241
0.0026	-0.183	-0.198	-0.209	-0.217	-0.224	-0.229	-0.234
0.0021	-0.176	-0.190	-0.201	-0.209	-0.216	-0.222	-
0.0016	-0.166	-0.180	-0.191	-0.199	-	-	-
0.0011	-0.152	-0.167	-0.177	-	-	-	-
0.0006	-0.130	-0.145	-	-	-	-	-
0.0001	-0.064	-	-	-	-	-	-

Bed shear velocity, u_* (m/s)

Figure 5.8: Example 'lookup' chart giving the depth of the 'active layer' (m) for different bed shear velocities and particle diameters

With the incorporation of the 1D model specific scenarios can be modelled. For given sediment and flow conditions, the depth to which pollutants are likely to penetrate within a certain exposure time could be estimated. Measurements from field sites could be used to set realistic water column concentrations and the permitted (safe) environmental concentration could be used to determine the depth of pollutant penetration that may be of concern.

This can be applied both within the waste water and chemical/pestercide in-

dustries, where both are concerned with chemical concentration within the natural environment, particularly aquatic ecosystems. Although the in-bed concentrations are not accurately predicted within the 1D model, the model is quick to run and requires few inputs to give realistic predictions of the temporal and spatial concentrations within a sediment bed.

The model can be used to estimate the length of time erosimeter tests would take to show mixing to a particular depth. This would enable a more informed decision on the length of time tests are conducted for in future work (Section 6.3). The model allows an estimate of the time test 15_625_2 would need to be run for to confirm (5.3) holds to molecular diffusion. Test 15_625_2 would need to be run for around 125 days (approximately 4 months).

Chapter 6

Conclusion

The aims of this study were to improve the fundamental understanding of hyporheic exchange and specifically to determine the vertical variation in diffusion coefficient below the sediment water interface. A unique data set has been generated demonstrating the vertical variation in diffusion coefficient within a sediment bed exposed to turbulence driven hyporheic exchange using the erosimeter system. The vertical variation in diffusion coefficient was approximated by an exponential function, with the magnitude of the diffusion coefficient decreasing with depth below the sediment water interface until molecular diffusion is reached. This allowed an active layer to be defined, as a region where the magnitude of the vertical diffusion coefficient is greater than molecular diffusion.

6.1 Use of Erosimeter

The original EROSIMESS-system (erosimeter) described in Section 3.2 was redesigned to improve its use within a laboratory environment and to incorporate an in-situ permeability test (Section 3.3) and a fibre optic measurement system within the bed sediment (Section 3.5.2). Through a comparison of the initial experimental results [Chandler *et al.*, 2010], and the water column data derived diffusion coefficient (Section 4.4) with the effective diffusion scaling relationship (2.51) [O'Connor and Harvey, 2008] (Figure 3.3 and Figure 4.16 respectively) the erosimeter was demonstrated to be a viable option for studying hyporheic exchange.

The hyporheic exchange coefficients obtained from the erosimeter compare favourably with previous experimental studies which used laboratory flumes. The advantages of the erosimeter over laboratory flumes are the smaller volumes of sediment and water involved, which reduces both financial and time costs whilst avoiding

the need to scale the experiment. The only disadvantage is that the exchange mechanism is limited to turbulence driven exchange, without the other driving forces such as pumping that will occur in a laboratory flume.

The flow field within the erosimeter was evaluated using particle image velocimetry (PIV), which validated the calibration between the propeller speed and the bed shear velocity (Section 3.4.3). The flow field at the sediment water interface appears uniform although the experimental data, discussed in Section 5.2.2, suggest some non-uniformity in a minority of tests.

The erosimeter is an effective research tool for studying hyporheic exchange and could be used as the basis for improvements to current chemical degradation studies such as OECD 308 [OECD, 2002], current industry standard test. The current OECD 308 tests do not incorporate sediment or fluid flow, resulting in conditions far removed from those found in the field.

6.2 Vertical Variation in Diffusion Coefficient

Fibre optic fluorometers, developed for this study, have enabled concentration profiles to be measured within the bed sediment. This has enabled the vertical variation in diffusion coefficient with depth below the sediment water interface to be quantified. The variation in diffusion coefficient was approximated by an exponential function (5.3), which is applicable over the full range of parameter combinations tested. The test parameters dictate the magnitude of the coefficient at the sediment water interface, through (2.51) [O'Connor and Harvey, 2008], from which the reduction with depth is governed by (5.3). Equation (5.3) is re-stated below and has been validated over a range of bed shear velocities from 0.01 to 0.04m/s, sediment diameters of 0.15 to 5.00mm (permeabilities from 4.63×10^{-11} to 1.16×10^{-8}m^2) and to a depth below the sediment water interface of -0.134m. Figure 6.1 shows diffusion coefficient profiles calculated using (5.3), with experimental diffusion coefficients also plotted.

$$D = \begin{cases} D_{pred} \exp(60y + 3) & \text{for } D_{pred} \exp(60y + 3) > D'_m \\ \\ D'_m & \text{for } D_{pred} \exp(60y + 3) \leq D'_m \end{cases} \tag{5.3}$$

Where: D is diffusion coefficient at a particular depth (m^2/s), D_{pred} is the diffusion coefficient predicted using O'Connor and Harvey [2008] scaling relationship (2.51) (m^2/s), y is vertical distance (m) and D'_m is the molecular diffusion coefficient in sediment pore water (2.2) (m^2/s).

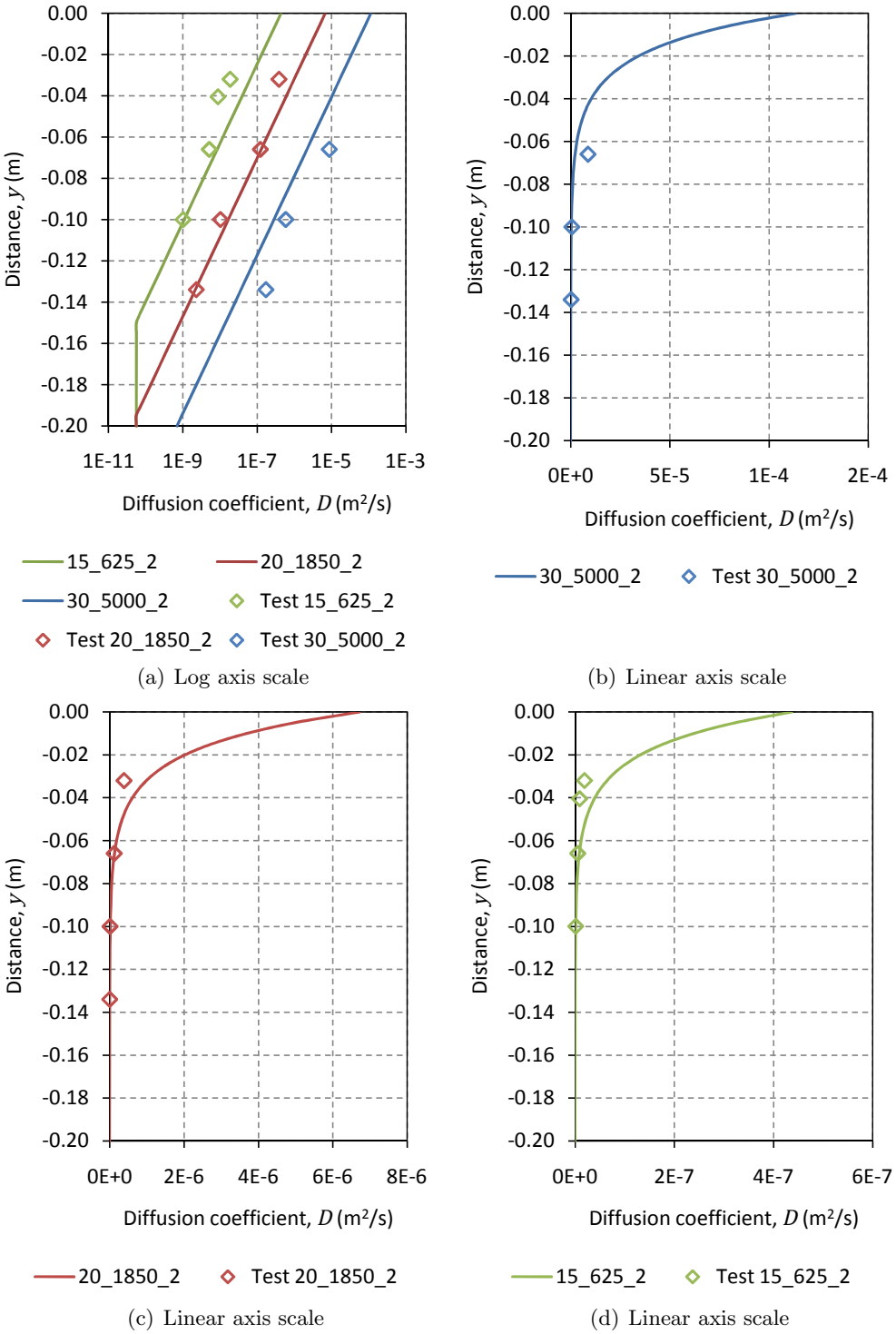

(a) Log axis scale

(b) Linear axis scale

(c) Linear axis scale

(d) Linear axis scale

Figure 6.1: Comparison of predicted vertical variation in diffusion coefficient with experimental coefficients

Model simulations were conducted using a 1D finite difference formulation of Fick's second law, using the experimental parameters and (5.3) to predict the temporal and spatial concentrations within the erosimeter. These simulations were compared to experimental profiles which showed good general agreement with R_t^2 values greater than 0.9 in most cases. There are some discrepancies between the model simulation profiles and the experimental data, particularly within the bed. The model suggests a more gradual mixing throughout a particular layer, whereas the experimental data suggest that tracer at a particular depth mixes relatively quickly, indicated by the steep gradient in the concentration profiles (Section 5.4).

Quantifying the variation in diffusion coefficient within sediment beds, even when it is based on single size glass spheres, will allow chemical concentrations within sediment beds to be modelled more accurately. The relationship enables predictions of the depth to which harmful concentrations of pollutants will penetrate into the bed sediment and the production of 'lookup' charts, allowing the active layer (the region where exchange will occur faster than molecular diffusion) to be assessed quickly.

6.3 Further Work

There are numerous topics that could be considered for further investigation based on the research presented in this thesis. A number are outlined below:

- A more comprehensive investigation into the flow field within the erosimeter, using either volumetric PIV or 3D laser doppler anemometry (LDA) would help to validate the findings from this study and the use of the erosimeter to study hyporheic exchange. Conducting a series of tests with the fibre optic fluorometers positioned radially at the same depth would allow a direct comparison of the rates of exchange throughout the erosimeter, determining the uniformity of the exchange. Gel water beads, with the same refractive index as water, present an opportunity to try laser induced fluorometry and other visualisation techniques within the sediment bed, allowing both concentration and flow measurements to be taken, however the sorptive qualities of the beads has not yet been ascertained.

- The 1D numerical model could be used directly in the analysis of the experimental data. This could be achieved by optimising the diffusion coefficients within the model so the best fit was achieved with all the measured concentration profiles from each test. This would allow a consistent analysis technique

to be applied to all the data instead for separate water column and in-bed techniques. The major challenge with optimising the 1D model is the number of diffusion coefficients that need to be optimised and the effect that coefficients below a certain point in the model have on regions above this point.

- Time restraints within the study (due to supply and equipment issues) prevented mixed diameter sediment beds from being investigated. These are more representative of the sediment beds found in natural streams. The effect of stratification within the sediment bed could also be investigated within the erosimeter, including effects of surface armouring on hyporheic exchange and the variation in the diffusion coefficient within the bed. The erosimeter's original function was the study of sediment motion, which is another area that could be investigated for its impact on hyporheic exchange.

- Cored natural sediments could be used in the erosimeter, either mixed or removed straight from the corer into the erosimeter base. This would be the closest to a field test that could be conducted within the laboratory. The advantages of this would be that the permeability of the sediment could be measured accurately and after the test the sediment could be analysed to get the exact composition, not always possible in the field. This work would further investigate the vertical variation in diffusion coefficient identified in this study.

- The effect of biofilms on hyporheic exchange has become an area of interest in recent years [Bottacin-Busolin *et al.*, 2009]. The erosimeter is ideal for studying its effects as a test can be conducted without a biofilm, then the base removed, a biofilm grown, and the test repeated. This would allow a direct comparison between hyporheic exchange with and without a biofilm.

- The effects of chemical sorption to the sediment particles has been excluded from this investigation but remain an important factor within pollutant modelling. The use of natural sediments, different tracers or specific chemicals would allow the effects of sorption to be investigated within the erosimeter. The use of different tracers/chemicals would require modifying the fibre optic fluorometers or developing different measurement techniques to allow concentrations to be measured within the bed sediment.

- The further work suggested above may result in a system that could reproduce conditions within natural steams and monitor the exchange and biodegradation of chemical pollutants within the laboratory. This system could be used

to improve the current OECD 308 [OECD, 2002] tests for biodegradation, which do not include either sediment or fluid flow. Both these parameters could significantly influence the biodegradation of chemicals and could lead to a more realistic evaluation of chemical persistence in the natural environment.

- The erosimeter was originally designed as a field instrument and could be developed, along with the fibre optic fluorometers to allow field measurements of hyporheic exchange and the variation in diffusion through out the sediment bed to be conducted. This would allow hyporheic exchange to be measured directly in the field and not inferred from transient storage models fitted to concentration break through curves, which is the technique currently employed (Section 2.5).

Notation

b, c, d - Scaling exponents or equation constants (-)

A - cross-sectional area of channel (L^2)

A_s - Surface area of sediment bed (L^2)

a - Plan area of sediment bed (L^2)

APE - Average percent error (%)

C - Solute concentration (ML^{-3})

C_D - Forchheimer form drag coefficient (-)

C_T - Apparent measured concentration (measured by fluorescence) at temperature T (ML^{-3})

C_{T0} - Concentration (measured by fluorescence) at 0°C (ML^{-3})

C_e - Equilibrium concentration (ML^{-3})

C_s - Surface or interface concentration (ML^{-3})

C_t - Measured concentration profile (ML^{-3})

C_{wc} - Solute concentration in water column (ML^{-3})

C_z - Chézy resistance coefficient (-)

C_0 - Initial solute concentration (ML^{-3})

C^* - Normalised solute concentration (-)

D - Diffusion or effective diffusion coefficient (L^2T^{-1})

D_b - Bio-diffusivity coefficient (L^2T^{-1})

D_d - Dispersion coefficient (L^2T^{-1})

D_m - Molecular diffusion coefficient (L^2T^{-1})

D'_m - Molecular diffusion coefficient in sediment pore water (L^2T^{-1})

D_{max} - Largest diffusion coefficient in vertical profile (L^2T^{-1})

D_{wc} - Diffusion coefficient in water column (L^2T^{-1})

D_y - Depth average vertical diffusion coefficient (L^2T^{-1})

D_1 - Average diffusion coefficient of region between sensors (L^2T^{-1})

D_2 - Average diffusion coefficient of region below sensors (L^2T^{-1})

D_* - Time dependent effective diffusion coefficient (L^2T^{-1})

d_g - Geometric mean particle diameter (L)

d_{ch} - Characteristic particle diameter (L)

d_{cr} - Critical sediment mobility parameter (-)

$\mathrm{d}t$ - Sampling interval (T)

d_{90} - Particle size for which 90% of sediment is finer (L)

d_{10} - Particle size for which 10% of sediment is finer (L)

d_* - Dimensionless particle diameter (-)

Da_{ds} - Damköholer reaction number (-)

F - Force (MLT^{-2})

$\mathbf{F}_b$ - Net body force (LT^{-2})

f - Equation variable (-)

g - Gravity (MLT^{-2})

H - Flow/stream depth (L)

H_s - Depth of sediment bed (L)

h - Dynamic pressure head (L)

h_m - Amplitude of the dynamic pressure head at the bed surface (L)

h^* - Normalised dynamic pressure head (-)

i - Spatial co-ordinate (-)

I_1 - Image intensity for first interrogation window (-)

I_2 - Image intensity for second interrogation window (-)

J - Solute flux ($\mathrm{ML}^{-2}\mathrm{T}^{-1}$)

j - Temporal co-ordinate (-)

K - Permeability (L^2)

K_c - Hydraulic conductivity (LT^{-1})

K_m - Main channel partitioning coefficient ($\mathrm{L}^3\mathrm{M}^{-1}$)

K_{ow} - Octanol-water partitioning coefficient ($\mathrm{L}^3\mathrm{M}^{-1}$)

K_{OC}^{irr} - Organic carbon normalised partitioning coefficient (-)

K_{sr} - Sediment reaction partitioning coefficient ($\mathrm{L}^3\mathrm{M}^{-1}$)

K_{ss} - Sediment sorption partitioning coefficient ($\mathrm{L}^3\mathrm{M}^{-1}$)

$K_{s,tot}$ - Total sediment partitioning coefficient ($\mathrm{L}^3\mathrm{M}^{-1}$)

k_s - Roughness height (L)

L - Total longitudinal length of experimental flume/stream reach or distance between sensors (L)

M - Mass (M)

M' - Effective depth of penetration (L)

M_s - Mass accumulation in bed (ML^{-2})

M_w - Mass accumulation in water (ML^{-2})

m - Momentum (MLT^{-1})

N - Number of rows/columns/vector fields or size of correlation window (-)

n - Sediment type constant (-)

$\mathbf{n}$ - Unit vector normal and into the bed surface (-)

P_t - Predicted concentration profile (ML^{-3})

p - Pressure ($\mathrm{ML}^{-1}\mathrm{T}^{-2}$)

Pe_{em} - Exchange Péclet number for the main channel (-)

Pe_{em} - Exchange Péclet number for the storage zone (-)

Pe_K - Permeability Péclet number (-)

Q - Discharge ($\mathrm{L}^3\mathrm{T}^{-1}$)

q - Volume flux into bed (LT^{-1})

$\bar{q}$ - Average volume flux into bed over bed surface (LT^{-1})

R - Residence time function or resistance ($\mathrm{ML}^2\mathrm{I}^{-2}\mathrm{T}^{-3}$)

R_H - Hydraulic radius (L)

R_s - First order reaction rate coefficient (T^{-1})

R_T - Temperature correction factor for permeability test (-)

R_t^2 - Coefficient of determination (-)

$\bar{R}$ - Average residence time function (-)

$\tilde{R}_H$ - Spatially weighted hydraulic radius (L)

r - Equation variable or 2D correlation coefficient (-)

Re - Stream Reynolds number (-)

Re_K - Permeability Reynolds number (-)

Re_* - Shear Reynolds number (-)

S - Bed slope (-)

$S(\mathrm{d}x, \mathrm{d}y)$ - Correlation strength at a displacement $\mathrm{d}x, \mathrm{d}y$ (-)

s - Distance along bed surface (L)

T - Temperature (θ)

T_e - Time when concentration profile reaches $1/e$ of equilibrium concentration (T)

t - time (T)

t^* - Integration upper limit (T)

U - Average velocity of the overlying water/main stream (LT^{-1})

U_b - Bed-form propagation speed (LT^{-1})

u - Instantaneous velocity in x-direction (LT^{-1})

$\mathbf{u}$ - Velocity vector (LT^{-1})

u' - Instantaneous velocity fluctuation in x-direction (LT^{-1})

u'_{rms} - Root-mean-square of instantaneous velocity in x-direction (LT^{-1})

$\bar{u}$ - Ensemble average velocity in x-direction (LT^{-1})

u_s - Slip velocity (LT^{-1})

u_{s+} - Normalised slip velocity (-)

u_+ - Normalised horizontal velocity (-)

u_* - Shear velocity (LT^{-1})

V_g - Potential difference across wheatstone bridge ($\mathrm{ML}^2\mathrm{I}^{-1}\mathrm{T}^{-3}$)

V_r - Length scale representative of relative water column and pore water volumes (L)

V_s - Volume of pore water in sediment bed (L^3)

V_{sup} - Supply voltage ($\mathrm{ML}^2\mathrm{I}^{-1}\mathrm{T}^{-3}$)

V_T - Total volume (L^3)

V_v - Volume voids (L^3)

V_w - Volume of overlaying water (L^3)

v - Instantaneous velocity in y-direction (LT^{-1})

$\mathbf{v}$ - Volume average interstitial velocity vector (LT^{-1})

v' - Instantaneous velocity fluctuation in y-direction (LT^{-1})

v'_{rms} - Root-mean-square of instantaneous velocity in y-direction (LT^{-1})

$\bar{v}$ - Ensemble average velocity in y-direction (LT^{-1})

W_b - Wetted bathymetry (L^2)

W_p - Wetted perimeter (L)

w - Instantaneous velocity in z-direction (LT^{-1})

w' - Instantaneous velocity fluctuation in z-direction (LT^{-1})

w'_{rms} - Root-mean-square of instantaneous velocity in z-direction (LT^{-1})

$\bar{w}$ - Ensemble average velocity in z-direction (LT^{-1})

x - Horizontal co-ordinate (L)

x^* - Normalised horizontal co-ordinate (-)

y - Vertical co-ordinate (L)

y^* - Normalised vertical co-ordinate (-)

y_+ - Normalised elevation above interface (-)

z - Lateral horizontal co-ordinate (L)

α - Dimensionless scaling or surface constant (-)

β - Sediment diffusion correction term accounting for tortuosity (-)

γ - Time dependent variable (-)

Δ - Bed-form height (L)

ε - Dummy variable (-)

η - Elevation of bed surface above mean bed surface height (L)

θ - Porosity (-)

κ - Von Kármán constant (-)

λ - Bed-form wavelength (L)

μ - Dynamic viscosity ($\mathrm{ML}^{-1}\mathrm{T}^{-1}$)

ν - Kinematic viscosity ($\mathrm{L}^2\mathrm{T}^{-1}$)

ν_e - Effective viscosity ($\mathrm{L}^2\mathrm{T}^{-1}$)

ξ -Time lag (T)

ρ_r - Relative density (-)

ρ_{Rhod} - Density of Rhodamine WT (ML^{-3})

ρ_s - Sediment particle density (ML^{-3})

ρ_w - Fluid density (ML^{-3})

σ - Standard deviation (various)

τ - Stress or bed shear stress ($ML^{-1}T^{-2}$)

τ_{cr} - Critical bed shear stress for sediment motion ($ML^{-1}T^{-2}$)

ψ_+ - Normalised velocity profile displacement (L)

ω - Porosity depth function (-)

References

A. J. Basu and A. Khalili. Computation of flow through a fluid-sediment interface in a benthic chamber. *Physics of Fluid*, 11:1395–1405, 1999.

J. Bear. *Dynamics of fluids in porous media.* American Elsevier, New York, 1972.

G. S. Beavers and D. D. Joseph. Boundary conditions at a naturally permeable wall. *Journal of Fluid Mechanics*, 30:197–207, 1967.

K. E. Bencala and R. A. Walters. Simulation of solute transport in a mountain pool-and-riffle stream: A transient storage model. *Water Resources Research*, 19 (3):718724, 1983. doi: 10.1029/WR019i003p00718.

P. Berg, N. Risgaard-Petersen, and S. Rysgaard. Interpretation of measured concentration profiles and sediment pore water. *Limnology and Oceanography*, 43: 1500–1510, 1998.

R. A. Berner. *Early Diagenesis: A Theoretical Approach.* Princeton University Press, Princeton, N. J., 1980.

A. Bottacin-Busolin, G. Singer, M. Zaramella, T. J. Battin, and A. Marion. Effects of streambed morphology and biofilm growth on the transient storage of solutes. *Environ. Sci. Technol.*, 43(19):7337–7342, 2009.

B. P. Boudreau. The diffusive tortuosity of fine-grained unlithified sediments. *Geochimica et Cosmochimica Acta*, 60:3139–3142, 1996.

M. A. Briggs, M. N. Gooseff, C. D. Arp, and M. A. Baker. A method for estimating surface transient storage parameters for streams with concurrent hyporheic storage. *Water Resources Research*, 45:W00D27, 2009. doi: 10.1029/2008WR006959.

BS1377-5. *: Soils for civil engineering purposes: Compressibility, permeability and durability tests.* British Standards Institution, 1990.

P. C. Carman. Fluid flow through granular beds. *Trans. Inst. Chem. Eng.*, 15: 32–48, 1937.

A. Chadwick, J. Morfett, and M. Borthwick. *Hydraulics in Civil and Environmental Engineering*. Spon Press, fourth edition, 2004.

I. D. Chandler, J. M. Pearson, I. Guymer, and R. Van-Egmond. Quantifying hyporheic exchange coefficients using the erosimess-system. In G. C. Christodoulou and A. I. Stamou, editors, *Environmental Hydraulics*, volume 2, pages 765–770. 6$^{\text{th}}$ International Symposium on Environmental Hydraulics, CRC Press, 2010.

R. Courant, K. Friedrichs, and H. Lewy. On the partial difference equations on mathematical physics. *IBM Journal*, page 215234, 1967.

J. Crank. *The Mathematics of Diffusion*. Oxford University Press, Oxford, UK, 2 edition, 1975.

J. Crank and P. Nicolson. A practical method for numerical evaluation of solutions of partial differential equations of the heat-conduction type. *Proc. Camb. Phil. Soc. math. phys. Sci.*, 43:50–67, 1947.

P. M. Dennis. *Longitudinal dispersion due to surcharged manholes*. PhD thesis, University of Sheffield, 2000.

R. Dutton. *Modelling Transient Storage Processes*. PhD thesis, University of Sheffield, 2004.

A. H. Elliott and N. H. Brooks. Transfer of nonsorbing solutes to a streambed with bedforms: Theory. *Water Resources Research*, 33:123–136, 1997a.

A. H. Elliott and N. H. Brooks. Transfer of nonsorbing solutes to a streambed with bedforms: Laboratory experiments,. *Water Resources Research*, 33:137–151, 1997b.

H. Eylers, N. H. Brooks, and J. J. Morgan. Transport of adsorbing metals from stream water to a stationary sand-bed in a laboratory flume. *Marine and Freshwater Research*, 46:209–214, 1995.

H. B. Fischer. Dispersion predictions in natural streams. *Journal of Sanitary Engineering*, 94(5):927–943, 1968.

H. B. Fischer, E. J. List, R. C. Y. Koh, J. Imberger, and N. H. Brooks. *Mixing in Inland and Coastal Waters*. Academic Press, 1979.

K. J. Forsman, H. Johansson, and K. Jonsson. The effect of partly irreversible solute exchange: comparison between conservative and sorptive transport in streams. *Journal of Hydrology*, 256:1–15, 2002.

S. Forster and G. Graf. Impact of irrigation on oxygen flux into the sediment: intermittent pumping by *Callianassa subterranea* and "piston-pumping" by *Lanice conchilega*. *Marine Biology*, 123:335–346, 1995. ISSN 0025-3162.

R. A. Freeze and J. A. Cherry. *Groundwater*. Prentice-Hall, Englewood Cliffs, N. J., 1979.

J. S Fries. Predicting interfacial diffusion coefficients for fluxes across the sediment-water interface. *Journal Hydraulic Engineering*, 133:267–272, 2007.

C. Gell, D. J. Brockwell, G. S. Beddard, S. E. Radford, A. P. Kalverda, and D. A. Smith. Accurate use of single molecule fluorescence correlation spectroscopy to determine molecular diffusion times. *Single Molecule*, 2(3):177–181, 2001. doi: 10.1002/1438-5171(200110)2:3<177::AID-SIMO177>3.0.CO;2-4.

C. Gray, C. A. Greted, D. R. McCluskey, and W. J. Easson. An analysis of the scanning beam piv illumination system. *Measurement Science and Technology*, 2 (8):745–750, 1991.

I. Guymer, P. Dennis, R. OBrien, and C. Saiyudthong. Diameter and surcharge effects on solute transport across surcharged manholes. *Journal Hydraulic Engineering*, 131(4):312–321, 2005.

F. Habel, C. Mendoza, and A. C. Bagtzoglou. Solute transport in open channel flows and porous streambeds. *Advances in Water Resources*, 25:455–469, 2002.

D. R. Hart. Parameter estimation and stochastic interpretation of the transient storage model for solute transport in streams. *Water Resources Research*, 31(2): 323–328, 1995.

D. R. Hart, P. J. Mullholland, E. R. Marzolf, D. L. DeAngelis, and S. P. Hendricks. Relationships between hydraulic parameters in a small stream under varying flow and seasonal conditions. *Hydrological Processes*, 13:1497–1510, 1999.

J. W. Harvey, B. J. Wagner, and K. E. Bencala. Evaluating the reliability of the stream tracer approach to characterize stream-subsurface water exchange. *Water Resources Research*, 32(8):2441–2451, 1996.

N. Iversen and B. B. Jrgenson. Diffusion coefficients of sulphate and methane in marine sediments: Influence of porosity. *Geochimica et Cosmochimica Acta*, 57: 517–578, 1993.

H. Johansson, K. Jonsson, K. J. Forsman, and A. W′orman. Retention of conservative and sorptive solutes in streams - simultaneous tracer experiments. *The Science of the Total Environment*, 266:229–238, 2001.

K. Jonsson, H. Johansson, and A. W′orman. Hyporheic exchange of reactive and conservative solutes in streams - tracer methodology and model interpretation. *Journal of Hydrology*, 278:153–171, 2003.

S. Jubb. *The effect of sediment resuspension on river water quality.* PhD thesis, Sheffield University, UK, 2001.

S. Jubb, I. Guymer, G. Licht, and J. Prochnow. Relating oxygen demand to flow: development of an in-situ sediment oxygen demand measurement device. *Water Science and Technology*, 43(5):203–210, 2001.

A. T. Kan, G. Fu, M. Hunter, W. Chen, C. H. Ward, and M. B. Tomson. Irreversible sorption of neutral hydrocarbons to sediment: Experimental observations and model predictions. *Environ. Sci. Technol.*, 32(7):892–902, 1998.

S. Kashefipour and R. Falconer. An improved model for predicting sediment fluxes in estuarine water. In *Proceedings of the Fourth International Hydroinformatics Conference*, Iowa, USA, 2000.

R. D. Keane and R. J. Adrian. Theory of cross-correlation analysis of piv images. *Applied Scientific Research*, 49(3):191–215, 1992. doi: 10.1007/BF00384623.

B. A. Kimbal, R. E. Broshears, K. E. Bencala, and D. M. McKnight. Coupling of hydrologic transport and chemical reactions in a stream affected by acid mine drainage. *Environ. Sci. Technol.*, 28:2065–2073, 1994.

J. L. Lai, S. L. Lo, and C. F. Lin. Effects of hydraulic and medium characteristics on solute transfer to surface runoff. *Water Science Technology*, 30:145–155, 1994.

LaVision. *DaVis FlowMaster Software Manual for DaVis 7.1.* LaVision, LaVision GmbH, Anna-Vandenhoeck-Ring 19, D-37081 Göttingen, November 2006.

LaVision. *Product-Manual for DaVis 7.2.* LaVision, LaVision GmbH, Anna-Vandenhoeck-Ring 19, D-37081 Göttingen, November 2010.

R. Liem, V. Spork, and J. Koengeter. Investigations on erosional processes of cohesive sediment using an in-situ measuring devive. *Internatinoal Journal of Sediment Research*, 13(3):139–147, 1997.

C. Manes, I. Pokrajac, D. McEwan, V. Nikora, and L. Campbell. Application of uvp within porous beds. *Journal of Hydraulic Engineering*, 132(9):983–986, 2006.

A. Marion, M. Bellinello, I. Guymer, and A. I. Packman. Effect of bed form geometry on penetration of nonreactive solute into a streambed. *Water Resources Research*, 38(10):1209, 2002.

A. Marion, M. Zaramella, and A. I. Packman. Parameter estimation of the transient storage model for stream-subsurface exchange. *Journal of Environmental Engineering*, 129(5):456–463, 2003.

A. Marion, M. Zaramella, and Bottacin-Busolin A. Solute transport in rivers with multiple storage zones: The stir model. *Water Resources Research*, 44:W10406, 2008. doi: 10.1029/2008WR007037.

D.C. McAvoy, P. Masscheleyn, Peng C., S.W. Morrall, A.B. Casilla, J.M.U. Lim, and E.G. Gregorio. Risk assessment approach for untreated wastewater using the qual2e water quality model. *Chemosphere*, 52:55–66, 2003.

R. Meynart and L. M. Lourenco. Laser speckle velocimetry in fluid dynamics applications: digital image processing in fluid dynamics. *Von Karman Institute Lecture Series*, 3:12, 1984.

C. T. Miller and J. A. Pedlt. Use of a reactive surface-diffusion model to describe apparent sorption-desorption hysteresis and abiotic degredation of lindane in a subsurface material. *Environ. Sci. Technol.*, 26:2088–2095, 1992.

P. J. Mulholland. Hydrometric and stream chemistry evidence of three storm flowpaths in walker branch watershed. *Journal of Hydrology*, 151:291–316, 1993.

P. J. Mulholland, J. D. Newbold, J. W. Elwood, L. A. Ferren, and J. R. Webster. Phosphorus spiralling in a woodland stream: Seasonal variations. *Ecology*, 66(3): 1012–1023, 1985.

H. Nagaoka and S. Ohgaki. Mass transfer mechanism in a porous riverbed. *Water Research*, 24:417–425, 1990.

B. L. O'Connor and J. W. Harvey. Scaling hyporheic exchange and its influence on biogeochemical reactions in aquatic ecosystems. *Water Resources Research*, 44: 1–17, 2008. doi: 10.1029/2008WR007160. W12423.

OECD. *Guideline for the testing of chemicals: 308 - Aerobic and Anaerobic Transformation in Aquatic Sediment Systems*. Paris, 2002.

A. I. Packman and J. S. MacKay. Interplay of stream-subsurface exchange, clay particle deposition, and stream bed evolution. *Water Resources Research*, 39(4): 4–1–4–9, 2003. doi: 10.1029/2002WR001432.

A. I. Packman and M. Salehin. Relative roles of stream flow and sedimentary conditions in controlling hyporheic exchange. *Hydrobiologia*, 494:291–297, 2003.

A. I. Packman, N. H. Brooks, and J. J. Morgan. Kaolinite exchange between a stream and streambed: laboratory experiment and validation of a colloid transport model. *Water Resources Research*, 36:2363–2372, 2000.

A. I. Packman, M. Salehin, and M. Zaramella. Hyporheic exchange with gravel beds: Basic hydrodynamic interactions and induced advective flows. *Journal of Hydraulic Engineering*, 130:647–656, 2004.

D. Pokrajac and C. Manes. Velocity measurements of a free-surface turbulent flow penetrating a porous medium composed of uniform-size spheres. *Transport in Porous Media*, 78(3):367–383, 2009.

J. Pontolillo and R. P. Eganhouse. The search for reliable aqueous solubility (sw) and octanol-water partioning coefficient (kow) data for hydrophobic organic compounds: Ddt and dde as a case study. Water-Resources Investigation Report 01-4201, U.S. Geological Survey, Reston, Virginia, 2001.

M. Raffel, C. Willert, and J. Kompenhans. *Particle Image Velovimetry, A practical guide*. Springer, 1998.

K. J. Rehg, A. I. Packman, and J. Ren. Effects of suspended sediment characteristics and bed sediment transport on streambed clogging. *Hydrological Processes*, 19: 413–427, 2005. doi: 10.1002/hyp.5540.

H. Reichardt. Vollstandige darstellung der turbulenten geschwindigkeitsverteilung in glatten leitungen. *Z. Angew. Math. Mech.*, 31(7):208–219, 1951.

C. E. Reimers, R. A. Jahnke, and L. Thomsen. *The benthic boundary layer: transport processes and biochemestry*. Oxford University Press, 2001. In-situ sampling in the benthic boundary layer (chapter).

J. Ren and A. I. Packman. Stream-subsurface exchange of zinc in the presence of silica and kaolinite colloids. *Environmental Science Technology*, 38:6571–6581, 2004. doi: 10.1021/es035090x.

O. Reynolds. On the dynamical theory of incompressible viscous fluids and the determination of the criterion. *Philosophical Transactions of the Royal Society of London, Series A*, 186:123–164, 1895.

C. P. Richardson and A. D. Parr. Modified fickian model for solute uptake by runoff. *Journal of Environmental Engineering*, 114:792–809, 1988.

P.J. W. Roberts and D. R. Webster. *Environmental Fluid Mechanics Theories and Applications*. ASCE, 2002. Chapter 2: Turbulent Diffusion.

J. F. Ruff and L. W. Gelhar. Turbulent shear flow in porous boundary. *Journal Engineering Mechanics*, 98:975–991, 1972.

R. L. Runkel. One dimensional transport with inflow and outflow (otis): a solute transport model for streams and rivers, us geological survey water resources investigation report 98-4018. Technical report, US Geological Survey, Denver, Colorado, USA., 1998.

R. L. Runkel, B. A. Kimball, D. M. McKnight, and K. E. Bencala. Reactive solute transport in streams: a surface complexation approach for trace metal sorption. *Water Resources Research*, 35(12):3829–3840, 1999.

J. C. Rutherford. *River Mixing*. J. Wiley and Sons Ltd, 1994.

Y. Shimizu, T. Tsujimoto, and H. Nakagawa. Experiment and macroscopic modelling of flow in highly permeable porous medium under free-surface flow. *Hydroscience and Hydraulic Engineering*, 8(1):69–78, 1990.

A. Skeen. *The Development of High-Speed PIV Techniques and Their Application to Jet Noise Measurement*. PhD thesis, University of Warwick, December 2006.

P. L. Smart and I. M. S. LaidLaw. An evaluation of some fluorescent dyes for water tracing. *Water Resources Research*, 13(1):161–172, 1977.

M. Solan, B. D. Wigham, I. R. Hudson, R. Kennedy, C. H. Coulon, K. Norling, H. C. Nilsson, and R. Rosenberg. In situ quantification of bioturbation using time-lapse fluorescent sediment profile imaging (f-spi), luminophore tracers model simulation. *Marine Ecology Progress Series*, 271:1–12, 2004.

F. Sonnenwald, V. Stovin, and I. Guymer. Correlation measures for solute transport model evaluation. Unpublished.

V. Spork, J. Jahnke, J. Prochnow, and J. Koengeter. Stabilising effect of benthic algae on cohesive sediments. *International Journal of Sediment Research*, 12(3): 399–406, 1997.

H. Tennekes and J. L. Lumley. *A First Course in Turbulence*. MIT Press, 1972.

TGD. *Technical Guidance Document (TGD) in Support of Commission Directive 93/67/EEC on Risk Assessment for New Substances and Commission Regulation (EC) No. 1488/94 on Risk Assessment for Existing Substances*, 2003.

D. Tonina and J. M. Buffington. Hyporheic exchange in gravel bed rivers with pool-riffle morphology: Laboratory experiments and three-dimensional modelling. *Water Resources Research*, 43:W01421, 1–16, 2007. doi: 10.1029/2005WR004328.

L. C. van Rijn. Sediment transport, part iii: Bed forms and alluvial roughness. *Journal Hydraulic Engineering*, 110:1733–1754, 1984.

P. Venkataraman and P. Rama Mohan Rao. Darcian, transitional, and turbulent flow through porous media. *Journal of Hydraulic Engineering*, 124:840–846, 1998.

J. H. A. Vlaskamp. *An Experimental and Numerical Investigation into the Vertical Dependence of Taylor-Columns Generated by a Rotating Disc*. PhD thesis, University of Warwick, 2011.

P. J. Wierenga and M. Th. Van Genuchten. Solute transport through small and large unsaturated soil columns. *Ground Water*, 27(1):35–42, 1989.

A. Wörman. Comparison of models for transient storage of solutes in small streams. *Water Resources Research*, 36(2):455–468, 2000.

A. Wörman, M. Forsman, and H. Johansson. Modeling retention of sorbing solutes in streams based on a tracer experiment using ^{5}1cr. *J. Environ. Eng.*, 124:122130, 1998.

A. Wörman, A. I. Packman, H. Johansson, and K. Jonsson. Effect of flow-induced exchange in hyporheic zones on longitudinal transport of solutes in streams and rivers. *Water Resources Research*, 38(1):1–15, 2002.

S. Wu and P. M. Gschwend. Sorption kinetics of hydrophobic organic compounds to natural sediments and soils. *Environ. Sci. Technol.*, 20:717–725, 1986.

P. Young, A. Jakeman, and R. McMurtrie. An instrumental variable method for model order identification. *Automatica*, 16:281–294, 1980.

M. Zaramella, A. I. Packman, and Marion A. Application of the transient storage model to analyze advective hyporheic exchange with deep and shallow sediment beds. *Water Resources Research*, 39(7):1198, 2003. doi: 10.1029/2002WR001344.

D. Zhou and C. Mendoza. Flow through porous bed of turbulent stream. *Journal Engineering Mechanics*, 119:365–383, 1993.

Appendix A

Schematic of original EROSIMESS-system

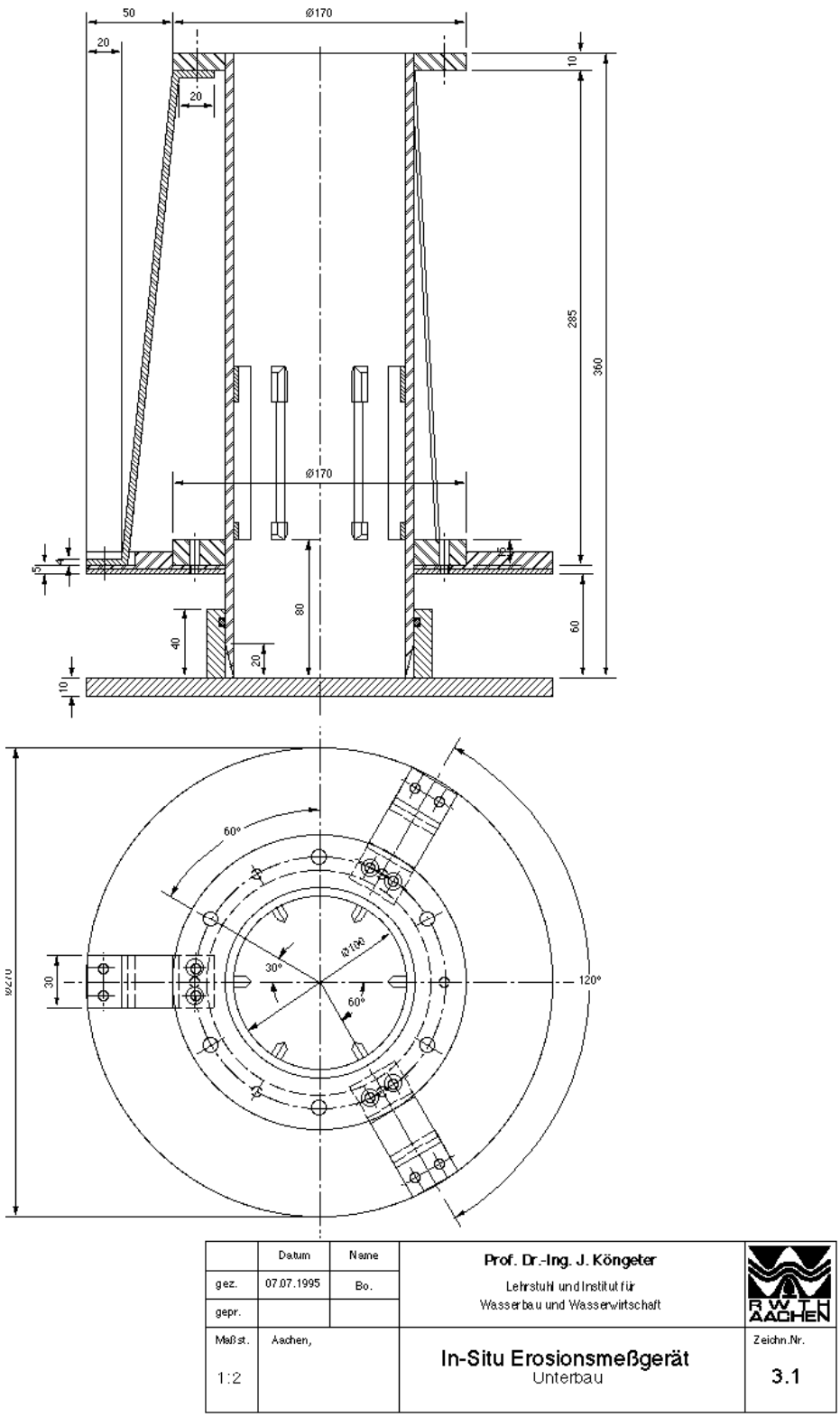

Figure A.1: Schematic of the original erosimeter showing side elevation and plan view [Jubb, 2001]

Appendix B

Chandler, Pearson, Guymer, and Van-Egmond [2010]

Quantifying hyporheic exchange coefficients using the EROSIMESS-system

I.D. Chandler, J.M. Pearson & I. Guymer
School of Engineering, University of Warwick, Coventry, Warwickshire, England

R. Van-Egmond
Unilever Safety & Environmental Assurance Centre (SEAC), Colworth Science Park, Sharnbrook, Bedfordshire, England

ABSTRACT: This paper describes a new laboratory method for studying hyporheic exchange, through the use of a modified EROSIMESS-System (erosimeter). This method requires much smaller volumes of water and sediment than traditional re-circulating flume studies, which reduces the testing time and allows a wider variety of parameters to be investigated in one test series. The erosimeter allows full scale study of hyporheic exchange, but with reduced quantities of sediment and fluid. The technique typically has a reduced time scale for each test, allowing a wider variety of conditions to be examined within one test series. The experimental exchange coefficients obtained with the erosimeter are compared with previous experimental work, obtained with laboratory flumes, through an effective diffusion scaling relationship. The experiments presented compare well with the previous laboratory flume studies, demonstrating the validity of the erosimeter technique for quantifying hyporheic exchange.

1 INTRODUCTION

Historically there have been two main systems for studying hyporheic exchange, field or laboratory studies. The majority of laboratory studies over the past two decades have been conducted on re-circulating flumes (e.g. Packman et al. (2000), Elliott and Brooks (1997b), Marion et al. (2002)). These tests take typically 10 to 100 hours to run, restricting the range of conditions that can be tested in one series. Smaller volumes of both sediment and water would significantly reduce the time required by each test, however this is difficult to achieve in a laboratory flume, whilst maintaining a realistic physical scale. The solution would be to use apparatus smaller than a flume, but the difficulty in generating realistic scale turbulence driven exchange becomes a problem. This led to the adoption of a modified EROSIMESS-System to study hyporheic exchange.

The EROSIMESS-System is an in-situ erosion-meter (shortened to erosimeter) developed at The Institute of Hydraulic Engineering and Water Resources Management, Aachen University of Technology in Germany (IWW, RWTH). Originally used for determining the critical bed shear stress of sediments deposited in small hydropower plant reservoirs, it has also been used extensively to determine the stabilising effect of benthic algae on cohesive sediments (Spork et al., 1997) and the effects sediment re-suspension have on dissolved oxygen content of river water (Jubb et al., 2001). The erosimeter consists of two parts, the main measurement section and the top motor section. A shaft runs from the motor into the main section and ends in a 20 mm diameter tri-bladed propeller. This propeller generates the bed shear stress that was originally used to quantify sediment erosion, but is now used to generate hyporheic exchange.

2 THEORY

The erosimeter works in a similar way to a re-circulating flume, there are two zones within the system: the sediment zone with its pore water and the overlying fluid zone. During a test the tracer placed in one zone mixes and exchanges with the clean in the other until the system reaches equilibrium. There are many different parameters and processes that can affect hyporheic exchange which are combined in the exchange coefficient. In recognition of this and to compare hyporheic exchange coefficients driven by different processes, the coefficient is referred to as an effective diffusion coefficient (D_e) throughout this paper. Effective diffusion coefficients can be obtained from measurements taken within either zone. When combined with the two possible initial tracer locations, four different scenarios are possible. Each scenario requires a specific equation to calculate the effective diffusion coefficient.

The approach used to determine effective diffusion coefficients directly from the experimental data are the same as those used by O'Connor and Harvey (2008). When the sampling and initial dye locations are the same and the system is closed, such as the erosimeter, the exchange coefficient can be derived as follows. Consider a re-circulating flume where the concentration (C) is initially zero in the bed sediment and the concentration in the overlying water (C_w) is equal to an initial concentration (C_0) (well mixed system). Once the experiment starts, hyporheic exchange will drive the tracer into the sediment pore water releasing interstitial fluid of zero concentration, resulting in a decrease of concentration in the overlying fluid with time. O'Connor and Harvey (2008) demonstrate that an effective diffusion coefficient can be obtained from the normalised concentration break through curve. This equation can be rearranged for the situation where the sampling and tracer are both located within the bed, which is the arrangement used in the tests presented in this paper. In this case the effective diffusion is given by:

$$D_e = \left(\frac{\sqrt{\pi}}{2} \frac{V_s}{A_s} \frac{dC_s^*}{d\left(t^{1/2}\right)} \right)^2 \tag{1}$$

where D_e = effective diffusion coefficient (m^2/s); V_s = volume of fluid in the sediment pores (m^3); A_s = sediment surface area (m^2); and $C_s* = C / C_{0,s}$ = normalised solute concentration in the sediment pore water; C = solute concentration (kg/m^3); $C_{0,s}$ = initial solute concentration within the sediment pore water (kg/m^3); t = time (s).

During the erosimeter tests there is another instrument positioned in the overlying fluid, so the sampling and initial dye location are different. This requires the use of (2) (O'Connor & Harvey, 2008) to calculate the effective diffusion coefficient from the resulting concentration breakthrough curve.

$$D_e = \left(\frac{\sqrt{\pi}}{2C_{0,s}} \frac{dM_w}{d\left(t^{1/2}\right)} \right)^2 \tag{2}$$

where M_w = accumulated mass of solute tracer in the overlying fluid (kg/m^2).

O'Connor and Harvey (2008) propose a scaling relationship (3) that allows hyporheic exchange to be predicted from several test parameters.

$$\frac{D_e}{D'_m} = \begin{cases} 5\times10^{-4} Re_* Pe_K^{6/5} & \text{for } Re_* Pe_K^{6/5} \geq 2000 \\ 0 & \text{for } Re_* Pe_K^{6/5} < 2000 \end{cases} \tag{3}$$

where D'_m = molecular diffusion coefficient through the sediment pore water (m^2/s); Re_* = shear Reynolds number (4); and Pe_K = permeability Péclet number (5).

$$Re_* = u_* \frac{k_s}{\nu} \tag{4}$$

where u_* = bed shear velocity (m/s); k_s = roughness height (m); and ν = kinematic viscosity (m^2/s).

$$Pe_* = u_* \frac{\sqrt{K}}{D'_m} \tag{5}$$

where K = permeability (m^2).

This relationship is derived from 11 sets of laboratory flume studies which was presented and is reproduced in Figure 1.The studies used cover a wide variety of flow, sediment and test conditions, including bed-forms. Figure 1 demonstrates the good agreement of the scaling relationship to the flume data, which now forms the basis for the comparison of previous laboratory flume data with the erosimeter tests.

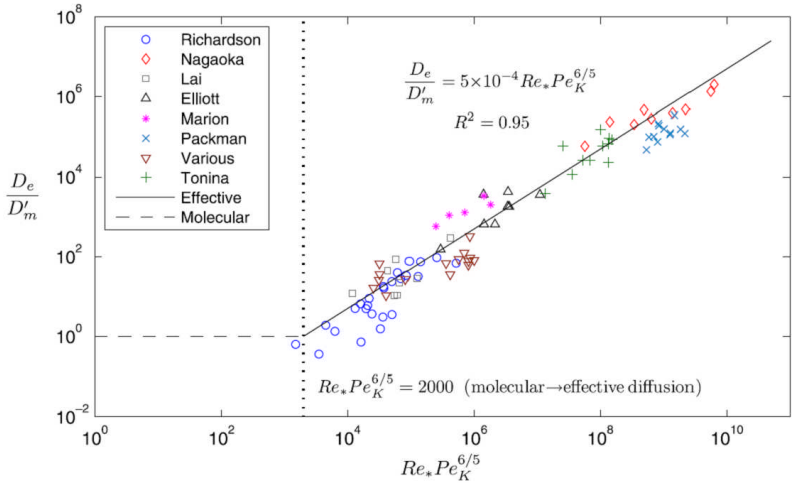

Figure 1. Effective diffusion scaling relationship plotted with experimental data used to derive the relationship (O'Connor & Harvey, 2008).

3 EXPERIMENTAL SETUP

The erosimeter setup for studying hyporheic exchange is similar to the laboratory calibration adopted by Jubb et al. (2001). The main section of the erosimeter is 300 mm deep with an internal diameter of 97 mm. The base section is 70 mm deep, but could be extended if a bed depth greater than 70 mm was being tested. The motor sits on top of the main section as shown in Figure 2 with the 260 mm shaft bringing the propeller to 40 mm above the bed sediment. 6 baffles around the diameter at the height of the propeller create a uniform bed shear stress at the sediment surface (Liem, 1997).

The calibration base plate has been extended to allow a Turner Designs Cyclops 7 fluorometer (set for Rhodamine WT) positioned through the base to take in-bed measurements. A second Turner Designs Cyclops 7 is placed through an earlier modification that allowed a dissolved oxygen (DO) probe access to the main chamber, allowing in-flow measurements to be taken.

Before the experiment starts the in-bed Cyclops 7 is placed at the desired height (in the tests presented this is 20mm from the base) and a mesh hat fitted. This prevents the measurement volume being obscured by the bed sediment. The sediment is placed within the erosimeter base section to a depth of 70mm and the pores are filled with a known concentration of Rhodamine WT. Two litres of clean water are placed in the main body and the motor started. The propeller speed has been calibrated against bed shear velocity by observing under increasing rotations, the commencement of single size sediment motion and relating this to critical bed shear stress for motion.

The tests are run until equilibrium concentrations are achieved, which can be determined from the quantity of Rhodamine WT solution and the volume of clean water used. The equilibrium concentration can then be converted into an output voltage from the Cyclops 7's through a standard concentration to voltage calibration. A series of experiments have been conducted to

test the capabilities of the erosimeter, and the range over which it can study hyporheic exchange. A number of repeat experiments were conducted with the same parameters to check the repeatability of the procedure. The parameters of the tests conducted are given below in Table 1.

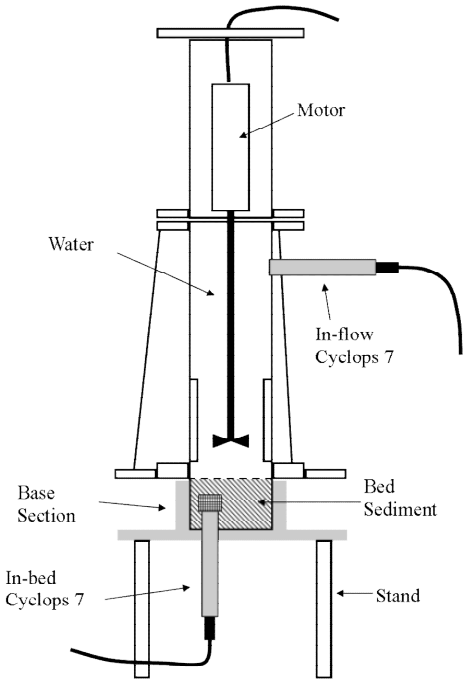

Figure 2. Modified EROSIMESS-System with Turner Designs Cyclops 7 fluorometers shown in measurement locations.

Table 1. Erosimeter test parameters

Test No.	u_* (m/s)	d_g (m) ($\times 10^{-3}$)	k_s (m)	K (m^2) ($\times 10^{-9}$)
1	0.0171	2	0.00708	2.55
2	0.0171	2	0.00708	2.55
3	0.0175	2	0.00708	2.55
4	0.0176	2	0.00708	2.55
5	0.0162	2	0.00708	2.55
6	0.0278	75	0.03	94.9
7	0.028	75	0.03	94.9
8	0.0099	1	0.00354	0.64

where d_g = mean sediment diameter (m).

Table 2. Experimental values

Test No.	D'_m (m^2/s) ($\times 10^{-11}$)	V_s (ml)	Initial Gradient In-flow ($\times 10^{-8}$) ($kg/m^2s^{1/2}$)	Initial Gradient In-bed ($\times 10^{-2}$) ($s^{-1/2}$)
1	5.61	300	8.1544	
2	5.61	245	9.6922	
3	5.61	300	13.466	
4	5.61	300	6.7560	
5	5.61	300	7.4234	-4.3300
6	5.71	300	59.946	-16.647
7	5.71	275	34.067	-12.004
8	6.65	300	0.67593	-0.1362

4 RESULTS AND DISCUSSION

The output voltages from the in-flow and in-bed Cyclops 7 fluorometers were converted into concentrations. The in-bed concentrations are normalised using the initial concentration and the in-flow concentrations are converted into accumulated mass of Rhodamine WT. Both in-flow and in-bed traces are plotted against the square root of time. Figure 3 shows an example of both in-flow and in-bed traces from the same test.

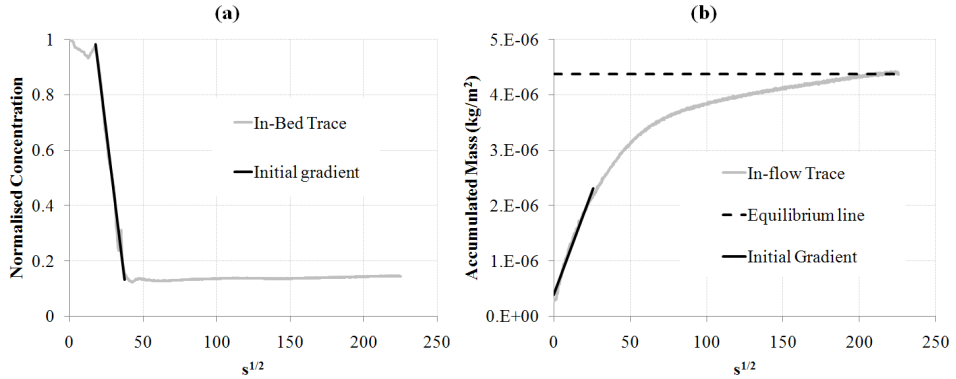

Figure 3. Example in-bed (a) and in-flow (b) breakthrough curves from erosimeter test no. 5.

The in-flow graph shows a steady initial increase, which flattens to constant value, when the system is fully mixed. In Figure 3(b) this occurs at approximately 250 $s^{1/2}$. The poorly defined initial slope meant that the gradient of all the data up to 50% of the equilibrium value was used. This allowed all the tests to be analysed using the same method and was chosen after studying the change in gradient with time. The in-bed instrument gives a different shape with the initial drop in concentration small, but then rapidly decreases to the equilibrium value. This rapid decrease was used as the initial gradient as it indicates the point at which the removal of tracer (by exchange) reaches the depth of the in-bed instrument. Once the exchange of tracer has occurred at the surface the next layer is available for exchange which continues through the bed until all the tracer has been exchanged, and the system is fully mixed. The initial gradients of both the in-bed and in-flow breakthrough curves are taken and used in Equations 1 and 2 respectively to determine an experimental value of effective diffusion coefficient. These are plotted against the predicted value of effective diffusion gained from Equation 3 (Figure 4).

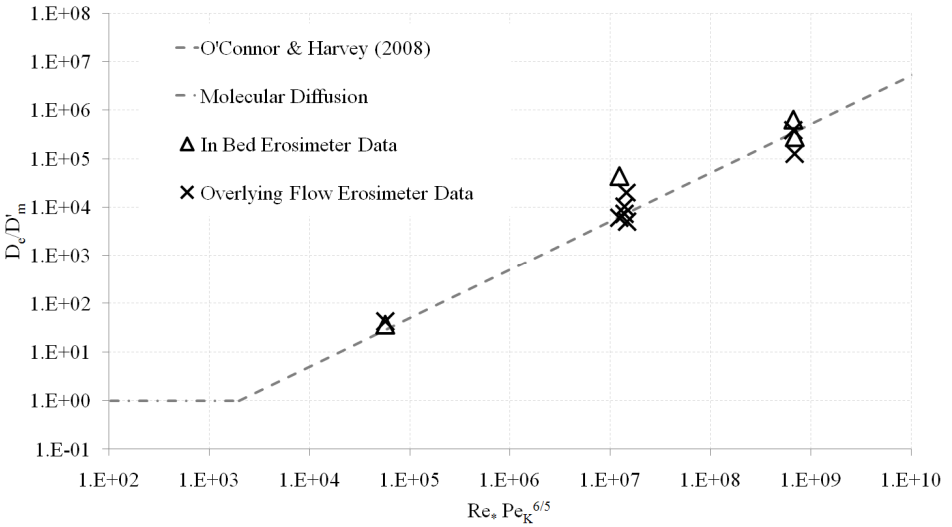

Figure 4. Erosimeter experimental results plotted against O'Connor and Harvey (2008) scaling relationship.

Figure 4 shows close agreement between the experimental effective diffusion coefficients and those predicted by the scaling relationship. All the tests are within the scatter of the previous experimental data (Figure 1). The central group show the repeatability of the erosimeter technique, with all the effective diffusion coefficients within half an order of magnitude (5×10^{-7} m^2/s) of each other. The other tests demonstrate the range of coefficients that can be studied using this technique.

The in-flow and in-bed diffusion coefficients are similar; however the in-bed coefficients are generally higher than the equivalent in-flow coefficients. This is due to the nature of the exchange process. The in-flow coefficient is a product of the exchange throughout the bed, whereas the in-bed coefficient (as shown in Figure 3(a)) is dependent on the depth of the instrument within the bed, and predominantly shows the exchange at the level of the instrument head, not an average of the exchange throughout the whole depth, since the exchange is assumed to be vertical only

The effect of sediment depth is one of many possible avenues open to exploration with the erosimeter system. Others are the effects of initial pollutant location (whether there is a different exchange coefficient into and out of the bed) and the effects chemical sorption may have on exchange. One parameter that could not be examined within the erosimeter is bed forms. Small bed forms could be created within the sediment surface, however these would not be of any significant height and may alter the fluid flow characteristics within the system creating unreliable data.

5 CONCLUSION

The tests presented in this paper indicate that the EROSIMESS-System can be used to study hyporheic exchange for a wide range of parameters. It provides a repeatable, efficient alternative to using a laboratory flume. A number of tests have been presented that compare well with the scaling relationship proposed by O'Connor and Harvey (2008), which in turn was derived from previous laboratory flume studies. The scatter of erosimeter derived exchange coefficients is within the scatter of the previous flume studies, when plotted against the scaling relationship.

There is the potential for the erosimeter system to be used to study many factors that affect hyporheic exchange, including the effects of chemical sorption and the initial location of the tracer. The effects of sediment depth and stratification on hyporheic exchange could also be examined with slight modifications to the base unit. The ability to generate a wide range of bed shear velocities within the erosimeter, the small quantities of sediment and fluid required and the reduced testing time, whilst still achieving full scale hyporheic exchange make it an ideal alternative to traditional laboratory flumes.

REFERENCES

Crank, J. (1975), The Mathematics of Diffusion, 2nd edition, Oxford University Press, Oxford, UK, pp 20-21.

Elliott, A. H., and Brooks, N. H. (1997b), Transfer of nonsorbing solutes to a streambed with bedforms: Laboratory experiments, *Water Resources Research*, 33, 137-151.

Jubb, S., Guymer, I., Licht, G., and Prochnow, J. (2001), Relating Oxygen Demand to Flow: Development of an in situ sediment oxygen demand measurement device. *Water Science Technology*, 43(5), 203-210.

Lai, J. L., Lo, S. L., and Lin, C. F. (1994), Effects of hydraulic and medium characteristics on solute transfer to surface runoff, *Water Science Technology*, 30, 145-155.

Liem R., Spork, V., and Koengeter, J. (1997), Investigations on Erosional Processes of Cohesive Sediment Using an In Situ Measuring Device, *International Journal of Sediment Research*, 12(3), 139-147.

Marion, A., Bellinello, M., Guymer, I., and Packman, A. (2002), Effect of bed-form geometry on the penetration of non-reactive solutes into a streambed, *Water Resources Research*, 38(10), 1209, doi:10.1029/2001WR000264.

Nagaoka, H., and Ohgaki, S. (1990), Mass transfer mechanism in a porous riverbed, *Water Research*, 24, 417-425.

O'Connor, B. L., and Harvey, J. W. (2008), Scaling hyporheic exchange and its influence on biogeochemical reactions in aquatic ecosystems, *Water Resources Research*, Vol. 44, W12423, doi:10.1029/2008WR007160.

Packman, A. I., Brooks, N. H. and Morgan, J. J. (2000), Kaolinite exchange between a stream and streambed: laboratory experiment and validation of a colloid transport model, *Water Resources Research*, 36, 2363-2372.

Packman, A. I., and MacKay, J. S. (2003), Interplay of stream-subsurface exchange, clay particle deposition, and stream bed evolution, *Water Resources Research*, 39(4), 10.1029/2002WR001432, 4-1-4-9.

Packman, A. I., Salehin, M. and Zaramella, M. (2004), Hyporheic exchange with gravel beds: Basic hydrodynamic interactions and induced advective flows, *Journal of Hydraulic Engineering*, 130, 647-656.

Rehg, K. J., Packman, A. I., and Ren, J. (2005), Effects of suspended sediment characteristics and bed sediment transport on streambed clogging, *Hydrological Processes*, 19, 413-427, doi:10.1002/hyp.5540.

Ren, J., and Packman, A. I. (2004), Stream-subsurface exchange of zinc in the presence of silica and kaolinite colloids, *Environmental Science Technology*, Vol. 38, 6571-6581, doi:10.1021/es035090x.

Richardson, C. P., and Parr, A. D. (1988), Modified Fickian model for solute uptake by runoff, Journal of *Environmental Engineering*, 114, 792-809.

Spork, V., Jahnke, J., Prochnow, J. and Koengeter, J. (1997), Stabilising Effect of Benthic Algae on Cohesive Sediments, *International Journal of Sediment Research*, Vol. 12, 3.

Tonina, D., and Buffington, J. M. (2007), Hyporheic exchange in gravel bed rivers with pool-riffle morphology: Laboratory experiments and three-dimensional modelling, *Water Resources Research*, Vol. 43, W01421, doi:10.1029/2005WR004328.

Appendix C

Vector fields

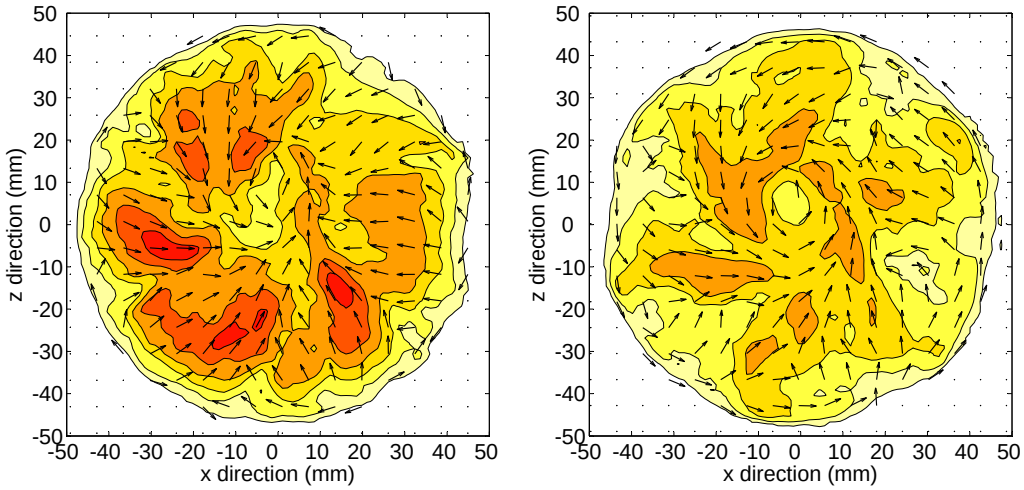

(a) 23mm above fixed bed, 128rpm

(b) 13mm above fixed bed, 125rpm

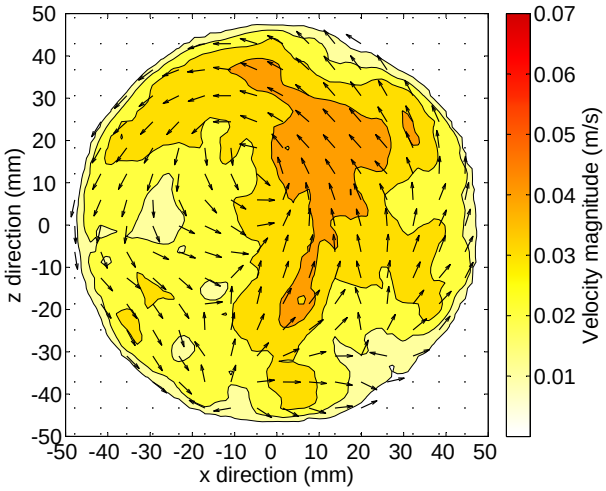

(c) 3mm above fixed bed, 124rpm

Figure C.1: Time averaged HLS, Dial = 190

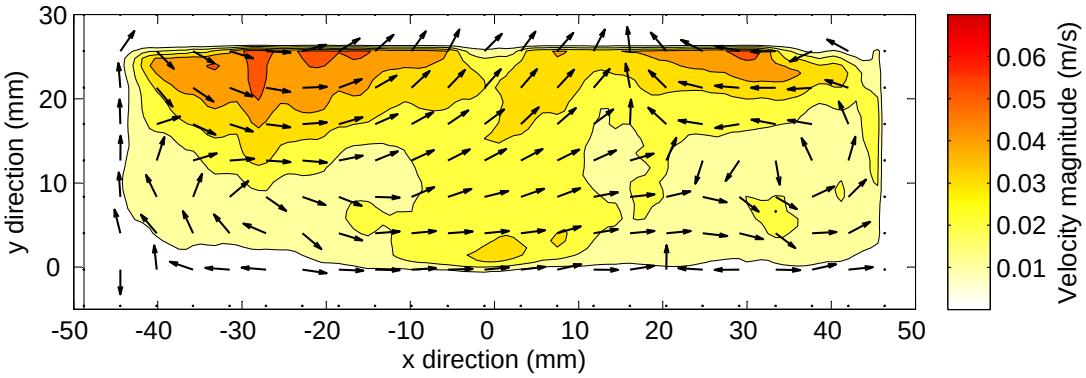

(a) Fixed bed, 109rpm

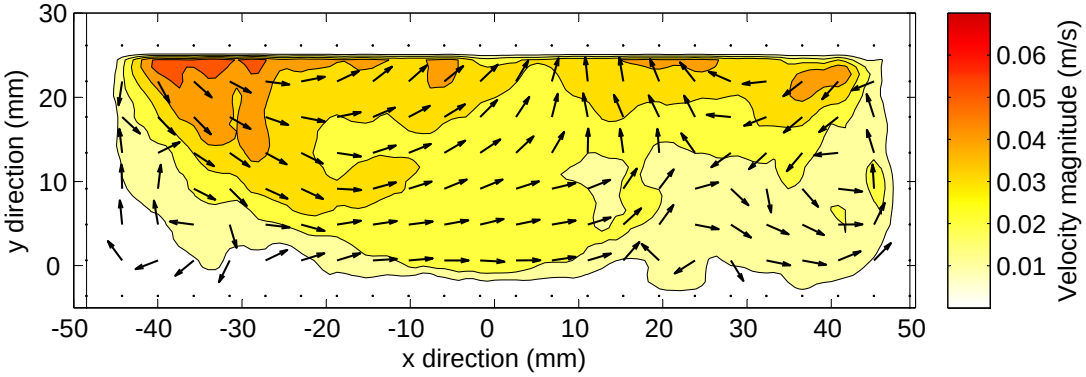

(b) Mobile bed, 109rpm

Figure C.2: Time averaged VLS, Dial = 190

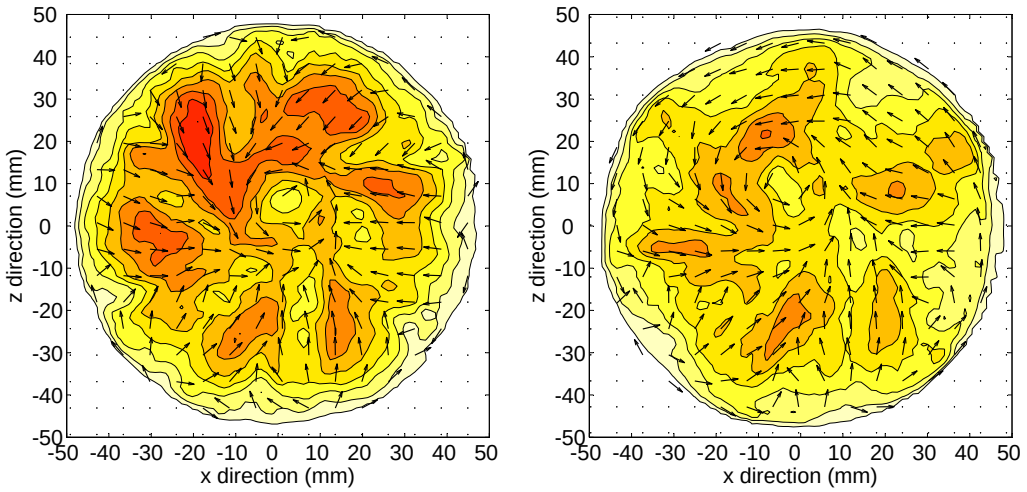

(a) 23mm above fixed bed, 180rpm

(b) 13mm above fixed bed, 178rpm

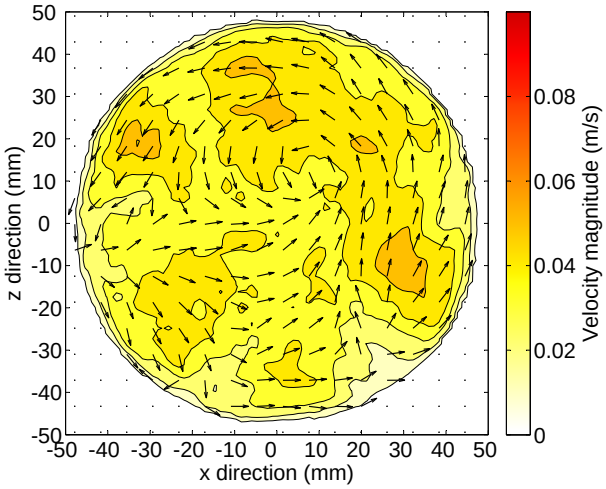

(c) 3mm above fixed bed, 179rpm

Figure C.3: Time averaged HLS, Dial = 270

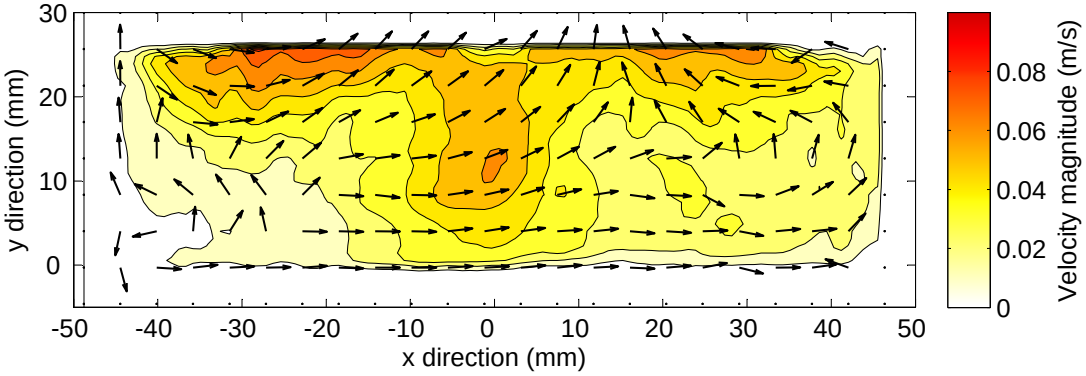

(a) Fixed bed, 161rpm

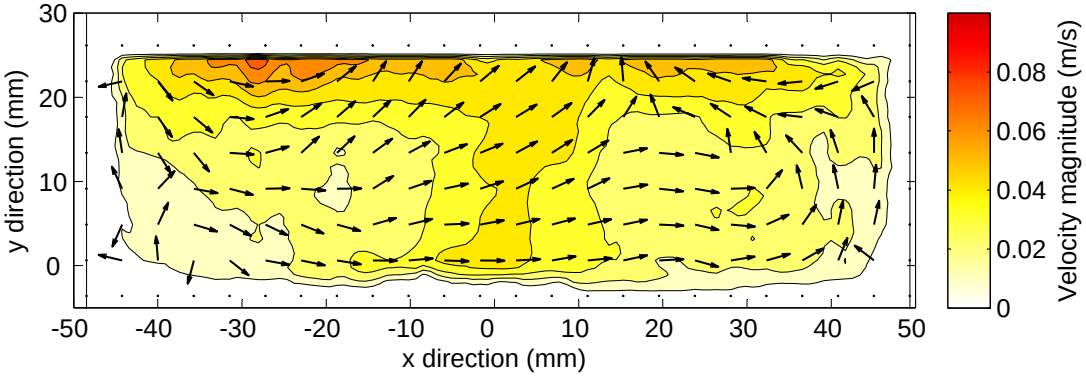

(b) Mobile bed, 162rpm

Figure C.4: Time averaged VLS, Dial = 270

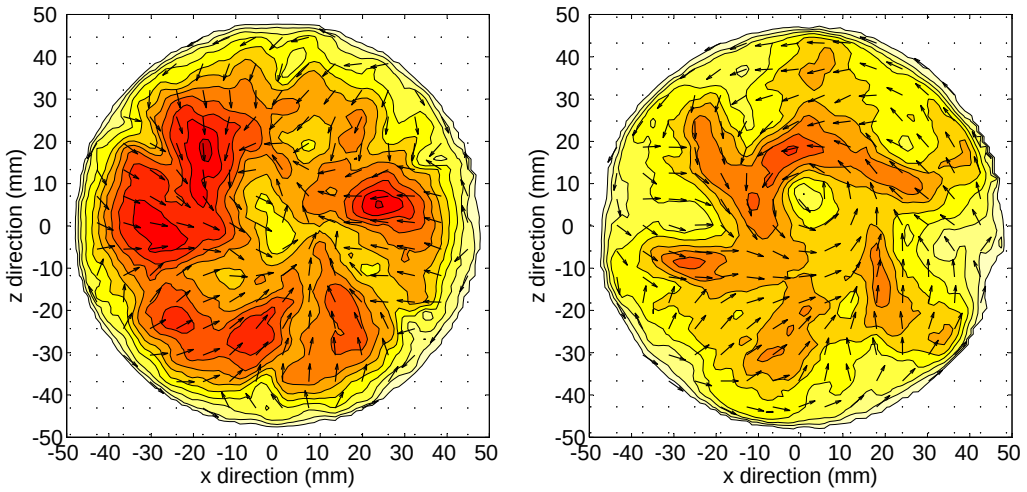

(a) 23mm above fixed bed, 227rpm

(b) 13mm above fixed bed, 225rpm

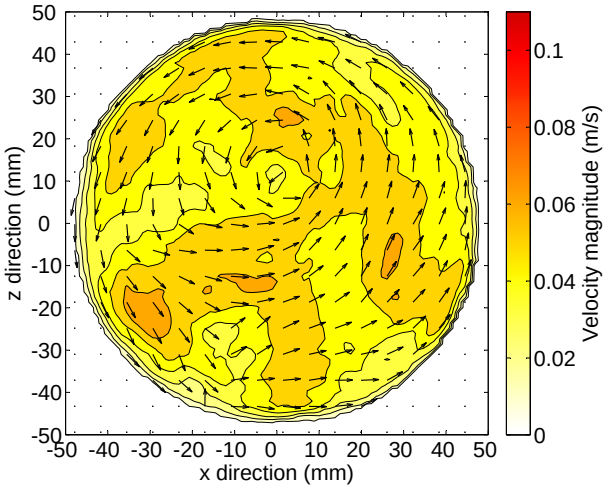

(c) 3mm above fixed bed, 226rpm

Figure C.5: Time averaged HLS, Dial = 340

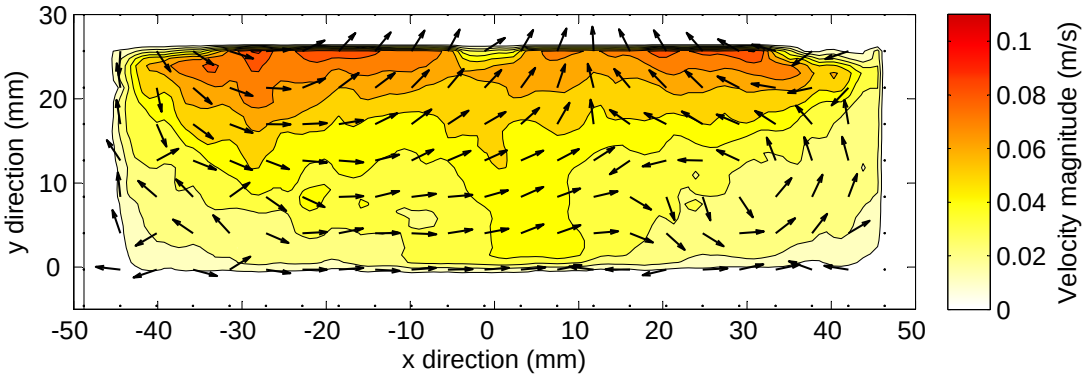

(a) Fixed bed, 206rpm

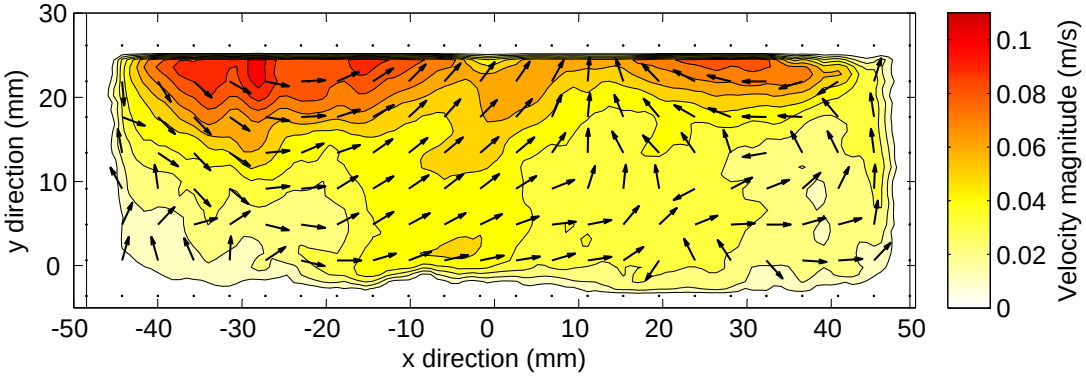

(b) Mobile bed, 208rpm

Figure C.6: Time averaged VLS, Dial = 340

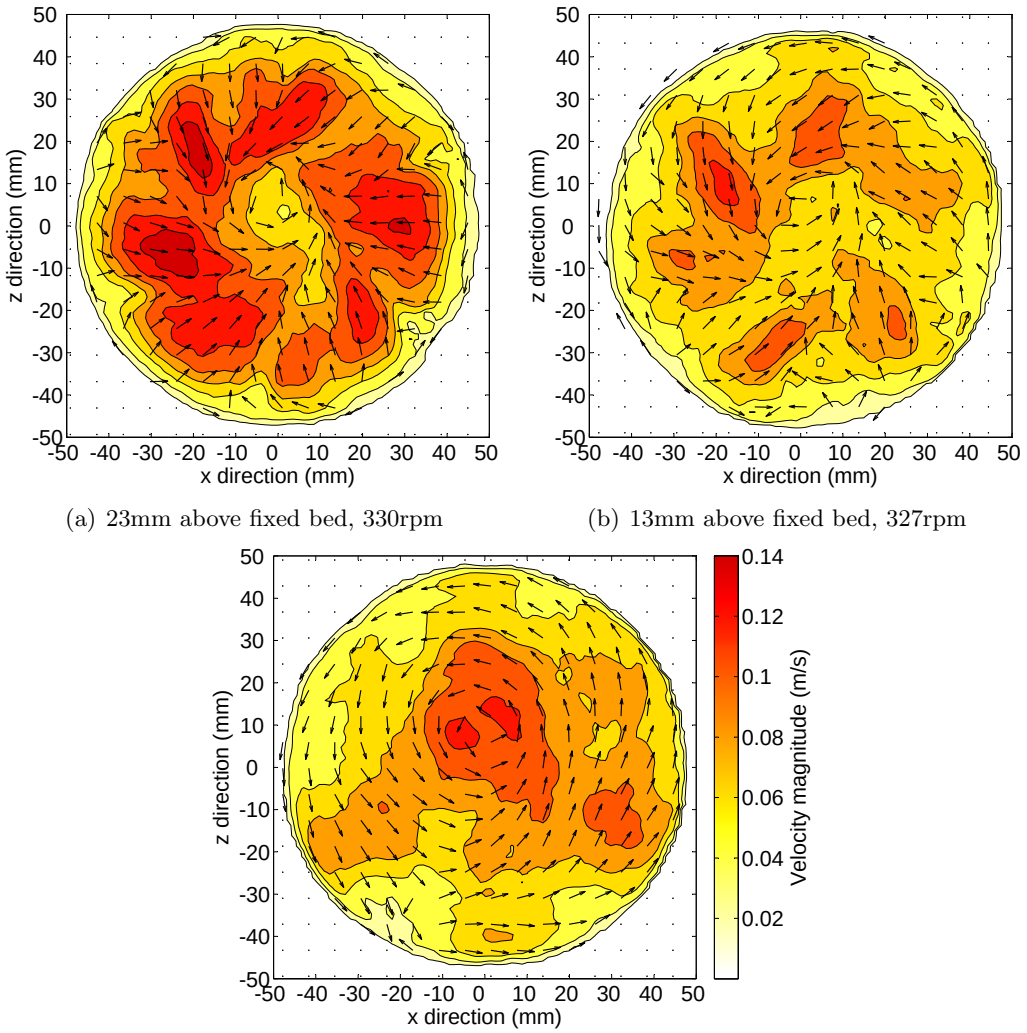

(a) 23mm above fixed bed, 330rpm

(b) 13mm above fixed bed, 327rpm

(c) 3mm above fixed bed, 329rpm

Figure C.7: Time averaged HLS, Dial = 490

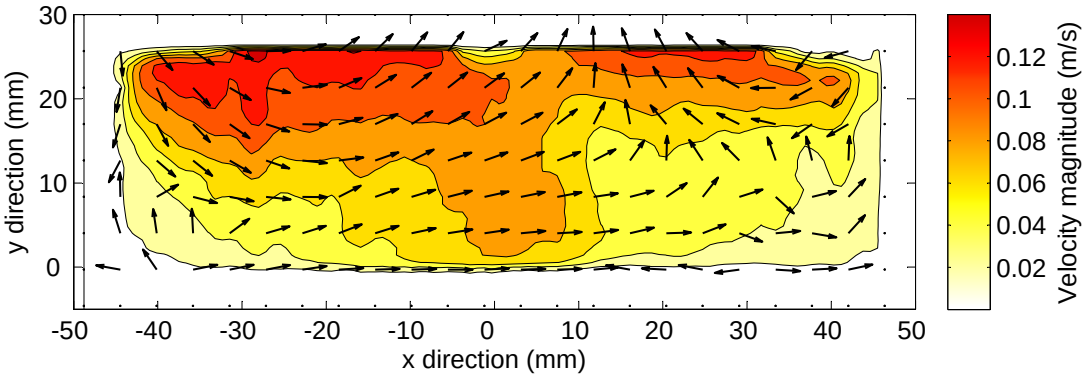

(a) Fixed bed, 312rpm

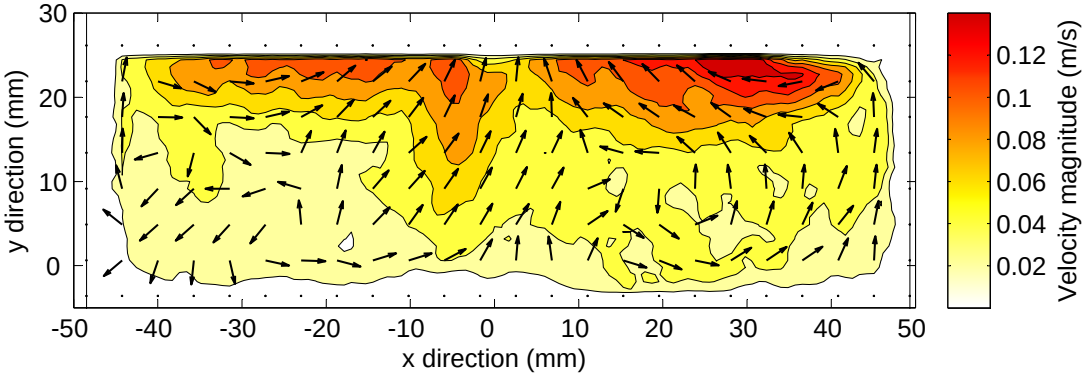

(b) Mobile bed, 308rpm

Figure C.8: Time averaged VLS, Dial = 490

Appendix D

Full Experimental Results and Parameters

Test name	WC	D (10^{-8}m^2/s) -0.032m	-0.066m	-0.100m	-0.134m	-0.0405m
40_5000_1	192	S	485	146	11.6	–
40_5000_2	189	S	1360	408	349	–
40_5000_3	165	S	781	142	52.4	–
30_5000_1	129	S	379	71.8	17.3	–
30_5000_2	145	S	867	58.8	17.2	–
20_5000_1	61.9	S	321	90.4	×	–
20_5000_2	78.0	1200	132	12.1	1.21	–
15_5000_1	38.0	191	53.0	4.39	0.292	–
15_5000_2	71.9	279	48.5	6.98	0.671	–
10_5000_1	41.3	162	43.3	1.42	0.262	–
10_5000_2	32.6	128	32.6	3.61	0.273	–
30_1850_1	×	S	49.0	5.94	2.02	–
30_1850_2	48.6	98.5	39.8	4.61	0.426	–
20_1850_1	20.6	34.4	10.6	1.19	0.314	–
20_1850_2	18.6	38.5	12.1	1.02	0.229	–
15_1850_1	8.79	S	13.4	0.775	0.163	–
15_1850_2	8.79	18.0	5.08	0.619	0.128	–
10_1850_1	2.92	S	1.01	0.118	NC	–
10_1850_2	3.28	9.57	1.73	0.186	NC	–
15_625_1	1.24	2.10	0.571	0.085	NC	–
15_625_2	0.957	1.87	0.516	0.103	NC	0.881
10_625_1	0.289	0.958	0.282	NC	NC	–
10_625_2	0.419	1.27	0.277	NC	NC	0.415
15_350_1	0.253	1.02	0.189	NC	NC	S
10_350_1	0.106	0.740	0.120	NC	NC	S
10_150_1	0.009	S	S	NC	NC	S

Table D.1: Experimentally derived diffusion coefficients given relative to the midpoint between the instruments used to obtain them

Symbol	Reason
–	No instrument at -0.032m (FOF3)
×	Instrument malfunction
S	Setup or instrument problem
NC	No concentration change during test

Table D.2: Symbols used in Table D.1 indicating reason why a coefficient could not be obtained

Test name	d_g (10^{-3}m)	K (10^{-10}m^2)	u_* (m/s)	D_{pred}, (2.51) (10^{-8}m^2/s)
40_5000_1	5.000	112	0.041	1170
40_5000_2	5.000	97.0	0.041	1070
40_5000_3	5.000	116	0.040	1170
30_5000_1	5.000	107	0.030	572
30_5000_2	5.000	102	0.030	585
20_5000_1	5.000	103	0.020	228
20_5000_2	5.000	102	0.020	233
15_5000_1	5.000	103	0.015	128
15_5000_2	5.000	108	0.015	134
10_5000_1	5.000	109	0.010	53.5
10_5000_2	5.000	109	0.010	51.9
30_1850_1	1.850	20.7	0.030	80.6
30_1850_2	1.850	20.3	0.030	80.6
20_1850_1	1.850	21.1	0.020	33.0
20_1850_2	1.850	20.6	0.020	32.3
15_1850_1	1.850	20.2	0.015	18.4
15_1850_2	1.850	19.6	0.015	17.9
10_1850_1	1.850	20.4	0.010	7.10
10_1850_2	1.850	20.3	0.010	6.84
15_625_1	0.625	3.15	0.015	2.21
15_625_2	0.625	3.18	0.015	2.26
10_625_1	0.625	3.20	0.010	0.915
10_625_2	0.625	3.21	0.010	0.876
15_350_1	0.350	1.69	0.015	0.813
10_350_1	0.350	1.07	0.010	0.248
10_150_1	0.150	0.46	0.010	0.0712

Table D.3: Experimental parameters

Appendix E

Further Comparison of Model Simulations and Experimental Data

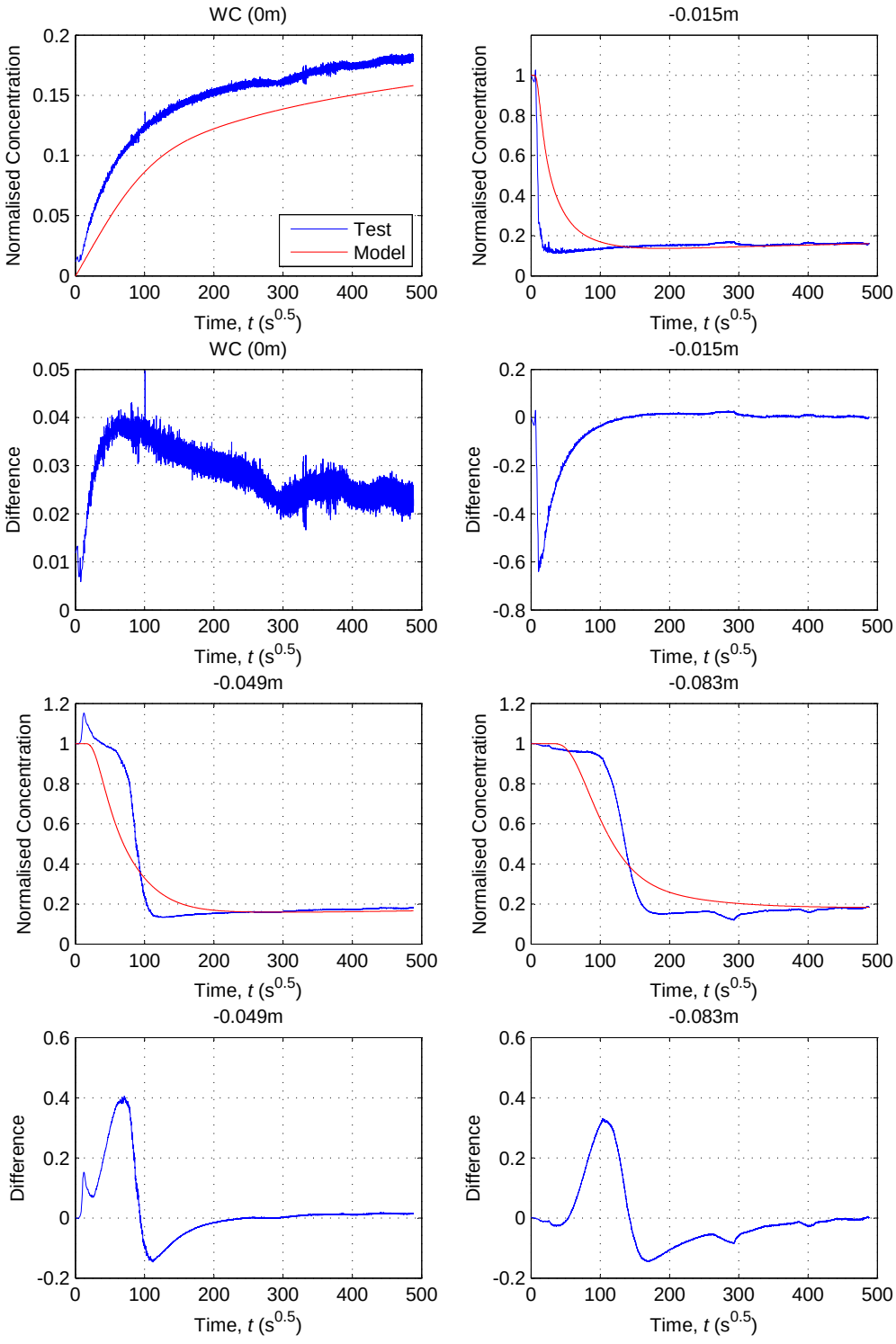

Figure E.1: Comparison of 7 zone model simulation using experimental coefficients with experimental profiles for test 20_1850_2 (WC, −0.015, −0.049 and −0.083m profiles)

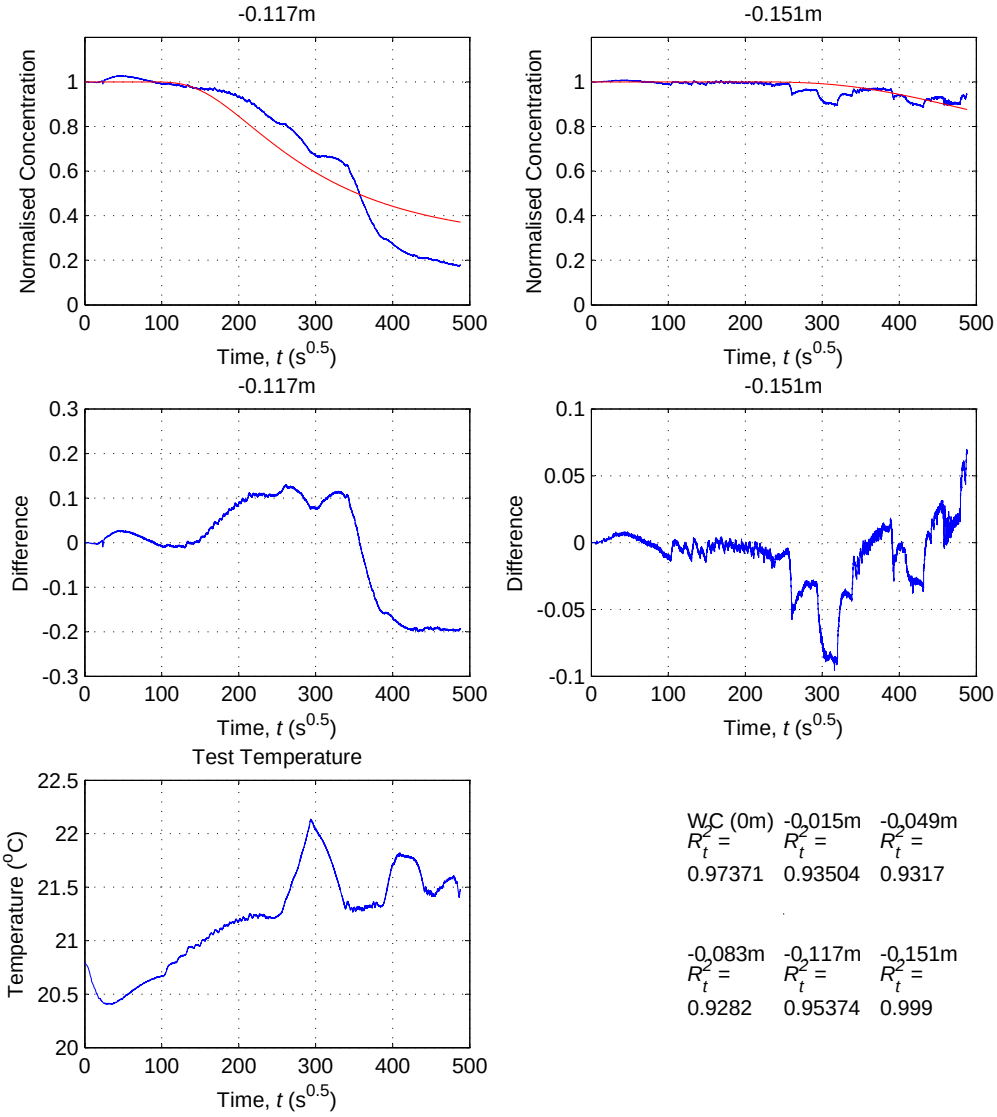

Figure E.2: Comparison of 7 zone model simulation using experimental coefficients with experimental profiles for test 20_1850_2 (-0.117 and -0.151m profiles) and R_t^2 coefficients for all profiles

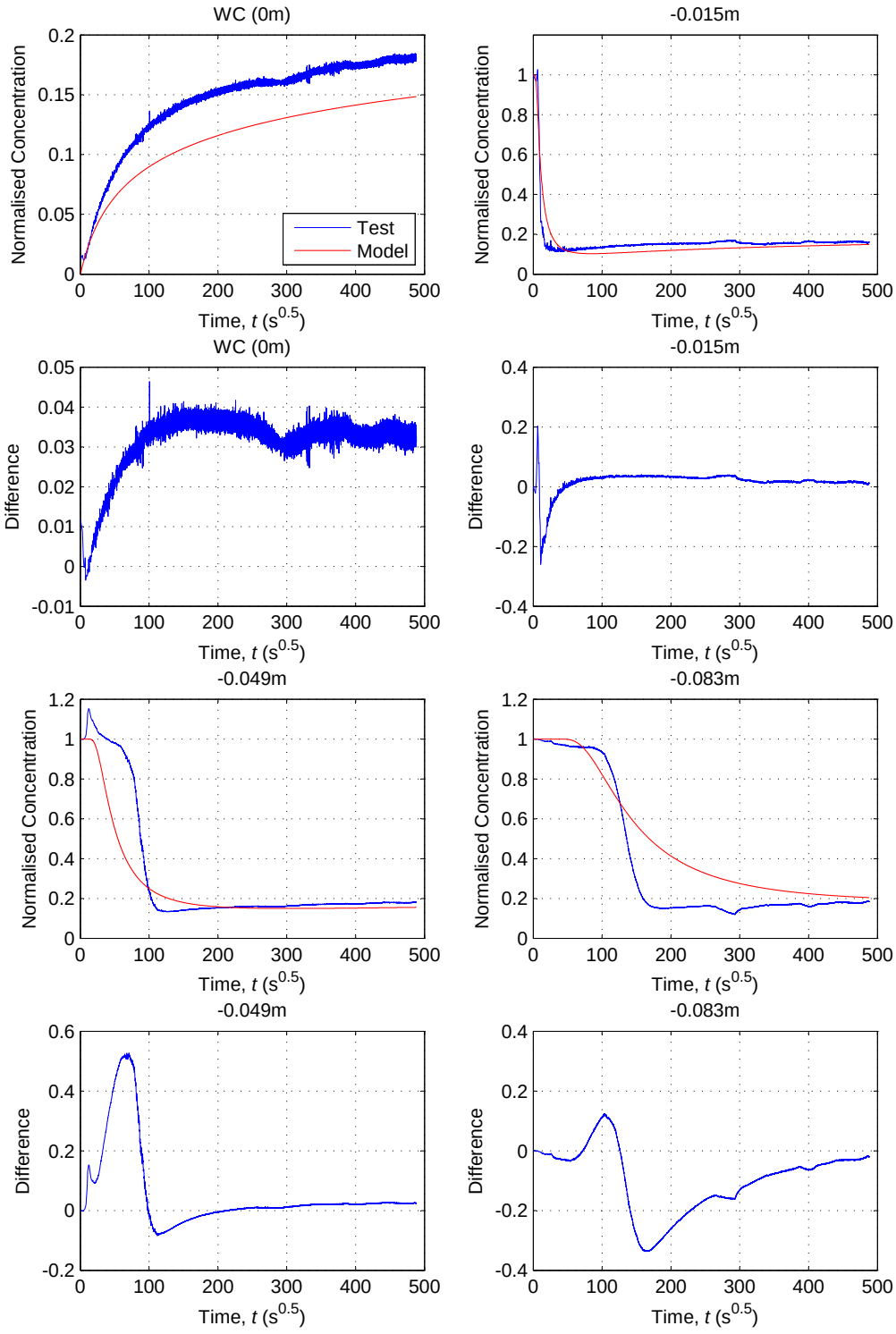

Figure E.3: Comparison of model simulation using (5.1) with $D_{max} = D_{pred}$ and experimental profiles for test 20_1850_2 (WC, −0.015, −0.049 and −0.083m profiles)

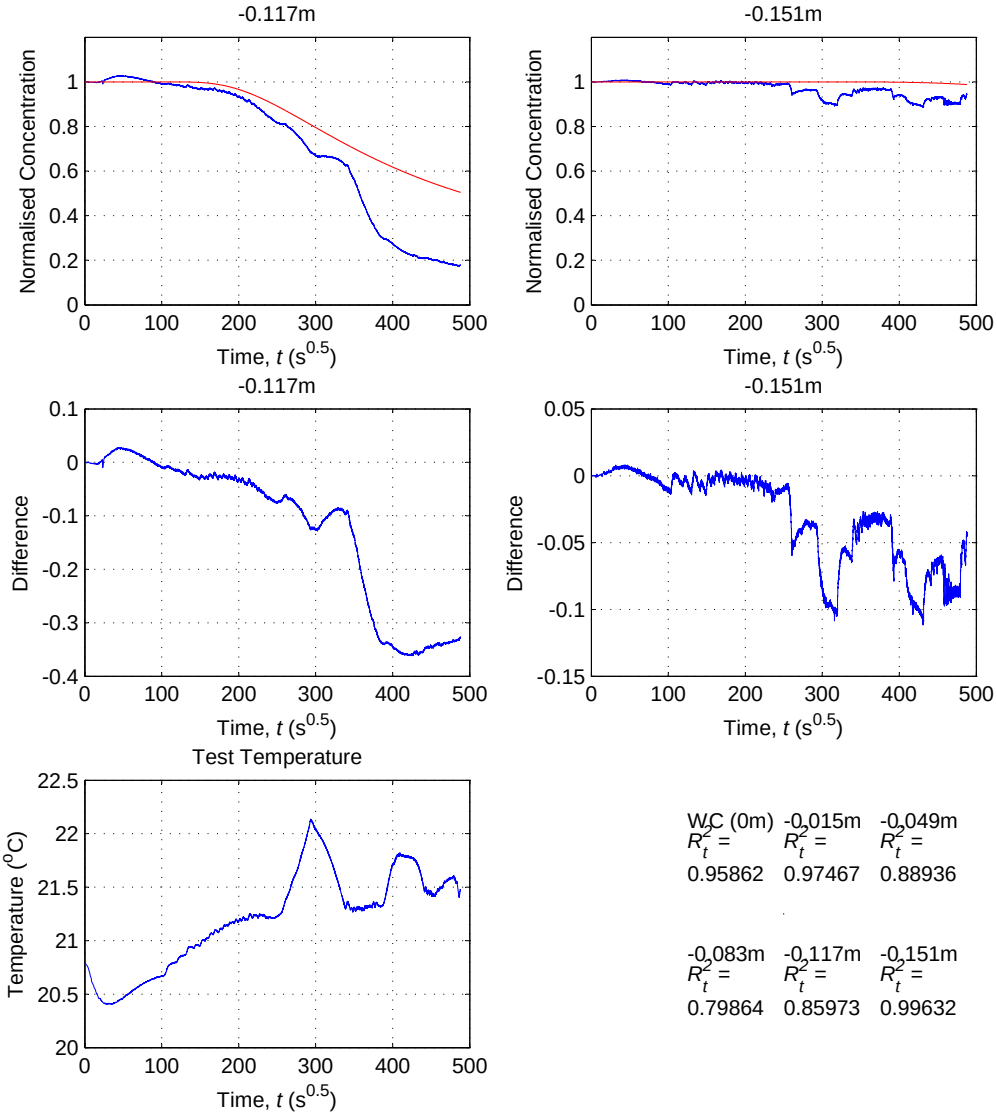

Figure E.4: Comparison of model simulation using (5.1) with $D_{max} = D_{pred}$ and experimental profiles for test 20_1850_2 (-0.117 and -0.151m profiles) and R_t^2 coefficients for all profiles

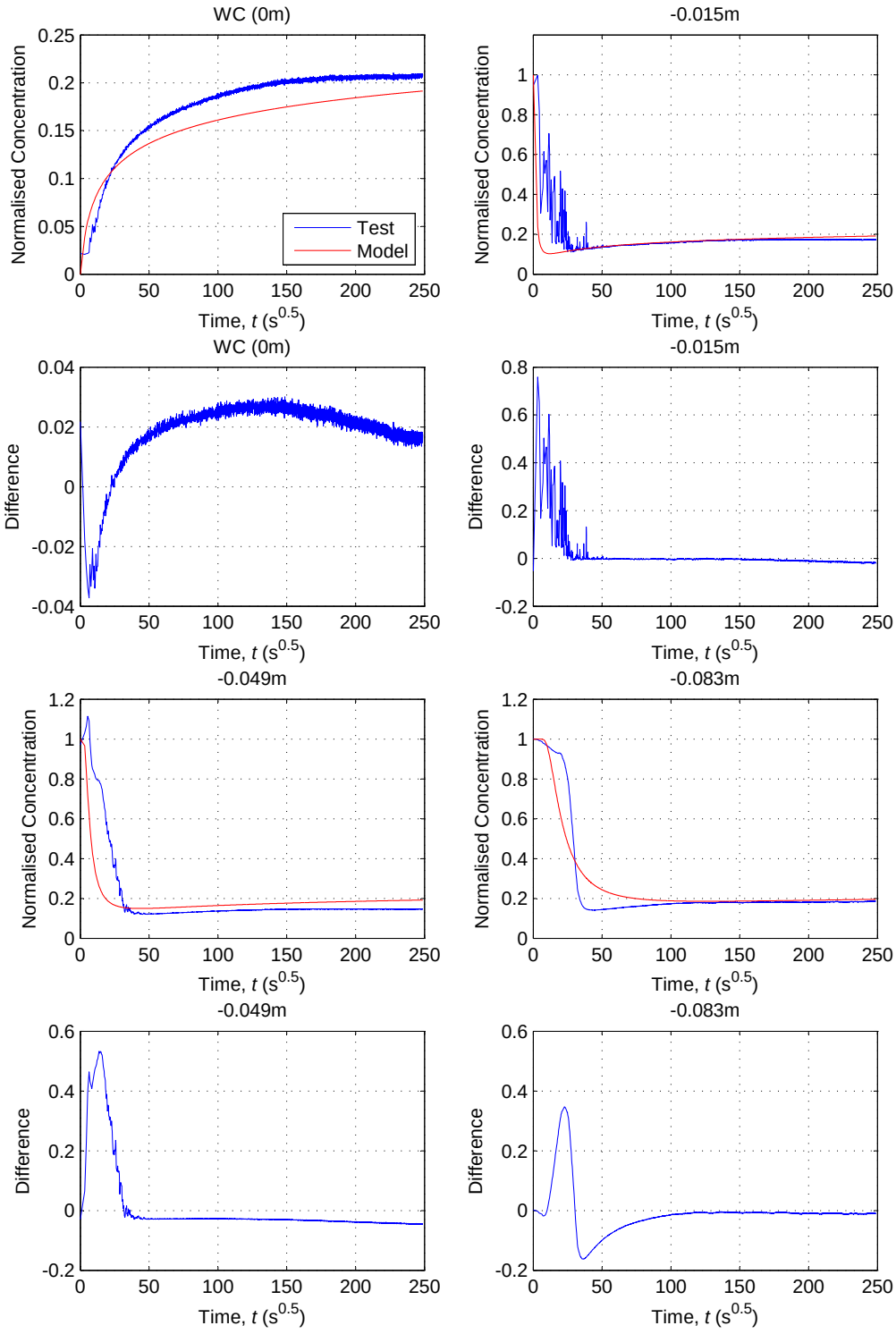

Figure E.5: Comparison of model simulation using (5.3) with experimental profiles for test 30_5000_2 (WC, −0.015, −0.049 and −0.083m profiles)

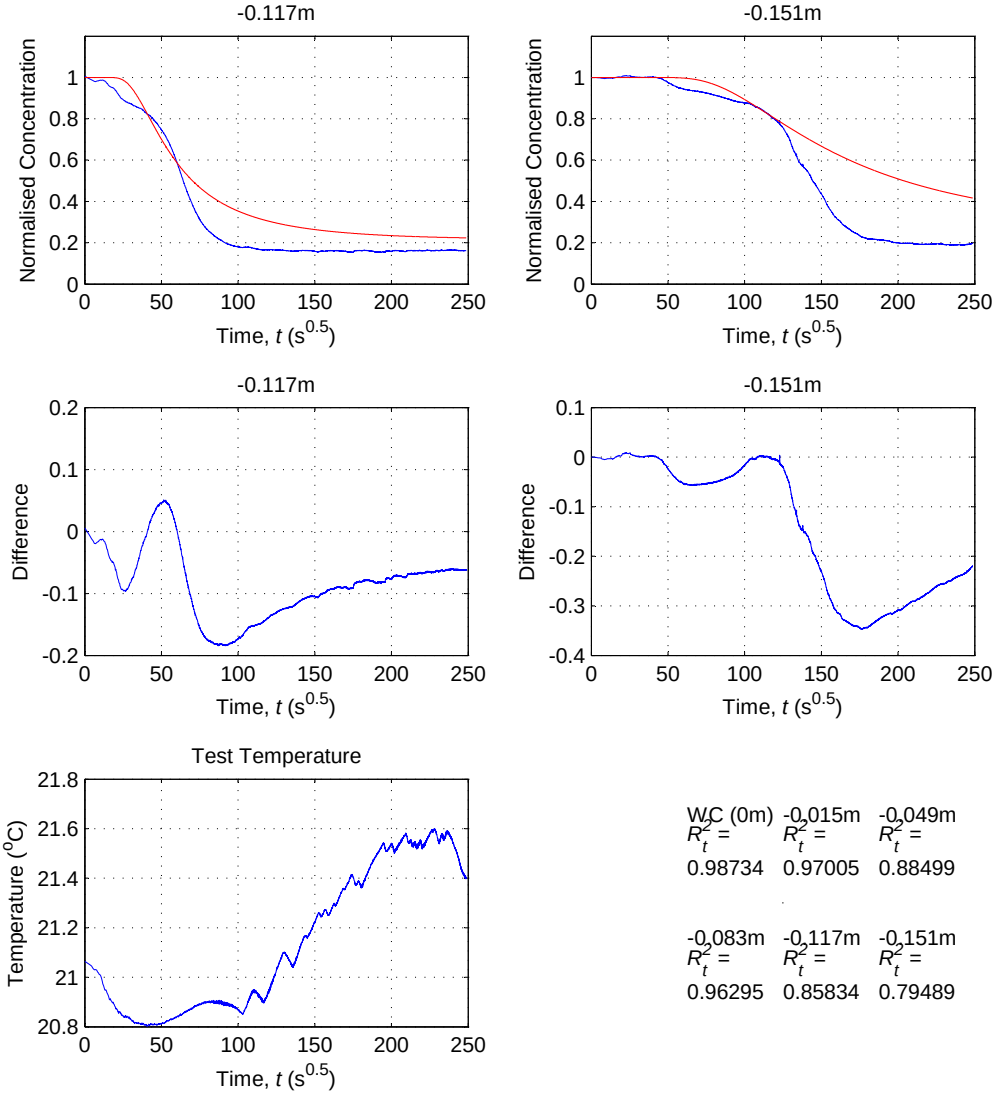

Figure E.6: Comparison of model simulation using (5.3) with experimental profiles for test 30_5000_2 (-0.117 and -0.151m profiles) and R_t^2 coefficients for all profiles

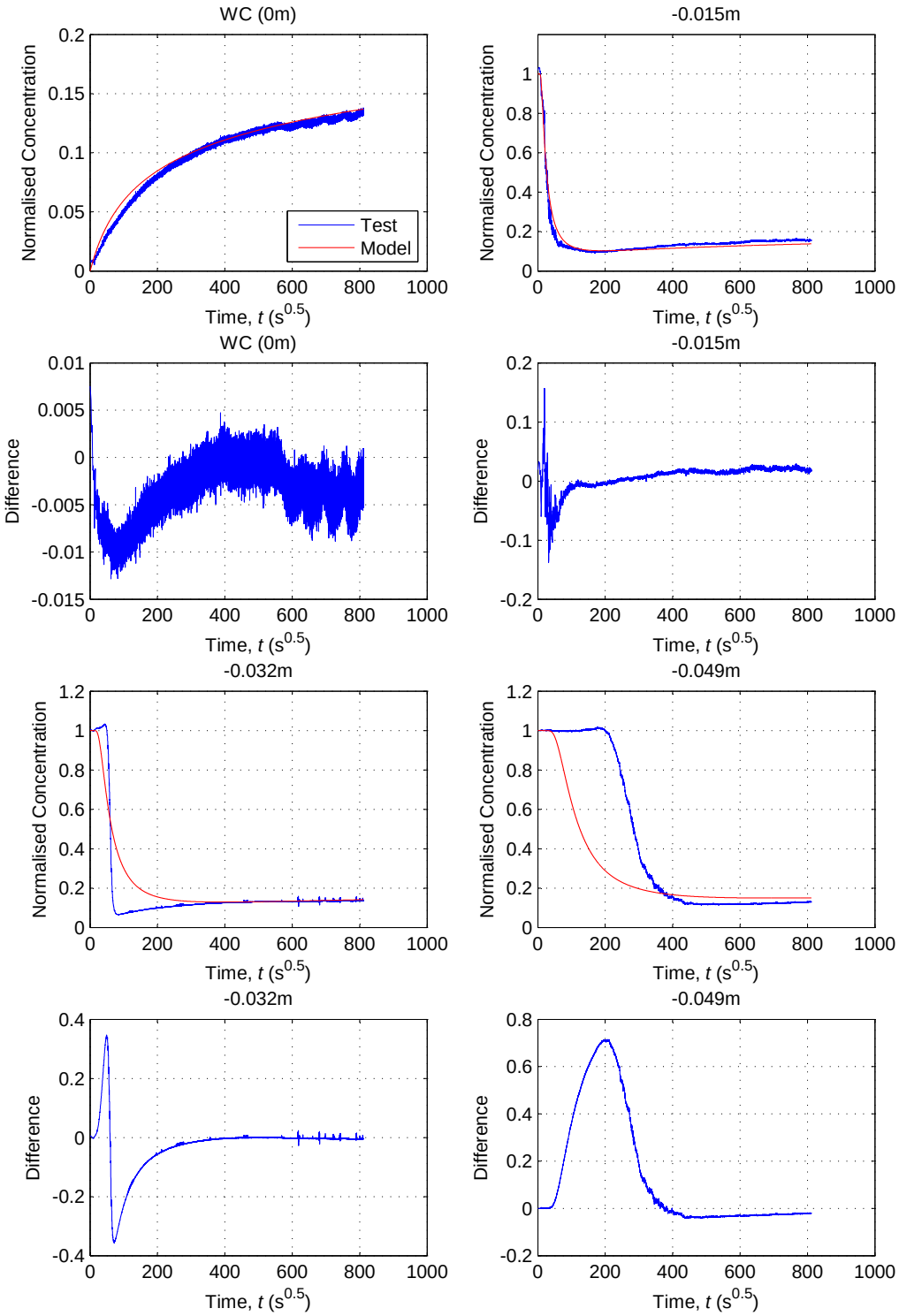

Figure E.7: Comparison of model simulation using (5.3) with experimental profiles for test 15_625_2 (WC, −0.015, −0.049 and −0.083m profiles)

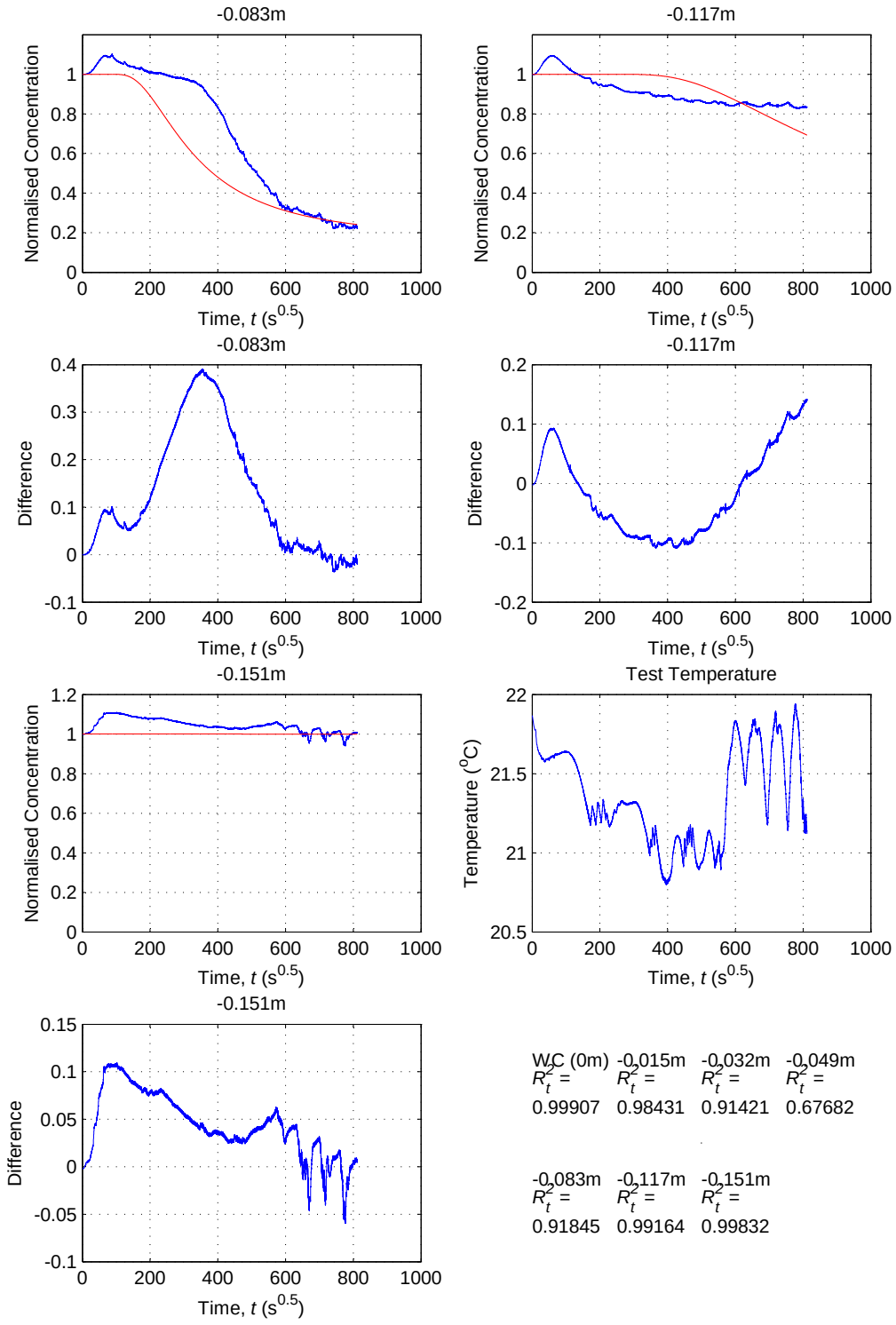

Figure E.8: Comparison of model simulation using (5.3) with experimental profiles for test 15_625_2 (-0.117 and -0.151m profiles) and R_t^2 coefficients for all profiles